UNIVERSITY OF SOUTHAMPTON

Modelling of reactive absorption in gas-liquid flows on structured packing

by

Jason J. Cooke

Thesis for the degree of Doctor of Philosophy

in the
Faculty of Engineering and the Environment
School of Engineering Sciences

May 2016

UNIVERSITY OF SOUTHAMPTON

ABSTRACT

FACULTY OF ENGINEERING AND THE ENVIRONMENT
SCHOOL OF ENGINEERING SCIENCES

Doctor of Philosophy

MODELLING OF REACTIVE ABSORPTION IN GAS-LIQUID FLOWS ON STRUCTURED PACKING

by Jason J. Cooke

Carbon capture & storage (CCS) is at the technological forefront in the challenge of reducing carbon emissions. The most viable approach to implementing CCS within existing coal and natural gas power stations is the post-combustion capture of CO_2 by absorption into amine solutions within packed column absorbers.

CFD modelling is an important aspect in the design and optimisation of this process. However, significant challenges arise due to the large range of spatial scales and the complexity of the physics being modelled. Therefore, simplification of the problem is required to complete such simulations using the computational resources currently available.

This thesis explores some of the approaches used to model flow within packed columns. It concludes that, with current computing resources, standard modelling approaches are not viable for large scale simulations of CCS. This led to the development of the Enhanced Surface Film (ESF) model. The ESF approach was able to simulate chemically enhanced absorption of gaseous species into thin liquid films. The method significantly reduced the computational resources required and is a significant step to enable future researchers to model larger domains in CCS.

The ESF approach has wide ranging applications due to the ubiquitous nature of liquid films across the industrial and environmental sectors. In many industries the dynamics of thin liquid films play a crucial role in the overall performance. Further applications may include thin film microreactors, surface coating, biofluids and medical applications.

Acknowledgements

First of all, I would like to thank my supervisors, Dr Lindsay-Marie Armstrong and Dr. Edward Richardson, for all of their support and invaluable advice.

I am eternally grateful to my girlfriend, Florinela for all of her support, love and friendship over the years. I am happy, and I'm sure she will be, that I will be able to spend my weekends with her now that this thesis is complete. Last but not least, I would like to thank my family for everything they have done for me and for helping me to achieve my goals.

I also acknowledges the use of the IRIDIS High Performance Computing Facility, and associated support services at the University of Southampton, in the completion of this work.

Declaration of Authorship

I, Jason J. Cooke, declare that this thesis and the work presented in it are my own and has been generated by me as the result of my own original research.

MODELLING OF REACTIVE ABSORPTION IN GAS-LIQUID FLOWS ON STRUCTURED PACKING

I confirm that:

- This work was done wholly or mainly while in candidature for a research degree at this University.
- Where any part of this thesis has previously been submitted for a degree or any other qualification at this University or any other institution, this has been clearly stated.
- Where I have consulted the published work of others, this is always clearly attributed.
- Where I have quoted from the work of others, the source is always given. With the exception of such quotations, this thesis is entirely my own work.
- I have acknowledged all main sources of help.
- Where the thesis is based on work done by myself jointly with others, I have made clear exactly what was done by others and what I have contributed myself.
- Parts of this work have been published as given in the list of publications.

Signed: _____

Date: _____

Publications

Journal Articles

Cooke, J., Armstrong, L., Luo, K. & Gu, S. (2014) *Adaptive Mesh Refinement of Gas-Liquid Flow on an Inclined Plane.* Journal of Computers & Chemical Engineering, 60, 297-306.

Conference Papers

Cooke, J., Gu, S., Armstrong, L. & Luo, K. (2012) *Gas-Liquid Flow on Smooth and Textured Inclined Planes.* World Academy of Science, Engineering and Technology, 68, 1712-1719.

Contents

List of Figures

List of Tables

Nomenclature

A_w	Wetted area
a_w	Specific wetted area
A_i	Interfacial area
a_i	Specific interfacial area
AMP	Isobutanolamine
AMR	Adaptive mesh refinement
b	Reactants mole ratio
C	Concentration
Ca	Capillary number
CCS	Carbon Capture and Storage
CFD	Computational Fluid Dynamics
CSF	Continuum surface force
D	Diffusion coefficient
DEA	Diethanolamine
DTSF	Diffusion through Stagnant Film
E	Enhancement factor
E_i	Instantaneous enhancement factor
ESF	Enhanced Surface Film
G	Gas-phase
$\mathcal{H}$	Characteristic thickness
Ha	Hatta number
He	Henry's constant
HETP	Bed height equivalent to a theoretical plate
int	Liquid interface
IPCC	Intergovernmental Panel on Climate Change
k	Reaction constant
k_{avg}	Average mass transfer coefficient
k_G	Gas-side mass transfer coefficient
k_L	Liquid-side mass transfer coefficient
K_G	Overall mass transfer coefficient
$\mathcal{L}$	Characteristic length
L	Liquid-phase

LBM	Lattice Boltzmann Method
LMPD	Log mean pressure difference
MEA	Monoethanolamine
MDEA	Methyldiethanolamine
EMCD	Equi-Molar Counter Diffusion
N	Flux
$\overline{p}$	Depth-averaged pressure
r	Forward reaction rate
Re	Reynolds number
REUs	Representative elementary units
RST	Reynolds Stress Transport
t_H	Liquid-film exposure time
$t_{H,SV}$	Liquid-film exposure time (Calculated using surface velocity)
$t_{H,RT}$	Liquid-film exposure time (Calculated using residence-time equation)
τ	Residence time
$\overline{u}$	Depth-averaged velocity
u''	Deviation from depth-averaged velocity
We	Weber number
VOF	Volume-of-fluid

α	Volume fraction
α_f	Wetted fraction
δ	Delta function
δ_G	Two-film theory gas film thickness
δ_L	Two-film theory liquid film thickness
δ_n	Threshold film thickness
Δ_x	Cell length
ϵ	Lubrication parameter
κ	Curvature
σ	Surface tension
Θ	Contact time
θ	Plate inclination angle
θ_w	Static contact angle

Chapter 1

Introduction

1.1 Carbon Capture and Storage (CCS)

Clean coal technologies encompass a wide range of engineering solutions developed to reduce the level of pollutant gases released into the environment. A fairly recent development within this field, namely Carbon Capture & Storage (CCS), involves pre-combustion or post-combustion processes to separate CO_2 from carbon-rich fossil fuels. The resulting CO_2 is then stored to prevent it from entering the atmosphere. This research will focus on the CFD modelling of post-combustion capture of CO_2 utilising amine solutions within packed columns.

1.2 CCS with Packed Columns

CCS using packed columns involves the capture of CO_2 using an amine solution, usually monoethanolamine (MEA). Aqueous MEA undergoes a reversible reaction with CO_2, whereby the chemical equilibrium and mass transfer rates are dependent upon many factors. CO_2 is removed from exhaust gases in the absorber, where cooled MEA flows counter-current to the gas flow. CO_2 is subsequently removed from the solution in a stripper using a counter-current flow of steam [5]. The amine solution is heated by the stream to shift the chemical equilibrium of the system. The regenerated MEA is cooled before re-entering the cycle. A diagram of a typical absorber and stripper configuration for carbon capture is shown in Figure 1.1.

Packed columns are used to enhance heat and mass transfer by providing large gas-liquid interfacial areas. Packing materials within the packed columns come in two distinct categories; structured and unstructured. Structured packing is optimal since it provides high mass transfer efficiency and low pressure drop within the columns.

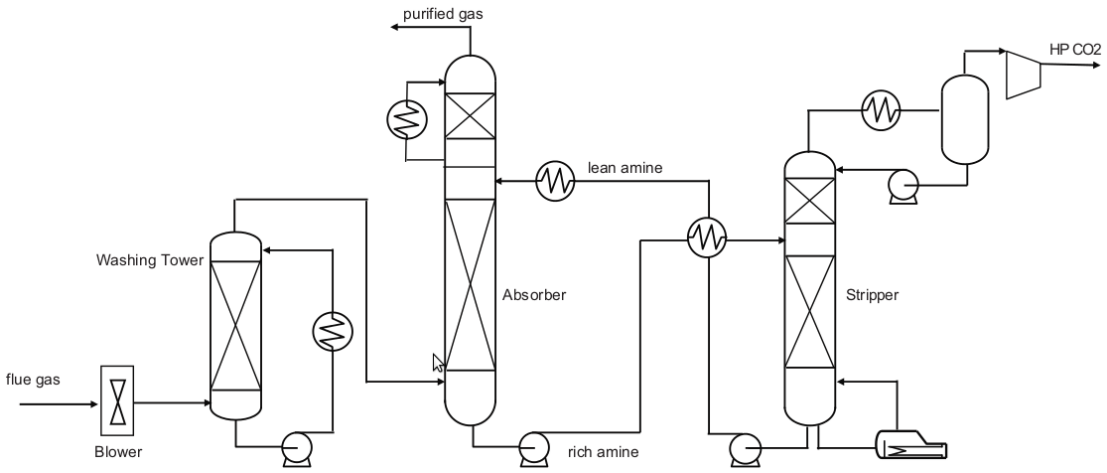

FIGURE 1.1: CO_2 absorber and stripper (image adapted from L. Raynal, P. A. Bouillon, A. Gomez, and P. Broutin, "From MEA to demixing solvents and future steps; a roadmap for lowering the cost of post-combustion carbon capture," *Chemical Engineering Journal*, vol. 171, pp. 742-752, 2011 [1])

The efficiency with which CO_2 is absorbed is an important factor in the design process of packed columns, since greater efficiencies means that the columns can be smaller, reducing the capital investment required. Smaller columns would result in a reduced pressure drop over the entire structure, which is beneficial because flue gases from power stations are at low pressures. The efficiency of the carbon capture process is affected by numerous factors, including the choice of solvent, packing, gas-liquid flow rates etc.

Structured packings usually consist of layers of corrugated metal sheets orientated with various inclination angles. This arrangement helps to promote gas-liquid mixing within the packing, increasing absorption rates. Figure 1.2 and Figure 1.3 show some typical unstructured and structured packings used for acid-gas absorption in packed columns.

(a) Single elements (b) Packed bed

FIGURE 1.2: Example of stainless steel unstructured packing IMTP 50 (images adapted from P. Alix and L. Raynal, "Liquid distribution and liquid hold-up in modern high capacity packings," *Chemical Engineering Research and Design*, vol. 86, no. 6, pp. 585-591, 2008. [2])

The design of packing materials is dependent on what type of mass transfer process they will be used for. Compromises must be made between the capacity and the efficiency

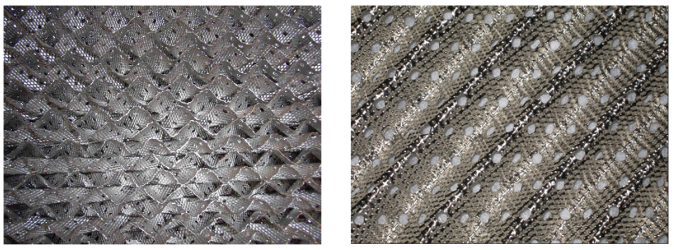

(a) Top view (b) Side view

FIGURE 1.3: Example of metallic structured packing MellapakPlus 252.Y. (images adapted from P. Alix and L. Raynal, "Liquid distribution and liquid hold-up in modern high capacity packings," *Chemical Engineering Research and Design*, vol. 86, no. 6, pp. 585 – 591, 2008. [2])

of the packing. High efficiency requires large surface areas to enhance the mass transfer process, but this in turn reduces the capacity of the column. Packed columns used in carbon capture are required to have a very low pressure drop ($< 100\,\text{mbar}$) because the flue gas is not pressurised prior to entering the absorber [2]. Packing which results in high gas-phase pressure drop would require the flue gas to be forced through the column using fans. This would increase the energy consumption of the process which is undesirable. Structured packings have been designed for low pressure drop applications and exhibit void fractions of approximately 90% [6]. These packings also exhibit relatively large geometric areas ranging from 250 to 750 m^2/m^3 [6], due to surface textures and corrugations of the sheets. This means that they can maintain good mass transfer efficiencies along with low pressure drop. Random packings generally have lower effective areas and exhibit higher pressure drop, making these less useful for carbon capture processes [7].

Alix & Raynal [2] performed a comparative study of a random packing to a structured packing. They concluded that the liquid distribution within both types of packing were good, which is required for maintaining the efficiency of the column. Overall, structured packings are more suited to CO_2 absorption in terms of pressure drop and efficiencies.

The main disadvantage of using carbon capture is the expense that is incurred due to the additional energy input required in the regeneration of CO_2 from the amine solution. Improvements in the efficiency of packed columns can help to reduce the costs involved and make the use of packed columns more economically viable.

1.3 Motivation for Research

Climate is a measure of the average weather patterns over a long period of time and it is known that natural variations in the global climate can occur. Glacial and interglacial periods are a result of periodic warming and cooling of the earth over millions of years. However, the dramatic increase in the rate of global temperatures increase in the last

50 years is unprecedented over millennia [8]. The Intergovernmental Panel on Climate Change (IPCC) [8] has estimated that the global temperature has risen by 0.65-1.06 °C between the period 1880-2012 and they state that it is 95-100% certain that human influences were the dominant cause global warming between 1951-2010.

Greenhouse gases are comprised mainly of carbon dioxide, methane, sulphur dioxide, nitrous oxide and fluorinated gases. The layer of greenhouse gases in the atmosphere absorbs heat which is reflected from the surface of the earth. This process increases the temperature of the earth and prevents the thermal radiation of the sun from being reflected back into space. It is known that naturally present greenhouse gases in the atmosphere are vital to the survival of life on the planet by maintaining a habitable climate.

Global manmade emissions of greenhouse gases has increased significantly over the last 100 years. According to Marland *et al.* [9], carbon emission have risen by about 90% between 1970 and 2011, increasing from approximately 4000 million metric tons of carbon to 9500 million metric tons of carbon per annum. Carbon dioxide emissions from fossil fuels and industrial processes account for 65% of total greenhouse gas emissions [8]. Therefore, the recent increase in carbon emissions has caused a significant increase in greenhouse gases within the atmosphere. The rising level of greenhouse gases in the atmosphere will increase the warming of the earth, which has been observed in temperature data, the reduction in arctic sea-ice and rising sea levels [8]. Furthermore, rising global temperatures can cause positive feedback, where CO_2 can be desorbed from the ocean as a direct result of higher oceanic temperatures. This is because the equilibrium between the concentration of CO_2 in the air and in the ocean is shifted by changes in temperature.

According to the IPCC [8], without climate change mitigation there could be an increase in global temperatures of 3.7-4.8 °C by the year 2100. This would significantly increase the adverse effects of higher global temperature, such as rising sea levels and unpredictable weather events. In order to reverse the effects of manmade global warming mitigation is required to reduce the levels of greenhouse gas emissions into the atmosphere.

Power and heat generation from the burning of coal, natural gas and oil is the largest source of global greenhouse gas emissions, accounting for 25% of emissions in 2010 [8]. Therefore, mitigation of carbon emissions from these sources could greatly reduce the impact of manmade emissions on climate change. Carbon Capture & Storage is one of the various methods that can be used to reduce the carbon footprint of the energy sector. These large, point sources of carbon dioxide can be targeted by CCS technologies to reduce the level of emission. This research will help to provide cost-effective solutions to the capture of CO_2 from flue gases emitted from both coal and natural gas power stations.

Agriculture, forestry and land use accounted for 24% of global greenhouse gas emissions in 2010, whilst industrial sources and transportation accounted for 21% and 14%, respectively. These sources of emissions are usually much smaller on an individual basis and so are less suited to current CCS technologies. For example, an individual car or factory will represent a tiny fraction of the total emissions for their respective sectors. Therefore, research is better focussed on the power and heat generation sector where an individual investment into CCS technology will represent a greater reduction in greenhouse gas emissions.

Stabilisation of CO_2 emissions at the current level would not result in the stabilisation of CO_2 concentration in the atmosphere, it would in fact continue to increase [8]. In order to stabilise or reduce the level of CO_2 in the atmosphere the level of emissions would need to be reduced significantly, by as much as 80% [8]. Therefore, in order to make a significant impact on mitigation of greenhouse gases in the atmosphere, CCS in the energy production sector would need to reduce emissions by a similarly large amount.

There are a vast range of CCS technologies, using methods including chemical and physical absorption, adsorption, cryogenics and membranes [10]. The advantage of post-combustion carbon capture methods, like those employed with packed columns, is that they can be retro-fitted to current coal/gas-fired power stations. This significantly reduces the capital investment, since no major modifications need to be made to existing power stations.

However, at the present time, these technologies consume large amounts of energy and they drain the electrical energy being produced by the power stations. As a result, this reduces the overall efficiency of power stations causing a surge in operating costs, which would inevitably be passed onto customers. This research topic is not just about developing the technology to remove the maximum volume of carbon dioxide, it also involves aspects of design optimisation to reduce the overall operating costs. In fact, reducing the energy consumption of carbon capture via packed columns would be considered the most important factor from an industrial and economic viewpoint.

Due to the fact that the flue gas is at a relatively low pressure, of the same order as atmospheric pressure, packed columns are required to have very low pressure drops over the whole column height. Otherwise, the gas would need to be pressurised prior to the absorption process, which would further increase operating costs. Therefore, packed columns need to be designed to take this into account, whilst maintaining high gas-liquid interfacial areas to ensure adequate absorption rates.

CFD modelling provides a method to simulate the processes which occur within packed columns. However, at the present moment, there are major difficulties in modelling the process as a whole. This is due to the large range of spatial scales and the significant impact of small-scale features on the column efficiencies. Difficulties also arise in mass transfer modelling, which is a crucial element of the process.

1.4 Novel Research

The work detailed in this Thesis represents an extension of knowledge in the fields of CFD and CCS. As a result of initial investigations it was concluded that an alternative approach was required to model thin films in CCS, due to computational limitations. Thus, the Enhanced Surface Film (ESF) model was developed and implemented in OpenFOAM. This development was based on the depth-averaged Navier-Stokes equations, and was aimed at simulating thin liquid films that occur within packed columns. The ESF solver models surface tension using the continuum surface force (CSF) model [11]. The application of the CSF model to the depth-averaged equations required the development of an additional model for the threshold film thickness. It was shown that the ESF approach was able to accurately predict the hydrodynamics of thin films across a range of fluids, including water, acetone and glycerol at various flow rates.

The ESF model was extended to include physical mass transfer, utilising Higbie penetration theory [12] to simulate interfacial mass transfer. The surface-age required by Higbie penetration theory was determined by the development a residence-time transport equation, applicable to depth-averaged flow. This allowed the mass transfer coefficient to predicted, in parallel with the hydrodynamics of the liquid film.

The final addition made by this work was the inclusion of chemically enhanced mass transfer with the ESF model. This was achieved using the Enhancement factor model and allowed both 1st and 2nd order reaction kinetics to be simulated in addition to interfacial mass transfer and film hydrodynamics. The ESF model not only has applications within CCS, but also across a range of industries where the efficiency of equipment is dependent on the structure of thin liquid films.

1.5 Structure of this thesis

Chapter 1: Introduction

This chapter gives an introduction to carbon capture, detailing the carbon capture process within packed columns. An overview of motivation for the research in this field is then given.

Chapter 2: Literature Review

An extensive literature review is performed, focussing on the computational fluid dynamics modelling research. This includes single-phase flows and multi-phase flows with mass transfer and reaction kinetics.

Chapter 3: CFD Modelling

This chapter gives an introduction to CFD modelling and provides the governing equations for the simulations used throughout this thesis. An overview of the discretisation process of the finite volume method in given. The chapter also details the approach that is used to map solutions between different meshes, required during adaptive mesh refinement techniques.

Chapter 4: Microscale Hydrodynamics

The results of multi-phase flow simulations at the microscale are detailed in this chapter. Flow on the packing surfaces is simplified to flow down an inclined plane. A novel surface texture pattern was designed and tested in terms of wetted area.

Chapter 5: Adaptive Mesh Refinement at the Microscale

This chapter gives the results of adaptive mesh refinement at the microscale. Comparison of the results are made with those using a highly refined static mesh and experimental data from the literature.

Chapter 6: Enhanced Surface Film Model

The development of the Enhanced Surface Film (ESF) model is detailed. The model is tested and validated against experimental data. Simulations are performed for a range of fluids, including water, acetone and glycerol.

Chapter 7: Surface Film Modelling with Mass Transport & Chemical Reaction

In this chapter the ESF model is extended to included mass transfer. This allows gas separation processes to be modelled along with the hydrodynamics of thin liquid films. Chemically enhanced absorption is also implemented using the Enhancement factor approach. The final model is validated against experimental data of CO_2 absorption in a wetted wall column. The ESF model is then used to simulate CO_2 absorption into a partially wetted film.

Chapter 8: Conclusion

The final conclusions are made, along with suggestions for future research. This includes additional application of the ESF model and further extensions that could be made to it.

Chapter 2

Literature Review

This chapter reviews the body of literature in the area of carbon capture using packed columns. Initially, a broad discussion of packed columns is detailed, leading onto the computational fluid dynamics modelling work which has researched. This involves work investigating the variety of scales within the absorbers. Since thin liquid films are an important feature of carbon capture using packed columns a review of theoretical works on thin film is detailed. Research into mass transfer is then discussed. Finally, literature detailing the inclusion of reaction kinetics into the models is reviewed.

2.1 CCS with Packed Columns

The use of experiments to analyse proposed advances in technology is very expensive, especially at full-scale. Despite this, several pilot-plant studies have been performed in the literature [13, 14] studying the effects of variations of parameters, such as liquid flow rates, gas flow rates, packing types and CO_2 loadings. Many other experimental investigation have been reported in the literature, including the determination of the effects of packing texture on liquid-side mass transfer, pressure drop through structured packing and liquid hold-up in packed columns [15–17]. However, these mainly focus on reduced-scale equipments and it is important to understand that results and correlations derived at this scale may not necessarily apply or may include further errors at full-scale.

Computational modelling provides an alternative research tool to experimental investigations, since the cost is significantly reduced. Simulations can easily be repeated with different parameters, such as packing geometry, without the expense involved in manufacturing test samples. Process simulation tools and rate-based modelling have been used in the literature to study mass transfer efficiencies of packed columns [18]. However, these types of models do not directly take into account the internal structure and the packing and the complex hydrodynamics inherent in packed columns.

It is important to model the hydrodynamics because flow patterns can have a distinct effect on the absorption and reaction characteristics. This type of detailed modelling also provides information that is out of the reach of experimental investigations, which can be crucial in the understanding and the optimisation of the processes involved in CO_2 absorption within packed columns. Computational fluid dynamics is a computational modelling approach which enables simulations to be performed with the inclusion of hydrodynamics and reaction kinetics.

As noted by some authors [19], the use and applicability of more rigorous models is dependent upon the situations being modelled. In some circumstances a simplified approach may adequately model the physical problem and the use of more rigorous models can unnecessarily increase the complexity of the problem. This emphasises the importance of evaluating each problem on the basis of simplifications that can be made.

2.2 Computational Fluid Dynamics Modelling

Computational fluid dynamics modelling is a numerical method used to solve fluid flow problems. It involves discretising the governing equations and the flow domain to form a set of algebraic equations, which are then solved using computational algorithms.

The major difficulty that arises when modelling carbon capture through packed columns is the large range of spatial scales that exist throughout the process. To accurately model the whole system, near wall effects must be accounted for, requiring detailed modelling of the liquid films. However, absorbers and strippers have characteristic sizes on the scale of meters and so even with the current computing power it is extremely time-consuming to resolve all of these spatial scales simultaneously during a numerical simulation. Furthermore, the inclusion of reaction kinetics into the model introduces additional complexity. To overcome these difficulties researchers make approximations or simplifications to models that allow simulations to be performed, including reducing the problem to single-phase flow or segmenting the problem into ranges of spatial scales [20].

According to Øi [19], the modelling of CO_2 absorption using packed columns can be subdivided into the following processes; absorption and reaction kinetics, the gas-liquid equilibrium, gas-liquid flows and pressure drop. As mentioned in section 1.2, the pressure drop encountered through a packed column is a crucial factor in the design of packed columns. A large pressure drop is undesirable and would reduce the overall efficiency of the system, due to the increased energy consumption because of the requirement for gas pumping, or due to the decreased CO_2 absorption as a result of column height compromises. Computational fluid dynamics is a suitable tool that can be used to determine the pressure drop within the packed columns.

Single-phase models have been used to evaluate pressure drop, since it is assumed that the dry pressure drop can be simply correlated to the wet pressure drop, due to the same pressure loss mechanisms. Larachi *et al.* [21] and Petre *et al.* [22] evaluated the pressure drop within a column by reducing the whole packing layer into small mesoscale sections, known as representative elementary units (REUs). The pressure drop contributions from each of these elements was determined by relation with the loss coefficients of the flow. Simulations with REUs are less computationally expensive and combinations of these REUs can be used to evaluate the overall pressure drop within the column.

The main energy losses occur due to the collision of flows in the criss-crossing channels of the packing and due to the sudden change in direction between successive layers of packing [21,22]. It has been observed that increasing the inclination angle of the packing from the standard 90^0 to 135^0 resulted in reduced turbulence and smoother flow through the packing transition layers.

Attempts have been made to increase the capacity (reduce the pressure drop) of structured packing by making modifications to the packing itself. Saleh *et al.* [23] used an Eulerian-Eulerian approach to model dry and wet pressure drop in MellapakPlus 752.Y structured packing. This method was considered appropriate because they aimed to determine the pressure drop where sharp resolution of the gas-liquid interfacial region was not considered important. In this particular packing the channels are bent around to vertical at the inlet and outlet regions. Simulations showed that these modifications reduced the dry pressure drop by as much as 10% and the wet pressure drop by 11.5%. The addition of a flat sheet between the layers of packing was also studied by Saleh *et al.* [23] and they found that the dry pressure drop decreased for the whole range of F-factors tested. The additional plates separated the criss-crossing channels, removing the pressure drop created by opposing flows within the channels. This also had the advantage of increasing the wetted area of the packing, which should in theory increase mass transfer and therefore increase CO_2 absorption efficiencies, as long as the observed increase in wetted also resulted in an increase in the interfacial area.

Pressure drop results directly from energy losses throughout the packing. Olujic *et al.* [24] noted that only a small fraction of the energy lost in the packing goes towards enhancing the mass transfer. Pressure loss sources, such as gas-gas interactions at the criss-crossing sections of packing, have little contribution to the mass transfer efficiency. Therefore, by reducing these types of pressure losses the overall pressure drop within the column can be reduced without adversely affecting the efficiency of the column. Sheets placed between the packing layers can eliminate these pressure loses. However, in reality, adverse effects of these sheets, such as liquid maldistribution, reduced gas mixing and liquid rivulet formation could reduce the mass transfer efficiency significantly, especially below the loading point [24].

Some authors have developed new packing geometries in order to optimise the capacity of columns. Wen *et al.* [25] developed a novel structured packing design, with the premise of decreasing the pressure drop whilst maintaining mass transfer efficiencies. The novel design comprised of vertical sheets, with spacers punched and bent from the sheet itself to reduce build costs. The spacers were used to maintain the structural integrity of the packing, help to promote good liquid distribution and to induce turbulence to increase mixing of the gas and liquid phases. CFD simulations were used to optimise the designs, in terms of liquid distribution. Finalised designs were constructed and compared experimentally with a commercial packing, Gempak 2.5A (Koch-Glitsch Inc.), with the same surface area ($250\,m^2/m^3$). It was found that the novel packing reduced the pressure drop by as much as 45%, with at least 23% higher capacity and similar performance in terms of mass transfer efficiency. Therefore, the new design was able to reduce the pressure drop, whilst maintaining good efficiency. However, the surface area of this novel design is at the lower range of the surface areas found in structured packings and the observed results may not scale well to larger surface areas. Further investigation is required in this area.

Raynal *et al.* [26] performed a combination of CFD simulations to determine the wet pressure drop through a packed bed during co-current flow. Firstly, 3-dimensional single-phase simulations were performed in order to determine the dry pressure drop. Secondly, 2-dimensional multi-phase calculations were used to determine the liquid hold-up within a section of packing. Finally, the wet pressure drop was evaluated from a combination of the dry pressure drop and the liquid hold-up within the packing.

Raynal *et al.* [26] also questioned the use of REUs to calculate pressure drop within a whole section of packing. Using the criss-crossing channel REU [21, 22] the authors were able to show that the pressure drop was highly dependent upon the inlet and outlet lengths, before and after the crossing region. This was attributed to the large proportion of the area of the domain that was composed of inlet and outlet boundaries, meaning that the boundary conditions had a significant impact on the solution. The authors stated that REUs can be used to provide qualitative comparisons between different packing geometries, but should not be used to derive macroscopic flow characteristics.

To overcome the difficulties that arise by deriving macroscopic quantities (such as pressure drop) from combinations of REUs, the work of Raynal *et al.* [27] and Raynal and Royon-Lebeaud [20] proposed a novel elementary unit, being the smallest periodic element within the packing. This allowed periodic boundary conditions to be imposed on the open parts of the element, avoiding the challenges faced by REUs. However, the use of periodic elements is also questionable in regions where the flow is not periodic in nature, such as near the column walls. The multiple-scale approach was utilised in these papers. Firstly, 2-dimensional VOF simulations were performed at the micro-scale to determine the interfacial velocity and liquid hold-up. These results were then used at the

mesoscale (periodic elements) to determine the pressure drop within the column. Single-phase simulations were performed and the liquid was indirectly taken into account by transforming the gas superficial velocity into an interstitial velocity. The liquid hold-up was used to derive the interstitial velocity. The velocity at the interface was also taken into account by applying moving wall boundary conditions to the walls of the periodic element. The pressure drop data was then used at the macroscale, by representing the packing as a porous media where the associated pressure loss coefficient was derived from the mesoscale pressure drop data.

Fernandes *et al.* [28, 29] performed CFD simulations to calculate dry and wet pressure drop within structured packing. Pressure drop is calculated from the results of CFD simulations of gas flow through the structured packing. Dry pressure drop involves simulations of gas flow only, whereas wet pressure drop includes the effect of liquid flow within the structured packing. Dry pressure drop calculations were made using two different domains. The first domain consisted of the region between two layers of the corrugated sheets and the second consisted of a full section of packing. It was found that the larger scale simulations, on a full section of packing, produced results closer to experimental data. Wet pressure drops were performed in a similar method to that previously. This again shows that the choice of computational domain is crucial. Segmentation of the domain into periodic elements can reduce computational effort considerably (due to the smaller number of cells required), but this can induce errors due to the inherent simplifications being made.

Due to the turbulent nature of the gas flow within packed columns the choice of turbulence model is important. This is particularly relevant during simulations to determine the pressure drop. Various papers in the literature have reviewed different turbulence models [26, 30]. It was found that more advanced models, such as the RNG $k-\epsilon$ or the SST $k-\omega$ models were more appropriate than standard $k-\epsilon$ models. However, all these models rely on the eddy viscosity concept as a closure model for the Reynold's stress terms that arise in the Reynold's averaged Navier-Stokes equations. An assumption of the eddy viscosity concept is that the eddy viscosity and turbulence is isotropic. However, due to the complex flow through structured packing the flow is highly anisotropic and therefore, the applicability of the eddy viscosity concept to these flows is highly limited. On the other hand, Reynolds stress transport (RST) models apply a second-order closure by solving transport equations for the Reynolds stress terms. Therefore, RST models should be more applicable to flows within structured packing, since the limitation of isotropic eddy viscosity is avoided.

Other aspects of packed columns which can be analysed using CFD are gas and liquid distributors. The distribution of gas and liquid throughout the packed column is of great importance, considering that maldistribution can reduce the column efficiency. It has been shown, during a macro-scale simulation using the multiple-scale method, that a simple horizontal inlet provides the best gas distribution when compared to a

vertical pipe inlet with or without a baffle [27]. In relation to this, it is also important to consider the orientation of the layers of packing with respect to the inlet flow. It has been shown for a particular inlet configuration that the orientation of the layers can have a noticeable effect on the homogeneity of the gas flow [20]. Wehrli *et al.* [31] used CFD to investigate more complex gas distributors and their effect on the inlet flow.

Beugre *et al.* [32] used a different approach to conventional CFD to study the hydrodynamics within structured packing. They used the Lattice Boltzmann Method (LBM) to simulate the single-phase flow between two sheets of packing. Good agreement was observed with experimental data. Comparisons with conventional CFD approaches showed that the LBM was able to capture more of the variety of flow behaviours seen during turbulent flow. However, the authors pointed out that this was at a higher computational cost and is the major disadvantage of this method.

Wen *et al.* [33] used a two-component single-phase model to simulate flow within structured packing and the distribution of CO_2 from a point source. This approach was able to show the anisotropic nature of structured packing and how CO_2 spreads throughout the column. However, the absorption process can not be modelled using a single-phase approach and therefore, multiphase approaches must be used for accurate modelling of CO_2 absorption.

Multiphase models have been used extensively in the literature to study the hydrodynamics of packed columns, including single- and two-fluid models. Two-fluid models consider the gas and liquid phases to be two distinct, separate fluids. Constitutive equations are then required to take account of the influence of each phase on the other, such as interfacial drag [34]. However, in situations where the location and structure of the interface is important, such as during reactive absorption, these models encounter difficulties due to the diffuse nature of the interface. Large concentration gradients can exist at the interface, which are not accurately modelled when the interface is diffuse. One-fluid multiphase models, such as the volume-of-fluid (VOF) method, enable good reconstruction of the interface to be made. However, these types of simulations are mainly restricted to the flow at the microscale, due to the requirement to have large numbers of cells in the interfacial region for accuracy. Hydrodynamics at the microscale will be detailed further in section 2.2.1.

Mahr & Mewes [35, 36] proposed an alternative method to simulate two-phase flow within packed columns at the macroscale. The proposed method used the elementary cell method, whereby the elementary cell is taken to be the smallest periodic element of packing. All variables of the flow field are then averaged over this elementary cell. It is assumed that the flow entering and leaving each cell is similar and so the intricate flow behaviour inside the cell does not need to be accounted for. Due to the preferential spreading of fluid in the direction of the corrugations, the liquid phase is split into two distinct phases, each with a preference for either of the two corrugation directions. This

allows the highly anisotropic nature of structured packing to be accounted for in the elementary cell method. CFD calculations were then performed using two liquid phases and a single gas phase. This enabled simulations to be performed at the macroscale, whilst taking into account the anisotropic nature of structured packing. However, this approach neglects to model the flow within the periodic elements where mass transfer may be effected, since the rate of absorption is highly dependent on the local structure of the interface which is neglected in this approach.

2.2.1 Microscale

Liquid films are an important feature throughout many areas of engineering, ranging from falling film microreactors [37,38] to Carbon Capture & Storage. It is important to determine the fluid dynamics of liquid films because the efficiency of CO_2 absorption is closely related to the structure of the liquid films within the packing materials. Liquid films can exhibit a range of flow regimes, including full-film, rivulet and droplet flow. The formation and structure of these features is dependent upon various flow parameters, such as liquid flow rate, plate surface texture, plate geometry etc.

Previous experimental studies have been undertaken to investigate the effect of surface texture on liquid-side mass transfer during liquid film flows [15]. It was found that a textured surface, typically found in commercial packing materials, can increase the mass transfer by as much as 80% in comparison to a smooth plate [15]. CFD investigations have been performed of heat and mass transfer on structured packing [34, 39, 40]. However, these papers do not examine the effect of surface texture on heat and mass transfer, exclusively investigating smooth corrugated packing materials.

Haroun *et al.* [41] performed direct numerical simulations of gas-liquid flow on two-dimensional structured surfaces using a modified VOF approach. Szulczewska *et al.* [42] also used the VOF method to study liquid film flow using a two-dimensional approach. They studied the dependency of the interfacial area on the gas and liquid flow rates during counter-current flow. However, liquid films can exhibit highly three-dimensional structures, such as rivulets, and these can not be observed when using a two-dimensional model.

There have been many papers in the literature specifically looking at liquid films in an effort to understand the hydrodynamic behaviour of packed columns and other gas-liquid contactors at the micro-scale. Lan *et al.* [43] used a combined experimental and three-dimensional, isothermal CFD approach to study thin film flow on inclined planes. They focused on the effects that surface tension, contact angle, film flow rate and inclination angle had on the film velocity, width and thickness. However, this investigation did not specifically focus on liquid films within packed columns and so surface texture was not taken into account.

Johnson *et al.* [44] performed an experimental investigation of thin film flow down an inclined plane. Specifically, they investigated the moving contact line and the formation of rivulets. This included the effect of flow parameters on the wavelength of the rivulets that form.

The analysis of counter-current gas-liquid flow at the micro-scale is of particular importance in the understanding of the processes involved in packed columns. Counter-current gas flow has been observed to increase the thickness and fluctuation of liquid films [45]. Furthermore, thin films may be susceptible to break-up and hence, thicker films are more suitable when this flow arrangement is used [46].

Microscale surface texture on packed columns has been found to have a large effect on the structure of liquid films [46]. Valluri *et al.* [47] developed an analytical model for film flow over sinusoidal and doubly sinusoidal surfaces at moderate Reynolds numbers. A CFD approach was used to assess the viability of the model. The analytical model was shown to provide good correlation with the CFD results for $Re_l < 30$.

Full films provide the greatest efficiency because the large surface area is conducive to CO_2 absorption. The formation of rivulets, or any other phenomena which could reduce the interfacial area of a film flowing on structured packing, could hinder heat and mass transfer. These three-dimensional phenomena have been successfully modelled using the VOF approach and it has been shown that the structure of a film is highly dependent upon the geometry and the choice of boundary conditions during numerical simulations [48, 49].

Following on from this, Iso and Chen [50] examined the transition behaviour between the different flow regimes exhibited on inclined plates. Three-dimensional, isothermal VOF simulations were used to analyse the transition between rivulet flow and full film flow. It was observed that a hysteresis phenomena occurred, depending on whether the liquid flow rate was increasing or decreasing, suggesting that the flow is also affected by historic flow patterns.

This emphasises the importance of performing time-dependent simulations to accurately resolve the film flow features. Iso and Chen [50] also showed that a particular surface texture on the packing material was able to increase the wetted area, which could enhance heat and mass transfer if interfacial area also increased. However, it is important to examine the negative effects of surface texture, which may hinder heat and mass transfer. For example, sinusoidal structures of certain amplitudes have been shown to cause recirculation in the film, resulting in regions of stagnant fluid [46, 47]. These regions will reduce the efficiency of CO_2 absorption within packed columns.

Hoffmann *et al.* [49] performed an experimental investigation of film flow down an inclined plane to provide validation for their CFD simulations. The experiment consisted of a small steel plate of 0.06m in length by 0.05m in width, with steel walls at the sides.

This setup was chosen to be representative of a small section of structured packing. The inclination angle was chosen to be either 45^o or 60^o to the horizontal, which represents common inclination angles used in commercial structured packing [49]. The liquid at the top of the plate was introduced by an overflowing weir to ensure a uniform film at the inlet. Various flow rates were tested and the wetted area of the plate was determined from pictures taken during the experiment.

Iso *et al.* [51] also performed a similar experiment to validate their CFD results. A single inclination angle of 60^o was chosen and a range of liquid flow rates were tested. The plate was longer than that of Hoffmann *et al.* [49], but the measurement region was the same size (i.e. 0.06m in length). They also measured the wetted area of the plate.

The experimental results of Hoffmann *et al.* [49] and Iso *et al.* [51] will be used to provide validation for the initial simulations in this thesis. It is noted that the experimental results report the wetted area, rather than the interfacial area of the liquid film. The interfacial area is important for mass transfer, since mass transfer occurs through the interfacial area of the film surface. However, determination of the interfacial area in an experiment is difficult to achieve and was not considered important for the validation of the hydrodynamics of liquid film flow.

An alternative approach to modelling thin films is to solve the depth-averaged Navier-Stokes equations. These surface film models provide much greater flexibility for modelling realistic absorption equipment due to the reduction in computational requirements. The application of this approach has been used in many areas of research. These include thin film microreactors [37, 38], surface coatings [52, 53], biofluids and medical applications [54,55]. Another such application is within internal combustion engines where thin films are an important feature that can effect both the efficiency of combustion and the resulting emissions.

2.3 Thin Liquid Films

Thin liquid films are an important feature in gas absorption equipment and so an in-depth understanding of thin film flows is important in the modelling of acid-gas absorption within structured packing. Oron *et al.* [56] and Craster & Matar [57] performed in-depth reviews on the theoretical literature focussing on the dynamics and stability of thin liquid films.

The following discussion looks at two different flow situations. The first of these is full film flow where the substrate is completely covered by the liquid film. Here the instabilities arise at the film surface, which can lead to the formation of long-wave structures. Secondly, a discussion of contact line dynamics is given. Here the substrate is partially covered by the film, resulting in the formation of a contact line between the

fluid interface and the underlying solid surface. This gives rise to instabilities that can occur at the contact line, which can result in the formation of rivulets. Contact line dynamics is of particular importance to the work performed in this thesis. Both of these mechanisms can have a significant effect on mass transfer.

2.3.1 Full Film Dynamics

Full film dynamics involves situations where the fluid film completely covers a substrate, or in other words, there exists no contact line between the fluid and solid surface. The effect of contact lines and resulting instabilities of those contact lines will be discussed in the following section.

The interface between a liquid film and the surrounding gas is a deformable interface [56], and therefore any instability on an initially flat interface can create surface waves. It has been shown that these interfaces exhibit long wavelength deformations, where the wavelength of the deformation is much larger than the film thickness [58]. According to Oron *et al.* [56], wave steepening at higher flow rate can even result in transitions to quasiperiodic or chaotic structures, which can eventually lead to film rupture. This behaviour can have a significant impact on the overall flow structure and the resulting rate of mass transfer through a liquid film interface.

According to Kalliadasis *et al.* [58] there are three main mechanisms that have a direct impact of long-wave instabilities. If an initially flat surface is exposed to a long-wave perturbation the crest and troughs of the wave will be acted on by gravity. It is known that the net streamwise flow rate in a film increase with fluid depth [58]. Therefore, gravity will draw fluid from the centre of the crest towards the front of the crest, causing the interface to rise upwards. Fluid is also drawn from the rear of the crest which causes the interface to fall downwards. The result of this is that the initial perturbation moves downstream with a phase velocity larger than the fluid velocity [58]. The streamwise gravity does not cause the perturbation to grow in size.

The second mechanism that affects long-wave instabilities is inertia which causes fluid to accumulate underneath the crest of the moving perturbation [58]. This is due to the fact that the surface waves move at a greater velocity than the underlying fluid. This causes perturbations to grow in size as they move downstream.

The third mechanism is the cross-stream component of gravity, which causes hydrostatic pressure within the film [58]. Therefore, this mechanism is only relevant in inclined flows and is not present in vertically falling films. The larger depth of fluid at the crests causes an increase in hydrostatic pressure. This increase in pressure pushes fluid from the crests to the troughs, effectively stabilising the flow [58].

Long waves are always present on the surface of vertically falling films and these wave structures can significantly influence mass transfer across a fluid interface [59]. In small length films these long waves are of an ordered, 2D nature, at moderate liquid film Reynolds numbers [59]. Vertically falling films have been shown to be unstable at all Reynolds numbers and due to these instabilities, small perturbations to an initially smooth film will grow in size to form 2D waves [59]. As the amplitude of these waves grow, the 2D waves become unstable and break into 3D waves structures. Alekseenko *et al.* [59] developed a model equation to describe the nonlinear, nonstationary waves that occur on thin film interfaces.

Alekseenko *et al.* [60] performed an experimental study of 3D solitary wave formation in gravity-driven film flow down a vertically inclined plane. They state that quite a long distance is required to reach the fully developed wavy regime with 3D solitary wave formation, due to the nonlinear nature of the wave formation. To excite the formation of 3D solitary waves Alekseenko *et al.* [60] used a pulse jetlet to create point, surface perturbations. The development of the waves downstream was monitored at a range of low liquid film Reynolds numbers. From this experimental work the features of 3D solitary waves are easily observed; a steep leading edge along with small capillary waves ahead of this leading edge.

Due to the small plate dimensions used throughout this thesis it may be possible that there is not the required distance for solitary waves to grow to a significant level. Park & Nosoko [61] performed an experimental investigation of film flow down a vertical plane, without forcing at the inlet, at Reynolds number, $Re = 32.7$. They observed that the film was initially flat for the first 5cm, which subsequently developed 2D waves. These 2D waves then developed into 3D surface waves at a distance of approximately 15cm from the inlet. This further suggests that the simulations in this thesis will not see significant development of surface waves due to the small size of domain. The simulations in this thesis are also performed on inclined plates and so the resulting hydrostatic pressure within the film will dampen wave formation [58].

There are various methods that are available to simplify the governing, Navier-Stokes equations for thin film flow. The applicability of which will depend on the flow conditions being modelled. The main approaches are the thin-film long-wave approximation and the weighted integral boundary layer method. These will be discussed in the following sections.

The first attempt to simplify the governing Navier-Stokes equations for film flow was Nusselt [62]. Nusselt was able to derive a parabolic velocity profile for film flow under the assumption of a constant film thickness. However, this approach is unable to model the development of waves on the surface of the film.

2.3.2 Thin-film long-wave approximation

The thin-film long-wave approximation is an approach used to reduce the dimensionality of the Navier-Stokes equations. It relies on the fact that the cross-stream scale is much smaller than the streamwise or span-wise scales [58].

Initially, the governing Navier-Stokes equations and associated boundary conditions are non-dimensionalised using suitable scaling [57]. These scaling parameters are derived from the disparity between the characteristic thickness, $\mathcal{H}$ and the characteristic length scale along the film, $\mathcal{L}$. The assumption is that $\mathcal{H} << \mathcal{L}$, which is the case for the flow of thin films over a substrate. A small parameter, $\epsilon \equiv \mathcal{H}/\mathcal{L}$ can then be introduced which is used to eliminate terms that vary slowly across and along the thin film [57]. The resulting equations are known as the boundary layer equations. These equations are simpler than the original Navier-Stokes equations, but they are of the same dimensionality [63]. Therefore, these equations are less computationally expensive, but are still very complex. Further simplification can be made by the use of the long-wave approximation.

According to Craster & Matar [57], the long-wave approximation is performed by taking the lubrication parameter, $\epsilon = \mathcal{H}/\mathcal{L}$ to be asymptotically small. This allows a perturbation expansion to be performed by expanding the variables in powers of ϵ. Assuming that the Reynolds number, $Re = O(1)$ then the inertial terms can be neglected from the equations. Substitution of the asymptotic series into the non-dimensionalised governing equations allows a solution to be found for the first-order velocity and pressure. These are then substituted into the the first order kinematic boundary condition at the free surface, resulting in an evolution equation for the film thickness. The final result of this perturbation analysis is a single non-linear partial differential equation for the film thickness. This equation is much simpler than the original Navier-Stokes equations that describe the flow. The first-order film evolution equation can then be used to performed stability analysis by introducing a normal mode perturbation of the base-state film thickness [58].

The resulting film evolution equation is accurate for non-inertial flow, such is the case when gravity terms are of comparable magnitude to the viscous terms. However, the model breaks down when the Reynolds number is greater than $O(1)$, leading to finite-time blow-up of the solution [58]. According to Kalliadasis *et al.* [58], this is due to the fact that the velocity field is slaved to the kinematics of the free surface because only the film evolution equation is solved. Therefore, the long-wave approximation is limited to low Reynolds number film flow and is not suitable for modelling flow in the inertial regime where the Reynolds number is higher than than $O(1)$.

The flow regimes modelled within this thesis and those that occur within structured packing are at relatively high Reynolds numbers. Here the inertial terms are significant

and so the long-wave approximation would not be suitable to model these types of film flows.

2.3.3 Weighted Integral Boundary Layer Method

When inertial effects are important, at higher Reynolds numbers, an alternative approach is the integral boundary layer method. Shkadov [64] developed the integral boundary layer method by integrating the boundary layer equations over the film depth. This leads to two governing equations where all variables are enslaved to the film thickness and the flow rate. The resulting equations require closure models for the wall shear stress and the momentum transport. Shkadov [64] developed these closure models by assuming a self-similar parabolic velocity profile. However, the integral boundary layer method of Shkadov does not predict well the critical Reynolds number for the onset of unstable long waves on the film. Indeed, for a vertically falling film it does not predict the correct critical Reynolds number and for inclined film flow the critical Reynolds number is 20% away from the correct value [58].

Ruyer-Quil & Manneville [63, 65] improved the integral boundary layer method by developing a model based on the weighted residual method. The velocity field was defined by polynomial test functions, rather than the self-similar parabolic velocity profile used by Shkadov. These works also improved the closure model of the wall shear stress, leading to a shear stress which is first order accurate. This was shown to improve the main deficiency of Shkadov's integral boundary layer method. The weighted integral boundary layer method of Ruyer-Quil & Manneville was able to accurately predict the critical Reynolds number for the onset of unstable long waves on the free surface.

Tseluiko & Kalliadasis [66] utilised the weight integral boundary layer method to study counter-current flow down an inclined channel. They made a number of assumptions that allowed the turbulent gas flow to be isolated from the liquid flow by replacing the gas-liquid interface with a no-slip wavy wall. This model was subsequently used to examine flooding flow within the channel.

Vellingiri *et al.* [67] also used the weighted integral boundary layer method to study counter-current gas-liquid flow using a similar approach to Tseluiko & Kalliadasis [66]. They used this approach to examine absolute and convective instabilities on the film. The authors found that the weighted integral boundary layer method gave good agreement with the full governing equations and was in better agreement than the long-wave approximation, as would be expected.

The works of Tseluiko & Kalliadasis [66] and Vellingiri *et al.* [67] examine situations involving very high gas flow rates, where the film velocity could be neglected. However, this assumption is not valid when the liquid and gas flow velocities are of a comparable

magnitude. Lavelle *et al.* [68] sought to improve this restriction by coupling a low-dimensional model for the liquid phase with the full Navier-Stokes equations for the gas phase. This involved solving the liquid phase using the long-wave film model and coupling this with the gas-phase using a moving mesh technique. The advantage of this approach is that there is no restriction on the thickness of the gaseous phase and the position of this interface is taken account of within the gas-phase as a result of the moving mesh technique. The approach was able to accurately predict surface waves at the gas-liquid interface. However, the effect of contact line dynamics on the liquid films was not included.

A similar approach to modelling thin films is used in this thesis, whereby the liquid and gas domains are separated. Within the gas domain the full Navier-Stokes equations are solved and within the liquid domain the depth-averaged Navier-Stokes equations are solved.

2.3.4 Contact Line Dynamics

A contact line is the position where a fluid interface comes into contact with the solid substrate over which the fluid flows. The contact line is also unstable to perturbations and so flows with contact lines can exhibit interesting dynamics. When a fluid is released onto an inclined plane the contact line will initially be straight in the spanwise direction to the flow [56]. According to Oron *et al.* [56], a ridge will form at the contact line caused by an induced high pressure at the contact line, which deforms the interface to produce the ridge. The induced high pressure is created by recirculation as fluid flows from the film surface to the contact line and then to the plate.

Instabilities at the contact line will cause the contact line to develop into a series of fingers or rivulets [56]. These fingers will develop into either triangular periodic waves or straight fingers parallel with the streamwise direction, depending on the flow conditions [56]. According to Oron *et al.* [56], the fingering instabilities will develop with a certain frequency across the plate.

Troian *et al.* [69] performed a study of contact line instabilities using the lubrication approximation. They performed a linear stability analysis and found that an initially straight contact line is unstable to perturbations over a range of wave numbers. The most unstable wavelength is given by $\lambda = 14l$, where $l = h(3Ca)^{-\frac{1}{3}}$. The parameter l is a length scale where surface tension and gravitational forces balance and h is the film thickness. Ca is the capillary number given by, $Ca = \frac{\mu U}{\sigma}$, where μ is the fluid viscosity, U is the characteristic velocity and σ is the surface tension.

The simulations performed in this thesis involve moving contact lines, produced by fluid flowing down an inclined plane. Due to contact line instabilities, the initially straight contact line is likely to form rivulets with a certain frequency across the width of the

plate. However, these simulations also include walls at the sides of the plate in order to compare directly with the experimental data of Hoffmann *et al.* [49] and Iso *et al.*. These side walls are likely to have an influence on the resulting pattern of rivulet formation, due to the contact angle at the side walls. The stability analyses in the literature do not typically include the effect of side walls, so a direct comparison with the theoretical analysis of Troian *et al.* [69] may not be possible.

2.4 Mass Transfer and Reaction Kinetics

The determination of mass transfer across gas-liquid interfaces can be achieved by using either numerical models or by direct numerical simulation. Numerical models have been developed throughout the literature to provide a description of the mass transfer process and to enable approximations of the physical process to be made. The stagnant film model [70] is a classical example which gives a qualitative understanding to the absorption process. However, this approach is limited to its application since it assumes that the liquid and gas films at the interface are stagnant. Improvements to this model have been made to include dynamic absorption of species at the interface. These include the Higbie penetration model [12] and the Danckwerts surface renewal model [71]. The following sections describe the stagnant film model and the Higbie penetration model. The Higbie penetration model is often selected over the Dankwerts surface renewal model since it is easier to implement and provides a good description of dynamic absorption at the interface.

The Higbie penetration model can be used to derive mass transfer coefficients using data from CFD simulations. However, these numerical models can give no indication of the actual distribution of species throughout the domain. Direct numerical simulation is a method whereby the evolution of species within the domain is determined as part of a CFD simulation using species transport equations. This approach enables mass transfer coefficients to be determined from the distribution of species near the interface and gives a much greater understanding of the physical processes involved. Direct numerical simulation approaches from the literature are detailed further in the following sections.

2.4.1 The Stagnant Film Model

Mass transfer at the microscale can be described by the two-film theory developed by Whitman [70]. This is a simplified model since it assumes stagnant films, which is not the case in packed columns. However, it suitably explains the mass transfer characteristics from a qualitative viewpoint.

The two-film model assumes that there exists a thin interface between the gaseous and liquid phases and that there is a thin layer either side of the interface known as the liquid

and gas films, with thickness's δ_L and δ_G, respectively. These films separate the interface from the liquid and gas bulk (see Figure 2.1). Mass transfer through the interface is limited by resistance within the gas or liquid films, the main contribution during acid-gas absorption coming from the liquid film resistance [72]. The concentration of the solute j, $C_{G,j}$ is considered to be constant in the gas bulk, falling linearly through the gas film region until it reaches the concentration at the interface, $C^{int}_{G,j}$ [73]. Equilibrium is assumed at the interface, whereby the concentration in the liquid film, $C^{int}_{L,j}$ is determined by a relation such as Henry's law, given by:

$$C^{int}_{G,j} = He_j \, C^{int}_{L,j}, \tag{2.1}$$

where He_j is Henry's constant for species j. Henry's constant is temperature dependent considering that the solubility of a gas is affected by temperature. The temperature dependence of Henry's constant can be taken account of by the equation given by Versteeg & Dijck [74]. The concentration drops further until it reaches the concentration in the liquid bulk, $C_{L,j}$. The flux of species j through the interface, N^{int}_j can therefore be given by:

$$N^{int}_j = \rho k_G (C_{G,j} - C^{int}_{G,j}) = \rho k_L (C^{int}_{L,j} - C_{L,j}), \tag{2.2}$$

where k_G and k_L are the mass transfer coefficients for the gas and liquid films, respectively.

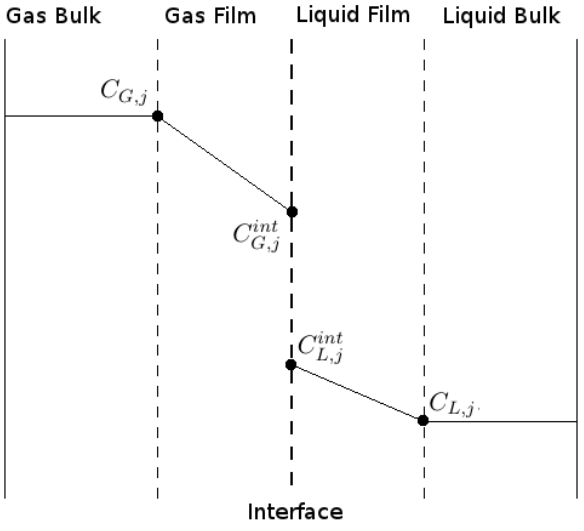

FIGURE 2.1: The two-film model for mass transfer

From this representation it is easy to derive expressions for the gas and liquid mass transfer coefficients in terms of the diffusivities of the species and the thicknesses of the gas and liquid films:

$$k_G = \frac{D_{G,j}}{\delta_G} \qquad k_L = \frac{D_{L,j}}{\delta_L}, \tag{2.3}$$

where $D_{G,j}$ is the diffusivity of species j in the gaseous phase and $D_{L,j}$ is the diffusivity of species j in the liquid phase. However, this approach only provides a qualitative

description of the mass transfer process and can not be used to determine the mass transfer coefficients, since this model does not provide a method to estimate the film thicknesses [75].

2.4.2 The Higbie Penetration Model

The stagnant film model assumes that mass transfer takes place by steady-state molecular diffusion through the interface. However, in many physical situations mass transfer occurs under dynamic conditions, where the diffusion of species through the interface is time-dependent. The Higbie penetration model [12] assumes that unsteady mass transfer occurs when fluid elements are in contact with the interface. Equilibrium is assumed between the liquid-side and gas-side species concentration at the gas-liquid interface and each fluid element is assumed to spend equal time at the interface (see Figure 2.2). It is reasonable to assume equilibrium at the interface because the interface is infinitesimally thin and therefore, equilibrium at the interface is achieved almost instantaneously. This is also the case for the stagnant film model. Under these conditions, the convection terms in the diffusion equation can be neglected [75], resulting in the following equation in the liquid phase,

$$\frac{\partial C_j}{\partial t} = D_{L,j} \frac{\partial^2 C_j}{\partial x^2}, \tag{2.4}$$

with boundary conditions:

$$t = 0, \qquad x > 0 \quad : \quad C_j = C_{L,j}^{\infty}$$

$$t > 0, \qquad x = 0 \quad : \quad C_j = C_{L,j}^{int},$$

where the interface is located at $x = 0$ and the liquid phase is located at $x > 0$.

The solution of this partial differential equation is given by:

$$\frac{C_{L,j}^{int} - C_j}{C_{L,j}^{int} - C_{L,j}^{\infty}} = \text{erf}\left(\frac{x}{2\sqrt{D_{L,j} t}}\right), \tag{2.5}$$

where $\text{erf}(x)$ is the error function defined by:

$$\text{erf}(x) = \frac{2}{\sqrt{\pi}} \int_0^x \exp(-z^2) dz. \tag{2.6}$$

The mass flux of species j, N_j [Kg m^{-2} s^{-1}] is given by:

$$N_j = -\rho D_{L,j} \left(\frac{\partial C_j}{\partial x}\right)_{x=0}, \tag{2.7}$$

considering that mass transfer in gas absorption is by unidirectional diffusion [75]. An expression for the rate of mass transfer at time t can be found by substituting Equation 2.5 into Equation 2.7, giving:

$$N_j(t) = \rho\sqrt{\frac{D_{L,j}}{\pi t}}(C_{L,j}^{int} - C_{L,j}^{\infty}). \tag{2.8}$$

The resulting liquid-side mass transfer coefficient is given by:

$$k_L(t) = \sqrt{\frac{D_{L,j}}{\pi t}}, \tag{2.9}$$

and the average mass transfer coefficient over the contact time, Θ is given by:

$$k_{L,avg} = \frac{1}{\Theta}\int_0^{\Theta} k_L(t)dt = 2\sqrt{\frac{D_{L,j}}{\pi\Theta}}. \tag{2.10}$$

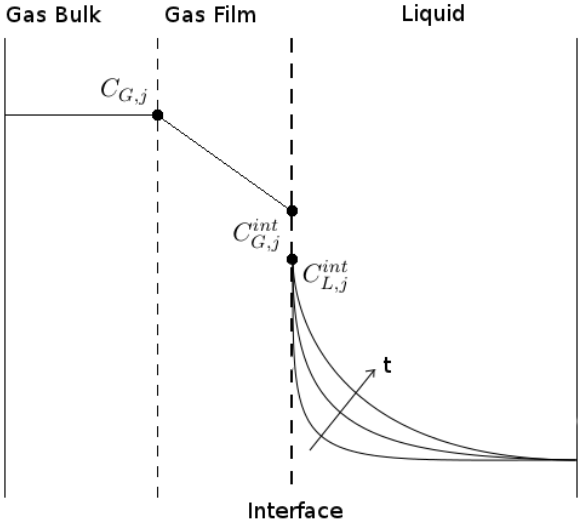

FIGURE 2.2: Representation of the Higbie Penetration Model

It can be seen from Figure 2.2 that the Higbie penetration theory solves for time-dependent mass transfer resulting in curved concentration profiles, whilst the stagnant film model gives a steady-state linear concentration profile (Figure 2.1). The thickness of the liquid-side film is therefore time-dependent, increasing as the exposure time increases, and is given by $2\sqrt{D_{L,j}t}$. Higbie penetration theory is a model used in circumstances where the concentration profile is not to be resolved and allows the mass transfer rate to be determined, as long as the interfacial concentration and the bulk concentration are known. For the Enhanced Surface Film approach developed in this thesis the concentration in the liquid phase is not resolved, however, the concentration in the gas-phase is resolved, using direct numerical simulation. Henry's law is used to determine the concentration at the liquid side of the interface and the bulk concentration is assumed to be negligible, due to the small diffusion coefficient of CO_2 in the liquid phase. This allows Higbie penetration theory to be used within the liquid phase

to determine the rate of mass transfer through the interface, without resorting to direct numerical simulation of the liquid-phase concentration (see Chapter 7).

The disadvantages of these models is that they both rely on the presence bulk regions adjacent to the gas and liquid films. In situations involving very thin liquid films the concentration boundary layer may stretch all the way to the wall. In these instances, models which rely on the presence of a liquid bulk are hindered and may become less accurate. The influence of liquid bulk on mass transfer has been studied by van Elk [76]. Direct numerical simulation methods are not restricted by the presence or lack of a liquid bulk and so may be more applicable to these situations.

2.4.3 Chemically Enhanced Absorption

As mentioned previously, mass transfer by physical absorption may be limited by the liquid-film resistance, especially during acid-gas absorption [72]. In these circumstances, chemically enhanced absorption is a method by which the liquid-film mass transfer coefficient can be increased [72], hence increasing the overall absorption of species from the gas to the liquid phase. However, the extent to which chemical reactions enhance mass transfer is dependent upon the rates of reaction of the system.

According to Kohl & Nielson [72], for slow reactions the absorption is still limited by the liquid-film resistance, since absorbed molecules diffuse into the bulk of the liquid before reactions occur. For fast reactions the absorbed molecules react within the liquid film, thereby enhancing additional absorption of species into the liquid from the gaseous phase. Large increases in the liquid-film absorption coefficient can lead to the overall absorption rate being limited by gas-film resistance. Turbulence in the flow can also enhance mass transfer by mixing the gas and liquid phases.

The optimal acid gas absorbents for CO_2 capture in packed columns are known as amines. These were first developed and patented by Bottoms [77] in 1930. An amine has the general formula $NR_1R_2R_3$, where R_1, R_2 and R_3 can either be organic groups of molecules or single hydrogen atoms [19]. Amines are classified as primary, secondary and tertiary depending upon the number of organic groups bonded to the nitrogen atom (i.e. one organic group is primary, two is secondary and three is tertiary). Amines can also be classified as alkanolamines if a hydroxyl group is present within any of the organic groups. The hydroxyl group increases the solubility of the amines in aqueous solutions [78]. Examples of industry-used amines include monoethanolamine (MEA), diethanolamine (DEA), methyldiethanolamine (MDEA) and isobutanolamine (AMP).

The generally accepted mechanism for the reaction of aqueous primary and secondary alkanolamines with CO_2 is the zwitterion mechanism [79,80]. An intermediate zwitterion is formed by the reaction of the alkanolamine with CO_2, followed by the deprotonation of the zwitterion by a base, B to form a carbamate [81]. The base, B represents the bases

present in the solution, which, in the case of an aqueous solution, are the amine itself, H_2O and OH^- ions. The reaction mechanism for a general alkanolamine, R_1R_2NH with CO_2 is given by:

$$CO_2 + R_1R_2NH \underset{k_1}{\overset{k_2}{\rightleftharpoons}} R_1R_2N^+HCOO^- \tag{2.11}$$

$$R_1R_2N^+HCOO^- + B \underset{k_{-B}}{\overset{k_B}{\rightleftharpoons}} R_1R_2NCOO^- + BH^+. \tag{2.12}$$

Under the assumption of a quasi-steady concentration of the zwitterion, the overall forward reaction rate can be determined by the following equation (see [78] for derivation):

$$r = \frac{k_2[CO_2][R_1R_2NH]}{1 + \frac{k_1}{\Sigma k_B[B]}} \tag{2.13}$$

An asymptotic analysis of the overall forward reaction rate reveals the variation of the reaction orders with respect to the amine, that have been observed in experimental investigations. As performed by Versteeg & van Swaaij [81], if the second term of the denominator of equation 2.13 is $\ll 1$, then the overall forward reaction rate is given by:

$$r = k_2[CO_2][R_1R_2NH]. \tag{2.14}$$

This describes simple second-order reaction kinetics, which is first order with respect to the amine and CO_2. On the other hand, if the second term of the denominator of equation 2.13 is $\gg 1$, then the overall forward reaction rate is given by:

$$r = k_2[CO_2][R_1R_2NH]\frac{\Sigma k_B[B]}{k_1} \tag{2.15}$$

This equation describes a reaction which can lie between first and second order with respect to the amine, in agreement with experimental data. Aqueous MEA solution are typically found to be first order with respect to the amine and hence, the overall forward reaction rate can be determined using equation 2.14. The rate constant of the reaction between monoethanolamine and CO_2 can be found using the equation derived by Versteeg & Dijck [74]. This equations takes into account the temperature dependence of the reaction rate constant, which is important for simulations of packed columns.

The industry standard alkanolamine based solvent is 30wt% aqueous MEA. The concentration of primary amines is usually limited to 30%wt because they are highly corrosive. MEA and other primary amines provide fast reaction rates with CO_2, but are limited to an approximate amine to CO_2 mole ratio of 2:1, due to the low rate of hydrolysis to form bicarbonates [72]. These reduce the capacity of primary amines to absorb CO_2, considering they are limited by the stoichiometry of the reactions and also limited by compromises in concentration to avoid excessive corrosion.

Tertiary amines do not react directly with CO_2 to form a carbamate. They react by protonation of the amine via hydrolysis and ionisation of the dissolved CO_2 [72]. This process means that tertiary amines have a greater capacity than other amines, due to an amine to CO_2 mole ratio of 1:1. Tertiary amines, such as MDEA are advantageous because they have low regeneration energies when compared to primary or secondary amines [19]. However, the rate of reaction of CO_2 by hydrolysis is much slower than the rate of reaction via carbamate formation [72, 82–85]. This means that the overall reaction rate of CO_2 with tertiary amines is slower than that of primary or secondary amines.

Couchaux *et al.* [86] performed a review of the kinetics of CO_2 reactions with amines. If the amine concentration is in excess, then the overall reaction can be considered first order with respect to CO_2, with a pseudo first order reaction rate constant, k_0. According to Couchaux *et al.* [86], in these circumstances k_0 depends on the nature of the amine, it concentration and temperature. For the same amine concentration and temperature, the pseudo first order reaction rate constant for the primary amine, MEA is 3 orders of magnitude larger than that of the tertiary amine, MDEA.

The reaction rate of CO_2 with MEA can be calculated using the equation of Versteeg & Dijck [74], to ensure that the temperature dependence of the reaction rate is taken account of, given by,

$$k_{\mathrm{MEA}} = 4.4 \times 10^{11}\, e^{-5400/T}\, \mathrm{L\,mol^{-1}s^{-1}}, \tag{2.16}$$

whereas the reaction rate of CO_2 with MDEA can be calculated using the equation of Kierzkowska-Pawlak and Chacuk [87], given by,

$$k_{\mathrm{MDEA}} = 2.07 \times 10^{9}\, e^{-5912.7/T}\, \mathrm{L\,mol^{-1}s^{-1}}. \tag{2.17}$$

Therefore, for an amine concentration of $1\,\mathrm{mol\,L^{-1}}$ at a temperature of 313K, the pseudo first order reaction rate constant for MEA is, $k_{0,\mathrm{MEA}} = 14152.5\,\mathrm{s^{-1}}$ whilst for MDEA it is, $k_{0,\mathrm{MDEA}} = 12.9\,\mathrm{s^{-1}}$. The pseudo first order reaction rate constant for MEA is 3 orders of magnitude larger than that of MDEA, in agreement with the observations of Couchaux *et al.* [86].

Recently, the development of mixed amines has helped to combine the advantageous properties of tertiary amines with those of primary and secondary amines. Due to the slower reaction rate of tertiary amines with CO_2, the addition of a small amount of primary or secondary amines can significantly increase the reaction rate with CO_2, whilst maintaining the high capacity and low regeneration energies of the overall amine mixture [88]. The simulations performed in this thesis focus exclusively on CO_2 and MEA reactions, considering that MEA is the industry standard amine for acid-gas absorption.

Puxty *et al.* [4] and Aboudheir *et al.* [89] performed experimental investigations of CO_2 absorption into aqueous monoethanolamine solution. Their aims were to determine the rate of mass transfer of CO_2 in a wetted wall column. The wetted wall column provides a controlled experimental setup to determine rates of mass transfer. This is because the flow rates of liquid and gas can be easily controlled and the interfacial area of the film is easily determined. The overall mass transfer coefficient for CO_2 being absorbed into a thin film of aqueous monoethanolamine was determined for 313K and 333K. These results will be used for validation of the simulations in this thesis.

2.4.4 Modelling of Mass Transfer

Mass transfer efficiency within packed columns can be described by the bed height equivalent to a theoretical plate (HETP). HETP can be expressed in terms of the gas- and liquid-phase superficial velocities, the gas- and liquid-phase mass transfer coefficients, the effective interfacial area and the stripping factor. These terms are often derived through correlations and a review of some of these is given in the review paper by Wang *et al.* [90]. However, these correlations are often based on experimental data or theoretical predictions, meaning that they must be used with caution. For situations involving different parameters, or different assumptions to the original experiments or theoretical predictions, the validity of the correlations is questionable.

Rate based models can be used to simulate packed columns using detailed reaction kinetics [18]. Further details of rate based models can be found in the review by Øi [19]. However, these types of models do not directly take into account the structure of packings and their effect on heat and mass transfer, relying on correlations for mass-transfer coefficients, specific wetted areas, liquid hold-up, and pressure drop [91]. Experimental investigations can be performed to determine these correlations, but this restricts the variation in parameters that can be made, due to the inherent costs involved.

Klöker *et al.* [91] combined CFD simulations with rate-based reaction kinetics. In this way, correlations were provided by the CFD results, allowing extensive variations in packing geometries to be easily investigated. The disadvantage of this approach is the distribution of species within the columns, during reactive absorption, cannot be resolved. This is important in determining the effect of changes of packing geometry on column efficiencies.

The computational modelling of mass transfer within packed columns requires a multiphase approach, since the mass transfer process takes place across the interfacial boundary between the liquid and gas phases. In order to fully capture the physics of the problem it is important to be able to resolve the interfacial region, especially when the absorption process is enhanced by reactions within the liquid film region. This makes the VOF method particularly attractive for these applications because good resolution

of the interface can be achieved. However, traditional VOF models do not account for the movement of species through the interface.

Physical and reactive absorption can be modelled using various approaches, using single-fluid and two-fluid models. Two-fluid models require correlations of mass transfer, whilst one-fluid models (also known as direct numerical simulations) can directly resolve the absorption process, without the need for correlations. The latter method is more accurate and can be used over a wider range of problems, since correlations are specific to particular laboratory set-ups. The most widely used single-fluid, multi-phase approach is the VOF model.

Khosravi Nikou *et al.* [34] used a two-fluid approach to determine the pressure drop, heat and mass transfer within a section of structured packing. The authors simulated flow between two sheets of the packing, Flexipac 1Y. Constitutive equations were used to account for the influences of each fluid on the other, in terms of mass and heat transfer across the interface. The simulated results were compared with experimental data and it was found that the pressure drop, HETP and temperature profile were predicted well by the model with mean absolute relative errors of 20.7%, 12.9% and 2.8% respectively. The disadvantage of using a two-fluid approach is that it creates a diffuse interface between the gas and liquid phases. Haroun *et al.* [92] have shown that during CO_2 absorption there is a very thin concentration boundary layer close to the gas-liquid interface and so the two-fluid model may not be able to fully resolve mass transfer across the interface.

To the best of the authors knowledge, the first publication to combine mass transfer with a VOF approach was written by Ohta & Suzuki [93] in 1996. They studied mass transfer from a bubble rising in a column during solvent extraction processes. The standard VOF model was supplemented with a species transport equation, under the assumption that mass transfer did not have an effect on the flow field. Davidson & Rudman [94] also performed a VOF-type simulation to determine mass and heat transfer across a deformable interface. However, these methods were only applicable in situations where the concentration of species was continuous across the interface, i.e. $He_j = 1$.

Bothe *et al.* [95] improved upon previous studies, allowing a discontinuity of concentration across the interface, governed by Henry's law. The authors incorporated Henry's law into the concentration field to create a new scalar, $\tilde{c}$, which is continuous across the interface. In the liquid phase $\tilde{c} = C_l$, whereas in the gaseous phase $\tilde{c} = C_g/He$. This then allows simulations to be performed with previous methods, using the new scalar to avoid problems with discontinuity. However, this approach creates a discontinuity in the local diffusive species flux across the interface, which has been avoiding by modifying the local gas diffusivity near the interface, $D_g = He\, D_g$. This ensures continuity of local diffusive species flux across the interface, but it also artificially modifies the diffusivity in the interface region causing inaccuracies in the diffusivity at the interface.

Yang & Mao [96] used the level-set method (an analogous approach to the VOF method) to simulate mass transfer with $He \neq 1$. A similar approach was used to that of Bothe *et al.* [95], in that a transformed concentration field, $\tilde{c}$ was used in the species transport equations. In the gaseous phase $\tilde{c} = C_g\, He^{0.5}$ and in the liquid phase $\tilde{c} = C_l\, He^{0.5}$, thereby forming a continuous concentration field across the interface. Again, this creates a discontinuity in the local diffusive species flux at the interface, which can be rectified by artificially modifying the diffusivities close to the interface. Yang & Mao made transformations to the diffusivity to rectify this problem. However, these transformations introduce further complexity into the problem.

Haroun *et al.* [41, 97] used direct numerical simulation to extend the functionality of the VOF method to include species transport, using an additional species transport equation. The difficulty that arises when using this method is the discontinuity of concentration at the interface between the two phases, for $He_j \neq 1$. This occurs due to the differences in the solubility of species in each of the phases. The VOF method is a one-fluid method and hence, the species transport equation must be adapted to deal with this discontinuity in concentration at the interface. Haroun *et al.* [41, 97] included an addition solubility flux term in the species transport equation, which was able to resolve the jump in concentration at the interface and ensure continuity of flux at the interface. This term is dependant on the gradient of the volume fraction and so is negligible away from the interface. They observed that high diffusivity ratios or large curvatures of the interface can create spurious concentration fluxes, analogous to the problem of spurious currents well known in the VOF approach. These spurious fluxes were damped dramatically by using harmonic interpolation for diffusivity, rather than the usual linear interpolation used in the VOF method, and by using a smoothing function for the volume fraction calculation.

One of the limitations of the methods proposed so far is they have made the assumption of a constant distribution coefficient, He_j. However, the distribution coefficient can depend on state variables, such as temperature, and so this dependence needs to be modelled to gain a more accurate solution [98]. Ganguli & Kenig [98] used a level-set method integrated with mass transfer to study the diffusion of oxygen from a rising gas bubble in liquid. The boundary conditions at the interface given by Henry's law and the continuity of local diffusive species flux were incorporated directly into the model by using source terms in the species transport equations. Two boundary conditions means that two species transport equations need to be solved, one for the gas phase and one for the liquid phase. The source terms in the equations were multiplied by a factor, α which was set to be very large close to the interface and zero away from it. Therefore, away from the interface the modified species transport equations reduced to the standard transport equations and at the boundary the equations were approximately equal to the interface boundary conditions, due to the large value of α.

A unique approach developed by Chasanis *et al.* [38] involved a combination of two-phase and single-phase simulations. They were analysing the mass transfer characteristics within a falling-film micro-contactor. Initially, numerical calculations of the two-phase flow were performed using the level-set method, in order to determine the location of the gas-liquid interface. The domain was then subdivided along the interface location into two separate gas and liquid domains. Finally, single-phase flow was investigated in each domain, including mass transfer across the fixed interfacial boundary. This method significantly reduced computational effort and provided good agreement with experimental data in the literature. However, this method is only valid at very low concentrations of solute in the gaseous phase, since the effect of absorption on the hydrodynamics is neglected. At higher CO_2 concentrations this method may introduce significant errors.

Mass transfer in gas-liquid, multi-component systems can proceed by two main mechanisms; Equi-Molar Counter Diffusion (EMCD) and Diffusion through Stagnant Film (DTSF) [99]. EMCD generally applies to distillation-type mass transfer problems where mass transfer occurs equally in both directions through the interface. Whereas, DTSF is more suited to absorption since it describes cases in which a single component has non-zero flux through the interface. It also directly takes into account the diffusion velocity at the interface caused by mass transfer.

Hassanvand & Hashemabadi [99] investigated DTSF using two different approaches. The first approach involved the addition of a source term to the volume fraction continuity equation to take account of the effect of mass transfer on the hydrodynamics of the flow, the source term being only applied at the interface. A standard transport equation for species concentration was used and an internal boundary condition was applied at the interface in order to take account of the concentration jump. The second method involved a modification to the species transport equation, which indirectly took account of the diffusion velocity caused by mass transfer. This approach is similar to the method used by Haroun *et al.* [41, 97], apart from the use of an internal boundary condition to take account of the discontinuity of concentration at the interface. It has been shown that the second method provided more accurate results than the first when comparisons were made to analytical solutions of some simple flows.

Initial investigations into mass transfer in this thesis utilise the method of Haroun *et al.* [41,97] to implement mass transfer into the VOF approach. This was selected because of its simple formulation and also its ability to effectively resolve the jump in concentration at the interface and ensure continuity of flux at the interface. The restriction of constant Henry coefficient was not considered limiting because the simulations were performed at constant temperatures. This is a valid assumption due to the small size of the domain, where temperature variations would be minimal. Simulations of larger domains with the VOF approach may require an alternative approach with variable Henry constant if the solubilities are significantly affected by changes in temperature along the column.

The inclusion of mass transfer and reaction kinetics into the VOF method can significantly increase the strain on computational resources. In order to simulate reaction kinetics, simplifications can be made to the domain to offset these additional problems. Wetted wall columns allow simulations to be made on a geometry which is far simpler than structured packing and enables computations to be made more easily. Comparisons can be made with experimental data of acid-gas absorption using wetted wall columns to validate developed models [4, 89, 100].

Chapter 3

CFD Modelling

This chapter introduces the CFD modelling used in this thesis. Firstly, the general governing equations of fluid flow are listed. Secondly, the equations used to simulate multiphase flow are detailed, along with the adaptations made to the VOF method to include mass transfer. An overview of the finite volume discretisation is then given. The changes required for adaptive mesh refinement calculations are also detailed.

3.1 Introduction

Computational fluid dynamic modelling is a computational approach used to solve the governing equations of fluid flow with numerical methods. Firstly, the governing equations are defined by derivation from first principles. Finally, the flow domain and equations are discretised to form a set of algebraic equations, which can then be solved numerically with the aid of a computer. The CFD software, OpenFOAM [101, 102] is used to perform the simulations in this thesis. OpenFOAM is an open-source set of C++ libraries used to solve fluid flow problems. The advantage over commercial CFD software is that the underlying code can be easily accessed and adapted to suit the particular problem being investigated.

3.2 General Governing Equations

The governing equations of fluid flow are derived from first principles. If the continuum assumption can be satisfied, then the fluid can be considered a continuous medium. This allows the solution of the flow variables to be represented by a set of partial differential equations. These partial differential equations are derived by considering a small element of fluid and by applying the principles of conservation of mass, momentum and energy.

Throughout the investigations in this thesis, the isothermal assumption is made and therefore, the energy equation can be neglected.

3.2.1 Continuity Equation

For a single-phase flow the continuity equation is derived from the conservation of mass and is given by:

$$\frac{\partial \rho}{\partial t} + \nabla \cdot (\rho \boldsymbol{u}) = 0, \tag{3.1}$$

where ρ is the fluid density and $\boldsymbol{u}$ is the fluid velocity field. For an incompressible flow, as is the case throughout this thesis, the continuity equation reduces to:

$$\nabla \cdot \boldsymbol{u} = 0. \tag{3.2}$$

3.2.2 Momentum Equations

In single-phase flow the momentum equation (also known as the Navier-Stokes equation) is derived from the principle of conservation of momentum. For the case of incompressible flow the Navier-Stokes equations and is given by:

$$\rho \left(\frac{\partial \boldsymbol{u}}{\partial t} + \boldsymbol{u} \cdot \nabla \boldsymbol{u} \right) = -\nabla p + \mu \nabla^2 \boldsymbol{u} + \rho \boldsymbol{g} + \boldsymbol{F_s}, \tag{3.3}$$

where p is the fluid pressure,μ is the dynamic viscosity, $\boldsymbol{g}$ is the gravitational vector and $\boldsymbol{F_s}$ is any additional sources of momentum, such as surface tension.

The Navier-Stokes equations can be further simplified for thin film flow by integrating the governing equations over the fluid depth. These are known as the depth-averaged Navier-Stokes equations and the derivation will be performed in Chapter 6.

3.3 Multiphase Flow

The main CFD approaches for multiphase flows are based on one- or two-fluid models. Two-fluid models require constitutive equations to account for the interaction between the two fluids. On the other hand, one-fluid models require methods to reconstruct the interface between the two phases, a popular approach being the volume-of-fluid (VOF) method [103].

The VOF method in OpenFOAM (known as interFOAM) can be used to solve multiphase flow of incompressible, isothermal, immiscible fluids. A single momentum equation is solved for the mixture and the fluid properties of each phase are combined to form fluid properties of this mixture. The interface between the phases is resolved using an

interface capturing technique. This is achieved by solving a transport equation for the volume fraction.

The volume fraction, α_i is used to determine the volume of phases within each computational cell. The total volume fraction for a cell is defined to be 1 and therefore, the volume fraction for each phase can lie in the range $0 \leq \alpha_i \leq 1$. If a cell is completely filled with the i^{th} phase then $\alpha_i = 1$ and if a cell is completely devoid of the i^{th} phase then $\alpha_i = 0$. The interface region can be constructed using the values of α_i in the cells across the domain. For a two-phase system, as is the case in this thesis, the volume fraction is determined for one phase and the other phase is tracked trivially, $\alpha_2 = 1 - \alpha_1$.

Fluid properties such as the density, ρ and the dynamic viscosity, μ are defined in each cell as a function of volume fraction and are given by:

$$\rho = \alpha_1 \rho_1 + (1 - \alpha_1)\rho_2, \tag{3.4}$$

$$\mu = \alpha_1 \mu_1 + (1 - \alpha_1)\mu_2, \tag{3.5}$$

where the subscripts relate to the individual properties of each phase.

The volume fractions throughout the domain can be determined by solving transport equations for α_i. In a two-phase flow a single transport equation for α_1 is required, since α_2 can be determined trivially. The transport equation for α_1 used in the interFOAM solver is defined by [104]:

$$\frac{\partial \alpha_1}{\partial t} + \nabla \cdot (\boldsymbol{u}\alpha_1) + \nabla \cdot (\boldsymbol{u_r}\alpha_1(1 - \alpha_1)) = 0, \tag{3.6}$$

where $\boldsymbol{u_r}$ is a suitable velocity field selected to compress the α_1 field around the interface [105]. This is beneficial because it reduces the numerical smearing of the interface which increases the accuracy of simulations utilising this interface capturing technique. Equation 3.6 is the continuity equation for α_1, with the notable addition of the 3^{rd} term. As described by Rusche [104], this is an artificial compression term used to provide interface compression without the use of a compressive differencing scheme, with the advantage that the solution for α_1 is bounded between 0 and 1, as required by the definition of volume fraction. Due to the form of this extra term it is only significant in the interfacial region, where it is required and hence, has negligible effect on the solution throughout the rest of the domain.

Surface tension in multiphase flow is modelled by the inclusion of a source term in the momentum equation. The contribution to the balance of momentum from surface tension, $\boldsymbol{F_s}$ is modelled using the continuum surface force model (CSF) model [11] and is given by:

$$\boldsymbol{F_s} = (\sigma\kappa(\boldsymbol{x})\boldsymbol{n} + \nabla_{\|}\sigma)\delta, \tag{3.7}$$

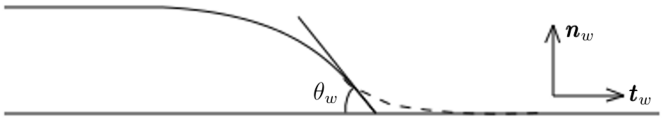

FIGURE 3.1: Definition of contact angle, θ_w, unit vector normal to wall, $\boldsymbol{n}_w$ and unit vector tangential to wall, $\boldsymbol{t}_w$

where σ is the surface tension, $\boldsymbol{n}$ (see equation 3.8 and 3.10) is the unit normal vector to the interface pointing into the liquid phase, $\kappa(\boldsymbol{x})$ (see equation 3.9) is the curvature of the interface, $\nabla_{\parallel}$ is the surface gradient and δ is the surface delta function. The delta function is usually taken as equal to $\delta = \frac{1}{|\nabla\alpha|}$. The second term of the surface tension force is significant in cases where the surface tension coefficient is a function of either temperature or concentration. However, in this thesis the term has been neglected since it was assumed that the concentration of species had little effect on the value of the surface tension coefficient and isothermal simulations were performed.

$$\boldsymbol{n} = \frac{\nabla\alpha}{|\nabla\alpha|}, \tag{3.8}$$

$$\kappa(\boldsymbol{x}) = -\nabla \cdot \boldsymbol{n}. \tag{3.9}$$

In cells adjacent to a wall boundary the definition of the unit normal vector is adjusted in order to take account of the liquid contact angle. The method in this thesis used a constant wall contact angle, θ_w and the unit normal vector is defined as [46]:

$$\boldsymbol{n} = -\boldsymbol{n_w} cos(\theta_w) - \boldsymbol{t_w} sin(\theta_w), \tag{3.10}$$

where $\boldsymbol{n_w}$ is the unit vector normal to the wall and $\boldsymbol{t_w}$ is the unit vector tangential to the wall (see Figure 3.1). Here again, $\boldsymbol{n}$ points into the liquid phase.

Therefore, for the cases studied in this thesis where the surface tension coefficient is constant the surface tension force is given by,

$$\boldsymbol{F_s} = \sigma\kappa(\boldsymbol{x})\nabla\alpha. \tag{3.11}$$

3.3.1 Mass Transfer Modelling

The inclusion of mass transfer in the VOF model can be achieved in a variety of ways. The authors preliminary investigations into mass transfer modelling (see chapter 7) use the method devised by Haroun *et al.* [97]. This approach is a direct numerical simulation method and so does not require any additional models, such as Higbie penetration theory, to resolve the mass transfer process. It uses an additional set of equations to determine

the evolution of species concentration throughout the domain, given by,

$$\frac{\partial C_i}{\partial t} + \nabla \cdot (\boldsymbol{u} C_i) = \nabla \cdot (D_i \nabla C_i + \Phi_i) + W_i, \tag{3.12}$$

and Φ_i is defined by:

$$\Phi_i = -\left(D_i \frac{C_i(1 - He_i)}{\alpha + He_i(1 - \alpha)} \nabla \alpha \right), \tag{3.13}$$

where C_i is the concentration of the i^{th} species, D_i is the diffusivity of the i^{th} species and W_i is the production term for the i^{th} species. In this thesis, the VOF formulation of mass transfer is only used to model physical mass transfer and therefore the production term, W_i is neglected. The lengthy derivation of the above equation along with the resulting additional flux term is given in the thesis by Haroun [106].

Equation 3.12 is a modified scalar transport equation with an additional solubility flux term to account for discontinuities in the concentration field at the interface between two immiscible fluids [97]. These mass transfer equations can account for the continuity of fluxes at the interface:

$$\sum_{L,G} \boldsymbol{j_i} \cdot \boldsymbol{n} \delta_i = 0, \tag{3.14}$$

and the discontinuity in concentration of species at the interface given by:

$$C_{G,i}^{int} = He_i C_{L,i}^{int}. \tag{3.15}$$

Henry's law is an equilibrium condition which could take some time to achieve equilibrium. The gas bulk and liquid bulk concentrations may take a long time to reach equilibrium. However, the interface concentrations will reach equilibrium very quickly so it is reasonable to assume equilibrium of concentration at the gas-liquid interface.

In accordance with Haroun *et al.* [97], the diffusivity is calculated using a harmonic formulation, rather than the standard linear formulation of the VOF method. The harmonic diffusivity is given by:

$$D_i = \frac{D_{i,L} D_{i,G}}{\alpha_1 D_{i,G} + (1 - \alpha_1) D_{i,L}}. \tag{3.16}$$

Haroun *et al.* [97] demonstrated that this approach reduces spurious fluxes that arise in the species concentration as a result of interface curvature. The thesis of Haroun [106] shows that the choice of harmonic diffusion over linear diffusion does not affect the structure of the species transport equation.

3.4 Discretisation of the domain

The domain is discretised into a number of control volumes, which may be structured or unstructured depending upon the preference for the problem being solved. Many CFD solvers store variables at nodes at the centre of these computational cells. It is assumed that variables are linear within a control volume. Therefore, it is important that control volumes are small enough to capture the physics of the problem and to suitably describe regions of large gradients. The governing equations of fluid flow are also discretised to produce numerical approximations of the flow fields at these nodes. Details of the discretisation of the governing equations are given in the following sections.

3.5 The Scalar-Transport Equation

The scalar-transport equation is a generic equation which describes the transport of a physical quantity, ϕ, due to advection and diffusion processes. In differential form the equation is given by:

$$\frac{\partial \rho\phi}{\partial t} + \nabla \cdot (\rho \boldsymbol{u}\phi) - \nabla \cdot (\rho\Gamma_\phi \nabla\phi) = S_\phi(\phi), \tag{3.17}$$

where Γ_ϕ is the diffusivity of ϕ. The first term in equation 3.17 is the temporal derivative, the second term is the convection term, the third term is the diffusion term and the fourth term is the source term. This governing equation is discretised over each control volume within the domain and so for a particular cell with volume, V the following equation must be satisfied [107]:

$$\int_t^{t+\Delta t} \left[\int_V \frac{\partial \rho\phi}{\partial t} \mathrm{d}V + \int_V \nabla \cdot (\rho \boldsymbol{u}\phi) \mathrm{d}V - \int_V \nabla \cdot (\rho\Gamma_\phi \nabla\phi) \mathrm{d}V \right] \mathrm{d}t = \int_t^{t+\Delta t} \left[\int_V S_\phi(\phi) dV \right] \mathrm{d}t. \tag{3.18}$$

The spatial discretisation of the terms in equation 3.18 are given in the following sections.

3.5.1 Discretising the Diffusion Term

Using Gauss' theorem the volume integral of the diffusion term can be transformed into a surface integral over the boundary of the volume. This can then be approximated by a summation over the faces of the control volume given by:

$$\int_V \nabla \cdot (\rho\Gamma_\phi \nabla\phi) \mathrm{d}V = \oint \rho\Gamma_\phi \nabla\phi \cdot \mathrm{d}\boldsymbol{A} = \sum_f (\rho\Gamma_\phi)_f \boldsymbol{A} \cdot (\nabla\phi)_f. \tag{3.19}$$

The gradient of ϕ at the face is calculated using central differencing and for orthogonal meshes:

$$\boldsymbol{A} \cdot (\nabla\phi)_f = |\boldsymbol{A}| \frac{\phi_N - \phi_P}{|\boldsymbol{x}|}, \tag{3.20}$$

where ϕ_P is the value of the scalar at the cell centre, ϕ_N is the value of the scalar at the centre of the cell adjacent to the current cell face, f. The vector, $\boldsymbol{x}$ is the vector between the two cell centres. For non-orthogonal meshes an alternative approach is required, but it not detailed here because orthogonal meshes have been used throughout this project.

3.5.2 Discretising the Source Term

The source term $S_\phi(\phi)$ can depend on the solution, ϕ and so is represented as a function of ϕ. The source term is linearised as follows:

$$S_\phi(\phi) = b_p + s_p\phi, \quad s_p \leq 0, \tag{3.21}$$

and so:

$$\int_V S_\phi(\phi)\mathrm{d}V = b_p V_p + s_p V_p \phi_p. \tag{3.22}$$

The condition of $s_p \leq 0$ arises from the requirement of negative feedback to ensure numerical stability of the problem.

3.5.3 Discretising the Advection Term

Again using Gauss' theorem the volume integral of the advective term can be transformed into a surface integral over the boundary of the control volume. Using the same approach as with the diffusion term, the surface integral can be approximated by a summation over the individual faces of the control volume centred about point, P. Therefore:

$$\int_V \nabla \cdot (\rho\boldsymbol{u}\phi)\mathrm{d}V = \oint (\rho\boldsymbol{u}\phi) \cdot \mathrm{d}\boldsymbol{A} = \sum_f \boldsymbol{A} \cdot (\rho\boldsymbol{u}\phi)_f = \sum_f C\phi_f, \tag{3.23}$$

where the mass flux through the face, $C = \boldsymbol{A} \cdot (\rho\boldsymbol{u})_f$.

The value of the scalar at the face, ϕ_f needs to be approximated by the values of ϕ at the adjacent cell centres in order to discretise the advection term. An advection scheme is needed to compute these values. The following sections are given as examples of advection schemes that can be used, central differencing and upwind. They are detailed to give information to the reader about the nature of advection schemes.

3.5.3.1 Central Differencing

Central differencing approximates the cell-face value, ϕ_f by averaging the values at the nodes on either side of the face, assuming that ϕ is linear between these two nodes. This gives [107]:

$$\phi_f = F_i\phi_P + (1 - F_i)\phi_N, \tag{3.24}$$

where the interpolation factor, F_i is the ratio of the distances between the cell face and its adjacent nodes ($d_{P,f}$ and $d_{N,f}$):

$$F_i = \frac{d_{P,f}}{d_{N,f}}. \tag{3.25}$$

Central differencing is second order accurate for ϕ_f, but can produce non-physical oscillations in the solution for advection dominated flows. This is due to the non-transportive nature of the scheme. Transportive schemes are upstream-biased and assign a higher weighting to the upstream node to account for the directionality of the advection process, since properties are transported in the direction of the flow.

3.5.3.2 Upwind Differencing

Upwind differencing is a transportive scheme and the cell-face value, ϕ_f is approximated by the value of ϕ at the upwind node, ϕ_U. Therefore,

$$\phi_f = \begin{cases} \phi_P & \text{if } C \geq 0 \\ \phi_N & \text{if } C < 0 \end{cases} \tag{3.26}$$

Due to the transportive nature of the upwind differencing scheme it is bounded and so does not produce unphysical oscillations in the solution. However, this scheme is only first order accurate. Many advances have been made on these two basic schemes to increase the accuracy, boundedness and stability of the advection schemes. Further information about more advanced schemes can be found in [108].

3.5.4 Temporal Discretisation

This section gives examples of temporal discretisation schemes that can be used in CFD simulations. They are detailed to give information to the reader about the nature of temporal discretisation schemes. The spatial discretisation of the terms in equation 3.18 have been determined and can be reduced into canonical form as follows:

$$\sum_f C\phi_f - \sum_f (\rho\Gamma_\phi)_f \boldsymbol{A} \cdot (\nabla\phi)_f - (b_p V_p + s_p V_p \phi_p) = a_P\phi_P - \sum_N a_N\phi_N - b_p, \tag{3.27}$$

and so the substitution of equation 3.27 into equation 3.18 gives:

$$\int_t^{t+\Delta t} \left[\left(\frac{\partial \rho \phi}{\partial t} \right)_P V \right] \mathrm{d}t + \int_t^{t+\Delta t} \left[a_P \phi_P - \sum_N a_N \phi_N - b_p \right] \mathrm{d}t = 0. \tag{3.28}$$

This equation is of the form:

$$\int_t^{t+\Delta t} \left(\frac{d\psi}{dt} \right) \mathrm{d}t = \int_t^{t+\Delta t} F \mathrm{d}t, \tag{3.29}$$

and so:

$$\frac{\Delta \psi}{\Delta t} = F^{av}. \tag{3.30}$$

Hence,

$$\psi^n = \psi^{n-1} + F^{av} \Delta t. \tag{3.31}$$

Therefore, the new value of ψ at the new time step ($\psi^n = \psi(t + \Delta t)$) can be calculated from the old value of ψ at the old time step ($\psi^{n-1} = \psi(t)$). However, the value of the average derivative, F^{av} is not known until the solution is known and so must be estimated. Estimations are made by temporal differencing schemes. The following temporal differencing schemes are given as information to the reader about the nature of the differencing schemes.

Forward differencing (Euler method) estimates the value of the average derivative as its value at the old time step, $F^{av} = F^{n-1}$. This method is easy to implement because it is explicit. However, it is only first order accurate in time and time-step restrictions must be imposed to ensure stability.

Backward differencing (Backward Euler) estimates the value of the derivative at the end of the time step, $F^{av} = F^n$. In CFD calculations this removes the limit to the time-step, but is still first order accurate. It is an implicit scheme and so iteration must be performed to determine the solution.

The Crank-Nicolson scheme is a centred differencing scheme and approximates the average derivative by, $F^{av} = \frac{1}{2}(F^n + F^{n+1})$. The advantage of this scheme is that it is second order accurate in time. However, time-step restrictions need to be imposed in CFD to ensure stability.

Using implicit temporal discretisation methods, equation 3.28 can be rewritten in canonical form as:

$$k_P \phi_P^n + \sum_N k_N \phi_N^n = j_P, \tag{3.32}$$

where the coefficients k_P, N and j_P are determined from the discretisation process. This equation is solved for each cell in the domain and due to the relation between the

equations, a matrix equation is formed:

$$|A||\Phi| = |j|, \tag{3.33}$$

where $|\Phi|$ is the vector of node values, $|j|$ is the vector of source terms and $|A|$ is a sparse matrix containing the coefficients of the canonical equations. This matrix equation is solved computationally in an iterative manner (see [108] for further information) to determine solutions to the differential governing equations of fluid flow.

3.6 Discretisation of the Navier-Stokes Equations

The Navier-Stokes equations are similar in form to the generic scalar transport equation. However, the equations for momentum differ in the fact that they are non-linear, coupled and must satisfy conservation of mass. Due to the coupled nature of the equations they must be solved together. In the OpenFOAM incompressible flow solvers, the mass and momentum equations are solved iteratively in a sequential manner, known as a segregated approach.

Pressure terms are present in the Navier-Stokes equations and this creates pressure-velocity coupling. In compressible flows the pressure equation is determined from an equation of state. Whereas, in incompressible flows a pressure equation is determined from the requirement of mass conservation. The momentum equation gives a relation between the velocity field and pressure field within a flow. The pressure equation is derived by substituting this into the continuity equation.

3.6.1 The Pressure Equation

According to Jasak [107], the pressure equation is derived using a semi-discretised version of the momentum equation:

$$a_P \boldsymbol{U_P} = \boldsymbol{H}(\boldsymbol{U}) - \nabla P, \tag{3.34}$$

where the term $\boldsymbol{H}(\boldsymbol{U})$ is given by:

$$\boldsymbol{H}(\boldsymbol{U}) = -\sum_N a_N \boldsymbol{U_N} + \frac{\boldsymbol{U^0}}{\Delta t}. \tag{3.35}$$

and so the velocity can be expressed as:

$$\boldsymbol{U_P} = \frac{\boldsymbol{H}(\boldsymbol{U})}{a_P} - \frac{1}{a_P}\nabla p, \tag{3.36}$$

and the cell-face velocities are given by:

$$\boldsymbol{U_f} = \left(\frac{\boldsymbol{H(U)}}{a_P}\right)_f - \left(\frac{1}{a_P}\right)_f (\nabla p)_f. \tag{3.37}$$

Thus, substituting equation 3.37 into the discretised form of the continuity equation will give the pressure equation. The discretised form of the continuity equation is given by:

$$\nabla \cdot \boldsymbol{U} = \sum_f \boldsymbol{A} \cdot \boldsymbol{U_f}, \tag{3.38}$$

and so the pressure equation is [107]:

$$\begin{aligned} \nabla \cdot \left(\tfrac{1}{a_P} \nabla p\right) &= \nabla \cdot \left(\tfrac{\boldsymbol{H(U)}}{a_P}\right) \\ &= \textstyle\sum_f \boldsymbol{A} \cdot \left(\tfrac{\boldsymbol{H(U)}}{a_p}\right)_f, \end{aligned} \tag{3.39}$$

which gives after discretisation of the left hand term:

$$\sum_f \boldsymbol{A} \cdot \left[\left(\frac{1}{a_P}\right)_f (\nabla p)_f\right] = \sum_f \boldsymbol{A} \cdot \left(\frac{\boldsymbol{H(U)}}{a_p}\right)_f. \tag{3.40}$$

The face flux, C is given by:

$$C = \boldsymbol{A} \cdot \boldsymbol{U_f} = \boldsymbol{A} \cdot \left[\left(\frac{\boldsymbol{H(U)}}{a_P}\right)_f - \left(\frac{1}{a_P}\right)_f (\nabla p)_f\right] \tag{3.41}$$

3.6.2 PISO Algorithm

The PISO algorithm [109] is a pressure-correction method used during transient CFD simulations. Pressure-correction methods are used to derive velocity and pressure fields that satisfy both the momentum equation and continuity. The following steps outline the PISO algorithm [107]:

- **Momentum predictor step** - Solve the momentum equation using the pressure field from the previous time-step. This gives an approximation to the velocity field.
- **Pressure solution** - Solve the pressure equation using the approximate velocity field.
- **Explicit velocity correction step** - The velocity field is corrected using the new pressure field to give a conservative velocity field. The mass flux is also calculated at this step.
- Repeat from step 2 for the specified number of PISO corrector loops.

3.7 Adaptive Mesh Refinement

Adaptive mesh refinement is a method whereby initial solutions are found on a coarse mesh, which is then refined in specified regions to improve the accuracy of the initial solution. The solution from the coarse mesh are mapped onto the refined mesh. Variables stored at cell centres can be easily mapped, but the mapping of face fluxes requires an alternative approach to ensure continuity. According to Jasak [107], variables stored at cell centres (ϕ_P) at the point, P in the new mesh can be mapped from the original coarse mesh using the equation:

$$\phi_P = \phi_T + \boldsymbol{p} \cdot (\nabla\phi)_T, \tag{3.42}$$

where $\boldsymbol{p} = x_P - x_T$ is the position difference between the cell centre, P and the nearest cell centre, T in the original mesh.

For a static non-changing mesh the pressure equation (Equation 3.39) ensures that the face fluxes satisfy continuity. The face fluxes are then calculated using Equation 3.41. To ensure that the mapped solution satisfies continuity the face fluxes are not mapped directly. The fields a_p and $\boldsymbol{H}(\boldsymbol{U})$ defined at cell centres are first interpolated to the new refined mesh. The pressure equation is then solved on the new mesh, which ensures continuity of the solution. The face fluxes can then be determined for the new mesh.

For VOF simulations the condition for refinement is usually based on the volume fraction, α. The volume fraction is defined to be $\alpha = 1$ in the liquid phase and $\alpha = 0$ in the gas phase with the interface located at $\alpha = 0.5$. In reality, due to numerical diffusion the interface is not located at exactly $\alpha = 0.5$ and is in fact spread over the width of a few cells. Therefore, for adaptive mesh refinement at the interface the refinement is usually carried out between a range of volume fractions about the value $\alpha = 0.5$. In this thesis the range was chosen to be $0.2 < \alpha < 0.8$ to ensure that adequate refinement was made about the interface. This fairly wide range was selected because if mass transfer was included in the simulations, adequate refinement in the vicinity of the interface would be required to capture concentration gradients at the interface.

Chapter 4

Microscale Hydrodynamics

This chapter focuses on the hydrodynamics of packed columns at the microscale. The first section of this chapter looks at gravity-driven film flow over smooth surfaces. The results are validated by comparison with experimental data from the literature and the Nusselt theory. Multiple inclination angles are investigated to determine the effect of the inclination angle on the wetted area. The second part of this chapter details the results of film flow over a textured plate. Comparisons are made between the smooth and textured plate, in terms of wetted area, interfacial area, interfacial velocities and thickness of the liquid films.

4.1 Introduction

This investigation involved simulating flow at the microscale. The intricate fluid flow behaviour throughout packing was simplified to film flow over an inclined plane. By reducing the number of parameters and complexity of the problem in this way, a detailed analysis of the film flow was performed. The findings in this chapter could be used as the basis for an optimisation study in order to determine the optimum packing structure for CCS.

It is important to determine the fluid dynamics of liquid films because the efficiency of CO_2 absorption is closely related to the structure of the liquid films within the packing materials. Liquid films can exhibit a range of flow regimes, including full-film, rivulet and droplet flow. The formation of these features is dependent upon various flow parameters, such as liquid flow rate, plate surface texture, plate geometry etc.

The efficiency of CO_2 absorption in packed columns is highly dependent on the structure of the liquid films within the column. In particular, a unique surface texture pattern for the structured packing was devised in order to increase the interfacial surface area and hence, increase mass transfer rates. To study the characteristics of liquid films

OpenFOAM is utilised to solve two-phase, isothermal film flow using the volume-of-fluid method.

The model was validated using existing experimental data and the Nusselt theory. It was found that smaller plate inclination angles, with respect to the horizontal plane, resulted in larger wetted areas on smooth plates. However, only a slight improvement in the wetted area was observed. Simulations were also performed using a ridged plate and it was observed that these surface textures significantly increase the interfacial area of the plate at the respective flow rates. This was mainly attributed to the effect of the ridges on the contact line of the film. Rivulet formations on the ridged plate were also flattened out and spread across a larger proportion of the plate width.

4.2 Numerical Methodology

4.2.1 Modelling and Governing Equations

This investigation used the solver interFOAM, enabling the solution of three-dimensional, multiphase, isothermal flow to be calculated, where reactions were neglected. The flow through packed columns is highly complex due to the multiphase, multiscale and reactive nature of the system. At present, this can only be accomplished by some form of simplification or decomposition of scales [20].

This investigation focuses on the micro-scale, where liquid film flow within packed columns can be approximated by flow down an inclined plane. Reaction kinetics were neglected in order to further simplify the approach. These simplifications allowed film flow to be studied in detail, examining the effects of variation of parameters and of surface texture on the wetted area and other characteristics of the flow.

4.2.1.1 Important Parameters

The liquid film Reynolds number, Re_l is an important non-dimensional parameter in the analysis of liquid-film flow and is defined by [50]:

$$Re_l = \frac{\rho_l \cdot V_l \cdot \delta}{\mu_l}, \tag{4.1}$$

where V_l is the average liquid film inlet velocity defined as

$$V_l = \frac{Q_l}{\delta \cdot w}. \tag{4.2}$$

The Re_l number is a ratio of momentum forces to viscous forces in a flow. Another important parameter in flows with surface tension is the Weber number, We which is a

ratio of inertia to surface tension forces. The Weber number is given by,

$$We = \frac{\rho_l \cdot V_l^2 \cdot \delta}{\sigma}, \tag{4.3}$$

where σ is the surface tension.

Q_l is the volumetric flow rate of the liquid and w is the width of the film, which is approximated as the full plate width during these simulations. The liquid-film thickness, δ is given by:

$$\delta = \left[\frac{3 \cdot \mu_l \cdot Q_l}{(\rho_l - \rho_g) \cdot g \cdot sin\theta \cdot w}\right]^{\frac{1}{3}}, \tag{4.4}$$

where θ is the plate inclination angle and the subscripts, l and g refer to the liquid and gas phases, respectively.

Another important parameter used in this investigation is the specific wetted area of a plate, a_w. It is calculated as the ratio of the wetted area to the total area of the plate,

$$a_w = \frac{A_w}{A_t}. \tag{4.5}$$

The value of the specific wetted area lies in the range $0 < a_w < 1$, where $a_w = 1$ represents a fully wetted plate. It is noted that interfacial area is a more significant parameter than wetted area for mass transfer problems, since mass transfer occurs through the interfacial area. Therefore, a larger interfacial area would indicate a larger mass transfer rate. The specific interfacial area, a_i is calculated as the ratio of the interfacial area to the total area of the plate,

$$a_i = \frac{A_i}{A_t}. \tag{4.6}$$

4.2.2 Computational Domain

The computational domains were chosen to be an inclined steel plate bordered by steel walls at the sides (see Fig. 4.1). The domain was chosen to allow comparison against experimental data in the literature [48–50]. This domain is an approximate representation of a small section of structured packing. The dimensions of the domain were $0.06\,\text{m} \times 0.05\,\text{m} \times 0.007\,\text{m}$ (width×height×depth). The depth of liquid inlet corresponds to the Nusselt film thickness. The gas and liquid flow was simulated within the computational domain.

The investigation used two different domains, one smooth plate and one with surface texture. A diagram of the smooth plate is shown in Fig. 4.1. The smooth plate was meshed with 1.0 million cells, which was selected after a grid independence study had been performed (see appendix A.1.1).

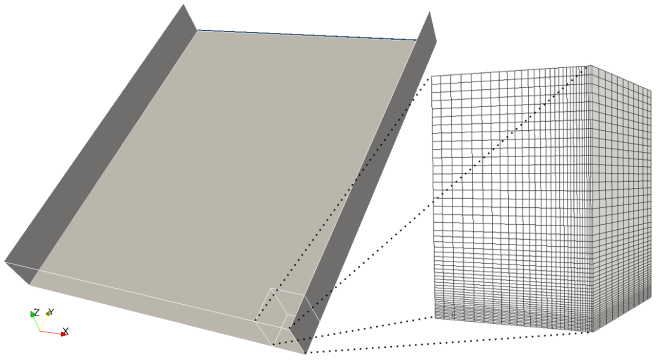

FIGURE 4.1: Computational domain and mesh for smooth plate

The textured plate maintained the same overall dimensions as the smooth plate and consisted of ridges running along the 0.06 m length. The ridges were 0.2 mm high, 0.4 mm wide and spaced 0.8 mm apart from each other. Usually structured packings have surface texture on a microscopic scale, which influences the contact angle between the fluid and the surface. This introduces difficulties in the specification of the contact angle in a CFD simulation and additional experimental investigations must be performed to determine the correct value for the contact angle. Therefore, the ridges were chosen to be of a similar scale to the liquid film thickness. This approach would allow the effect of larger scale surface textures to be examined. A diagram of the textured plate is shown in Fig. 4.2. The grid for the ridged plate consisted of 2.5 million cells, selected after a grid independence study (see appendix A.1.2).

All computational grids in this chapter use structured non-uniform hexahedral cells, so as to maintain a high degree of accuracy whilst using the VOF method. This approach resulted in a rather large number of cells for the textured plate domain, considering the level of refinement required around the ridges to fully resolve the flow. However, it was important to maintain the level of accuracy achieved by using structured grids. Due to the increased area of the textured plate it was important to introduce a correction to the specific wetted area calculation, so that direct comparisons could be made between the smooth and textured plate. The correction involved neglecting plate surfaces that were perpendicular to the film surface (e.g. side walls of the ridges), since inclusion of these surfaces would give a larger value for the wetted area.

4.2.3 Simulation Set-Up

The simulations were performed using various flow parameters. For the smooth plane, multiple inclination angles, θ were selected in order to determine the effect of inclination angle on the film flow. Simulations were run at angles, $\theta = 30^o$ and $\theta = 60^o$. The velocity of the liquid film at the inlet was altered to give a range of Re_l. During this investigation

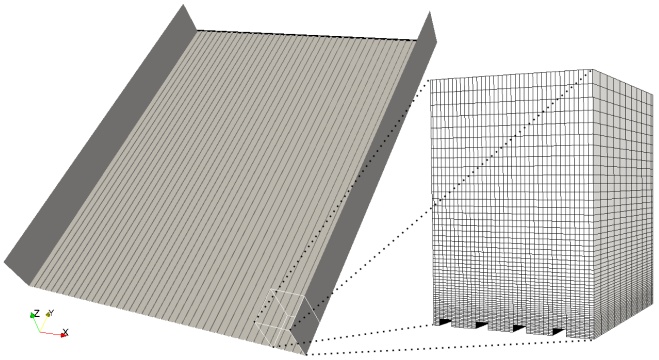

FIGURE 4.2: Computational domain and mesh for textured plate

counter-current flow of gas was neglected to allow comparison with literature data. In accordance with Hoffman *et al.* [48] and Iso & Chen [50] turbulence was not considered since $Re_l < 230$ and the flow could be considered to be in the laminar or pseudo laminar regime. It is noted that for falling liquid films the onset of turbulence can occur at $Re_l = 75$ due to wall-induced turbulence [110]. However, fully turbulent flow is not reach until $Re_l > 400$ [110] and so the laminar version of the governing equations were used in this chapter.

For the textured plate, the inclination angle was fixed at $\theta = 60^o$ for all simulations and the only varied parameter was the Re_l. The ridges on the textured plate had the effect of reducing the area of the liquid inlet and hence, the liquid flow velocity was increased in order to maintain equivalent Re_l. This allowed direct comparisons to be made between the results of the smooth and textured plates.

Simulations were conducted as time-dependent runs, stepping to steady or pseudo-steady states. All simulations were run using a variable time-step to keep the Courant number below 1.0. This resulted in time steps of the order $1 \times 10^{-5} s$. The two timescales present in these simulations are the viscous time-scale, $\tau_v = \frac{L^2}{\nu}$ and the advection time-scale, $\tau_a = \frac{L}{U}$, where L is the characteristic length scale or the cell size, ν is the kinematic viscosity and U is the characteristic velocity. In these simulations the smallest viscous timescale was approximately 16.2 times larger than the advection time scale, which confirms the choice of time-step based on the courant number, $C_r = \frac{U\tau_a}{L}$.

The simulations which resulted in the partially wetted regime were run until a steady state was reached. This was confirmed by monitoring the specific wetted area as a function of time. The dynamic viscosity and density of the constituent phases are given in Table 4.1. The surface tension was set to $\sigma = 0.0728\ \mathrm{N \cdot m^{-1}}$ and a static contact angle of $\theta_w = 70^o$ was selected [50] .

The initial conditions for the simulations were that the domain was initially filled with gas, $\alpha = 0$ and the velocity was zero everywhere. The plate surface and side walls were

TABLE 4.1: Phase Properties

Phase	μ [Pa · s]	ρ [Kg · m^{-3}]
Liquid	8.899×10^{-4}	997
Gas	1.831×10^{-5}	1.185

no-slip walls with a constant static contact angle of $\theta_w = 70^o$. The liquid inlet was set to a constant velocity with volume fraction, $\alpha = 1$. The remaining gas inlet and outlet were set to fixed pressure boundaries. The atmospheric open boundary was set to free-slip boundary condition.

The use of a no-slip boundary condition on the walls appears to be incompatible with dynamic contact line phenomena. The contact line is expected to move along the plate, but this contradicts the no-slip condition. This results in a stress singularity at the contact line [111]. Slip models can be used to remove the stress singularity at the contact line. These models allow slip at the contact line, whilst the no-slip boundary condition is applied elsewhere at the wall. The Navier-slip condition specifies the slip velocity at the contact line as being proportional to the shear stress, and is of the form,

$$u|_{z=0} = \beta \frac{\partial u}{\partial z}|_{z=0}, \tag{4.7}$$

where the wall is located at $z = 0$, β is the slip length and $u|_{z=0}$ is the slip velocity. The use of slip models then requires the slip length, β to be defined.

In the CFD simulations performed in this thesis fields are stored at cell centres. This means that numerical slip is imposed due to the fact that the velocity in the cell centre adjacent to the no-slip wall is not zero. If the mesh size is Δz in the cell adjacent to the wall, then a numerical slip length of $\frac{1}{2}\Delta z$ is imposed. According to Renardy *et al.* [112], for most applications the value of the slip length, β is of a much smaller magnitude than the mesh size. In these cases the numerical slip is greater than any imposed slip length, β. Walther *et al.* [113] state that the slip length of water on hydrophobic surfaces is of the order of 30nm, whilst for water on hydrophilic surface it is of the order of 9nm. These slip lengths are much smaller than the grid sizes used in this thesis and so the numerical slip is dominant. Therefore, the no-slip boundary condition is applied without any slip model, since a Navier-slip model with the appropriate slip length would have negligible effect in comparison to numerical slip.

The numerical slip means that the amount of slip at the contact line is dependent on the grid size. Therefore, the solution may be dependent on the grid size, if the contact line dynamics is the dominant process. However, grid refinement studies showed that finer mesh resolution had little effect on the overall solution at steady state. It may be due to the fact that the simulations were run until a steady state was reached. Here, the contact line was not in motion along the wall and so there is no paradox. Only

the time-dependence of the solution would be effected. Furthermore, the results were validated against experimental data to ensure that they were accurate, despite the above mentioned deficiencies in the numerical approach.

4.3 Results and Discussion

4.3.1 Validation

Validation of the methods used in this chapter were performed by comparison with previous studies in the literature and with the predictions of the Nusselt theory. Simulations were performed using the smooth plate with various liquid inlet velocities at an inclination angle of $\theta = 60^o$. The results are shown in Fig. 4.3, where the specific wetted area of the plate was plotted against Re_l. To provide comparative data, existing experimental results from the literature [48, 49] are also plotted in Fig. 4.3. As mentioned previously, it is noted that interfacial area is a more significant parameter than wetted area, since mass transfer occurs through the interfacial area. However, wetted area was used for validation because the experimental results, used to compare with the simulated results [48, 49], were given in terms of wetted area. A comparison of the interfacial area to the wetted area is given in section 4.3.3.

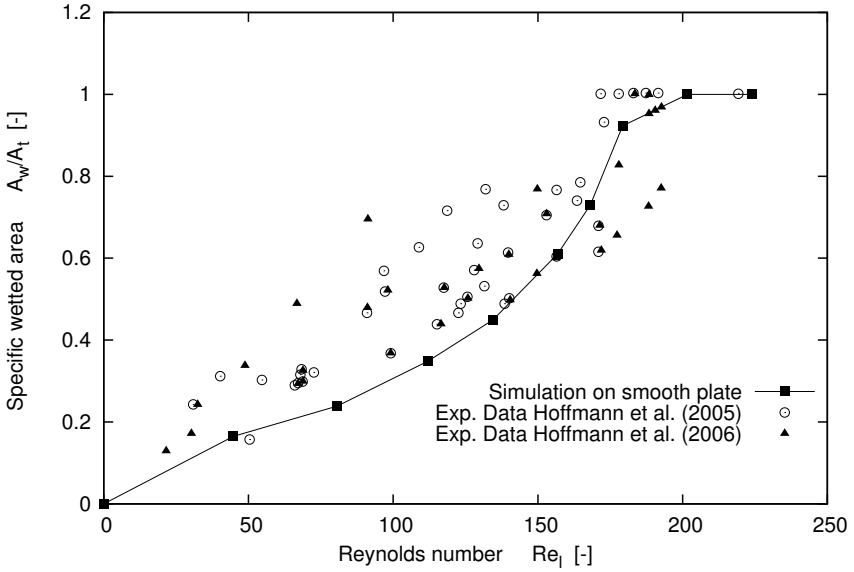

FIGURE 4.3: The specific wetted area against Re_l

It is noted that the numerical method under-estimates the wetted area at lower Re_l, but is able to correctly predict the wetted area at larger Re_l. This may be due to the fact that a constant velocity boundary condition was used at the liquid inlet, rather than the Nusselt profile. Therefore, the film would have to flow a certain distance down the plate before the proper Nusselt velocity profile was established. At lower Re_l the rivulets

formed at a position relatively close to the inlet. Here, the Nusselt velocity profile did not have sufficient time to develop and so this may have had an effect on the resulting position of the contact line. Whereas, at higher Re_l the rivulets were formed further down the plate, where the full velocity profile had sufficient time to established. It is also noted that the experimental data has a wide spread of data. This is probably due to the fact that the dynamics of the liquid film is sensitive to external factors, such as the smoothness of the plate surface. Small imperfections on the plate surface can effect the contact angle between the film and the plate, impacting the resulting wetted area. Despite these uncertainties, there is fairly good agreement between the the numerical and the experimental data and the numerical results follow the general trend observed in experiment.

The Nusselt theory [62] provides a theoretical prediction of the velocity profile within a liquid film during gravity-driven flow down an inclined plane. This theory is a model for gravity-driven film flow under the assumption of either 2D flow or in the case of an infinitely wide film. Therefore, side-wall effects are neglected. This is approximately true in the centre of the film where side-walls effects have negligible effect on the flow. The Nusselt theory predicts that the fluid velocity in the flow direction (y-coordinate direction), $v(z)$ is given by:

$$v(z) = \frac{(\rho_l - \rho_g)gsin(\theta)}{\mu_l}\left(z\delta_N - \frac{z^2}{2}\right), \tag{4.8}$$

where ρ_l is the liquid phase density, ρ_g is the gas-phase density, g is the gravitational constant, θ is the inclination angle of the plate, μ_l is the liquid viscosity, δ_N is the Nusselt film thickness and z is the plate normal distance. The Nusselt film thickness, δ_N is given by,

$$\delta_N = \left(\frac{3\mu_l Q_l}{(\rho_l - \rho_g)gsin(\theta)}\right)^{\frac{1}{3}}, \tag{4.9}$$

where Q_l is the liquid volumetric flow rate per unit width. The Nusselt velocity prediction was used to provide further validation of the computational approach used throughout this chapter. The simulation was performed at $Re_l = 224$ and inclination angles of $\theta = 30^o$ and $\theta = 60^o$. At this liquid film Reynolds number a full film had developed on the plate with no contact line. This is appropriate considering that the Nusselt theory neglects contact line effects. The film velocity profile was extracted from a central position on the plate in order to minimise the side-wall effects, which are also not considered in the Nusselt theory. A position 0.5 mm above the outlet (far from the inlet) was selected to ensure that the film was fully developed. Figure 4.4 shows the comparison between the predictions of the Nusselt theory and the data obtained using CFD simulations.

Figures 4.3 and 4.4 show that the numerical methods used in this chapter produced results in good correlation with previous experimental data and theoretical predictions.

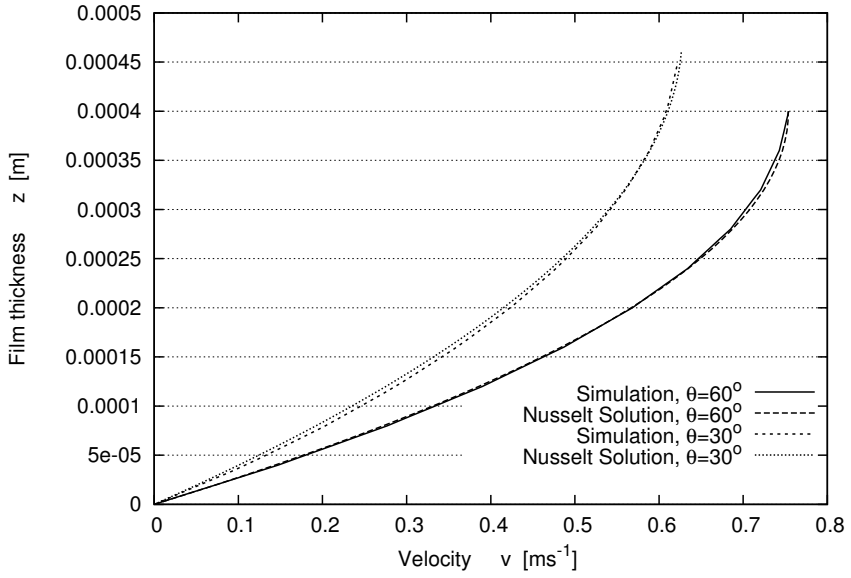

FIGURE 4.4: Comparison of film velocity profile against the Nusselt solution at $Re_l = 224$

Therefore, it can be assumed that these methods can be used with confidence in further simulations to accurately solve for film flow on inclined planes.

4.3.2 Smooth Plate

The inclination angle of surfaces within packed columns is an important choice to make when designing packing materials. The performance of packed columns depends on the inclination angle in a number of ways. As noted by Petre *et al.* [22], shallow angles of inclination (with respect to the horizontal) result in large pressure drops when compared to steeper inclination angles. During the carbon capture process the pressure drop through the column needs to be kept to a minimum, considering that the flue gas is at a relatively low pressure. The smaller the pressure drop, the taller the column can be, resulting in a greater volume of CO_2 absorption. From a pressure drop perspective, large inclination angles are optimal. However, it is also important to examine the effect that the inclination angle has on the resulting wetted area of the packing materials.

The wetted area was simulated for a range of Re_l for inclination angles of 30^o and 60^o. The results are plotted in Fig. 4.5. It can be seen that smaller inclination angles result in larger wetted areas, across the whole range of Re_l tested. If the increased wetted area results in an increase in interfacial area this would make a positive contribution to heat and mass transfer, but a higher pressure drop would be encountered. Further investigation will need to be performed to analyse whether any advantage gained by an increased interfacial surface area is offset by the increased pressure drop. The increased wetted area for the smaller inclination angle is probably due to the fact that the wall normal component of gravity is larger and therefore, hydrostatic pressure is larger. Increased

hydrostatic pressure within thin films has been shown to increase the stability of the interface [58]. In particular, the contact line ridge will be smaller and so is more stable against transverse perturbations. Therefore, the contact line will move further down the plate before contact line instabilities grow large enough to cause rivulet formation. This would result in larger wetted areas, as has been observed in the data.

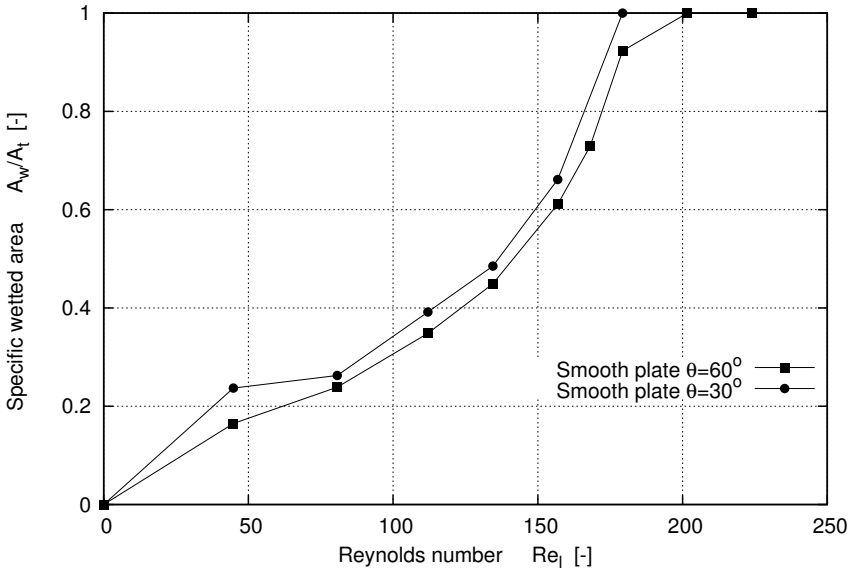

FIGURE 4.5: Comparison of specific wetted area for a range of Re_l at inclination angles of 30^o and 60^o

It is known that rivulet formation is caused by instabilities of the gas-liquid interface and of the contact line. In these simulations the perturbation of the interface, which creates the instabilities leading to rivulet formation, is likely to be created by the side walls of the plate. After the initial release of liquid onto the plate, surface tension causes the fluid to move up the side walls to adhere to the contact angle of the wall, as can be seen in Fig. 4.6. Fig. 4.6 plots the film interface contour and associated film depth 0.01s after the release of the liquid onto the plate, for the case of $Re_l = 156.85$.

In accordance with the observations of Oron *et al.* [56], when the fluid is released onto the inclined plane the contact line is initially straight in the spanwise direction. There is also a ridge formed at the contact line due to the induced high pressure at the contact line [56] (see Fig. 4.6). This contact line is unstable to perturbations and will form rivulets, which can be observed in Fig. 4.9. In this case a single rivulet is formed.

Observing Fig. 4.6, if we denote the initial film depth at the contact line ridge as, h_l, the film depth at the side-walls is greater than h_l. This in turn causes the film depth to reduce to below h_l in the regions between the side-walls and the centre of the plate, as can be seen in Fig. 4.6. This perturbation of the film interface grows in time, eventually resulting in the rivulet formation. This growth can be seen in Figures 4.7-4.8 which plot the liquid interface 0.08s and 0.12s after the release of the liquid onto the plate, for the

$Re_l = 156.85$ case. The liquid film eventually reaches a steady state where the contact line becomes stationary and there is no movement of the liquid interface (see Fig. 4.9).

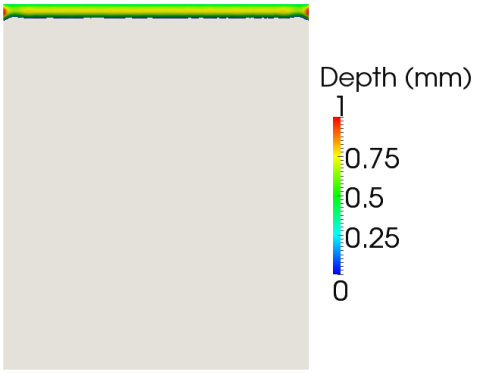

FIGURE 4.6: Thickness of liquid film at $Re_l = 156.85$ 0.01 seconds after release

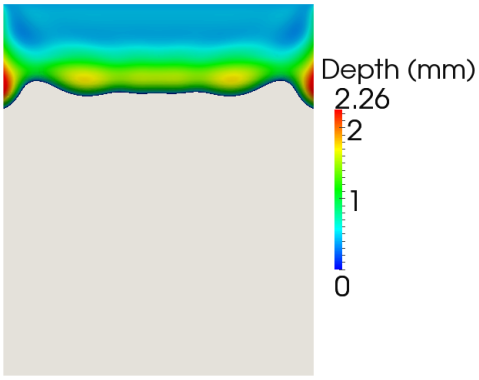

FIGURE 4.7: Thickness of liquid film at $Re_l = 156.85$ 0.08 seconds after release

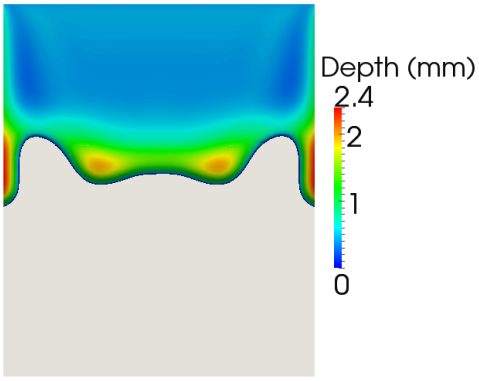

FIGURE 4.8: Thickness of liquid film at $Re_l = 156.85$ 0.12 seconds after release

It is noted that there is very little wave formation in the film prior to the contact line. In the region preceding the contact line ridge, the film is very flat, apart from the curvature near the side walls. The lack of wave formation is probably due to the small size of the plate, meaning that instabilities at the interface do not have sufficient time to grow. This is in agreement with the experiments of Park & Nosoko [61] who also found that

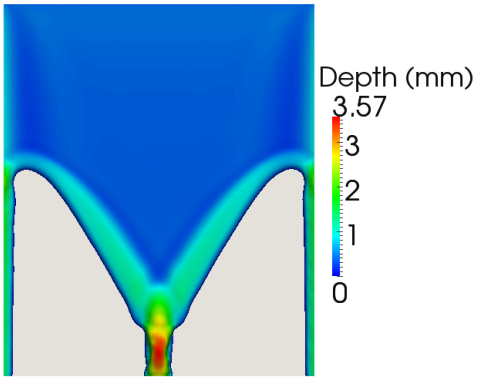

FIGURE 4.9: Thickness of liquid film at $Re_l = 156.85$ at steady state

an initially flat liquid interface required sufficient time before perturbations grew into 2D or 3D surface waves.

4.3.3 Textured Plate

This section discusses the results of film flow over inclined planes with surface textures. The ridged surface of the plate was devised in order to increase the wetted and interfacial area of the plate. Fig. 4.10 shows a comparison of the specific wetted and interfacial areas of the smooth plate and the ridged plate for a range of Re_l at $\theta = 60^o$. It was observed that the addition of ridges, running parallel to the flow direction, significantly increased the wetted area of the plate at all $Re_l < 200$. The observed increase in wetted area also resulted in an increase in the interfacial area at respective Re_l.

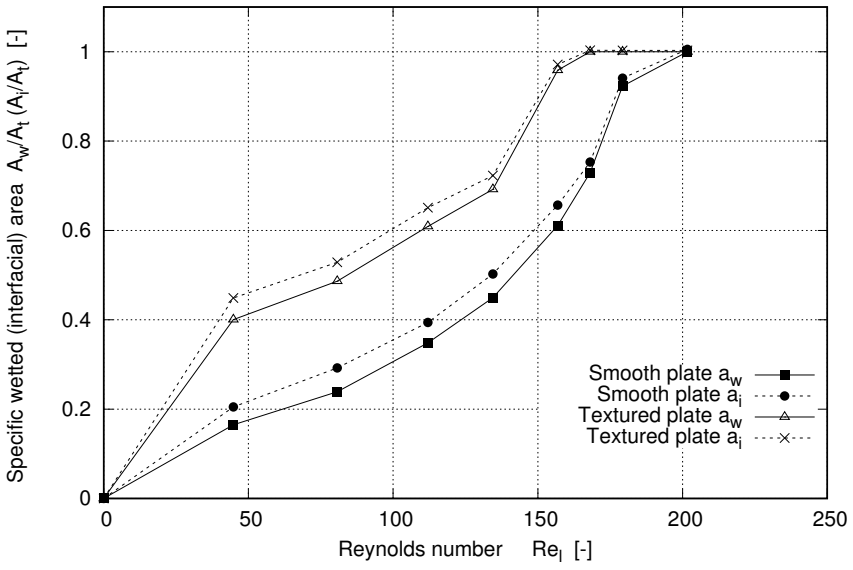

FIGURE 4.10: Specific wetted area, a_w and specific interfacial area, a_i against Re_l for the smooth and textured plate ($\theta = 60^o$)

At low-range and mid-range Re_l, rivulet flow, induced by surface tension forces and instabilities at the interface, cause a reduction in the wetted area. As can be seen in Fig. 4.11, rivulets can form with a thickness of several times that of the preceding film flow. It can be seen in Fig. 4.11 that ridges on the plate help to spread the rivulet over a much larger area across the width of the plate, thus increasing the wetted area. This is likely due to the ridges interfering with the contact line at the leading edge. The film interface must form the correct contact angle at all walls within these ridges.

The break up of the leading edge of the film observed within the channels is likely to be unphysical and a deficiency of the VOF method. Since the location of the interface in the VOF method is spread across a few cells, the approach breaks down when the number of cells is insufficient to resolve the interface. It was observed that in these simulations the interface was spread over approximately 3 cells. However, there are only 6 cells across the width of each channel. Therefore, it is concluded that the channeling flow observed within the ridges is caused by a numerical deficiency, rather than being physically accurate. Extra refinement within the channels could alleviate this problem, but the resulting increase in computational load would prove limiting. Adaptive mesh refinement at the interface is an approach that is likely to improve the inaccuracies of the computation within the channels.

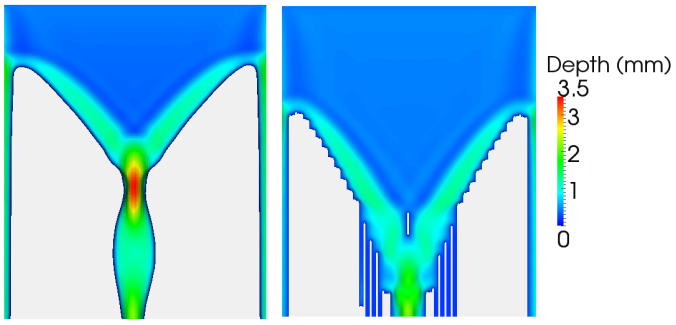

FIGURE 4.11: Thickness of liquid film at $Re_l = 134.44$ and $\theta = 60^o$ (left: Smooth plate, right: Textured plate)

It is interesting to note that the textured surface has a much larger effect on the wetted area at the lower range of Re_l tested. Table 4.2 shows the percentage increase in the wetted area from the smooth plate to the textured plate. It will be important to determine the effects of these ridges on other aspects of the system. For example, in a packed column, these ridges may prevent the transport of MEA throughout the liquid film, resulting in CO_2 rich regions near the film surface and CO_2 lean regions within the ridges. If MEA transport is inhibited, then the CO_2 absorption rate may be reduced, cancelling out the advantages created by the increased interfacial area. The exact nature of these effects is only speculative and is out of the scope of this investigation.

It is crucial to remember that idealisations have been made in order to reduce the complexity of the problem. In reality, the Re_l and the film structure will depend upon many factors, such as liquid flow rate, the distribution of liquid throughout the columns,

corrugation angle, inclination angle of the packing, etc. Further mesoscale simulations will need to be performed to determine the exact liquid distribution over the packing. This chapter shows that the addition of ridges should improve the wetted and interfacial area of full-scale packing up to a limiting Re_l. The limiting Re_l will be dependent on the specific problem being investigated and it can be defined as the point at which full film flow occurs.

Re_l [-]	A_w^{smooth}/A_t [-]	$A_w^{textured}/A_t$ [-]	Increase in Wetted Area [%]
0	0	0	0
44.81	0.164787	0.400508	143.05
80.67	0.238929	0.486207	103.49
112.04	0.348422	0.608895	74.76
134.44	0.449249	0.69194	54.02
156.85	0.610955	0.958555	56.89
168.05	0.729229	1	37.13
179.26	0.923153	1	8.32
201.66	1	1	0
224.07	1	1	0

TABLE 4.2: Specific wetted area for smooth and textured plate at $\theta = 60^o$

Fig. 4.12 shows the interfacial velocity magnitude for the smooth and textured plates at $Re_l = 179.26$ and $\theta = 60^o$ and Fig. 4.13 shows a close-up view of the velocity vectors within this film along the plane $y = 0.02\,\text{m}$. It is observed that the ridges on the plate create alternate layers of varying interfacial velocities along the surface of the film. This is attributed to the reduction in film thickness, due to the presence of the ridges. Fig. 4.13 shows that the addition of ridges along the plate does not result in regions of stagnant fluid within the channels. Furthermore, the variation in velocity throughout the film and the film surface may assist in the heat and mass transfer process, since different layers of fluid within the film move at different velocities. However, as mentioned previously, the impact of these structures on the CO_2 absorption process will have to be assessed in future investigations.

Packing materials also have a corrugation angle (usually 45^o) as well as an inclination angle. The corrugation angle was neglected in this chapter, but it is predicted that the effect of this would be to cause liquid to accumulate at the sides of the plate. The channels on the textured packing may help to prevent such accumulation of liquid and help to produce more evenly distributed films.

Also, it has been assumed that the liquid inlet spans across the whole width of the plate. However, in reality this may not be the case, especially well within the packed column.

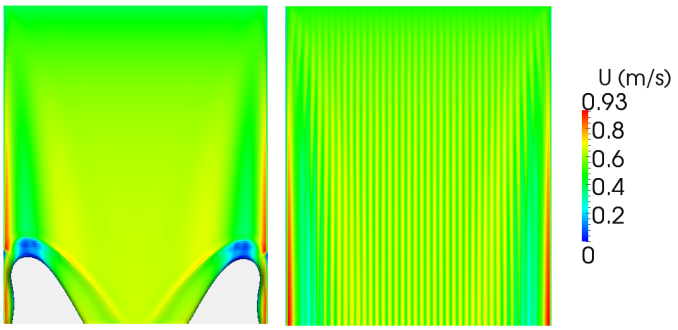

FIGURE 4.12: Interfacial velocity contours of liquid film at $Re_l = 179.26$ and $\theta = 60^o$ (left: Smooth plate, right: Textured plate)

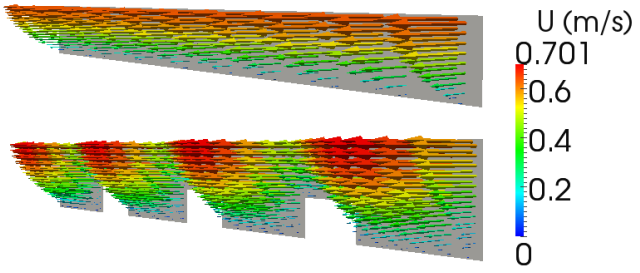

FIGURE 4.13: Velocity vectors within the liquid film along the plane $y = 0.02\,\text{m}$ at $Re_l = 179.26$ and $\theta = 60^o$ (top: Smooth plate, bottom: Textured plate)

In the case of a point source of liquid the channels may even reduce the wetted area. This will have to be investigated further and modifications to the design could help to increase the wetted area for various inlet conditions.

4.4 Conclusion

In this chapter the VOF method was used to study isothermal liquid film flow down inclined planes. Initially, simulations were performed on a smooth plate and the effect of inclination angle on the wetted area was studied for a range of Re_l. The methods used throughout this chapter were validated using existing experimental data and theoretical predictions. Also, it is noted that the experimental results for wetted area have large variation. Future research could focus on performing more experimental analysis of thin film flow down inclined plates to determine more accurately the relation between Re_l and wetted area.

It was found that a decrease in the inclination angle resulted in larger wetted areas at the respective Re_l. However, the increases observed were minimal. The advantage gained from using small inclination angles in packed columns is the increase in gas-liquid interfacial area, which should enhance heat and mass transfer. However, negative side-effects of shallow inclination angles, such as larger pressure drops, may negate these improvements.

A unique surface texture pattern on an inclined plate was also investigated. It was found that the addition of vertical ridges, of the same scale as the liquid film thickness, resulted in much larger interfacial areas at equivalent Re_l. It is reasonable to assume that an increase in interfacial area should enhance CO_2 absorption within packed columns.

Chapter 5

Adaptive Mesh Refinement at the Microscale

This chapter focusses on the use of adaptive mesh refinement (AMR) as a method to improve the accuracy of VOF simulations performed in Chapter 4, whilst maintaining or reducing the computational requirements. This is of significant importance in future investigations where the complexity of the problems may be increased, in terms of the scale of the domain and a reduced level of simplifications. Local adaptive mesh refinement is used to ensure improved resolution of the geometrical grids at the gas-liquid interface.

5.1 Introduction

The interface between a gas and a liquid phase should, in theory, have a thickness in the order of the distance between molecules [114]. This scale is significantly smaller than can be resolved in VOF simulations, so the interface is at least spread over 1 cell width. However, numerical diffusion of the volume fraction widens the reconstructed interface to a thickness of a few cells. Therefore, it is obvious that in order to accurately resolve the interface the cells must be as small as possible in the interfacial region. Due to the changing nature of the interface, standard VOF requires highly refined grids throughout the domain to ensure proper resolution at the interface, as it progresses through the domain. This can significantly affect the computational requirements.

An approach which attempts to address this problem is local adaptive mesh refinement. Local AMR allows for dynamic refinement of the mesh in regions of high error and un-refinement in regions of low error [107]. In terms of the VOF method, refinement is made at the interface in order to ensure that the mesh can accurately resolve it. As the interface moves through the domain, successive mesh refinement and un-refinement can

take place. Refinement is achieved using the addition of computational nodes, known as h-refinement [107].

The AMR approach has been used successfully in many different applications, from single-phase flows to multiphase flows. Jasak and Gosman [115] developed an AMR procedure based on a-posteriori error estimates and solution gradients. They used this approach to solve supersonic flow of an ideal gas flowing over a forward facing step resulting in strong shock wave formations. Shock waves exhibit large gradients and so require high cell densities to be resolved accurately. Jasak and Gosman showed that the use of AMR was able to suitably resolve these shocks.

In terms of multiphase flows, Theodorakakos and Bergeles [114] evaluated the effectiveness of AMR with the VOF method on various test cases. Simulations were performed on the convection of bubbles under prescribed flow velocities and droplet impact was also studied. They concluded that the AMR approach was able to reduce the computational time for simulations, whilst gaining very good accuracy of the interfacial region. In particular, they observed that a very small transition region between the gas and the liquid phases could be achieved, which is physically more realistic. Numerical diffusion of the interface was reduced, which addresses one of the disadvantages of the VOF method.

There have also been investigations using the VOF approach with AMR to study droplet impact onto thin liquid films [116, 117]. This approach is particularly useful in these situations because of the range of scales observed, for example, during the breakup of the crown of fluid formed after impact. These examples show that significant improvements can be made to the VOF method with the inclusion of local AMR.

This chapter uses the local AMR approach in an effort to improve upon the results gained using a static grid. Improvements are expected in terms of simulation accuracy and computational effort. Comparisons are made between the solutions obtained using AMR and those obtained using highly refined static meshes. It was observed that local AMR produced results with much better correlation to experimental data. However, it was shown that in order to reduce the computational requirements, careful consideration is required in the choice of AMR parameters, such an initial grid resolution or number of refinement levels. Inadequate selection of AMR parameters can even result in increased computational load.

5.1.1 Numerical Modelling

5.1.1.1 Adaptive Grid Refinement

Adaptive grid refinement is a method used to dynamically alter the mesh density throughout the domain. For example, in regions of high gradients, large numbers of cells are required to accurately resolve the solution. In principle, this can be achieved

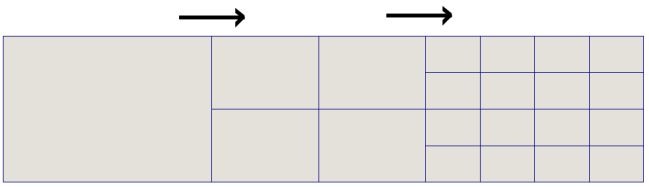

FIGURE 5.1: AMR refinement of a single computational cell in 2D for 2 levels of refinement

by producing an initial grid where mesh density is high in these specific regions, whilst being of low density in regions of less importance.

In the VOF method it is important to accurately resolve the interfacial region between two phases. The accuracy of the interface can be improved by using high densities of cells around the interfacial region. However, the location of the interface is not known a priori and so using a static grid method would require a high density mesh throughout the domain, creating excessive simulation run-times.

Adaptive Mesh Refinement allows one to initiate the simulation using a relatively coarse grid, which is then successively refined and un-refined according the specific location of the interface. This enables accurate resolution of the interface, whilst keeping run-time to a minimum. The only overhead is created by the process of mesh adaptation.

In this investigation the solver interDymFoam was used for the AMR simulations. This is an extension of the standard VOF solver, interFoam, to include dynamic manipulation of the computational grid. A dictionary file is used to specify the parameters for the grid manipulation. Grid refinement can be performed at specific time-step intervals and can be based on specific flow fields, for example, volume fraction. Cells are refined if this field is within a specified refinement range. If the value of the field within these cells moves outside of this range, the cells are un-refined back to the initial mesh. The grid refinement is performed by adding computational nodes along the mid-points of cells within the specified refinement regions [116]. Hence, a 3-dimensional hexahedral cell will be split into 8 new cells. Figure 5.1 shows the refinement of a single, 2D computational cell, with 2 levels of refinement. The arrow indicates an individual refinement step. The criteria for grid refinement used in this chapter is explained in the section 5.1.3.

5.1.2 Computational Domain

The computational domain was chosen to be the smooth inclined steel plate used in Chapter 4 (see Fig. 5.2). The domain dimensions were kept at $0.06\,\mathrm{m} \times 0.05\,\mathrm{m} \times 0.007\,\mathrm{m}$ (width×height×depth). The depth of liquid at the inlet was set by the Nusselt film depth.

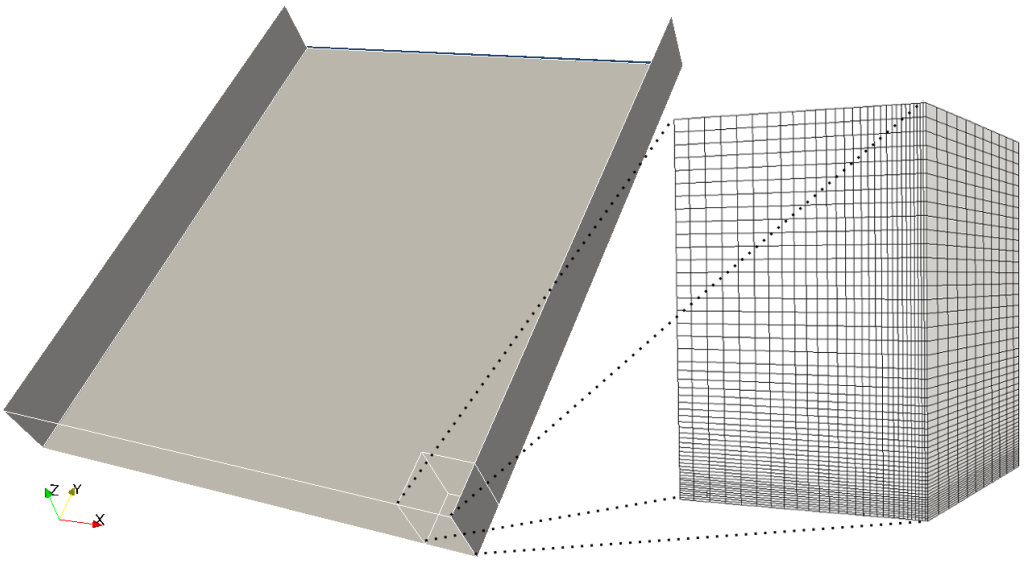

FIGURE 5.2: Computational domain and refined static mesh

This investigation used two different approaches to the meshing procedure (see Table. 5.1). Firstly, simulations were run using a structured, non-uniform, hexahedral static mesh, whereby mesh independence checks (see appendix A.1.1) were performed to determine an adequately fine grid resolution. The mesh is shown in Fig. 5.2, consisted of 1.0 million cells and will be denoted as the static mesh.

Secondly, simulations were run using the local AMR method, using two different conditions on the refinement (see Table 5.1). Refinement around the interface with volume fractions in the range, $0.2 < \alpha < 0.8$ is denoted as the partial-film mesh, whereas refinement around the interface and the whole film region with volume fractions in the range, $0.2 < \alpha < 1.0$ is denoted as the full-film mesh. An initial mesh was selected with 192000 structured non-uniform hexahedral cells. A grid independence study was performed to determine an adequate limit on the number of refinement levels. Levels of 2 and 3 were tested and the refinement level of 2 was found to be most appropriate. The extra level of refinement generated much larger cell numbers within the domain causing the run-time to increase approximately 20 times. However, the difference in the calculated specific wetted area was only 2.72%.

Figure 5.3 shows a comparison of the mesh used in the static grid and partial-film AMR grid simulations. The sections of mesh were selected from the plate surface at time, $t = 0.36$s with $Re_l = 156.85$. On the left, it can be seen that the static mesh is finer throughout the whole domain, whereas on the right it can be seen that the AMR mesh is refined just around the gas-liquid interface, denoted by the blue line. Figure 5.4 shows a closer view of the static mesh and the AMR mesh. Here it can be seen that the static mesh is highly refined throughout the domain, even in regions where it is not required.

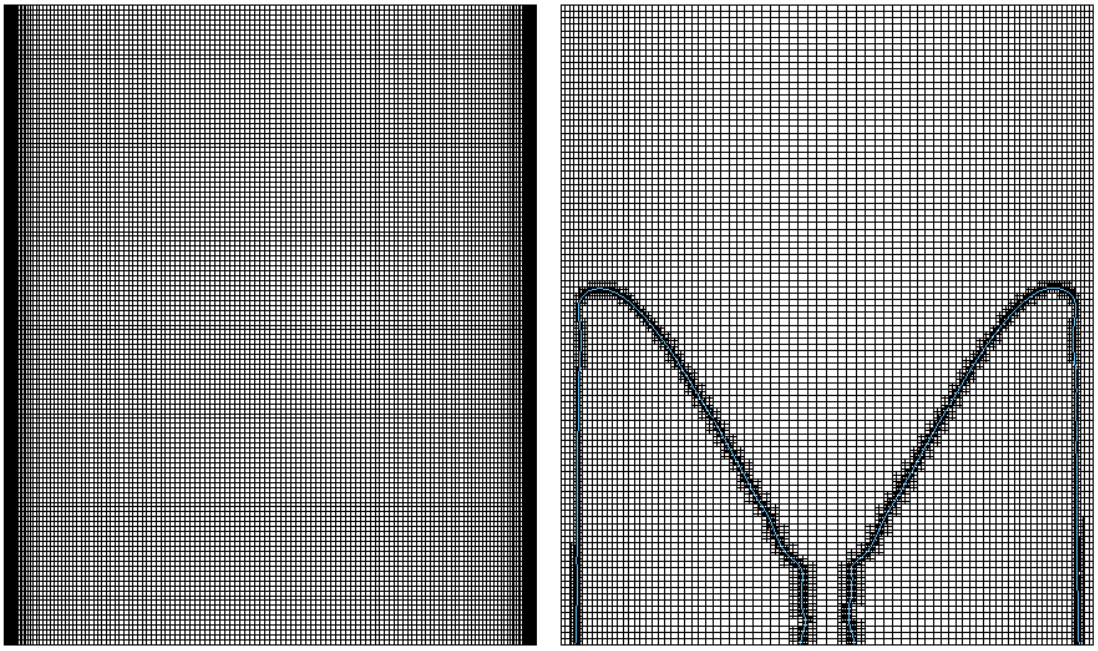

FIGURE 5.3: Comparison of the static mesh with a snapshot of the partial-film AMR mesh at $t = 0.36$s and $Re_l = 156.85$ (blue line is the gas-liquid interface)

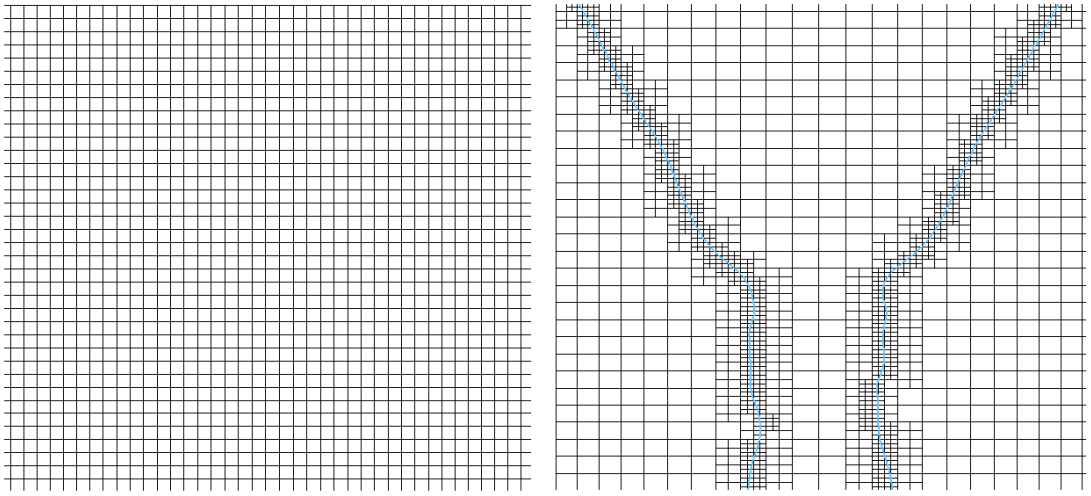

FIGURE 5.4: Closer view of comparison of the static mesh with the $t = 0.36$s snapshot of the partial-film AMR mesh at $Re_l = 156.85$ (blue line is the gas-liquid interface)

On the other hand, the AMR mesh is much more highly refined at the interface, where high grid density is required for accurate resolution of the interface. In other parts of the domain, the mesh is coarser, which helps to maintain reasonable simulation run-times.

5.1.3 Simulation Set-Up

For all simulations a constant inclination angle of $\theta = 60^o$ was chosen to allow comparisons with current data in the literature. A range of Re_l were tested by suitably altering

Table 5.1: Computational Meshes

Mesh Name	Initial Mesh Density	Refinement Conditions
Static Mesh	1.0×10^6	-
Partial-Film Mesh	1.92×10^5	$0.2 < \alpha < 0.8$
Full-Film Mesh	1.92×10^5	$0.2 < \alpha < 1.0$

Table 5.2: Phase Properties

Phase	μ [Pa · s]	ρ [Kg · m^{-3}]
Liquid	8.899×10^{-4}	997
Gas	1.831×10^{-5}	1.185

the velocity of the liquid film at the inlet. During this investigation counter-current flow of gas was neglected to again allow comparison with previous data in the literature. In accordance with Hoffman *et al.* [48] and Iso & Chen [50] turbulence was not considered since $Re_l < 230$ and the flow could be considered to be in the laminar or pseudo laminar regime. It is noted that for falling liquid films the onset of turbulence can occur at $Re_l = 75$ due to wall-induced turbulence [110]. However, fully turbulent flow is not reach until $Re_l > 400$ [110] and so laminar versions of the governing equations have been used in this chapter.

Time-dependent simulations were carried out using a variable time-step to ensure a Courant number below 1.0, resulting in time-steps of approximately $1 \times 10^{-5} s$. Simulations were allowed to run until a steady or pseudo-steady state was reached. This was assured by monitoring the specific wetted area of the plates as a function of time. During the AMR simulations the mesh adaptation was performed every 5 time steps. The two timescales present in these simulations are the viscous time-scale, $\tau_v = \frac{L^2}{\nu}$ and the advection time-scale, $\tau_a = \frac{L}{U}$, where L is the characteristic length scale or the cell size, ν is the kinematic viscosity and U is the characteristic velocity. In these simulations the smallest viscous timescale is approximately 9.7 times larger than the advection time scale, based on the smallest cell size after maximum refinement of the grid. This confirms the choice of time-step based on the courant number, $C_r = \frac{U\tau_a}{L}$.

The dynamic viscosity and density of the constituent phases are given in Table 5.2. The surface tension was set to $\sigma = 0.0728$ N · m^{-1} and a static contact angle of $\theta_w = 70^o$ was selected [50].

The initial conditions for the simulations were that the domain was initially filled with gas, $\alpha = 0$ and the velocity was zero everywhere. The plate surface and side walls were no-slip walls with a constant static contact angle of $\theta_w = 70^o$ [50]. The liquid inlet was set to a constant velocity with volume fraction, $\alpha = 1$. The remaining gas inlet and

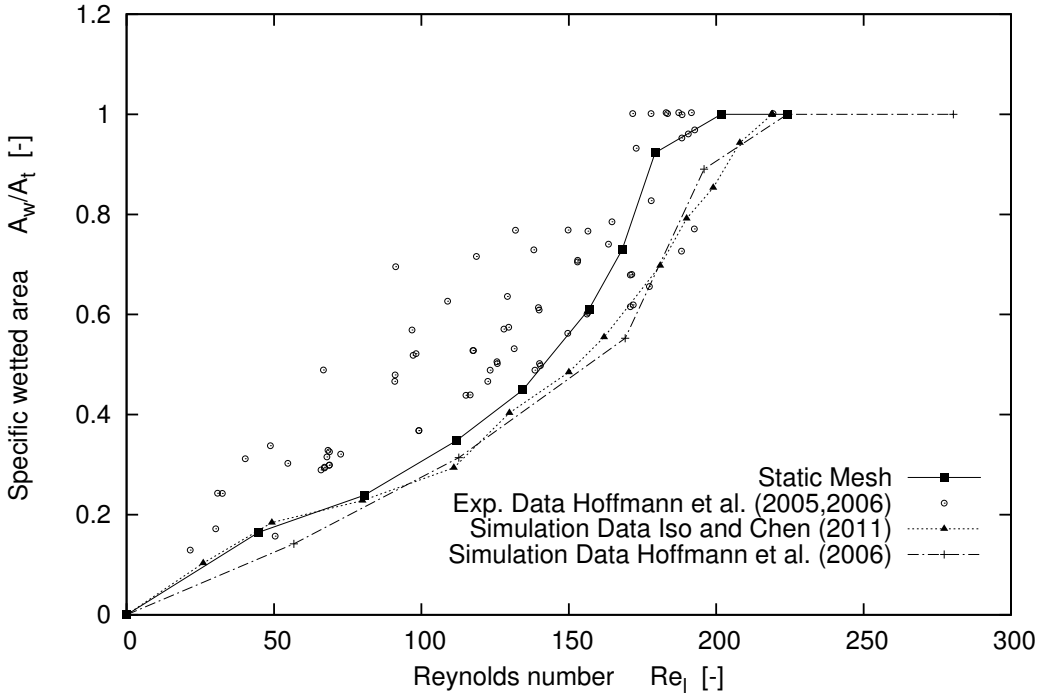

FIGURE 5.5: Comparison of Static Grid Simulation with Literature

outlet were set to fixed pressure boundaries. The atmospheric open boundary was set to free-slip boundary condition. Here again the slip length is much smaller than the grid size and so the no-slip condition is applied without a slip model. Numerical slip caused by locating the velocity fields at cell centres alleviates the contact line paradox.

5.2 Standard Grid Refinement

5.2.1 Results & Discussion

Comparison of the results obtained with the smooth static grid from Chapter 4 were made with other CFD data from the literature. Figure 5.5 shows a plot of the results of various of the simulations, along with the experimental data of Hoffmann *et al.* [48,49]. It is observed that improvements have been made in terms of the accuracy of the simulated data, possibly due to the much finer grid resolutions used in this thesis. At higher Re_l the wetted area is correctly predicted, but at lower Re_l the approach still under-estimates the wetted area in comparison to experimental data. Despite these improvements, significant differences between simulated and real-world phenomena are still observed.

5.3 Adaptive Grid Refinement

5.3.1 Refinement at the Interface

It was postulated that the differences between the data of CFD simulations and real-world data, especially at lower Re_l, were caused by inefficiencies of the VOF method. Since some improvement was observed by using a higher density grid resolution across the domain, it was assumed that further improvement could possibly be made by increasing the grid resolution at the interface. This should increase the accuracy of interface reconstruction. Local AMR was used to achieve the desired increase in grid resolution at the interface, whilst maintaining reasonable run-times by using a coarse mesh in regions of less physical interest.

5.3.2 Results

In order to assess the improvements made by using local AMR at the gas-liquid interface, the wetted area against Re_l was plotted (see Fig. 5.6). Figure 5.6 also displays the experimental data of Hoffmann *et al.* [48,49] and the CFD data obtained using the static grid from section 5.2.1. It is noted that the results from local AMR were improved at the lower and higher ranges of liquid film Reynolds numbers. An important observation is the fact that local AMR provides results in much greater correlation with experimental data in the range $50 < Re_l < 100$. In this region the specific wetted area initially falls before rising again, a behaviour which is expressed in the experimental data. Simulations with a highly refined static mesh were unable to replicate this behaviour, indicating the importance of using local AMR at lower Re_l.

It would be expected that as the liquid film Reynolds number increases the wetted area would also increase. However, as noted previously, it can be seen that between $Re_l = 44.8$ and $Re_l = 58.3$ the wetted area plateaus, falling at $Re_l = 71.7$ and then rising in the assumed manner as further increases in Re_l are made. This can be explained by the flow phenomena observed at each of these Re_l. At $Re_l = 44.8$, the flow forms 4 rivulets (see Fig. 5.7), reducing to 3 rivulets at $Re_l = 58.3$ (see Fig. 5.8) and forming a single rivulet at $Re_l = 71.7$ (see Fig. 5.9). At these lower Re_l, the increasing flow rate changes the behaviour of the flow. As the rivulets combine, the wetted area stays constant, or even falls. It can be assumed that the Re_l where a single rivulet is formed is in the region $58.3 < Re_l < 71.7$, which may explain the cluster of experimental points in this range (see Fig. 5.6).

By comparing the interface contours of simulations using the static grid and the partial-film grid it is possible to see why the static grid under-estimates at lower Re_l and does not correlate properly with the experimental data. Fig 5.10 shows the interface contours at $Re_l = 44.8$. It can be seen that the static grid only resolves a single rivulet, whilst

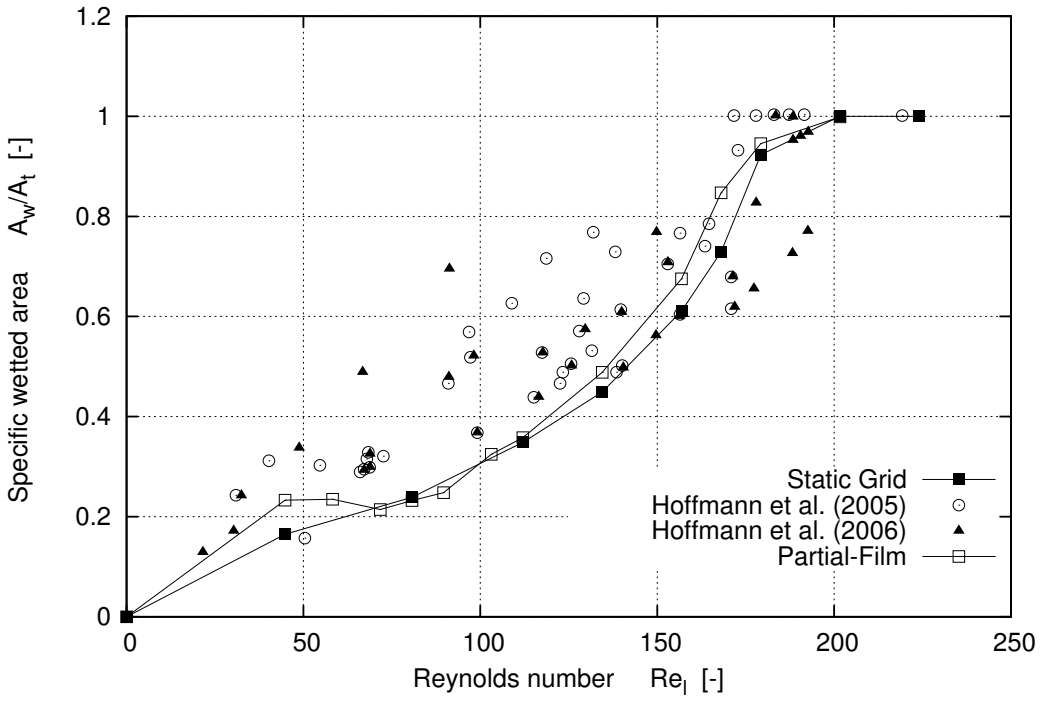

FIGURE 5.6: The specific wetted area against Re_l for AMR at the interface

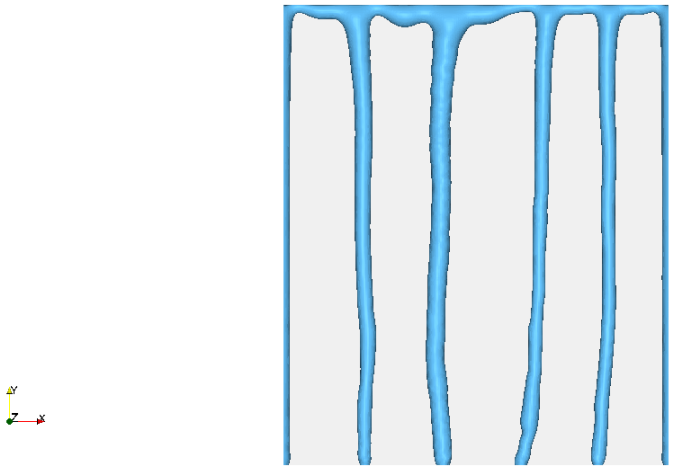

FIGURE 5.7: Contour plot of gas-liquid interface at $Re_l = 44.8$ (Partial-film mesh)

the partial-film grid resolves 4. This may be attributed to the fact that the partial-film AMR grid is much finer at the gas-liquid interface. If perturbations at the interface near the contact line are small, these may not have been resolved in the static grid. Therefore, these perturbations can grow in the AMR case, resulting in the formation of more rivulets. However, in the static grid case the mesh may not have been fine enough to resolve the perturbation, resulting in less rivulet formation. The surface area of a single rivulet is smaller than that of 4 rivulets, as can be observed in the data.

It is interesting to note that the results with adaptive mesh refinement indicate a slightly

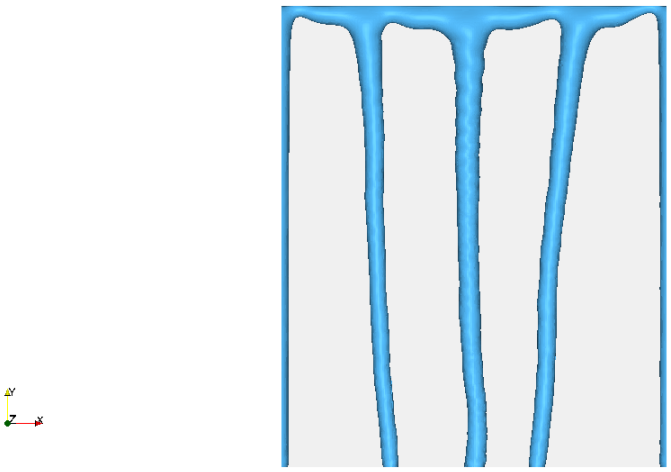

FIGURE 5.8: Contour plot of gas-liquid interface at $Re_l = 58.3$ (Partial-film mesh)

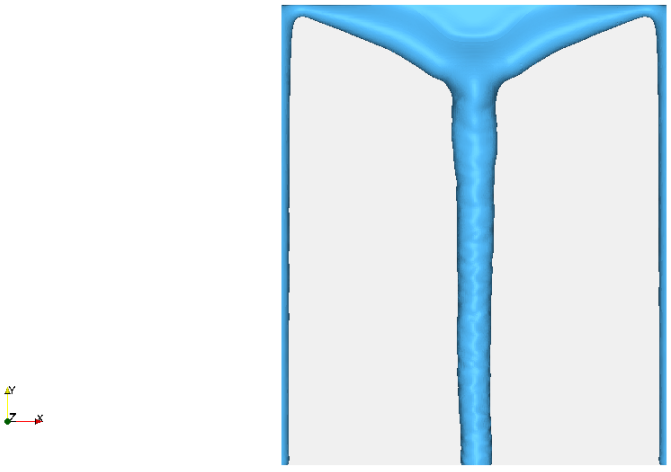

FIGURE 5.9: Contour plot of gas-liquid interface at $Re_l = 71.7$ (Partial-film mesh)

larger wetted area across the majority of Re_l when compared to the static grid, but they are broadly in agreement. This shows that the choice of a no-slip wall condition with numerical slip is not significantly mesh dependent. For the AMR grid the cells at the interface are significantly smaller than those of the static grid. This means that in the AMR simulations the slip length is much smaller, which would result in a smaller slip velocity at the no-slip wall. However, there is not a significant difference in the wetted area and overall shape of the interface from mid to high Re_l.

As mentioned previously, when mass transfer is to be modelled, the interfacial area is more significant than the wetted area. Mass transfer occurs through the gas-liquid interface and therefore, the rate of mass transfer is dependent on the interfacial area. Figure 5.11 compares the interfacial area against the wetted area for a range of Re_l. It is observed that the interfacial area is much larger than the wetted area at the lower range of Re_l. This is a direct effect of the contact line dynamics where high curvature

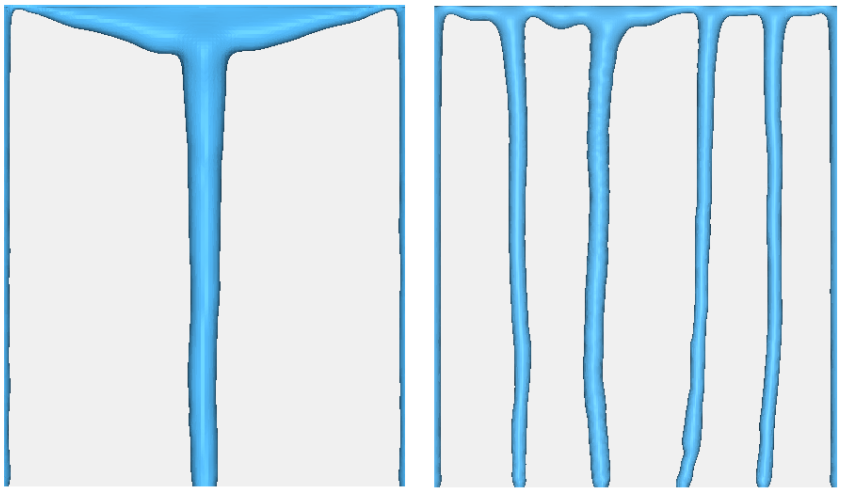

FIGURE 5.10: Contour plot of gas-liquid interface at $Re_l = 44.8$ for static grid (left) and Partial-film grid (right)

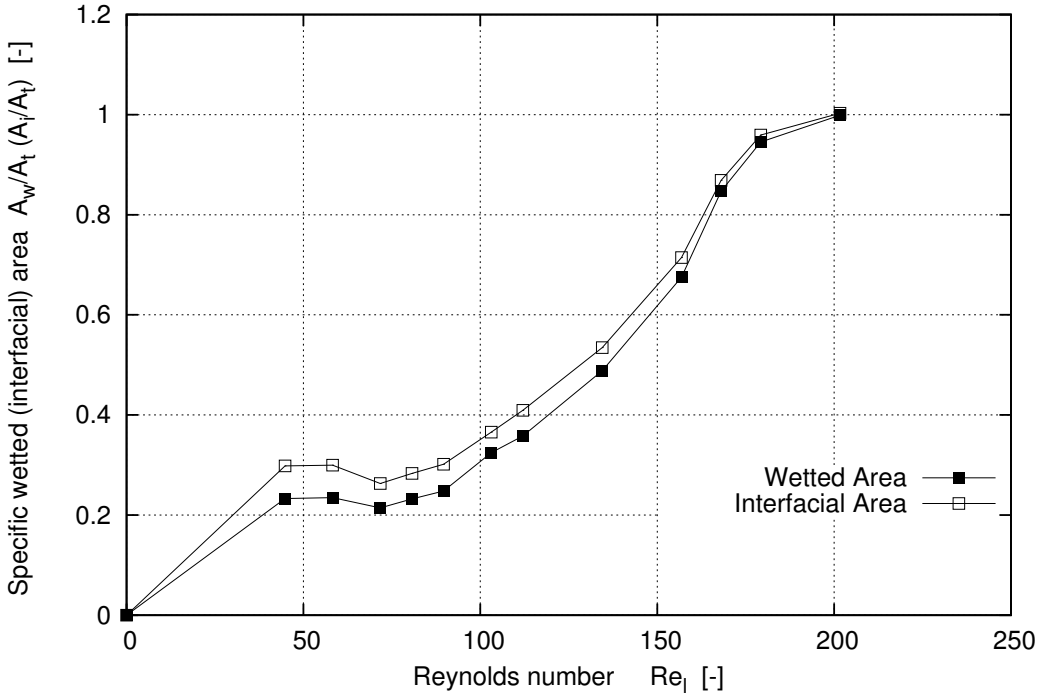

FIGURE 5.11: Comparison of specific wetted area and specific interfacial area against Re_l for the partial-film AMR simulation

of the interface results in an increase in interfacial area, in comparison to the wetted area. This exemplifies the importance of determining the interfacial area, rather than the wetted area when mass transfer is of consideration.

The flow within the gas phase is shown in Figure 5.12 for the case of $Re_l = 156.85$ at steady state. In these simulations the gas-phase is not forced at the gas inlet. The flow within the gas-phase is generated by the effect of shear force on the gas by the flowing

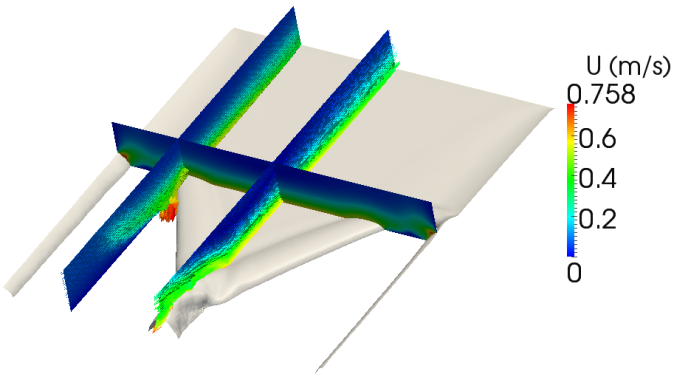

FIGURE 5.12: Flow within the gas phase for $Re_l = 156.85$ at steady state.

liquid film. It is observed that the flow of the liquid film has a significant influence of the gas phase, especially in regions near the gas-liquid contact line.

5.3.3 Full-Film Refinement

It has been shown that local AMR about the interface was more able to replicate the physical phenomena of the real-world flow. However, there was still an under-estimation of the wetted area at lower Re_l. It was considered that improvements may be made by refining the whole film, rather than just at the interface. The film within packed columns and on inclined plates is relatively thin. Therefore, shear layers at the wall may require extra refinement to be resolved accurately, especially if these shear layers have a significant impact on the interface, due to their close proximity.

AMR simulations were performed to determine the wetted area across a range of Re_l, refining the whole liquid film. Comparisons were made with the results of AMR simulations with refinement only around the interface (see Fig. 5.13).

It is observed that the results using the two methods are fairly consistent across the whole range of Re_l tested. Table 5.3 shows the run-times for each simulation. Data that is not available is denoted by "−" in the table. For the full-film simulation data was not obtained for $Re_l = 201.66$ due to excessive simulation run-times at these high Re_l.

Local AMR throughout the whole liquid film was shown to exhibit insignificant improvements. Run-times of the simulations were increased across the range of Re_l tested, with large increases seen at higher Re_l. It is obvious that under the situations tested in this investigation, local AMR throughout the whole of the liquid film was an over-complication resulting in dramatically increased run-times, with negligible improvement in accuracy. Therefore, local AMR about the interface is optimal. This finding is also important when scaling up the problem to determine the hydrodynamics within larger

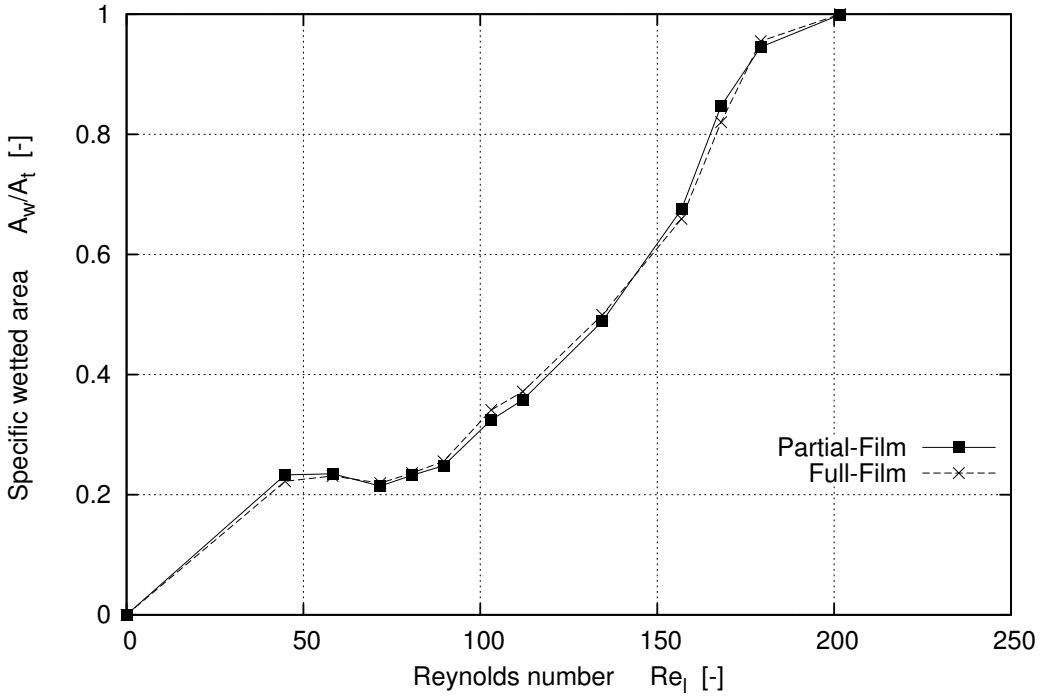

FIGURE 5.13: The specific wetted area against Re_l for various degrees of AMR

TABLE 5.3: Simulation time & actual time to convergence

	Simulation Time [s]			Actual Time [days]		
Re_l	Static Mesh	Partial-Film	Full-Film	Static Mesh	Partial-Film	Full-Film
44.81	0.54	0.63	0.47	0.14	1.75	1.90
58.26	-	0.51	0.44	-	1.55	2.09
71.70	-	0.78	0.53	-	1.52	2.47
80.67	0.65	0.5	0.56	0.39	0.89	2.74
89.63	-	0.5	0.44	-	0.85	2.23
103.07	-	0.45	0.38	-	0.80	1.87
112.04	0.8	0.47	0.37	0.15	0.84	1.94
134.44	0.8	0.52	0.55	0.38	0.99	3.49
156.85	0.33	0.36	0.28	0.16	0.56	1.50
168.05	1.85	1	0.98	0.42	2.20	6.91
179.26	2.4	1.01	1.36	0.53	1.98	9.60
201.66	0.78	0.56	-	0.26	0.93	-

sections of packing. In these situations an initial coarse grid can be selected and refinement made at the gas-liquid interface, ensuring that physically accurate results are

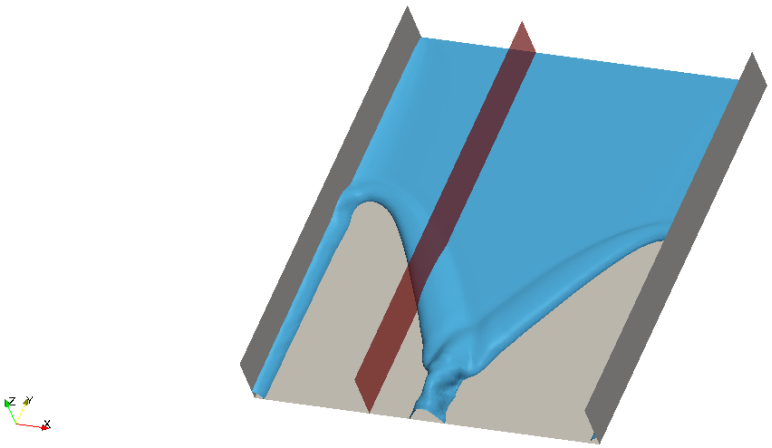

FIGURE 5.14: Cutting plane used for interface plots

achieved, whilst maintaining reasonable simulation run-times.

Despite the fact that the differences in specific wetted areas between the two types of AMR simulations was minimal, it was important to examine the structure of the liquid film to determine whether any major differences occurred. To determine the film depths down the plate a slice was taken ($x = 0.017$m), as shown in Fig. 5.14.

Figure 5.15 shows a comparative plot of the film depths for the full- and partial-film simulations at steady state along this slice. It was observed that the full-film simulations were able to resolve small waves preceding the contact line ridge. These were damped out in the partial-film simulations. This may be an important consideration to make when absorption is added to the model. Interfacial absorption is dependent on the shape of the interface and so the ripples observed may have an effect on the absorption of CO_2 across the interface. However, the observed differences in film interface structure is very minimal and so may not have a significant impact on the absorption of species across it.

If absorption and reaction kinetics are added to the AMR-VOF approach an important consideration needs to be made. In these cases, refinement is also required to resolve the large CO_2 concentration gradients in the vicinity of the interface. Here, adaptive mesh refinement could be determined by the gradient of concentration as well as the location of the interface.

In terms of packed columns, surface texture on structured packing has been shown to increase the wetted area [50, 118], as well as have an impact on the structure of the films [46]. In theory, this should enhance heat and mass transfer across the interface if an increase in the interfacial area is also observed. This has been confirmed by Kohrt *et al.* [15] who performed an experimental investigation to determine liquid-side mass transfer during flow over an inclined plate. The addition of a textured surface to a smooth plate increased the mass-side transfer by as much as 80%. It has also been

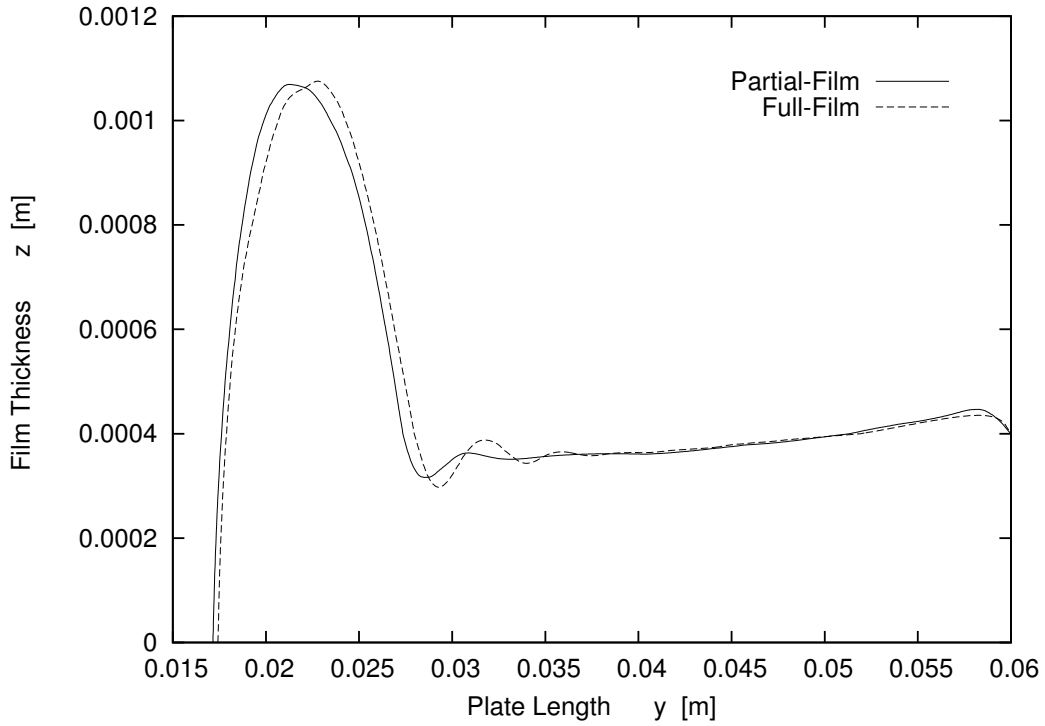

FIGURE 5.15: Interface plots along cutting plane at steady state

shown that certain surface structures can cause regions of recirculation in the film [46,47]. These regions of stagnant fluid would reduce the efficiency of CO_2 absorption.

These investigations raise the question of grid refinement at the surface of the packing. If these structures have such an influence on the flow dynamics, then it is reasonable to assume that grid densities must be high enough to resolve these effects. Therefore, adaptive mesh refinement close to the plate surface may be required in these cases, to adequately resolve these surface structures.

5.3.4 Improvements to Interface Refinement

It can be seen in Table 5.3 that the Partial-film simulations using local AMR at the interface increased the run-times, especially at $Re_l = 44.81$. These increases in run-time are acceptable considering the increases in accuracy gained. However, it was considered that, with careful consideration of AMR parameters, improvements might be made to the run-times, whilst maintaining the desired accuracy.

Further simulations were run using a much coarser initial grid of only 32640 cells, in comparison to the 192000 used originally. An extra level of refinement was used at the interface to try to maintain the accuracy. Simulations were run at $Re_l = 44.81$ and $Re_l = 156.85$ using this new set-up.

TABLE 5.4: Percentage change from original initial grid to coarser initial grid (AMR)

Re_l	Change in Wetted Area [%]	Change in Run-time [%]
44.81	-0.94	-81.49
156.85	-3.96	-74.49

Table 5.4 shows the percentage changes between the original AMR simulations and the AMR simulations with a coarser initial grid. There is only a small drop in the wetted areas, but a significant drop in the simulation run-times. This shows that the approach can be optimised to reduce the computational effort involved, whilst maintaining accuracy, by the choice of initial meshes and the number of refinement levels. This makes AMR approaches a promising option when the domain is scaled up to simulate larger sections of packed columns.

Another important consideration is the frequency of mesh updates. The process of updating the mesh creates a significant overhead, which takes of the order of a second to complete. Therefore, careful consideration of the required frequency of mesh updates may reduce simulation run-times even further.

5.4 Conclusion

In this Chapter the VOF method, along with local AMR, was used to study isothermal, non-reacting, gravity-driven flow. The domain was chosen as an approximate representation to a small section of packing. Initially, simulations were performed using a static mesh method, whereby suitable refinement to the mesh was made via a mesh independence study. This highly refined mesh was able to improve upon previous studies in the literature and was more able to replicate experimental data. However, the specific wetted area was still under-predicted at smaller values of the liquid film Reynolds number. This approach would also have significant disadvantages when the domain is scaled up because there are large regions of high density mesh where it is simply not required.

Local AMR was used to try to improve the prediction of wetted area. AMR refinement of the gas-liquid interface improved the computational results, especially at lower Re_l. The data was closer to experimental results and better replicated the trends observed at the lower range of Re_l. This approach has the advantage that mesh density is high in regions where it is required and lower in other regions. Therefore, this method may have better scalability and could be a viable approach to studying the hydrodynamics within larger sections of packing. However, under-predictions were still observed at lower Re_l.

Finally, local AMR was used to refine the whole film region to examine whether the close proximity of the plate surface had any affect on the results. It was found that simulation run-times were increased for all Re_l tested, as would be expected. However, the computational results showed marginal differences and so it was concluded that local AMR should only be applied at the interface. Also, at larger Re_l the run-times were significantly increased because the volume of the fluid film became larger, requiring more refinement. This shows that the approach of refining the whole film region would encounter difficulties scaling to larger domains, such as larger sections of structured packed.

Future investigations could focus on optimisation of the initial mesh density, the number of refinement levels and the frequency of mesh refinement in order to keep run-times to a minimum, whilst maintaining good accuracy.

Chapter 6

Enhanced Surface Film Model

Current approaches to modelling post-combustion carbon capture using computational fluid dynamics are hindered by the multiscale, multiphase characteristics. This chapter develops a novel Enhanced Surface Film (ESF) model, to simulate thin-film flow down an inclined plane, with a view to extending this method to be used in the carbon capture field. This modelling technique produced results inline with the established volume-of-fluid method, whilst giving a speed-up of 150 times.

6.1 Introduction

Thin film flows are ubiquitous across industrial and environmental sectors. Examples include thin film microreactors [37, 38], surface coatings [52, 53], biofluids and medical applications [54,55]. In the majority of these applications the dynamics of the thin liquid film play a crucial role to the overall performance.

Unfortunately, thin film flows are complex as their dynamics lead to numerous characteristics that can prevent even distributions over surfaces, such as rivulet formation, rippling effects and even rupture flows. If research is to continue into improving the performance of applications that exhibit such flows, then there needs to be a significant advancement in not only understanding the physics behind the flows, but also predicting the complex characteristics that are commonly seen.

An example of thin filmed flow in industry which is explored in this chapter is the absorption of CO_2 into liquid alkanolamines for use in the carbon capture industry [2,5,6,20,26]. Currently the liquid amines flow over inclined structured packing plates but the formation of droplets and rivulets reduces the coverage over the surface, thus requiring more structured packing to compensate. Before the process can be optimised to maximise the surface area of the liquid on the plate and subsequently improve performance at the larger scale we need to be better equipped to predict the complex dynamics.

With increasing computational capabilities, computational modelling is proving a valuable tool in predicting and optimising flow dynamics and overall processes without the additional cost and time of performing numerous experimental studies. Unfortunately the large range of spatial scales within packed columns can greatly inhibit the practical application of computational fluid dynamics to these situations. CFD solves numerical models to capture the flow dynamics over finite volumes, however, this leads to significant scaling issues as small-scale features cannot be resolved simultaneously with large scale dynamics. Numerous approaches have been used to model the flow of liquid over an inclined plate including the VOF model [43,48–50] and surface film modelling [3,119,120].

The volume-of-fluid approach is the favoured method for simulating a liquid film over a plate or structured packing [26, 41, 42] as it tracks the interface between the liquid and the air. Unfortunately, the scale of the interface is such smaller than the depth of the film itself and the averaging nature of CFD models incur inaccuracies as to its exact location. Refining all the cells which process the numerical modelling can tend to improve results but at the expense of increase computational exhaustivity and still are unable to capture this interface exactly. As has been shown in the previous chapter, adaptive mesh refinement [107,116,117,121] to perform extensive refinement only in the region of the interface can significantly improve the accuracy and simulation times, but these simulations times are still much too large for effective scale-up to larger domains.

In order to combat the scalability issues of VOF and AMR-VOF an alternative approach has been developed in this chapter. Using the depth-averaged Navier-Stokes equations the number of computational cells required within the liquid film is significantly reduced. The majority of simulations with the depth-averaged Navier-Stokes equations focus on flow regimes where the contact angle can be neglected. This simplifies the surface tension to the capillary pressure. However, in many film flow simulations the contact angle has a significant effect, causing rivulets to form which significantly reduce the interfacial surface area of the film. Meredith *et al.* [3] devised a method to include contact angle effect in the formulation of the surface film model. Using Young's Law, which states that forces along the contact line are balanced at equilibrium, and the balance of tangential surface forces due to interfacial tension, they derived an expression for the surface-tangential force normal to the contact line in terms of the surface tension coefficient and the contact angle. This surface-tangential force is then applied at the contact line, the interface between wet and dry regions of the flow. The contact line is defined as the minimum liquid thickness below which the film flow cannot exert enough force to overcome the contact angle force [3]. However, the contact-angle stress derived from this model includes a constant which is used to match the model with experimentally observed data. Therefore, experiments must be run in order to successfully use this model.

This chapter develops an enhanced surface film model which incorporates new models to account for the surface tension and contact-line phenomena. Firstly, we will demonstrate

that previous assumptions to simplify and neglect terms such as contact angle, surface tension and momentum dispersion were incorrect and develop new models based on data obtained from high refinement AMR-VOF. Comparisons are performed, to determine the accuracy and efficiency of this novel method, with existing approaches such as the standard VOF model and an existing surface film model.

6.2 Governing Equations

The surface film approach used in this thesis makes use of the depth-averaged Navier-Stokes equations. Initially, the full 3-D Navier-Stokes equations are listed, along with the mathematical tools required for depth-integration of the equations. Finally, the depth-averaged Navier-Stokes equation are given, along with the required closure models.

6.2.1 Full 3-D Navier-Stokes Equation

The incompressible Navier-Stokes equation for a 3-dimensional fluid and domain are determined by the conservation of mass and the conservation of momentum. If the velocity of the fluid is denoted by $\boldsymbol{u} = [u, v, w]$ and the fluid is incompressible, the conservation of mass leads to the continuity equation given by:

$$\nabla \cdot \boldsymbol{u} = 0. \tag{6.1}$$

The conservation of momentum is given by:

$$\rho \left(\frac{\partial \boldsymbol{u}}{\partial t} + \boldsymbol{u} \cdot \nabla \boldsymbol{u} \right) = -\nabla p + \mu \nabla^2 \boldsymbol{u} + \rho \boldsymbol{g} + \boldsymbol{F}_{st}, \tag{6.2}$$

where ρ is the density, p is the pressure, μ is the kinematic viscosity, $\boldsymbol{g}$ is the gravitational force and $\boldsymbol{F}_{st}$ is the surface tension force.

The assumption is made that the density is constant. The inclusion of mass transfer into the ESF model in the following chapter will involve non-constant densities, since the density is dependent on the distribution of species within the fluid film. However, in CCS the concentration of aqueous amine is much larger than the concentration of absorbed CO_2. Therefore, the choice of constant density is a reasonable assumption for the physical situations being modelled in the following chapter.

6.2.2 Tools for Depth Integration

Important tools for the depth integration of the Navier-Stokes equations are the Leibniz theorem, the fundamental theorem of integration, the kinematic boundary condition at

the free surface of the liquid and the kinematic boundary condition at the surface of the plate along which the fluid flows. It is assumed that the depth-integration is performed in the z-direction from $z(t,x,y) = z_0$ to $z(t,x,y) = z_o + h$, where h is the film depth and z_0 is the z-coordinate location of the underlying substrate. For a flat substrate this is usually assigned to the z-coordinate, $z_0 = 0$. The kinematic boundary condition at the free surface is given by:

$$w|_{z_0+h} = \frac{\partial h}{\partial t} + u|_{z_0+h}\frac{\partial(z_0+h)}{\partial x} + v|_{z_0+h}\frac{\partial(z_0+h)}{\partial y}. \tag{6.3}$$

The kinematic boundary condition at the plate surface is derived by assuming that there is no mass flux perpendicular to the plate and is given by:

$$w|_{z_0} = u|_{z_0}\frac{\partial z_0}{\partial x} + v|_{z_0}\frac{\partial z_0}{\partial y}. \tag{6.4}$$

The Leibniz theorem is stated as:

$$\frac{\partial}{\partial x}\int_{z_0}^{z_0+h} u\mathrm{d}z = \int_{z_0}^{z_0+h}\frac{\partial u}{\partial x}\mathrm{d}z + u|_{z_0+h}\frac{\partial(z_0+h)}{\partial x} - u|_{z_0}\frac{\partial z_0}{\partial x}, \tag{6.5}$$

when $u = u(x,y,z)$ and the fundamental theorem of integration is stated as:

$$\int_{z_0}^{z_0+h}\frac{\partial u}{\partial z}\mathrm{d}z = u|_{z_0+h} - u|_{z_0}. \tag{6.6}$$

6.2.3 Depth-Averaged Navier-Stokes Equations

The depth-averaging of the Navier-Stokes equations is applicable under the assumptions that the vertical velocity component is much smaller than the horizontal components and the pressure is linear with respect to the depth. Depth integrating equation 6.1 (see Appendix B for full derivation) over the z-direction from $z = 0$ to $z = h$ and dividing by $\rho = const$ leads to a continuity equation for the height of the free surface:

$$\frac{\partial h}{\partial t} + \nabla_s \cdot (h\overline{\boldsymbol{u}}) = 0, \tag{6.7}$$

where h is the film depth, $\overline{\boldsymbol{u}} = (\overline{u}, \overline{v})$ is the depth-averaged velocity and ∇_s is the 2D nabla given by,

$$\nabla_s = \left(\frac{\partial}{\partial x}, \frac{\partial}{\partial y}\right). \tag{6.8}$$

The derivation of the continuity equation does not contain any unclosed terms that require modelling, so therefore, this is an exact representation of the depth-averaged continuity equation.

Depth integration of the momentum equations (equation 6.2) leads to:

TABLE 6.1: Equation terms

Term No.	Term	Closure
1	Time Dependent	Closed
2	Total Convection	-
2i	Mean Convection	Closed
2ii	Momentum Dispersion	Unclosed
3	Pressure terms	Unclosed
4	Wall Shear Stress	Unclosed
5	Gas Shear Stress	Unclosed
6	Transverse Viscous Shear	Closed
7	Transverse Surface tension	Closed
8	Wall tangential gravity	Closed

$$\underbrace{\frac{\partial \rho \overline{\boldsymbol{u}} h}{\partial t}}_{1.} \underbrace{+\nabla_s \cdot (\rho h \overline{\boldsymbol{u}}\overline{\boldsymbol{u}})}_{2.} = \underbrace{-\nabla_s (h\overline{p}) + p|_h \nabla_s h}_{3.} \underbrace{+\boldsymbol{\tau}_w}_{4.} \underbrace{+\boldsymbol{\tau}_g}_{5.} \underbrace{+\nabla_s \cdot (\mu h \nabla \overline{\boldsymbol{u}})}_{6.} \underbrace{+ \int_0^h \boldsymbol{F}_{st} dz}_{7.} \underbrace{+\rho \boldsymbol{g} h}_{8.}, \tag{6.9}$$

where the definition of the terms is given in table 6.1 (see Appendix B for full derivation). The term $p|_h$ is defined as (see Appendix B),

$$p|_h = p_{gas,h} - \sigma \kappa(\boldsymbol{x}) n_z, \tag{6.10}$$

where $p_{gas,h}$ is the hydrodynamic pressure within the gas phase at the gas-liquid interface.

An equation for the depth-averaged z-momentum is not solved due averaging in the z-direction. This is a valid assumption considering that the wall normal length scale and velocity component are much smaller than the wall tangential length scales and velocity components. The averaging procedure also produces Reynolds stress type momentum dispersion terms. If the velocity field, $\boldsymbol{u}$ is decomposed into its depth-averaged value, $\overline{\boldsymbol{u}}$ and its deviation from the depth-averaged value, $\boldsymbol{u}''$ in the following manner,

$$\boldsymbol{u} = \overline{\boldsymbol{u}} + \boldsymbol{u}'', \tag{6.11}$$

then the product of the velocity is given by,

$$\boldsymbol{u}\boldsymbol{u} = \overline{\boldsymbol{u}}\,\overline{\boldsymbol{u}} + \boldsymbol{u}''\boldsymbol{u}'' + 2\overline{\boldsymbol{u}}\boldsymbol{u}''. \tag{6.12}$$

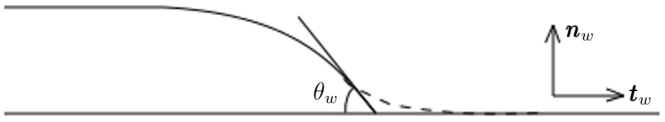

FIGURE 6.1: Definition of contact angle, θ_w, unit vector normal to wall, $\boldsymbol{n}_w$ and unit vector tangential to wall, $\boldsymbol{t}_w$

Taking the depth-averaged value (mean value) of this product gives,

$$\overline{\boldsymbol{u}\boldsymbol{u}} = \overline{\boldsymbol{u}}\,\overline{\boldsymbol{u}} + \overline{\boldsymbol{u}''\boldsymbol{u}''} + \overline{2\overline{\boldsymbol{u}}\boldsymbol{u}''}, \tag{6.13}$$

$$\overline{\boldsymbol{u}\boldsymbol{u}} = \overline{\boldsymbol{u}}\,\overline{\boldsymbol{u}} + \overline{\boldsymbol{u}''\boldsymbol{u}''} + \cancelto{0}{\overline{2\overline{\boldsymbol{u}}\boldsymbol{u}''}}. \tag{6.14}$$

Therefore, term 2 in equation 6.9 can be written as,

$$\underbrace{\nabla_s \cdot (\rho h \overline{\boldsymbol{u}\boldsymbol{u}})}_{2.} = \underbrace{\nabla_s \cdot (\rho h \overline{\boldsymbol{u}}\,\overline{\boldsymbol{u}})}_{2\text{i.}} \underbrace{+\nabla_s \cdot (\rho h \overline{\boldsymbol{u}''\boldsymbol{u}''})}_{2\text{ii.}}. \tag{6.15}$$

The solution of the above depth-averaged equations along with the continuity equation and appropriate closure models allows one to solve for fluid depth, h and depth-averaged velocity, $\overline{\boldsymbol{u}}$ using a CFD approach.

6.2.3.1 Surface Tension

Surface tension is an important term in the modelling of film flow, particularly at the leading edge of the film where surface tension and contact line instabilities can cause the formation of rivulets. In the majority of the literature on thin-film modelling, surface tension is included in the governing equations through a contribution in the pressure term, as the capillary pressure. This is suitable for regimes where the plate is fully covered by the liquid film and therefore, no contact line exists at the underlying substrate. In partially-wetted regimes the contact angle between the liquid and solid surface causes results in the surface tension deviating from the capillary pressure. This effect must be included in the governing equations to accurately model partially wetted flow regimes.

Meredith *et al.* [3] included this influence as an additional body force in the momentum equations. They defined a threshold film thickness, below which the surface was considered dry. This body force was applied at the interface between the wet and dry regions. However, this approach requires a fitting constant to match with experimental data and, for the simulations performed in this thesis, we were not able to get good agreement with VOF techniques (see Chapter 6.5).

This approach developed in this thesis applies the continuum surface force (CSF) model [11], developed for 3D VOF simulations, to the surface film approach. The contribution

to the balance of momentum from surface tension, $\boldsymbol{F}_{st}$ is defined in the CSF model by:

$$\boldsymbol{F}_{st} = \sigma\kappa(\boldsymbol{x})\boldsymbol{n}\delta, \tag{6.16}$$

where σ is the surface tension, $\boldsymbol{n}$ is the unit normal vector of the interface pointing into the liquid phase, δ is the Dirac Delta Function and $\kappa(\boldsymbol{x})$ is the curvature of the interface, given by:

$$\kappa(\boldsymbol{x}) = -\nabla \cdot \boldsymbol{n}. \tag{6.17}$$

In cells adjacent to a wall boundary the definition of the unit normal vector, $\boldsymbol{n}$ pointing into the fluid, is adjusted in order to take account of the liquid contact angle. For a constant wall contact angle, θ_w, the unit normal vector pointing into the liquid phase at the contact line is defined by [46]:

$$\boldsymbol{n} = -\boldsymbol{n}_w cos(\theta_w) - \boldsymbol{t}_w sin(\theta_w), \tag{6.18}$$

where $\boldsymbol{n}_w$ is the unit vector normal to the wall and $\boldsymbol{t}_w$ is the unit vector tangential to the wall (see Fig. 6.1).

A consistent approach has been adopted in this thesis to model the depth-averaged surface tension in the ESF model. Assuming that the z-component of velocity is much smaller than the horizontal components, the depth-averaged pressure is given by (see Appendix B for derivation),

$$\overline{p} = p_{gas,h} + \frac{1}{2}\rho g h cos(\theta) - \sigma\kappa(t,x,y)n_z, \tag{6.19}$$

where $p_{gas,h}$ is the hydrodynamic pressure within the gas phase at the gas-liquid interface.

The horizontal components of surface tension will be included directly as momentum source terms in equation 6.9. Therefore, according to the derivation in Appendix B,

$$\int_0^h \boldsymbol{F}_{st}\mathrm{d}z = \frac{1}{2}\sigma\kappa\boldsymbol{n}. \tag{6.20}$$

To calculate the normal of the interface (where the interface is defined as $z = h(x,y)$), we define the function $f(x,y,z) = z - h(x,y)$. The interface normal pointing into the liquid phase is then given by:

$$\boldsymbol{n} = -\frac{\nabla f}{|\nabla f|} = \frac{h_x\hat{x} + h_y\hat{y} - \hat{z}}{(1 + h_x^2 + h_y^2)^{0.5}}, \tag{6.21}$$

where the subscripts denote differentiation with respect to the coordinate directions and $\hat{x}$, $\hat{y}$ and $\hat{z}$ are the unit coordinate vectors.

For consistency with the 3D CSF model (equation 6.18), the interface normal vector must be fixed to ensure the correct contact angle. This requires the definition of a threshold liquid thickness where the definition of the interface normal switches (see section 6.4.2.1), called δ_n.

The unit vector tangential to the wall is also normal to the contact line and therefore can be defined by:

$$\boldsymbol{t}_w = \frac{-h_x\hat{x} - h_y\hat{y}}{(h_x^2 + h_y^2)^{0.5}}, \tag{6.22}$$

and so the interface normal close to the wall is given by:

$$\boldsymbol{n}_\delta = -\boldsymbol{n}_w cos(\theta_w) - \boldsymbol{t}_w sin(\theta_w) = -\hat{z}cos(\theta_w) + \frac{h_x\hat{x} + h_y\hat{y}}{(h_x^2 + h_y^2)^{0.5}} sin(\theta_w). \tag{6.23}$$

To switch the definition of the interface normal at the threshold liquid thickness we defined ω as:

$$\omega = \begin{cases} 1 & \text{if } h \geq \delta_n \\ 0 & \text{if } h < \delta_n \end{cases} \tag{6.24}$$

Therefore, the interface normal, $\boldsymbol{n}_{total}$, including the effect of the contact angle close to the wall, is given by:

$$\boldsymbol{n}_{total} = \omega\boldsymbol{n} + (1 - \omega)\boldsymbol{n}_\delta. \tag{6.25}$$

The curvature can then be calculated as:

$$\kappa(\boldsymbol{x}) = -\nabla \cdot \boldsymbol{n}_{total}. \tag{6.26}$$

6.2.4 Closure Models

6.2.4.1 Shear Stress

For laminar flow on a flat plate the wall shear stress can be defined from the Nusselt velocity profile [3]. According to Meredith *et al.* [3], if the velocity at the wall is zero and the velocity gradients at the gas interface are negligible, then the following velocity profile can be assumed:

$$u(z) = \frac{3\overline{u}}{h}\left(z - \frac{z^2}{2h}\right), \tag{6.27}$$

where $\overline{u}$ is the depth-averaged film velocity, z is the wall normal coordinate and h is the film depth. The wall shear stress can be derived from this assumed velocity profile and is given by [3]:

$$\tau_{w,i} \approx -\mu\frac{3u_i}{h}, \tag{6.28}$$

where μ is the viscosity of the liquid.

The assumption of a parabolic velocity profile is valid for wavy film flow [3] and so for the Re_l numbers observed throughout this thesis this assumption should be accurate in the majority of the flow field. However, in partially wetted flow the assumption of a parabolic velocity profile may not be accurate. The flow near the fluid front will deviate from the parabolic profile due to the contact line. According to Oron *et al.* [56], in the frame of reference of the contact line the flow recirculates, moving along the free surface to the contact line and then along the plate surface. Here the above expression may not accurately predict the actual wall shear stress and could introduce inaccuracies in the modelling approach. The relative importance of the wall shear stress terms and accuracy of the proposed model will be determined in the following sections.

Meredith *et al* [3] modelled the gas shear stress using the following expression,

$$\tau_g \approx -C\rho_g|u_g - \overline{u}|\overline{u}, \tag{6.29}$$

where C is a fitting constant and u_g is the gas phase velocity. However, the gas-phase will have negligible effect on the liquid-phase flow and so the gas shear stress terms will be neglected in the ESF formulation. This approximation is shown to be the case in the following sections.

6.2.4.2 Depth-Averaged Pressure

As mentioned above, the depth-averaged pressure is derived from the wall-normal momentum equation. Due to the assumptions of the thin-film equations, the wall-normal velocity is considered negligible. By including only the wall-normal component of the surface tension force in the pressure formulation (tangential surface tension forces are included as source terms in the thin-film equations), the depth-averaged pressure is given by,

$$\overline{p} = p_{gas,h} + \frac{1}{2}\rho g h cos(\theta) - \sigma\kappa(t,x,y)n_z. \tag{6.30}$$

6.2.4.3 Momentum Dispersion

The momentum dispersion terms are difficult to model since they require knowledge of the velocity profiles and also knowledge of the deviation of the velocity from the depth-averaged velocity within the flow. Since the depth-averaged Navier-Stokes equations only solve for the depth-averaged velocity, it is not possible to calculate the deviation of the velocity from the average during surface film simulations. Therefore, a model is required to determine the momentum dispersion terms. The standard approach for thin film flow is to neglect these terms. However, neglecting the momentum dispersion terms may not be valid in film flow down an inclined plate, so the relative magnitude of the momentum dispersion terms will be determined in section 6.4.1.

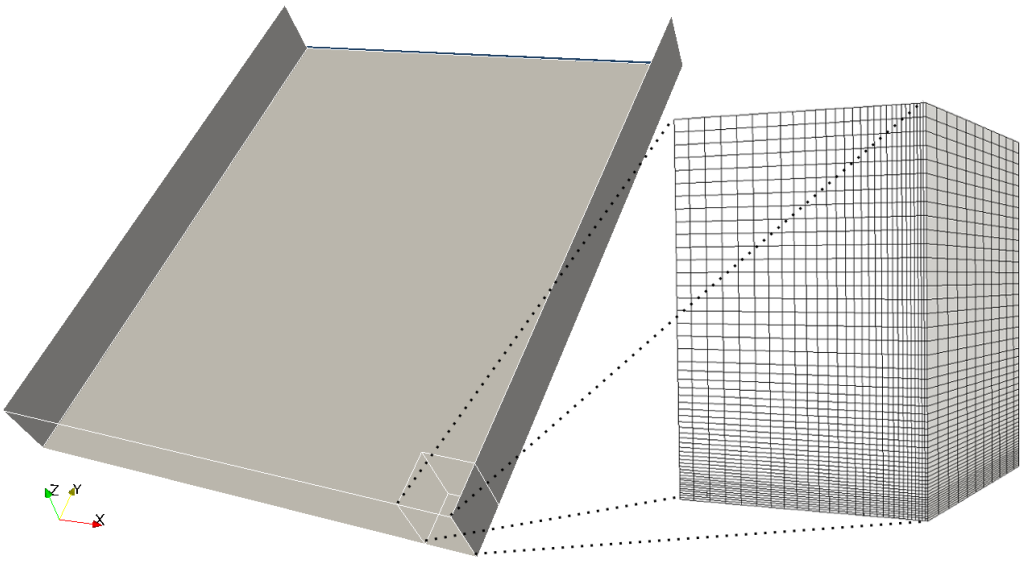

FIGURE 6.2: Computational domain used in the VOF approach

6.3 Numerical Methodology

6.3.1 Geometry & Mesh

The computational domain was chosen to be a smooth, inclined steel plate bordered by steel walls at the sides (see Fig. 6.2) [48–50]. This domain is an approximate representation of a small section of structured packing used for CO_2 absorption. For the VOF case the domain dimensions were $0.06\,\mathrm{m} \times 0.05\,\mathrm{m} \times 0.007\,\mathrm{m}$ (height×width×depth). The depth of liquid at the inlet was selected according to the Nusselt film thickness.

Depth-integration of the data with an AMR grid is very complex, due to the changing non-uniform nature of the grid. Therefore, the VOF approach without adaptive mesh refinement was used to analyse the data. A grid independence study was performed in Appendix A.1.1 to ensure that the mesh was refined enough. This mesh consisted of 1.0 million cells. The results of the ESF approach were compared with AMR-VOF, rather than just the VOF results because it has been found that AMR-VOF produced better results across a larger range of Re_l [121]. The AMR-VOF mesh consisted of an initial coarse grid of 192,000 cells, with 2 levels of adaptive refinement around the gas-liquid interface, in the region $0.2 < \alpha < 0.8$.

The computational domain for the ESF model consisted of a primary mesh (same dimensions as the VOF mesh) in which the gas-phase was computed. This domain was then extruded by one cell in the direction normal to the plate surface to create an additional secondary mesh, consisting of 27000 cells. The depth-averaged Navier-Stokes equations are solved within this secondary mesh to resolve the liquid flow over the plate.

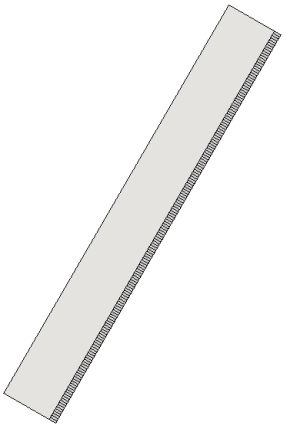

FIGURE 6.3: Computational domain used in thin film approach - side view

A side-view of the computational domain is shown in Fig. 6.3, which shows the cells within the secondary mesh and the extent of the primary mesh.

6.3.2 Simulation Set-up

For all simulations a constant inclination angle of $\theta = 60^o$ was chosen to allow comparisons with current data in the literature. A range of Re_l were tested by suitably altering the velocity of the liquid film at the inlet. During this investigation counter-current flow of gas was neglected to again allow comparison with published data. In accordance with Hoffman *et al.* [48] and Iso & Chen [50] turbulence was not considered since $Re_l < 230$ and the flow could be considered to be in the laminar or pseudo laminar regime. It is noted that for falling liquid films the onset of turbulence can occur at $Re_l = 75$ due to wall-induced turbulence [110]. However, fully turbulent flow is not reach until $Re_l > 400$ [110] and so the laminar governing equations have been used in this chapter.

Time-dependent simulations were carried out using a variable time-step to ensure a Courant number below 0.2, resulting in time-steps of approximately $8 \times 10^{-5} s$ for the surface film simulations. Simulations were allowed to run until a steady or pseudo-steady state was reached. This was assured by monitoring changes in the specific wetted area of the plates as a function of time. The two timescales present in these simulations are the viscous time-scale, $\tau_v = \frac{L^2}{\nu}$ and the advection time-scale, $\tau_a = \frac{L}{U}$, where L is the characteristic length scale or the cell size, ν is the kinematic viscosity and U is the characteristic velocity of the simulation. In these simulations the smallest viscous timescale was approximately 21.6 times larger than the advection time scale, which confirms the choice of time-step based on the courant number, $C_r = \frac{U\tau_a}{L}$.

The dynamic viscosity and density of the constituent phases are given in Table 6.2. The surface tension was set to $\sigma = 0.0728\ \mathrm{N \cdot m^{-1}}$ and a static contact angle of $\theta_w = 70^o$ was selected.

Table 6.2: Phase Properties

Phase	μ [Pa · s]	ρ [Kg · m^{-3}]
Liquid	8.899×10^{-4}	997
Gas	1.831×10^{-5}	1.185

These simulations did not calculate the flow within the gas-phase domain considering that the aim was to simulate the film flow. The influence of the gas flow on the fluid flow from the gas-phase shear stress is negligible. For simulations involving mass transfer in the following chapter the gas-phase domain is solved.

The initial conditions for the simulations were that the depth-averaged domain was initially devoid of fluid, with the film depth, $h = 0$ and zero depth-averaged velocity everywhere. The velocity boundary condition at the plate was set to no-slip condition. This is not a direct boundary condition on the depth-averaged velocity and is instead used to determine the wall shear stress. In the case of a moving plate the shear stress would be increased or decrease depending on the wall velocity direction. In reality, the boundary condition for the depth-averaged velocity at the plate is a free-slip condition because the grid in the depth-averaged domain is only one cell deep. The depth-averaged velocity boundary condition for the side-walls was set to the no-slip condition. The liquid inlet was set to a fixed value depth-averaged velocity with a fixed value for the fluid depth, representing the depth-averaged Nusselt velocity and Nusselt film thickness. For the side-walls the film depth, h was set to a fixed gradient boundary condition to ensure the correct contact angle was imposed at these side-walls. The outlet was set to zero gradient for both depth-averaged velocity and film depth. The free boundary at the top of the domain was set to a slip condition for depth averaged velocity and zero gradient for film depth.

In the case of the ESF model the contact line paradox is avoided because there is no explicit no-slip condition for velocity at the plate wall. Instead this approach solves for the depth-averaged velocity and the influence of the plate wall is taken account of by the wall shear stress calculation.

6.4 Analysis

This section provides an analysis of the surface film approach and the associated closure models. Initially, the results from 3D VOF simulations were integrated over the depth of the liquid film and budget plots were made to determine the relative importance of each of the terms in the surface film model. This approach revealed which terms must be included and which could be neglected in the implementation of the surface film model.

Secondly, an evaluation of the applicability of the CSF model to the thin film approach was made by comparing the depth-integrated surface tension from 3D VOF simulations with the ESF surface tension. A model for δ_{min} is derived and thoroughly tested on different fluids with varying properties.

Finally, the closure models used in the surface film approach were tested by comparison with the associated terms of the 3D VOF simulations. This allowed the suitability of the closure models to be determined for thin films on inclined plates. Throughout the analysis, terms of the surface film equations are evaluated using the depth-averaged values from the 3D VOF simulations (e.g. film depth, average velocity etc.).

6.4.1 VOF

The results of 3D VOF simulations of film flow down an inclined plane from the previous chapters were integrated over the thickness of the film to determine the relative significance of the terms in the surface film model. The integration was performed on the results after they had reached a pseudo steady-state, determined by the fact the the interface remained in a fixed location and wetted area was steady. A numerical integration was performed by calculating the individual terms in the governing equations. Due to the structured nature of the grid, columns of cells in the wall normal direction could be numerically integrated to find the depth-averaged value of the individual equation terms. The depth-averaged value was found by summing up the values within the cells over each of the columns, weighted by the volume fraction and cell size in the wall normal direction. The time-dependent terms were calculated by continuing the simulation for a single time-step. These terms should effectively be zero. However, the VOF simulations reached only a pseudo steady-state and so these terms may not be exactly zero for the single time-step calculated.

A mid-range Re_l was chosen where multiple flow regimes are observed (see figure 6.4). Close to the inlet a Nusselt profile flow is observed, but further down the plate a rivulet forms due to instabilities at the contact line. Slices were taken parallel to the y-axis at 3 important positions within the flow; a central slice, a slice through the oblique rivulet contact line and a slice through the stagnation point of the flow (see fig. 6.4). These positions were chosen because they show different flow structures where the relative magnitudes of the terms may differ. Figures 6.5-6.7 show budget plots of the integrated 3D terms. It is noted that the numerical integral of the 3D convection terms inherently includes the dispersive Reynolds stresses.

It can be seen that in Figure 6.5 that the time derivative is not equal to zero in the region where the rivulet combines into a thin ribbon a fluid. This is due to the fact that the simulations were run until a pseudo-steady state was reached and, whilst the total flow structure and wetted area remained constant, fluctuations in this region still occur.

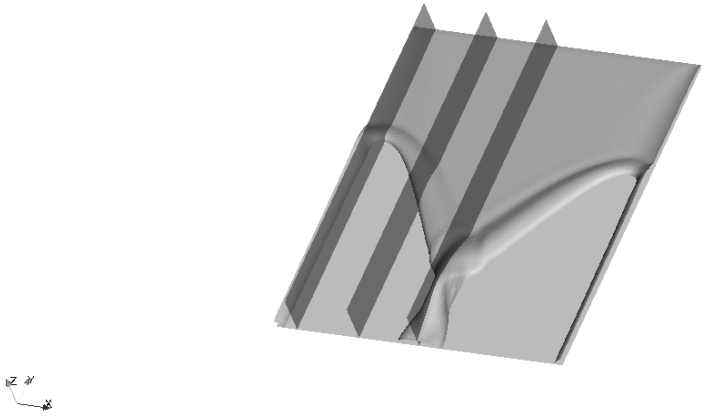

FIGURE 6.4: 3D VOF Interface Contour Plot with cut planes ($Re_l = 156.85$)

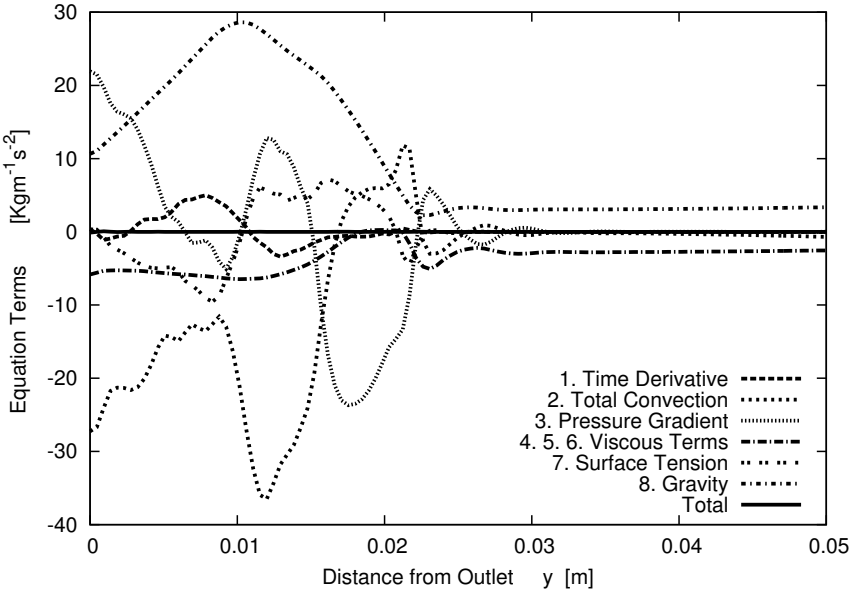

FIGURE 6.5: Budget Plot of Numerical Integration of 3D y-momentum equation terms - Central position

These budget plots show that all terms appear to be significant. However, the convection term is comprised of the mean convection (term 2i.) and momentum dispersion (term 2ii.) and the viscous term is comprised of wall shear (term 4.), gas shear (term 5.) and transverse shear stresses (term 6.). In order to asses the magnitude of these terms further budget plots are made below.

To determine whether the dispersive Reynolds stresses (term 2ii. in equation 6.15) are important, budgets showing the total integrated convection, the mean convection and the momentum dispersion terms are shown in figures 6.8-6.10. It is easy to see that these dispersion terms are not negligible in the rivulet regions of the flow. Therefore, it is may not be correct to neglect these terms without a loss of accuracy.

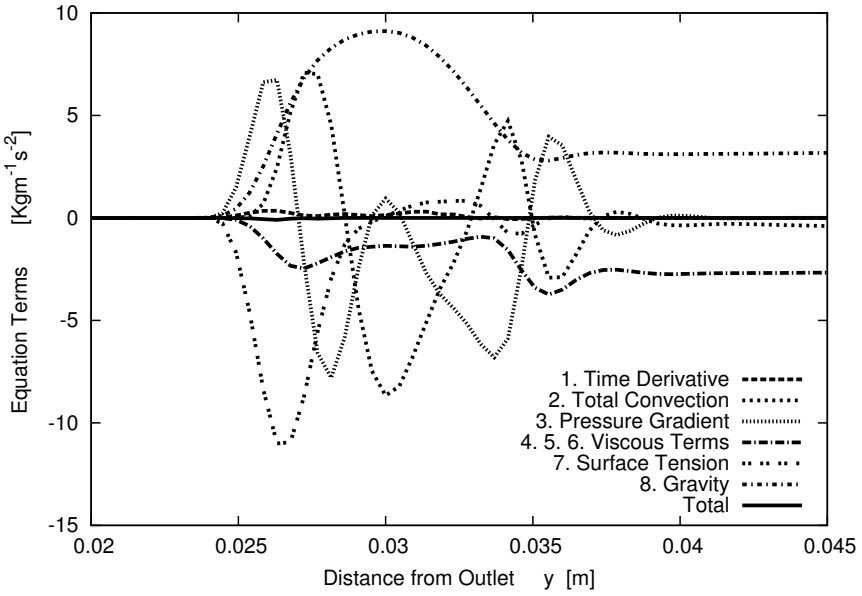

FIGURE 6.6: Budget Plot of Numerical Integration of 3D y-momentum equation terms - Oblique position

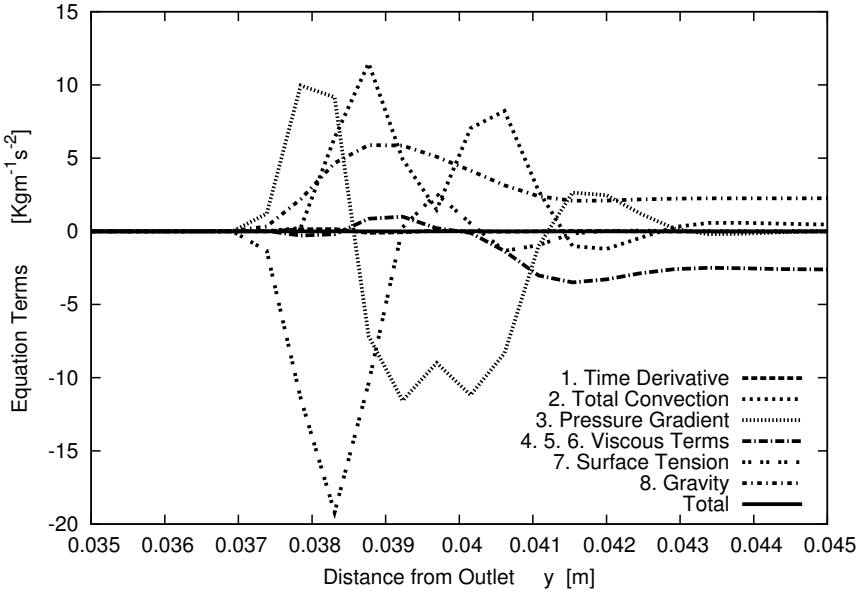

FIGURE 6.7: Budget Plot of Numerical Integration of 3D y-momentum equation terms - Stagnation position

6.4.2 Surface Film Model

6.4.2.1 Surface Tension

The surface tension model used in this thesis is an application of the Continuum Surface Force (CSF) model to the depth-averaged Navier-Stokes equations. The CSF model alters the definition of the interface normal close to the wall to take account of the contact angle between the fluid and the solid surface. The difference between the 3D and

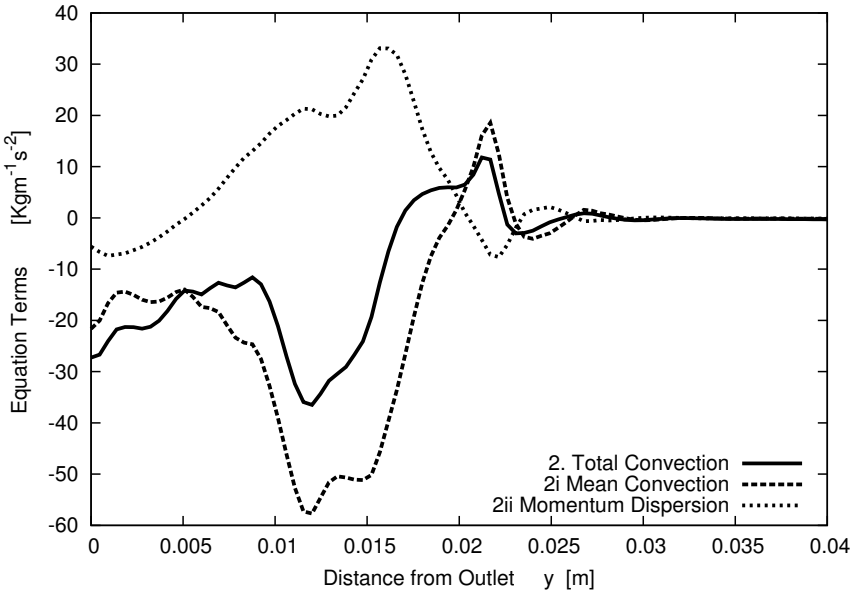

FIGURE 6.8: Budget Plot of Numerical Integration of 3D y-momentum Convection and Momentum Dispersion - Central position

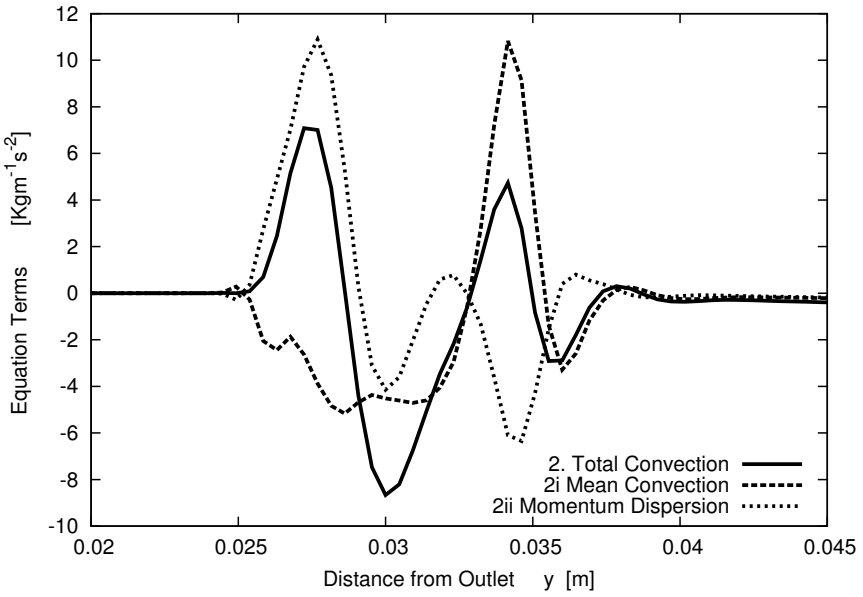

FIGURE 6.9: Budget Plot of Numerical Integration of 3D y-momentum Convection and Momentum Dispersion - Oblique position

depth-averaged implementations of the CSF model is the specification of the transition in the definition of the interface normal.

In the depth-averaged implementation of the CSF model a threshold thickness, δ_n is specified, which allows the definition of the interface normal to be adjusted so that it matches the contact angle close to the fluid-solid contact line. The effect of the value of δ_n can be seen in the budget plots of surface tension along the oblique and stagnation slices. As shown in Figures 6.13-6.14, neglecting the threshold thickness results in a

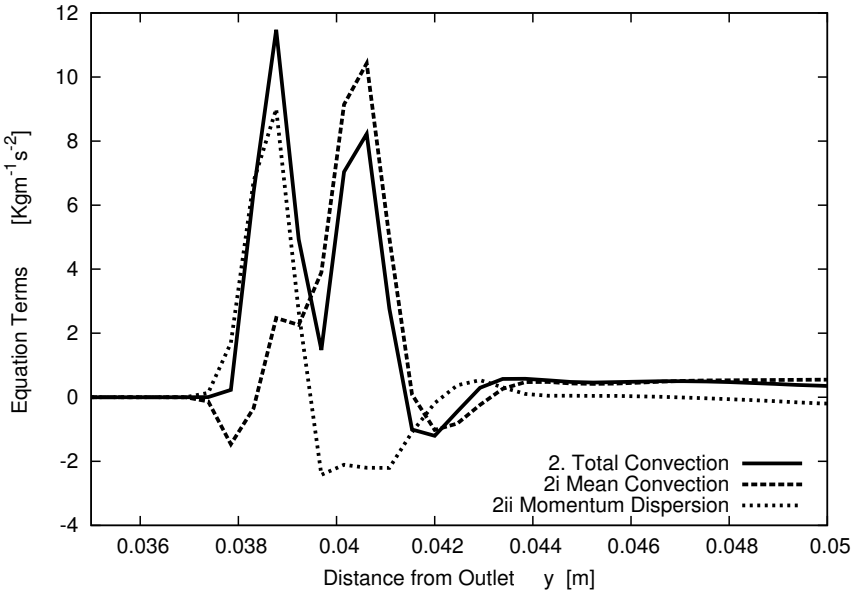

FIGURE 6.10: Budget Plot of Numerical Integration of 3D y-momentum Convection and Momentum Dispersion - Stagnation position

contact line force in the opposite direction than it should be. This clearly shows the importance of a good model for the threshold thickness.

In order to determine an appropriate value for δ_n a range of additional simulations were completed. Two dimensional simulations of a droplet of water flowing down an inclined plane were performed. Comparisons between the surface film model and the VOF results, enabled us to determine that the value of δ_n is proportional to the cell length in the direction of the flow, Δ_x. It is not always reliable to use 2D results for 3D phenomena due to the 3D nature of surface tension. However, this result was confirmed in the 3D simulations. It was postulated that the threshold thickness would also depend on fluid properties, such as density, surface tension or contact angle, for example. Therefore, further simulations were performed to determine a suitable formula.

Further simulations involved 3D modelling of fluid flow down a 60 degree inclined plane, under the influence of gravity. To provide a starting point for the investigation, an initial simulation was performed with water at $Re_l = 156.85$. A suitable value for the threshold thickness was determined by running many ESF simulations and comparing this to the results of the AMR-VOF approach. Using this threshold thickness as a baseline point, the fluid properties could then be varied to enable their influences on the threshold thickness formula to be investigated.

Starting with the properties of water, the density was increased by a factor of 50%. ESF simulations were performed using the previously determined threshold thickness. Comparisons were then made to AMR-VOF to determine whether the threshold thickness needed to change as a result of the increase in density, thereby determining the

TABLE 6.3: Range of fluid properties for determination of δ_n. (Fluid 0 is baseline - water)

Fluid	ρ[Kg m^{-3}]	μ[mPa s]	σ[N m^{-1}]	$\theta_w[^o]$	We[-]	Ca[-]
0	997	0.890321	0.0728	70	0.75949	0.00484
1	997	1.335482	0.0728	70	0.66347	0.00635
2	997	0.593547	0.0728	70	0.86939	0.00370
3	997	0.890321	0.1092	70	0.50632	0.00323
4	997	0.890321	0.04853	70	0.65023	0.00581
5	664.66	0.890321	0.0728	70	0.44231	0.00423
6	1495.5	0.890321	0.0728	70	0.74432	0.00443
7	997	0.890321	0.0728	46.6	0.75949	0.00484

relationship between threshold thickness and density. Simulations were also run by decreasing the density by 50% to give a larger range of values tested. This process was repeated for other fluid and flow properties to determine the relationship between these properties and the threshold film thickness. The full range of conditions tested are given in Table 6.3. These are listed numerically, which will be used to distinguish the results, henceforth.

Following this procedure, the relation between the threshold thickness and the fluid properties was determined. It was found that the threshold thickness could be approximated using the following formula,

$$\delta_n = 0.031416 \frac{\Delta_x Tan(\theta_w)}{Ca^{1/3}} \tag{6.31}$$

where Δ_x is the cell size, θ_w is the contact angle and Ca is the Capillary number defined by,

$$Ca = \frac{\overline{u}\mu}{\sigma}, \tag{6.32}$$

where $\overline{u}$ is the depth-averaged, Nusselt profile inlet velocity, μ is the liquid viscosity and σ is the surface tension coefficient.

Figure 6.11 compares the fluid depth between the AMR-VOF approach and the enhanced surface film model for the various fluid listed in Table 6.3. It is observed that the results are qualitatively similar, in terms of the overall film coverage and the angle created by the rivulet. The overall wetted areas are compared in Table 6.5. Again, the results between the two approaches are within good agreement, confirming the reliability of the equation developed for threshold thickness, at least in the range of properties tested.

As can be seen from the results, this formula works well for the fluid properties tested. This formula can be used without performing additional simulations or experiments to determine empirical constants. This is advantageous over the method of Meredith *et*

TABLE 6.4: Test Fluid Properties

Fluid	$\rho[\,\mathrm{Kg\,m^{-3}}]$	$\mu[\,\mathrm{mPa\,s}]$	$\sigma[\,\mathrm{N\,m^{-1}}]$	$\theta_w[^o]$	We[-]	Ca[-]
Water	997	0.890321	0.0728	70	0.75949	0.00484
Acetone	791	0.331	0.0229	40	0.30567	0.00320
Glycerol	1227	19.5	0.0671	56	0.04814	0.01977

TABLE 6.5: Wetted area for various fluids

Fluid	AMR-VOF A_w [%]	SF A_w [%]	Difference [%]
1	68.04	63.43	-6.78
2	64.66	65.27	0.94
3	42.90	44.69	4.17
4	54.02	56.28	4.18
5	42.86	43.92	2.47
6	54.37	57.74	6.20
7	72.29	72.51	0.30
Acetone	51.48	53.23	3.40
Glycerol	44.01	44.74	1.66

al. [3] because simulations do not need to be compared with experiment to determine an appropriate value for the threshold film thickness.

In order to test the accuracy and reliability of the derived threshold thickness formula, additional 3D simulations were performed. This included modelled the flow of acetone and glycerol down the same inclined steel plate. These fluids have wide ranging properties (Table 6.4), even compared to the test-cases used to determine the formula. Therefore, they are a good test of the models' reliability across a wider range of cases.

It can be seen in Figure 6.12 and Table 6.5 that, again, the results are within good agreement. This further strengthens the validation of the model, since it has been derived on one set of fluid and successfully tested on another separate set of different fluids.

6.4.2.2 Dispersion

It can be seen from the Figures 6.8-6.10 that the dispersive stresses are large close to the leading edge of the film. Observations of the velocity field from the VOF simulations reveal that the momentum dispersion stresses arise due to the recirculating flow structures created at the static contact line. However, it is difficult to distinguish the exact effect of these stresses on the overall flow characteristics. Modelling of these terms is out of the scope of this thesis. Furthermore, the differences in the results between the

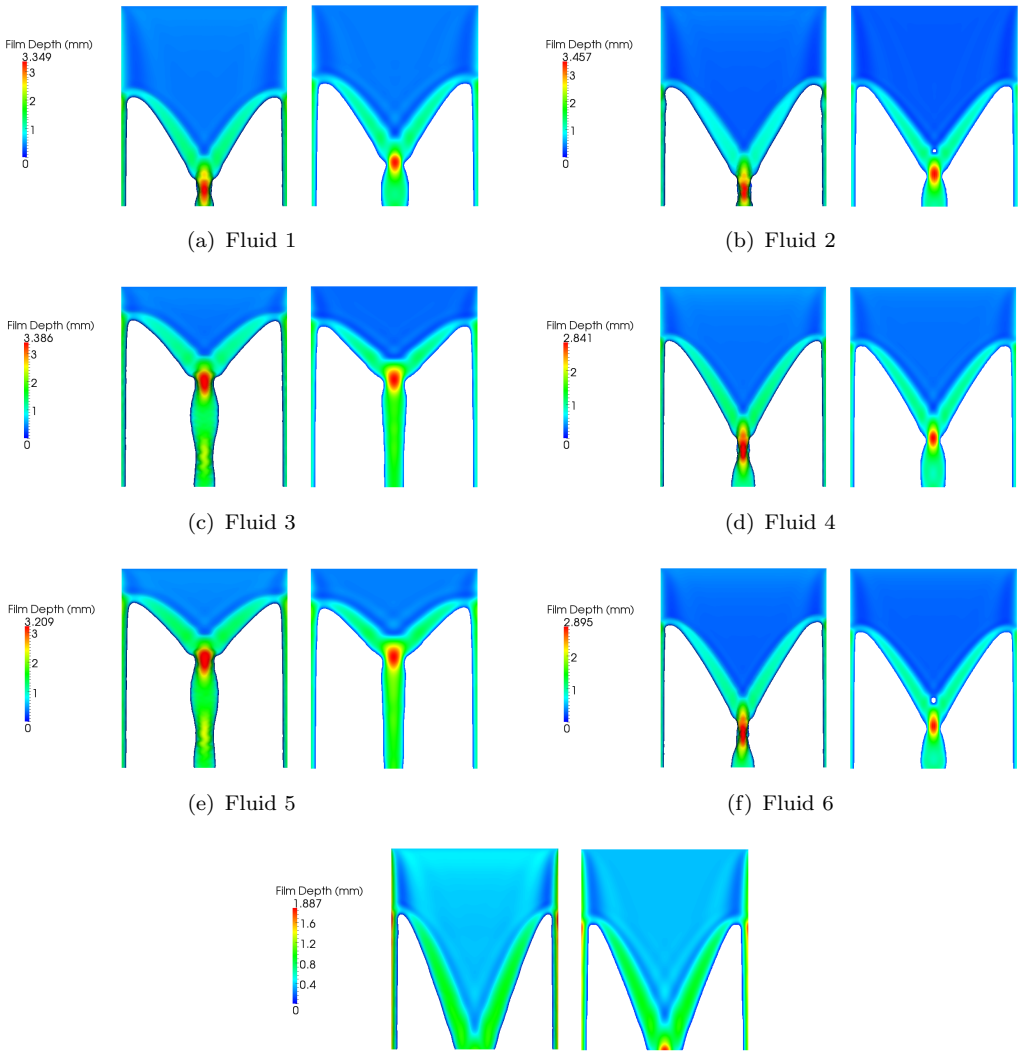

(a) Fluid 1 (b) Fluid 2

(c) Fluid 3 (d) Fluid 4

(e) Fluid 5 (f) Fluid 6

(g) Fluid 7

FIGURE 6.11: Film depth at steady state for AMR-VOF (left) and Surface Film Model (right)

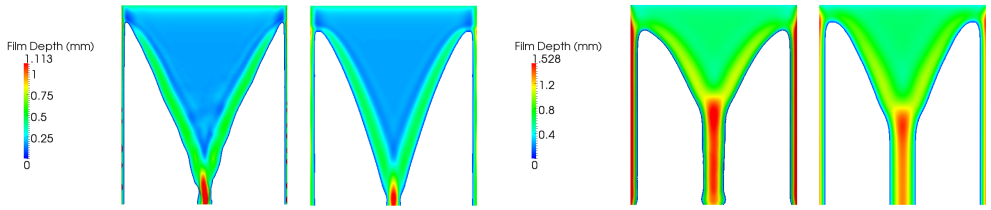

(a) Acetone (b) Glycerol

FIGURE 6.12: Film depth at steady state for AMR-VOF (left) and Surface Film Model (right)

ESF model and VOF will give insight into the magnitude of the momentum dispersion terms.

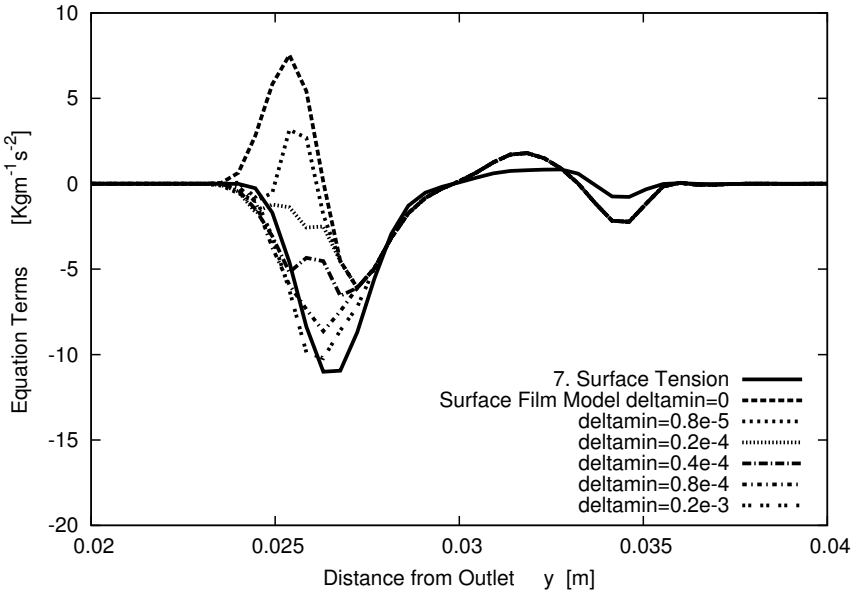

FIGURE 6.13: Budget Plot comparing the Closed and Modelled Surface Tension of the y-momentum equations for range of δ_n- Oblique position

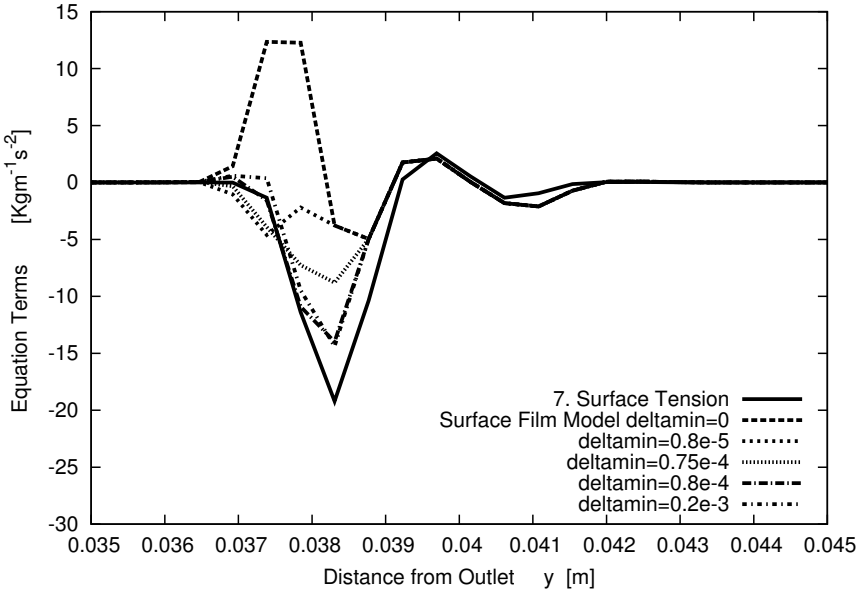

FIGURE 6.14: Budget Plot comparing the Closed and Modelled Surface Tension of the y-momentum equations for range of δ_n- Stagnation position

6.4.2.3 Viscous Terms and Wall Shear Stress

The total viscous terms in the Navier-Stokes equations are depth integrated in the following manner:

$$\underbrace{\int_0^h \mu\left(\frac{\partial^2 u}{\partial x^2}+\frac{\partial^2 u}{\partial y^2}+\frac{\partial^2 u}{\partial z^2}\right)\mathrm{d}z}_{\text{Closed Total Viscous Term}} = \underbrace{\tau_{w,y}}_{4.}\underbrace{+\tau_{g,y}}_{5.}+\underbrace{\frac{\partial}{\partial x}\left(\mu h\frac{\partial \overline{u}}{\partial x}\right)+\frac{\partial}{\partial y}\left(\mu h\frac{\partial \overline{u}}{\partial y}\right)}_{6.} \tag{6.33}$$

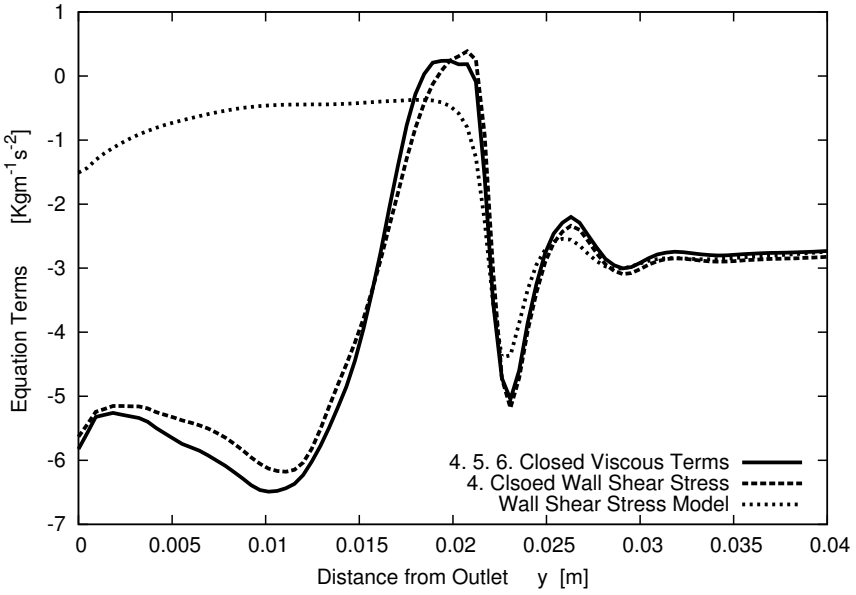

FIGURE 6.15: Budget Plot comparing the Closed and Modelled Viscous Terms of the y-momentum equations - Central position

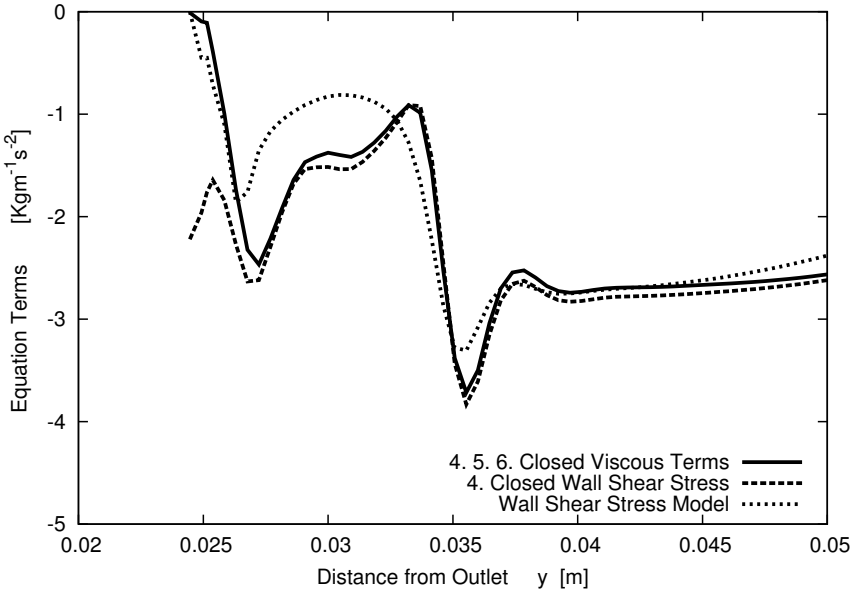

FIGURE 6.16: Budget Plot comparing the Closed and Modelled Viscous Terms of the y-momentum equations - Oblique position

It can be seen in Figures 6.15-6.17 that the closed total viscous term is approximately equal to the wall shear stress calculated directly during the 3D VOF simulations. Therefore, terms 5 and 6 of Equation 6.9 can be neglected in the calculations, and the viscous terms are solely comprised of the wall shear stress. The model for wall shear stress is also plotted on figures 6.15-6.17. It can be seen that the model is fairly accurate throughout most of the domain, only deviating largely in the central rivulet where the flow combines from both sides. However, this region will have little effect on the overall flow dynamics (wetted area etc.) and so the model was assumed adequate.

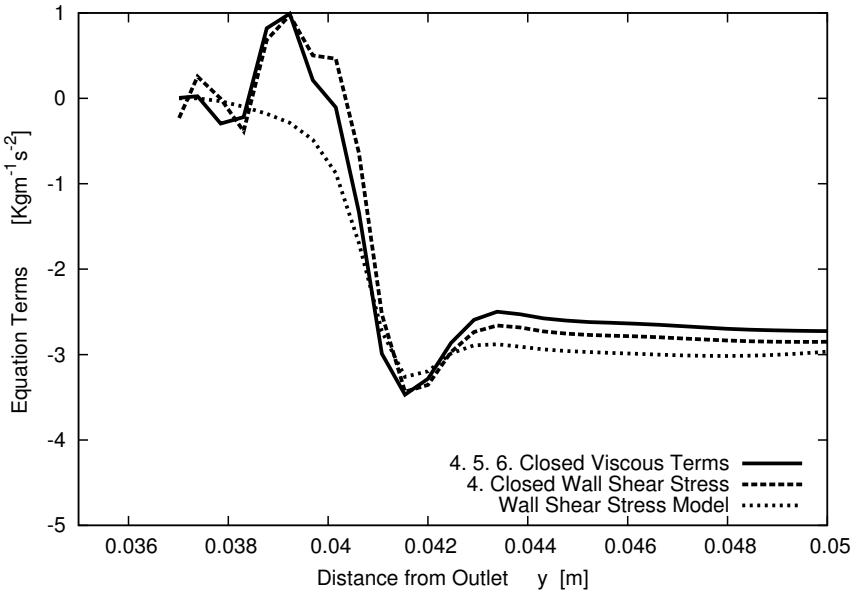

FIGURE 6.17: Budget Plot comparing the Closed and Modelled Viscous Terms of the y-momentum equations - Stagnation position

6.4.2.4 Depth-Averaged Pressure

The pressure terms in the depth-averaged Navier-Stokes equations are approximate, since the pressure is not solved during the simulation and is estimated based on the assumptions of the depth-averaged approach. Again, taking streamwise slices through the central, oblique and stagnation positions comparisons are made between the depth-averaged pressure ($h\overline{p}$) derived from the surface film model and the depth-averaged pressure from the 3D VOF simulations. Figures 6.18-6.20 show the comparisons. It is noted that the depth-averaged pressure model is in good agreement with the VOF derived depth-averaged pressure in most regions of the flow. Again, there is a deviation where the flow combines into a single rivulet, which is probably due to the fact that in this region the assumptions of the depth-averaged model are invalid. Particularly, there will be a large deviation from the Nusselt velocity profile in this region. However, as stated previously errors in this region will have little effect on the overall wetted area and interfacial area of the flow, which is of interest to mass transfer studies.

6.5 Results & Discussion

This section outlines the results from simulations of liquid film flow down an inclined plate using the depth-averaged ESF model. A range of Re_l were used to enable comparison with 3D AMR-VOF simulations of the same physical problem. The wetted area was plotted using data from both types of simulations, along with experimental data [48,49]. A comparison of simulation run-times for each method was made.

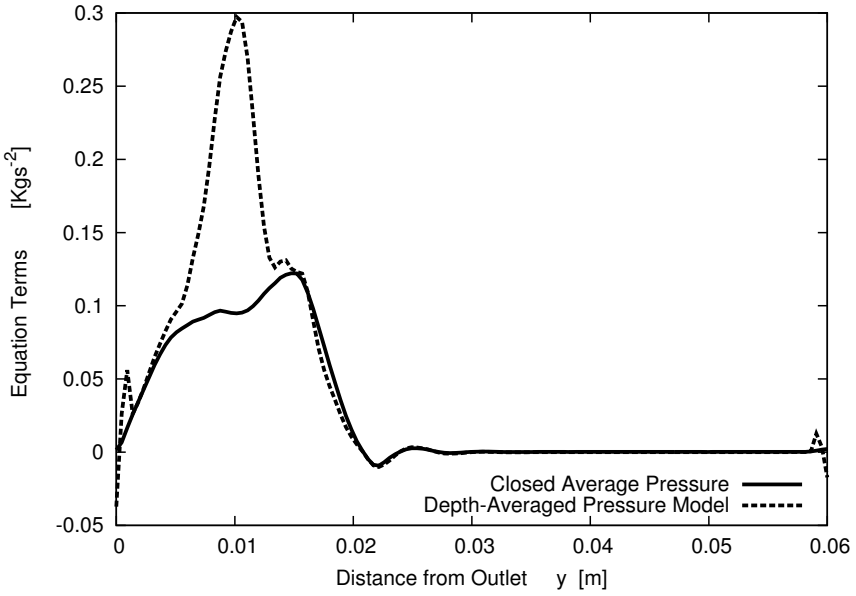

FIGURE 6.18: Budget Plot comparing the Closed and Modelled Depth Average Pressure Term ($h\overline{p}$) - Central position

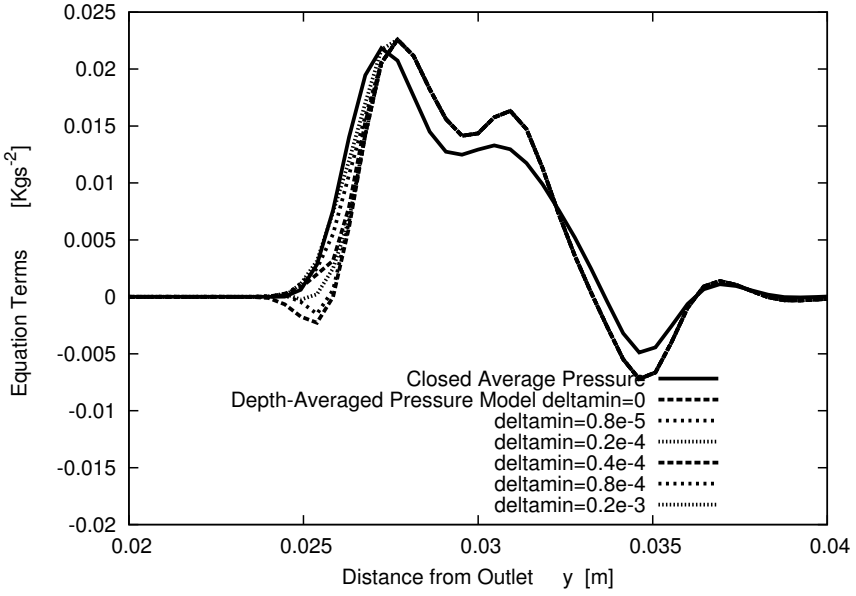

FIGURE 6.19: Budget Plot comparing the Closed and Modelled Depth Average Pressure Term ($h\overline{p}$) - Oblique position

Figure 6.21 shows a graph of the wetted areas for a range of Re_l using the enhanced surface film model, 3D AMR-VOF and experimental data [48, 49]. The ESF model was able to accurately simulate film flow down an inclined plate across a range of Re_l. At low Re_l there is a good agreement between the surface film approach and the AMR-VOF results, whilst at mid-range Re_l the wetted area is slightly over-predicted and at higher Re_l the wetted area is slightly under-predicted. However, the ESF model matched well with experimental data and it is concluded that the approach is a suitable way to model film flow down an inclined plane, even without the inclusion of a momentum

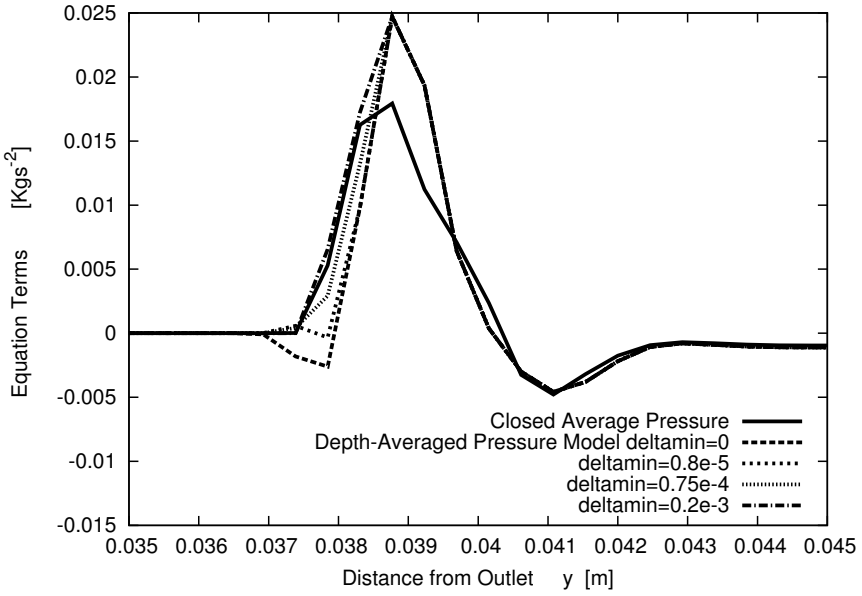

FIGURE 6.20: Budget Plot comparing the Closed and Modelled Depth Average Pressure Term ($h\overline{p}$) - Stagnation position

dispersion model. This suggests that the momentum dispersion terms have less effect, than previously thought, on the overall wetted area for these particular simulations. The deviation between the ESF model and AMR-VOF is acceptable given the assumptions that are made in the approach.

The biggest difference between the ESF and AMR-VOF was at the high Re_l. At these Re_l, once the initial rivulet formed, the contact line moved slowly down the plate until reaching a steady state position. This slow traversal of the contact line did not occur to the same degree in the ESF model. An explanation for this may be the effect of the momentum dispersion terms, because they become more significant, in comparison to surface tension, as Re_l increases.

The OpenFOAM-2.3.0 solver, reactingParcelFilmFoam is an implementation of Meredith *et al.'s* [3] surface film model. This includes a model for surface tension where the contact-angle stress is multiplied by a constant in order to fit with experimental data. However, despite varying this fitting constant, the solver was unable to replicate the results of the domain tested in the chapter. For all cases tested, at $Re_l = 156.85$, the flow was unable to maintain a partially wetted state (Figure 6.22). It is observed that the ESF model developed in this thesis gave results in greater correlation to the standard AMR-VOF approach, which in turn is in greater correlation with experimental data.

Figure 6.23 compares the film depth for a range of Re_l computed using the ESF model and AMR-VOF. The enhanced surface film model produced results very similar to the AMR-VOF approach, in terms of flow characteristics and film depth. It is noted that for $Re_l = 58.26$ the ESF model shows break-up up of the rivulets into droplets. These break-up events are likely to be mesh effects. Here the rivulets are very thin and so the

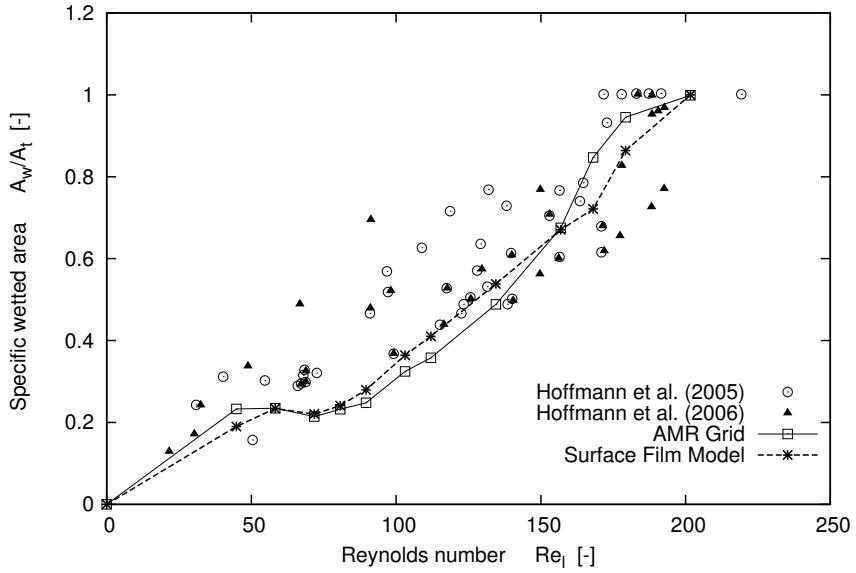

FIGURE 6.21: Comparison of wetted area for Surface Film Model with standard AMR-VOF and Experimental Data

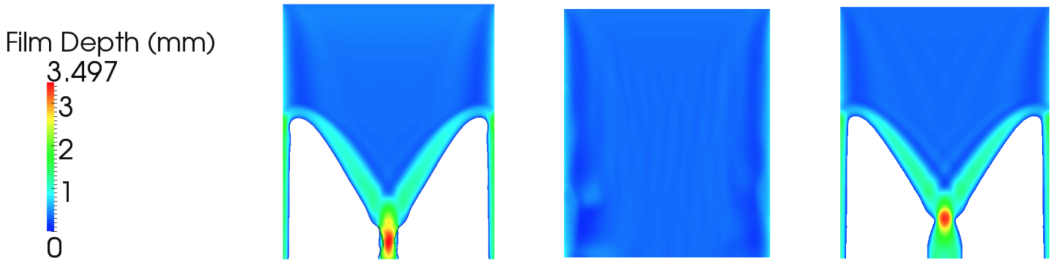

FIGURE 6.22: Film depth at $Re_l = 156.85$ (Left: AMR-VOF, Centre: Surface Film Model [3], Right: ESF Model)

mesh was probably not refined enough, across the width of the rivulets, resulting in a numerical break-up event. Further refinement of the grid should enable the rivulets to be more accurately resolved and prevent break-up for cases where thin rivulets form.

It is noted that good agreement is achieved between the ESF model and AMR-VOF approach, despite the fact the the dispersion terms have been neglected from the ESF model. In order to assess the reasons for this, the terms of the depth-averaged equations used in the ESF model are analysed along the central, oblique and stagnation slices (Figures 6.24, 6.26, 6.28). The figures only show the significant terms; the total convection, pressure gradient, wall shear stress, surface tension and gravity. These significant terms are also evaluated from the results of VOF simulations, to provide comparative data, and are shown in Figs. 6.25, 6.27, 6.29.

It is observed that the convection term in the ESF model does differ from the depth-averaged convection term derived from the VOF model. This is expected since the momentum dispersion terms were neglected. However, it can also be seen that these

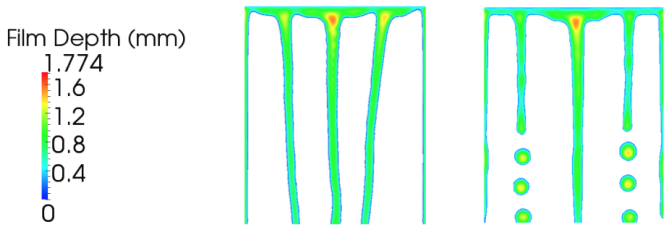

(a) $Re_l = 58.26$ Left: AMR-VOF, Right: ESF

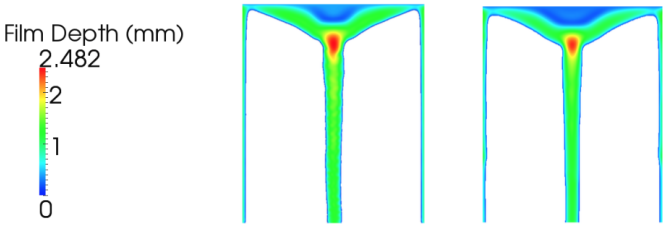

(b) $Re_l = 71.7$ Left: AMR-VOF, Right: ESF

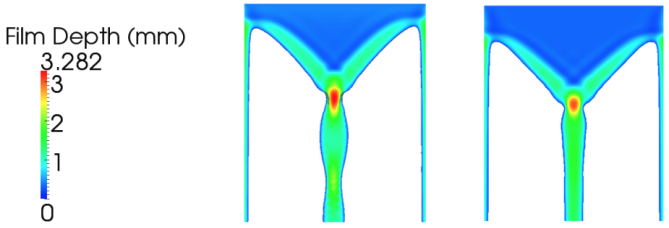

(c) $Re_l = 112.04$ Left: AMR-VOF, Right: ESF

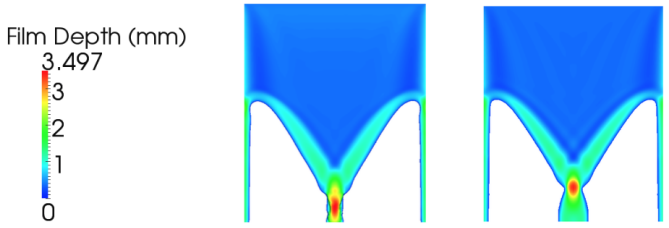

(d) $Re_l = 156.85$ Left: AMR-VOF, Right: ESF

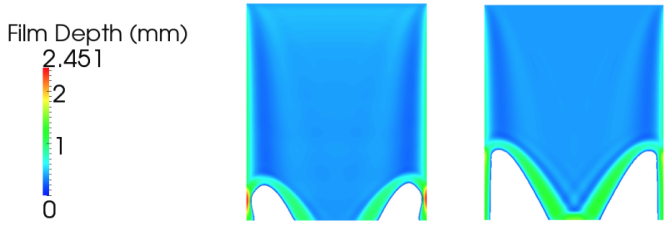

(e) $Re_l = 179.26$ Left: AMR-VOF, Right: ESF

FIGURE 6.23: Film depth for AMR-VOF and Surface Film Model at various Re_l

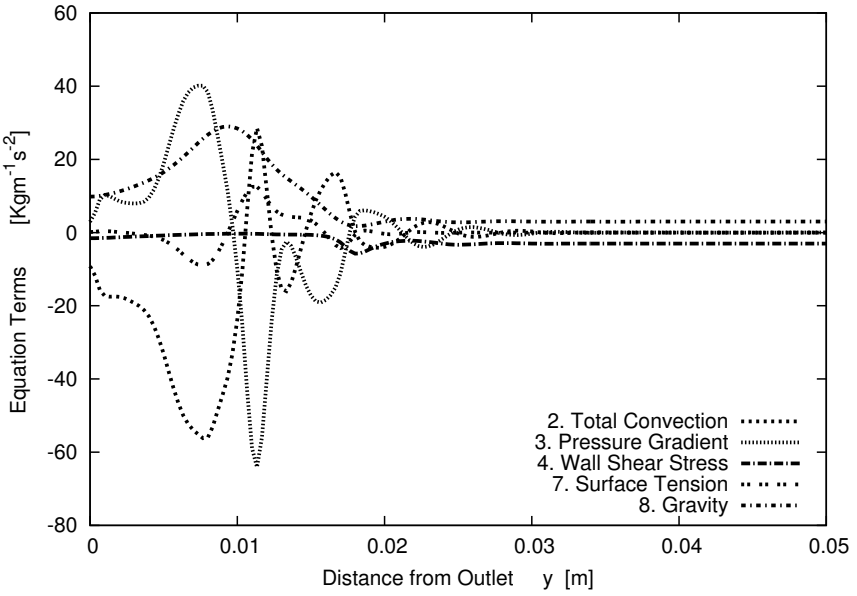

FIGURE 6.24: Budget Plot of Numerical Integration of ESF depth-averaged, y-momentum equation terms - Central position

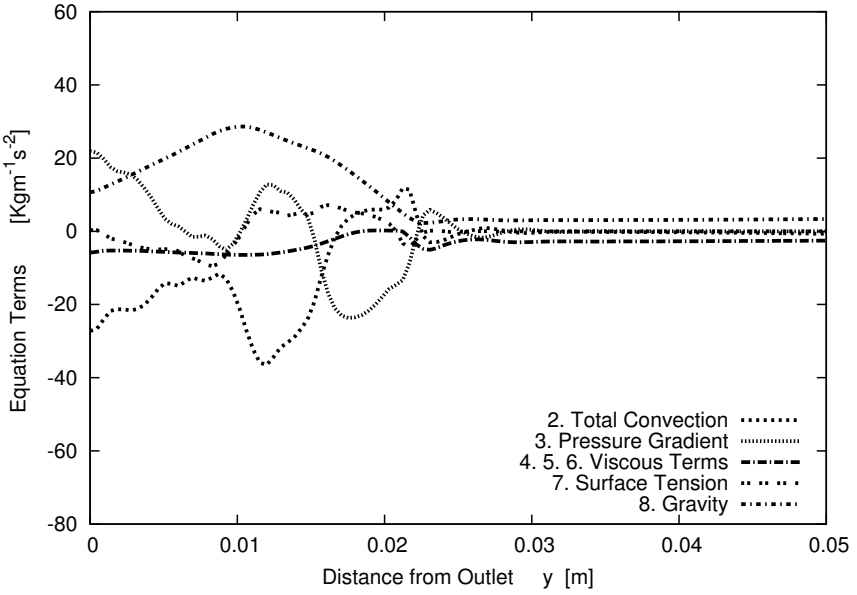

FIGURE 6.25: Budget Plot of Numerical Integration of 3D y-momentum equation terms - Central position

differences are balanced out by the gradient of pressure term and, close to the contact line, the surface tension terms.

The neglected dispersion terms appears not to have a significant effect on the results in the simulations tested within this thesis. However, these terms may become more significant for scale-up due to the increased Re_l. Therefore, any future work involving scale-up will have to determine an appropriate model for the dispersion terms.

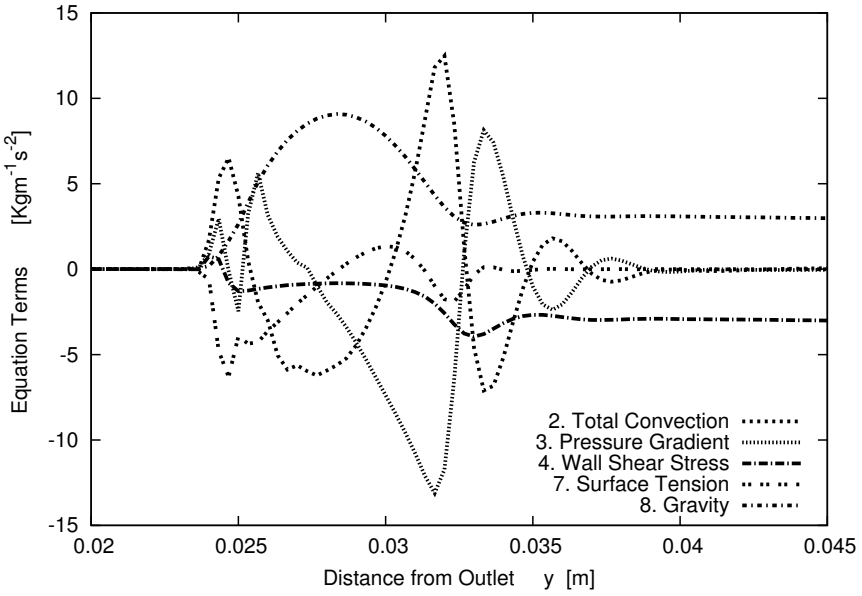

FIGURE 6.26: Budget Plot of Numerical Integration of ESF depth-averaged, y-momentum equation terms - Oblique position

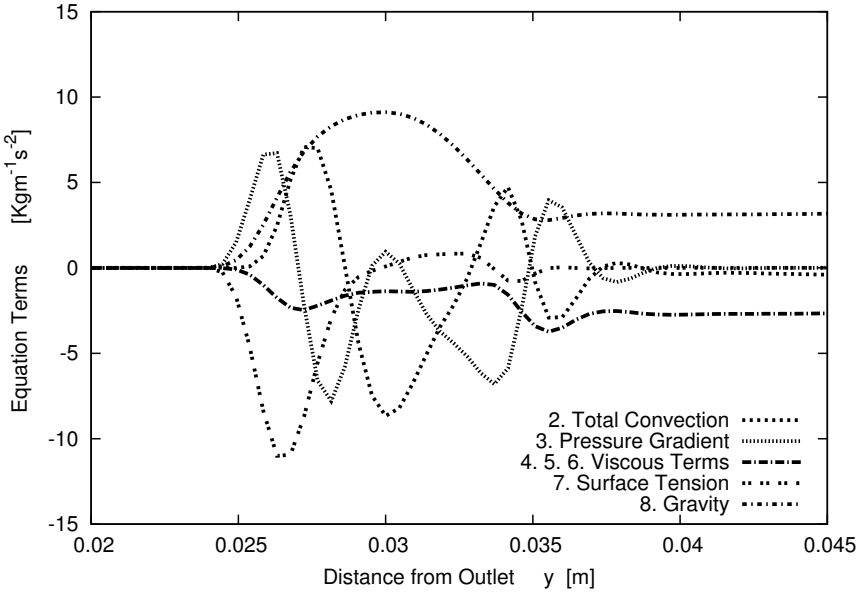

FIGURE 6.27: Budget Plot of Numerical Integration of 3D y-momentum equation terms - Oblique position

6.5.1 Comparison of Simulation CPU-Time

One of the main reasons for choosing to use a surface film approach for modelling film flow over an inclined plane is the computational speed-up achieved in comparison to alternative methods. Three-dimensional VOF methods using static grids require large numbers of computational cells throughout the entire domain to ensure that suitable resolution is achieved to adequately resolve the liquid interface. This results in fairly large simulation run-times, even on the small domains used in this thesis. Scaling up

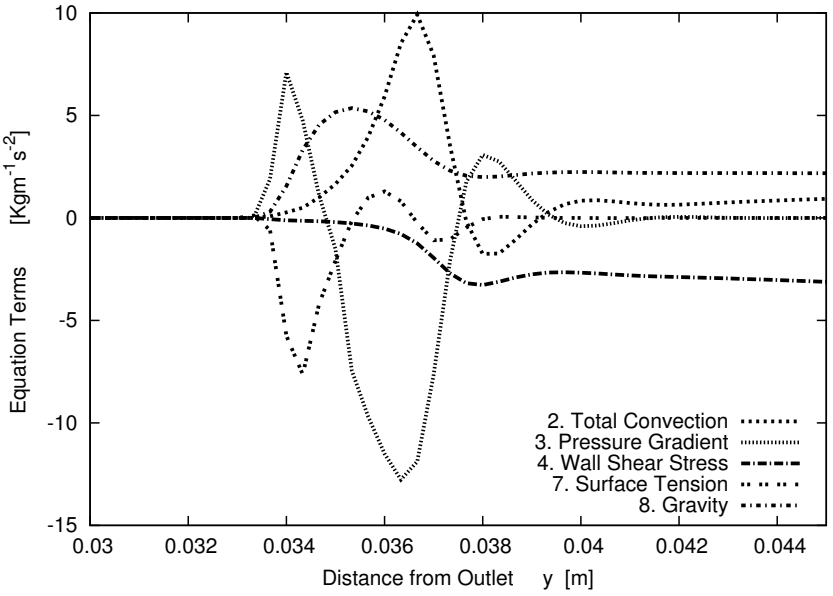

FIGURE 6.28: Budget Plot of Numerical Integration of ESF depth-averaged, y-momentum equation terms - Stagnation position

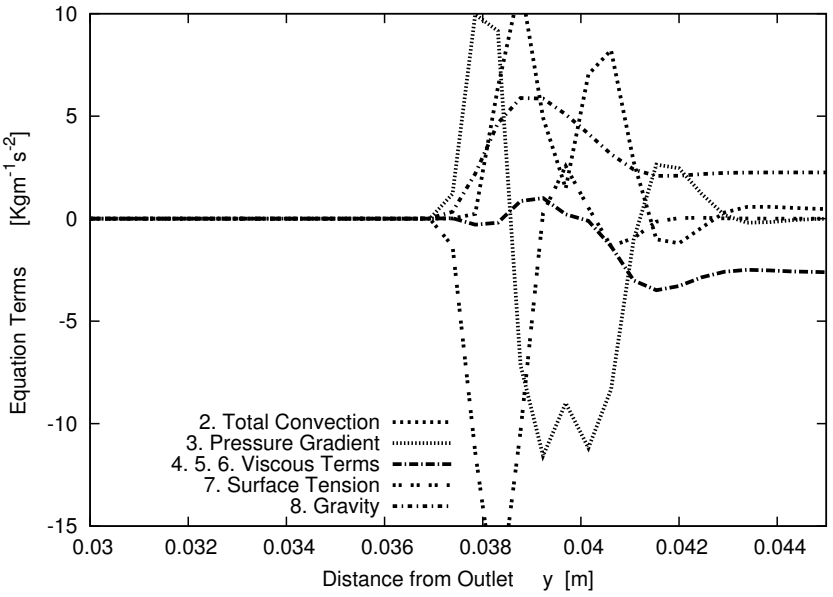

FIGURE 6.29: Budget Plot of Numerical Integration of 3D y-momentum equation terms - Stagnation position

to simulate large-scale flow over the structured packings used in carbon capture would be prohibitive in terms of the computational requirements. AMR simulations can help alleviate some of the computational requirements, by concentrating grid points in regions of numerical interest. However, simulation run-times would still be prohibitive at larger scales.

Table 6.6 compares the CPU time for simulations using the ESF model, the VOF approach and the AMR-VOF approach. It is clear that the ESF model vastly reduces

Table 6.6: CPU Time

Re_l	CPU-Time [hrs/sec] Static Grid	CPU-Time [hrs/sec] AMR Grid	CPU-Time [hrs/sec] Surface-Film Model
44.81	149.73	1598.50	1.56
58.26	-	1755.33	1.51
71.70	-	1121.67	1.60
80.67	349.73	1021.72	1.48
89.63	-	984.80	1.66
103.07	-	1029.84	1.50
112.04	107.55	1025.08	1.57
134.44	274.92	1097.63	1.45
156.85	287.21	900.93	0.94
168.05	129.78	1269.18	1.05
179.26	127.61	1129.49	0.99
201.66	192.99	953.54	1.14

the number of computational cells required and therefore, reduces the computational requirements for simulations, thereby making scale-up to mesoscale domains much more achievable. The approach was approximately 150 times quicker than standard VOF and 850 times quicker than AMR-VOF. The AMR-VOF results stated used two level of refinement about this liquid interface, however, it was shown previously that by using a very coarse initial grid and 3 levels of refinement around the liquid interface, the AMR run-times could be reduced by up to 80%. Even with this increase in efficiency, the ESF model is still vastly quicker than the standard approaches to modelling film flow.

6.6 Conclusion

In this investigation a surface film model was developed to simulate isothermal, non-reacting, gravity-driven flow down an inclined plane. The domain was chosen as an approximation to a small section of packing material used in CO_2 absorption. The results from three-dimensional VOF simulations were used to determine significant terms of the depth-averaged Navier-Stokes equations, and to verify the accuracy of modelled terms which arise due to the spatial averaging process in the derivation of these terms.

The ESF model developed in this chapter was able to replicate the results of more conventional VOF simulations. In particular, the transition from multiple rivulets to single rivulets was modelled well, and the wetted area across a range of Re_l matched well with previous numerical studies and experimental data. The deviation from previous numerical studies is attributed to the simplifications of the approach and the neglected

momentum dispersion terms. The neglected dispersion terms appear not to have a significant impact on the results for the simulations tested in this chapter. However, these terms may become more significant for scale-up due to the increased Re_l. Therefore, any future work involving scale-up will have to determine an appropriate model for the dispersion terms.

The main problem with using the VOF method for studying CO_2 absorption within packed columns is the prohibitive computational run-times required for larger domains. The main advantage of this method over other approaches is the significant reduction in computational requirements (of the order 150 times quicker). Therefore, this will allow the computational domains to be scaled-up and will allow simulations to be performed on larger sections of packing, whilst maintaining reasonable CPU-times. However, as mentioned previously, an appropriate model for the dispersion terms may have to be developed for scale-up. The ESF approach will also be of benefit in other industrial sectors where the modelling of thin film flow is vital to the understanding of the underlying processes and the subsequent optimisation studies that are often required.

The next chapters of this thesis will focus on the the addition of species absorption and reaction modelling to the ESF model. This will represent a significant step forward in the use of depth-averaged approaches for the modelling acid-gas absorption.

Chapter 7

Surface Film Modelling with Mass Transport and Chemical Reaction

7.1 Introduction

The ability to model species mass transfer is a vital component in the numerical simulation of carbon capture via packed columns. In particular, the absorption of CO_2 from the gaseous phase to the liquid phase is seen as a challenging prospect. Despite these challenges, several papers in the literature state methods of including species mass transfer within the framework of the VOF model. However, to the best of the author's knowledge, there is no literature detailing the inclusion of interfacial mass transfer and reaction kinetics with a depth-averaged approach.

This chapter details the implementation and validation of mass transfer with the enhanced surface film model. Due to the lack of experimental data for physical absorption, an alternative approach from the literature was used as validation. The method developed by Haroun *et al.* [97] was selected and coded into the interFOAM (VOF) solver to create a new solver capable of modelling species transport. This approach was validated by Haroun *et al.*, however, further validation is performed here to ensure that new solver was correctly implemented in OpenFOAM.

The method of Haroun *et al.* [97] was selected due to its simple formulation, being a single additional flux term in the species transport equation. The limitation of this method is that it requires a constant value for Henry's constant, He. However, simulations performed in this thesis are isothermal and so He will be constant over the domain. Initially, the developed code, capable of simulating mass transfer using the VOF method, was validated using a 1-dimensional model, whereby the simulated results were compared

against the exact analytical solution [97]. Secondly, validation was performed using a 2-dimensional approach, whereby the results were compared against the mass transfer coefficient derived from Higbie Penetration Theory.

The mass transfer implementation in the ESF model was then validated against the VOF approach, in a wetted wall column set-up. Comparisons were made in terms of concentration profiles and the surface age.

Physical mass transfer is only present in a small subset of real-world absorption equipment and so it was important to also include reaction kinetics in the ESF model. Chemically enhanced mass transfer involves the absorption of a gaseous component into the liquid phase, accompanied by a chemical reaction. This reaction is used to greatly enhance the rate of absorption of many absorption systems, including CO_2 capture in packed columns.

Thus, this chapter also details the implementation of reactive mass transfer with the ESF model, where validation is performed against the experimental data of Puxty *et al.* [4]. It will be shown that the ESF approach, with the inclusion of mass transfer, is more viable than VOF for realistic 3D simulations of gaseous absorption into a liquid film.

The validated model is ultimately used to model CO_2 absorption into an MEA solution in the partially wetted regime. This combines all the elements developed throughout this thesis, including thin-film hydrodynamics, mass transfer, reaction kinetics, and computes all of these aspects simultaneously in a very economical simulation. It exemplifies that this approach is viable for 3D simulations and clearly demonstrates that this ESF model could be extended to larger, more realistic problems in CCS with appropriate modifications.

7.2 Mass Transfer with the ESF Model

In order to include mass transfer within the ESF model it was required to solve a species transport equation in the gaseous domain. The inclusion of a sink term accounted for the mass transfer from the gaseous phase into the liquid phase, through the gas-liquid interface.

As detailed in Chapter 6, the surface-film approach solves equations in two separate domains, a 3D gaseous domain and a 2D depth-averaged fluid domain. In order to track the concentration of CO_2 (or other gaseous component to be absorbed), an additional species transport equation was included (equation 7.1), and solved for, in the gaseous domain,

$$\frac{\partial C_j}{\partial t} + \nabla \cdot (\boldsymbol{u} C_j) - \nabla^2 (D_{C_j,g} C_j) = S_{C_j}, \tag{7.1}$$

where C_j is the concentration of species, j, $D_{C_j,g}$ is the diffusion coefficient of species j in the gaseous phase and S_{C_j} is the source/sink of species j. In these simulations the density in the gaseous phase has been treated as a constant. This is only valid when the concentration of the absorbed species is low, the temperature differences are small and the flow is incompressible. This is a reasonable assumption to make since the concentration of CO_2 is flue gas is low, especially in carbon capture at gas-powered plants. At the scale of the simulations performed in this thesis the temperature range can also be considered small enough to warrant a constant density assumption. The flow configurations considered are also in the incompressible regime.

The source term in equation 7.1 is the rate of mass transfer of species j from the gas phase to the liquid phase. Considering that the surface film model solves on two separate domains, this source term can be applied in cells adjacent to the interface between these two domains. The liquid domain in the surface film model is depth-averaged, with only one cell in the film depth. Therefore, the concentration profile within the liquid phase can not be resolved. Therefore, Higbie penetration theory is utilised to model the liquid phase mass transfer process, which ultimately enables the rate of mass transfer through the interface to be determined.

According to two-film theory [70], the rate of mass transfer through a gas-liquid interface can be given by equation 2.2, stated again as,

$$N_j^{int} = k_L (C_{L,j}^{int} - \cancelto{0}{C_{L,j}}). \tag{7.2}$$

It is assumed that the concentration in the liquid bulk, $C_{L,j}$ is approximately zero. This is a reasonable assumption considering the small diffusion coefficient of CO_2 in the liquid phase, resulting in a very thin concentration boundary layer within the film at the liquid-side of the interface. This condition is exemplified in the 2D simulations of gas absorption using the VOF approach later in this chapter.

Henry's law provides an equilibrium condition at the interface, given by,

$$C_{G,j}^{int} = He_j \, C_{L,j}^{int}, \tag{7.3}$$

which allows the mass transfer rate through the interface to specified by,

$$N_j^{int} = k_L \, \frac{C_{G,j}^{int}}{He_j}, \tag{7.4}$$

and therefore, the source term in equation 7.1 is specified by,

$$S_{C_j} = -A\, k_L\, \frac{C_{G,j}^{int}}{He_j}, \tag{7.5}$$

where A is the interfacial area through which mass transfer can occur. This is taken as equal to the cell-face area at the boundary between the adjacent domains. However, a more accurate representation could be achieved by correcting this area by the slope of the interface. This would give a more accurate representation of the interfacial area, which would improve future simulations.

This equation is a valid approximation to the rate of mass transfer through a gas-liquid interface if the concentration gradient on the gaseous side of the interface can be resolved with adequate grid in the gaseous domain. Since, the diffusion coefficient in the gaseous phase is of the order of 100 times greater than in the liquid phase (for CO_2 in air and CO_2 in aqueous MEA), resolution of the concentration gradient on the gas-side of the interface is much more achievable than the liquid-side of the interface.

The mass transfer coefficient in the liquid phase, k_L can be obtained from Higbie Penetration Theory [12],

$$k_L(t) = \sqrt{\frac{D_{C_j,L}}{\pi t_H}}. \tag{7.6}$$

As detailed in section 2.4.2, the exposure time, t_H is the amount of time that each fluid element spends at the gas-liquid interface.

7.2.1 Liquid Film Exposure Time

Many articles in the literature which make use of Higbie Penetration Theory define the exposure time as the ratio of liquid surface velocity to the distance from the inlet,

$$t_{H,SV} = \frac{y_{inlet}}{|U_s|}, \tag{7.7}$$

where y_{inlet} is the distance from the liquid inlet and $|U_s|$ is the magnitude of the velocity at the liquid surface, at a particular point in space. The subscript, $_{SV}$ in the exposure time, $t_{H,SV}$ indicates that the exposure time is calculated using the surface velocity.

This approach gives viable approximation to the exposure time in simple flow configurations, such as wetted-wall column flow. However, no consideration is made to the history of the flow, since it is calculated at specific locations in space and time. It is also difficult to apply this approach to situations with complicated flow patterns, where the distance travelled by a fluid particle is not simply equivalent to the straight-line distance between the current position and the inlet. This situation arises, to a certain degree, in

flow down a partially wetted plate, where the flow direction is not always normal to the liquid inlet.

An alternative approach is to solve a Residence time equation, during the simulation, which can then be used to determine the exposure time, t_H. This exposure time can then be used for the calculation of the mass transfer rate, to be included in the species transport equation.

7.2.1.1 Residence Time Equation

In the VOF approach the Residence time equation is a transport equation for the variable τ, residence time. This transport equation is given by,

$$\frac{\partial \tau}{\partial t} + \nabla \cdot (\boldsymbol{u}\tau) = 1. \tag{7.8}$$

The boundary condition at any inlet is fixed to $\tau = 0$. All other boundaries have a zero gradient boundary condition. The initial condition for the residence time throughout the whole domain is $\tau = 0$. The solution of this transport equation along with the above stated boundary conditions allow the residence time, τ to be determined and is specified as a volumetric field. The exposure time, $t_{H,RT}$, as required in equation 7.6, is given by plotting τ on the liquid film interface (contour of $\alpha = 0.5$). The subscript, $_{RT}$ in the exposure time, $t_{H,RT}$ indicates that the exposure time is calculated from the residence time transport equation.

For the Enhanced Surface Film model, the residence time equation is solved within the liquid (depth-averaged) domain. The transport equation for residence time, τ is given by,

$$\frac{\partial \rho h \tau}{\partial t} + \nabla \cdot (\rho h \overline{\boldsymbol{u}} \tau) = \rho h, \tag{7.9}$$

where h is the solved-for film-depth and $\overline{\boldsymbol{u}}$ is the depth-averaged velocity. The boundary conditions are defined in the same manner as the VOF Residence time equation. Defining, α_f as the wetted fraction, where $\alpha_f = 0$ means that the cell is not wet and $\alpha_f = 1$ means that the cell is wet,

$$\alpha_f = pos(h - \delta_n), \tag{7.10}$$

where δ_n is the threshold film thickness and the function $pos(x) = 0$ if $x < 0$ or $pos(x) = 1$ if $x >= 0$. The exposure time, t_H to be used in equation 7.6, is then given by,

$$t_{H,RT} = \alpha_f \frac{2}{3} \tau, \tag{7.11}$$

where the term, α_f ensures that the exposure time is only applied in cells where the plate surface is wetted, since in non-wetted cells the exposure time is undefined. The subscript, $_{RT}$ in the exposure time, $t_{H,RT}$ indicates that the exposure time is calculated from the residence time transport equation.

Validation of the ESF version of exposure time, $t_{H,RT}$ will be made by comparison with the VOF exposure time, $t_{H,RT}$ and the usual approach of equation 7.7, $t_{H,SV}$. Comparisons will be made on a 2D domain (wetted-wall column) and a 3D domain (partially-wetted plate).

7.2.1.2 Reactions Kinetics with the ESF Model

The absorption of gases, such as CO_2, into liquid films is limited by the small diffusion coefficient of those gases in the liquid phase. This is often, as in the case of CO_2, much smaller than the diffusion coefficient in the gaseous phase, which results in the rate of absorption being limited by the liquid-side resistance.

In order to increase the rate of absorption, chemical reactions can reduce the concentration of CO_2 in the liquid film, thus reducing the liquid film resistance. In the case of CO_2 absorption, aqueous monoethanolamine is the baseline solvent used to enhance the rate of absorption.

The modelling of reactions, along with the hydrodynamics and mass transfer adds additional complexity to the simulations, but it must be included to ensure that simulations of industry relevant absorption equipment can be completed accurately.

The approach used in this chapter is the Enhancement factor model [122]. The Enhancement factor, E is defined as the ratio of the rate of absorption into the liquid film with reaction to the rate of absorption without chemical reaction. This allows all of the effects of chemical reaction to be confined to one parameter, E. The rate of absorption without reaction is known from the previous sections, so determination of the enhancement factor is all that is required to model chemically enhanced absorption.

The Enhancement factor is expressed as a function of the Hatta number, Ha for both first and second order reactions. The Hatta number is a dimensionless number which relates the rate of reaction in a liquid film to the rate of diffusion through the film. For example, in the case of CO_2 absorbing from the gaseous phase into the liquid phase and thus reacting with MEA in the liquid phase, the Hatta number would be given by,

$$Ha^2 = \frac{k\, C^{bulk}_{MEA,L}\, D_{CO_2,L}}{k_L^2}, \tag{7.12}$$

where k is the rate of chemical reaction between CO_2 and MEA, $C^{bulk}_{MEA,L}$ is the concentration of MEA in the bulk of the liquid phase, $D_{CO_2,L}$ is the diffusion coefficient of CO_2 in the liquid phase and k_L (given by equation 7.6) is the rate of mass transfer of CO_2 into the liquid film that would occur without any reaction. According to Danckwerts [122], for an irreversible, first order reaction the Enhancement factor is given by,

$$E = \sqrt{1 + Ha^2}. \tag{7.13}$$

The enhancement factor takes a different form for irreversible, second-order reaction kinetics and an approximate solution developed by Decoursey [123], is given by:

$$E = \frac{M}{2(E_i - 1)} + \left(\frac{M^2}{4(E_i - 1)^2} + \frac{E_i M}{(E_i - 1)} + 1 \right)^{1/2}, \tag{7.14}$$

where $M = Ha^2$ and Ei is the enhancement factor for an instantaneous irreversible reaction, given by:

$$E_i = 1 + \frac{D_{MEA,L} C^{bulk}_{MEA,L}}{b D_{CO_2,L} C^{int}_{CO_2,L}}, \tag{7.15}$$

where $D_{MEA,L}$ is the diffusion coefficient of MEA in the liquid phase, b is the number of moles of MEA required to react with one mole of CO_2, and $C^{int}_{CO_2,L}$ is the concentration of CO_2 at liquid-side of the interface.

Whichever order of reaction is selected the enhancement factor is included in the ESF model within the source term of equation 7.1, so that S_{C_j} is given by,

$$S_{C_j} = -E\, A\, k_L\, \frac{C^{int}_{G,j}}{He_j}. \tag{7.16}$$

The assumption of a first-order reaction can be made due to the fast reaction kinetics and the relatively low concentrations of CO_2 in the gas stream. This assumption will be tested in the following sections.

7.3 Simulations with Mass Transfer

To provide validation of physical mass transfer in the ESF model, the approach of Haroun *et al.* [41, 97] was implemented into OpenFOAM. This was primarily due to the lack of experimental data for physical mass transfer and would allow the mass transfer model used in this thesis to be validated. Further validation is performed in the final sections of this chapter, where reaction kinetics are included in the model. In this case, experimental data does exist for chemically enhanced absorption in wetted wall columns.

Initially, one-dimensional simulations were performed and validated against an exact solution to the governing equations of mass transfer. Secondly, two-dimensional simulations were performed and validated against the Higbie Penetration Theory of mass transfer.

7.3.1 1-Dimensional Mass Transfer

As stated by Haroun *et al.* [97], the case of one-dimensional mass transfer can be validated against an exact numerical solution. Under this simplification no flow occurs

and the species transport equation is simplified to a one-dimensional diffusion problem through a static gas-liquid interface. The exact steady-state solution for the concentration along the x-axis is given by:

$$C_L = \frac{C_G^0 - HeC_L^0}{He + \frac{D_L}{D_G}} \frac{x}{e} + C_L^0 \qquad 0 \leq x \leq e, \tag{7.17}$$

$$C_G = \frac{C_G^0 - HeC_L^0}{He\frac{D_G}{D_L} + 1} \frac{x - 2e}{e} + C_G^0 \qquad e \leq x \leq 2e, \tag{7.18}$$

where C denotes concentration, He is Henry's constant, $y = e$ is the location of the gas-liquid interface and the subscripts L and G correspond to the liquid and gas phases, respectively.

7.3.1.1 Computational Domain & Simulation Set-up

The computational domain was chosen to be one-dimensional along the x-axis with a length of 0.1m. The domain was subdivided into 150 cells, considered more than adequate for this particular simulation. A diagram of the mesh can be observed in Figure 7.1.

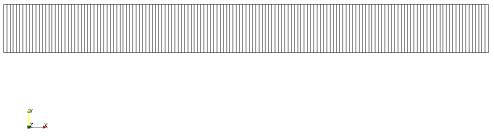

FIGURE 7.1: Mesh of the 1-D domain

In accordance with the validation performed by Haroun *et al.* [97], the diffusivity ratio was chosen to be $D_G/D_L = 10$ and the interface is located at $x = e$. The author of this thesis imposed the values, $e = 0.05$ and initial conditions of $C_L^0 = 0$ mol m^{-3} and $C_G^0 = 1$ mol m^{-3}. The boundary condition for concentration at the left wall was set to a fixed value of $C = 0$ mol m^{-3}, whilst for the right wall it was set to a fixed value of $C = 1$ mol m^{-3}. Due to the 1-dimensional nature of the domain, the interface would remain fixed and the gas/liquid phases would remain stagnant. Therefore, the properties of the fluids are arbitrary and Henry's constant was chosen to be $He = 0.1$.

The simulations were run as time-dependent with a time-step of 1×10^{-5}s until steady state was reached. The only time-scale present in this simulation was the diffusion time-scale, $\tau_v = \frac{L^2}{D}$, where L is the characteristic length scale or the cell size, D is the diffusion coefficient. The smallest diffusion time-scale was approximately 2×10^{-5}s, which confirms the choice of time step.

7.3.1.2 Results & Discussion

Initial validation of the absorption-VOF code was performed by using one of the validation cases of Haroun *et al.* [97]. Figure 7.2 shows a plot of the volume fraction, α_1. It can be seen that the interface is located at a central position with the liquid phase on the left and the gaseous phase on the right of the interface. As mentioned previously, the fluids will remain stagnant throughout the simulation and therefore, this distribution of volume fraction will remain constant.

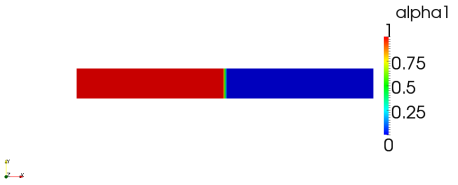

FIGURE 7.2: Liquid and gas distribution in 1-D domain

Figure 7.3 shows the contour fractions of species concentration throughout the domain. Initially, the species is fully confined to the gaseous phase (see Figure 7.3(a)). The converged solution is shown in Figure 7.3(b) and it can be seen that mass transfer has taken place across the interface in accordance with Henry's law at the interface.

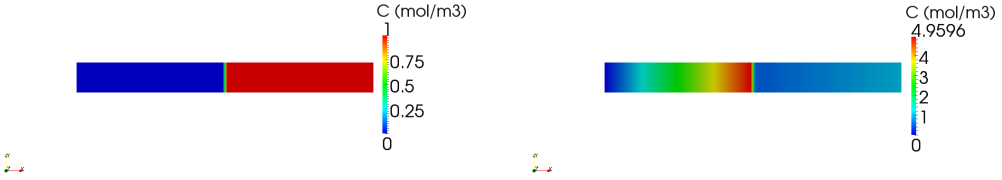

(a) Initial species concentration (b) Converged species concentration

FIGURE 7.3: Species concentration in 1-D domain for $He = 0.1$

Figure 7.4 plots the converged species concentration along the x-axis. The simulated results are compared to the exact solution. It can be seen that there is very good agreement between the simulated and analytical solutions, verifying the correct implementation of the method. The method was able to capture well the discontinuity in species concentration at the interface region, with good resolution of the concentration.

7.3.2 2-Dimensional Mass Transfer

Simulations were performed of 2D mass transfer on a 2D set-up of a wetted-wall column. Initially, the OpenFOAM implementation of the VOF approach of Haroun *et al.* [41, 97] was validated by comparing the calculated mass transfer coefficient with that of

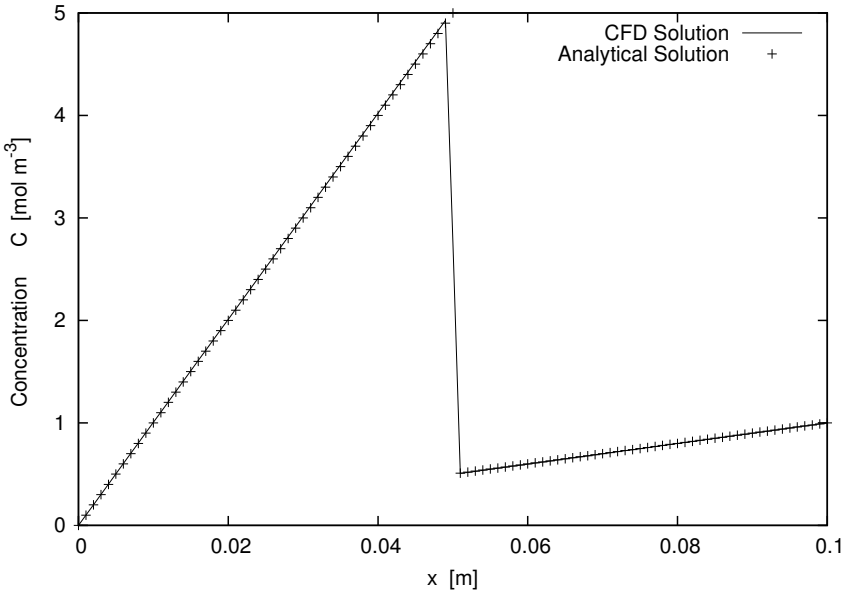

FIGURE 7.4: 1-dimensional species distribution for $He = 0.1$,$e = 0.05$, $C_L^0 = 0$ and $C_G^0 = 1$

Higbie Penetration Theory. The concentration of species was solved simultaneously with the hydrodynamics and the resulting steady-state concentration profiles were used to calculate the mass transfer coefficient.

The equivalent simulation was then performed with the enhanced surface-film model and comparisons were made between the two simulations. The surface age calculations were also compared within this domain.

7.3.2.1 Computational Domain

The computational domain in this section was selected to be a 2-dimensional representation of gravity-driven film flow down a vertical wall (see Figure 7.5). Given the small thickness of the liquid film, compared to the overall size of the domain, this could also be construed as a two-dimensional representation of a wetted-wall column. The domain has dimensions of 0.002m × 0.03m (width×height). The liquid inlet was chosen to be 0.0004m in depth to give a liquid film Reynolds number, $Re_l = 209$, which should allow a smooth, continuous thin film to form.

For the VOF simulations the computational mesh was composed of 88070 structured, non-uniform hexahedral cells (Fig. 7.5). This is a relatively large number of cells for the size of domain. This was chosen to ensure a large number of cells near the interface in order to accurately capture the large concentration gradients in this region. Due to the simplicity of the domain, it was thought of as advantageous to make the grid very fine to aid in validation and also analysis of the results. The grid is much finer near the liquid

inlet, where the gradients are largest, expanding down the plate as the concentration boundary layer grows.

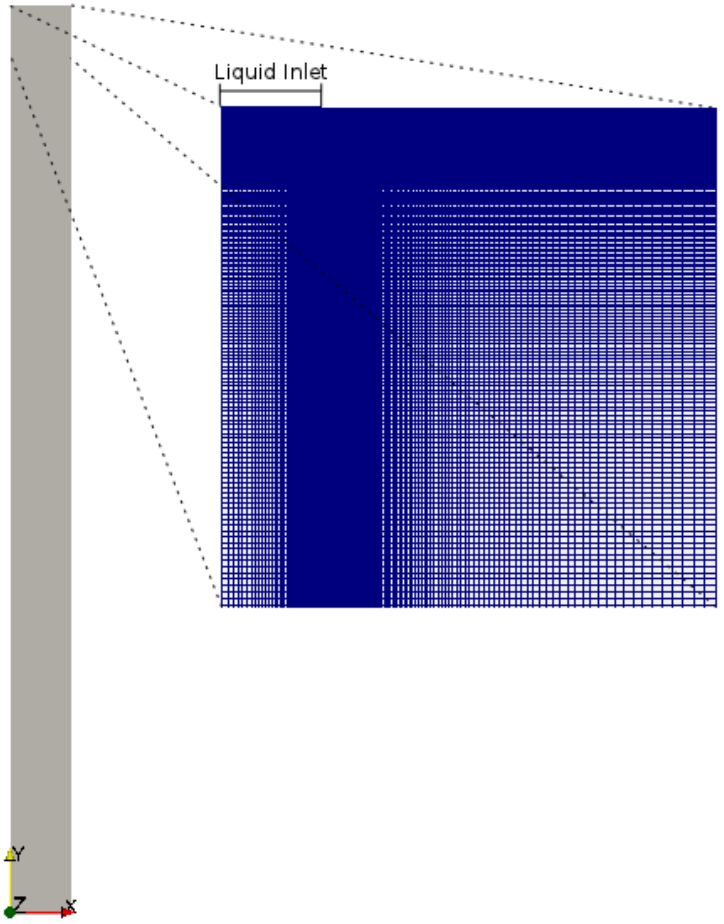

FIGURE 7.5: Mesh of the 2-D domain (VOF)

The ESF approach was also modelled on the same domain. This computational mesh consisted 8800 cells in the gaseous domain and 400 cells in the fluid domain (see Fig. 7.6). In this case a mesh independence check was performed to ensure the grid was fine enough to accurately resolve the flow features. Due to the large diffusion coefficient in the gaseous domain, the mesh could be fairly coarse, whilst still capturing the concentration gradients.

7.3.2.2 Simulation Set-up

To ensure the set-ups were as similar as possible it was important for the liquid inlet in the VOF case to have the correct velocity profile, considering that this is implicit in the surface film model. This is important because the rate of mass transfer across the interface is dependent on the velocity at the interface, which is affected by the velocity profile.

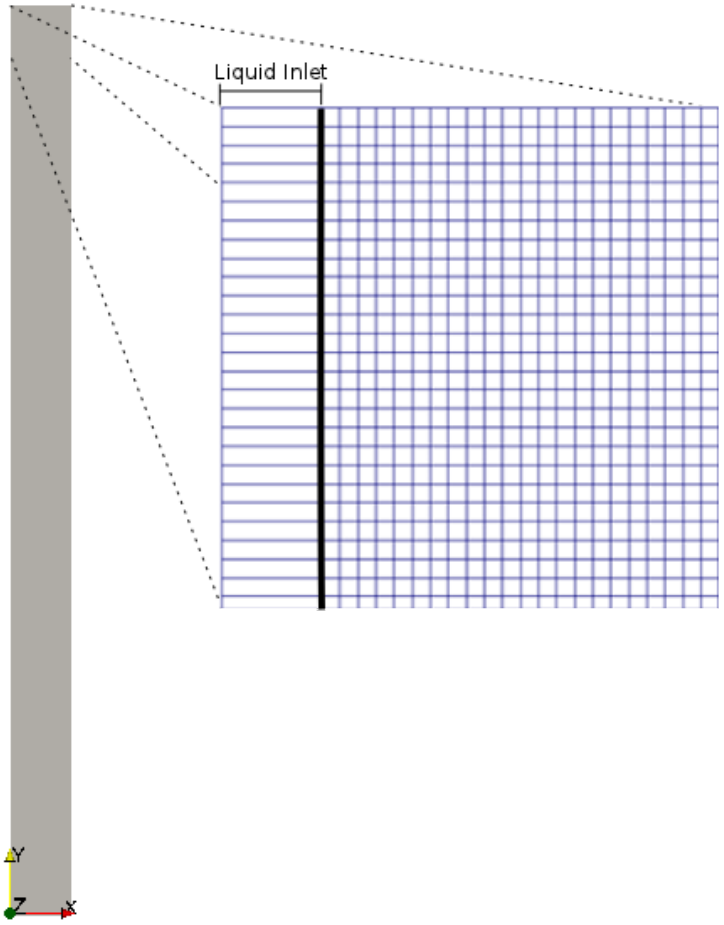

FIGURE 7.6: Mesh of the 2-D domain (Surface Film)

Therefore, for the VOF case, the simulation was initially run without mass transfer to set-up the velocity field within the domain. The velocity at the liquid inlet was mapped from a position further down the domain in a region where the velocity profile was fully developed. The mapping procedure ensured that the liquid mass flow rates between the cases were the same. Mass transfer was then included in the VOF model using the converged, fully-developed velocity field. The initial conditions for the ESF case were that the depth-averaged domain was initial devoid of fluid with $h = 0$ and zero velocity everywhere. In the gas-phase domain the velocity was initially zero everywhere.

For both cases, the average velocity at the liquid inlet in the direction of the flow was set to $U_L = -0.5232$ ms^{-1}, according to equations 7.19 & 7.20. Again for both cases, the outlet and gas inlet were set to fixed pressure boundaries and the right boundary was set to a free-slip atmospheric boundary condition. The left wall was set to a no-slip boundary. For the ESF case the velocity in the gas domain at the boundary between the depth-averaged domain was mapped from the liquid interface velocity calculated in the depth-average domain. The concentration of CO_2 at the gas inlet was set to, $C_G = 1$ mol m^{-3} and Henry's constant was set to an arbitrary value, He $= 0.5$.

TABLE 7.1: Phase Properties

Phase	μ [Pa · s]	ρ [Kg · m^{-3}]	D_{CO_2} [m^{2}s^{-1}]
Liquid	1.0×10^{-3}	1000	2.0×10^{-7}
Gas	1.48×10^{-5}	1.0	2.0×10^{-3}

The dynamic viscosity and density of the constituent phases are given in Table 7.1, along with the species diffusion coefficients used within the liquid and gas phases. The diffusion coefficients were set to 100 times the actual values for CO_2 to ensure that the simulation was able to accurately capture the concentration gradients near to the interface. This effectively increases the width of the concentration boundary layer, reducing the number of cells required. The surface tension was set to $\sigma = 0.0728$ N · m^{-1} and a static contact angle of $\theta_w = 70^o$ was selected.

The simulations were run until a pseudo-steady state was reached, to ensure convergence. The three timescales present in these cases are the viscous time-scale, $\tau_v = \frac{L^2}{\nu}$, the diffusion time-scale, $\tau_d = \frac{L^2}{D}$ and the advection time-scale, $\tau_a = \frac{L}{U}$, where L is the characteristic length scale or the cell size, D is the diffusion coefficient, ν is the kinematic viscosity and U is the characteristic velocity of the simulation. The VOF simulation used an adaptive timestep to keep the courant number below 0.2, resulting in a timestep of approximately 9.5×10^{-7}s. The smallest advection time was 4×10^{-6}s, the smallest diffusion time was 6×10^{-9}s and the smallest viscous time was 8.28×10^{-7}s. These timescales are based on the smallest cell within the grid because the grid was highly refined close to the inlet. The average diffusion time across the domain was 2.8×10^{-6}s, whilst the average viscous time was 3.8×10^{-4}s. It is noted that the small cells, within the highly refined region near to the inlet, result in very small diffusion times. The selected timestep is much larger than the diffusion time in these cells. A much smaller timestep would be required to accurately capture the time-dependence of the diffusion process. However, since the simulations were run until steady state, the choice of timestep larger than the diffusion time would have negligible effect on the final steady-state solution. Compromises had to be made due to computational limitations, and, for the numerical stability of the solution, the timestep was only required to be smaller than the advection time.

The ESF simulations used an adaptive timestep to keep the courant number below 0.2, resulting in a timestep of approximately 2×10^{-5}s. The smallest advection time was 9.4×10^{-5}s, the smallest diffusion time was 2.8×10^{-6}s and the smallest viscous time was 3.8×10^{-4}s.

If the characteristic length is taken as the hydraulic diameter of the representative wetted wall column, rather than the cell size, then the advection time was approximately 0.005s, the smallest diffusion time was approximately 0.008s and the smallest viscous time was approximately 1.08s.

7.3.2.3 Results & Discussion

Initially, for the VOF simulations, the velocity field was set-up within the domain, without mass transfer. The resulting velocity profile was compared against the predictions of the Nusselt Theory [62]. According to Nusselt, gravity-driven film flow will develop a parabolic velocity profile given by:

$$U(x) = U_{L,\text{eff}} \frac{x(2e - x)}{e^2}, \tag{7.19}$$

where the interface lies at $x = e$ and the interfacial velocity, $U_{L,\text{eff}}$ is given by:

$$U_{L,\text{eff}} = \frac{3U_L}{2} = \frac{\rho_L g e^2}{2\mu_L}. \tag{7.20}$$

The average velocity in the liquid film is denoted by U_L.

Figure 7.7 shows a comparison between the simulated velocity profile and the profile prediction by Nusselt theory. It can be seen that the results are in good agreement with the theoretical prediction.

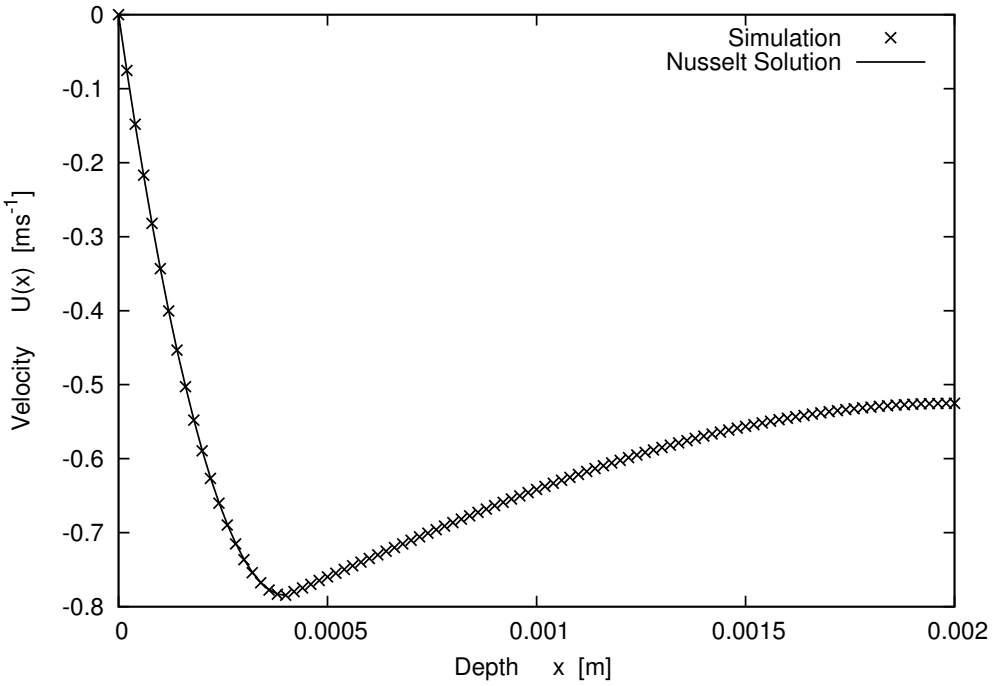

FIGURE 7.7: Comparison of velocity profile with Nusselt profile

Species transport was then included, where the concentration of CO_2 is denoted as C. The CO_2 was introduced at the gas inlet with a concentration of $C_G = 1$ mol m^{-3} and the concentration at the liquid inlet was kept at $C_L = 0$ mol m^{-3}.

According to Haroun *et al.* [97], the liquid-side local mass transfer coefficient can be calculated numerically within the CFD code by solving the following equation:

$$k_{L,\text{local}}^{\text{CFD}} = -\frac{(D\nabla C + \Phi) \cdot n_L}{\Delta C_{L,\text{local}}}, \tag{7.21}$$

where n_L is the normal to the interface pointing into the liquid, $\Delta C_{L,\text{local}}$ is the local concentration difference between the interface concentration and a reference concentration in the liquid phase close to the wall and Φ is the solubility flux defined in Equation 3.13.

The calculated mass transfer coefficient can then be compared with Higbie Penetration Theory (see Equation 2.9). The exposure time in this equation is determined from the CFD data,

$$t_{H,SV} = \frac{y_{inlet}}{|U_s|}, \tag{7.22}$$

where y_{inlet} is the distance from the liquid inlet and $|U_s|$ is the velocity at the gas-liquid interface. Therefore, the local mass transfer coefficient in the liquid phase, as determined by the Higbie Penetration Theory, is given by:

$$k_{L,\text{local}}^{Higbie} = \sqrt{\frac{D_{C,L}}{\pi t_H}} = \sqrt{\frac{D_{C,L}|U_s|}{\pi y_{inlet}}}. \tag{7.23}$$

The liquid-side mass transfers coefficient at the interface is plotted against the vertical y-axis (see Figure 7.8). Comparison is made with the theoretical value for the liquid-side mass transfer coefficient derived from the Higbie Penetration Theory. Figure 7.9 shows the mass transfer coefficient close to the inlet, where gradients are very large. It is observed that the numerical results are in good correlation with Higbie Penetration Theory.

Comparisons between the VOF and ESF approach can be made in terms of the concentration profiles within the domain. Figure 7.10 shows the concentration contours within the domains. It is noted that qualitatively the results are in good agreement. A vertical slice was then taken through the centre of the domain and the concentration along this slice is plotted in Figure 7.11. Again, good agreement is observed between the two approaches, providing further validation for the ESF approach.

The Residence time equation for the VOF model is simply a transport equation for the Residence time, τ with the appropriate boundary conditions, as described in section 7.2.1.1. By plotting this variable on the contour of volume fraction, $\alpha = 0.5$ it is possible to determine the exposure time, $t_{H,RT}$ that is used in the Higbie Penetration model of mass transfer.

The Residence time equation for the surface film model is slightly more complex due to the depth averaged nature of the liquid domain (Equation 7.9 and 7.11). In order to validate the exposure time, $t_{H,RT}$ determined using this approach, comparisons were

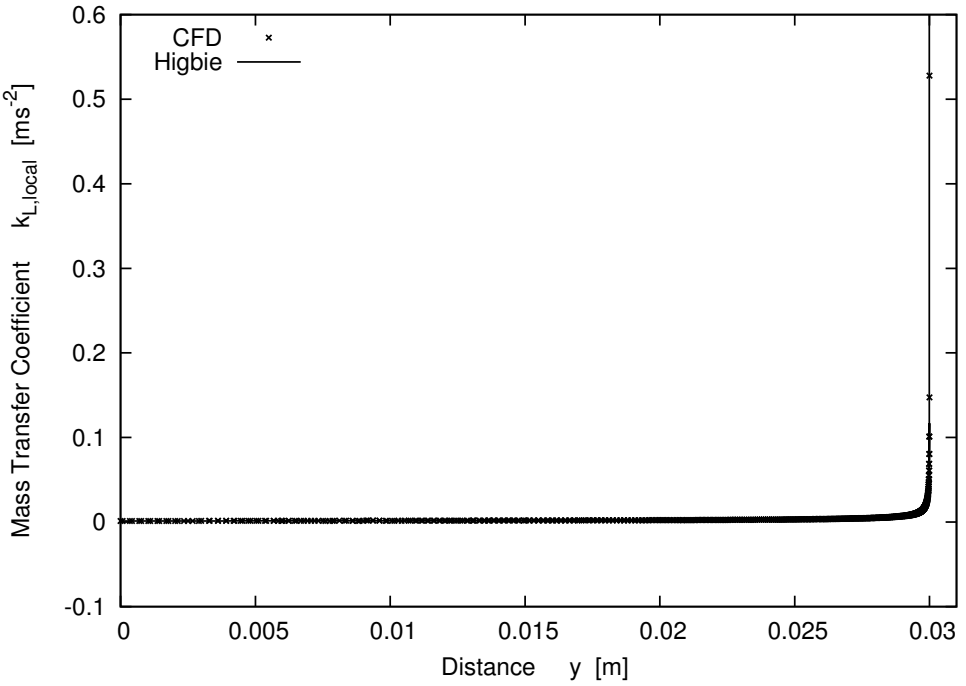

FIGURE 7.8: Comparison $k_{L,\text{local}}$ against the Higbie Penetration Theory

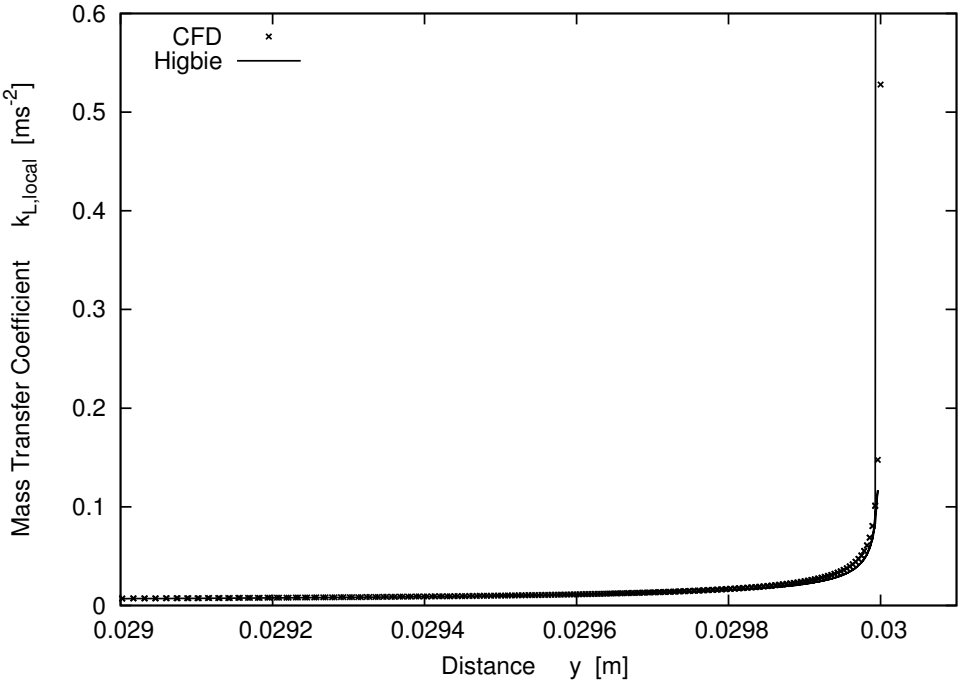

FIGURE 7.9: Comparison $k_{L,\text{local}}$ against the Higbie Penetration Theory (Close to inlet)

made against the exposure time determined by the VOF model and with the usual approach of Equation 7.7, denoted as $t_{H,SV}$, were the subscript, $_{SV}$ indicates that the exposure time was calculated from the surface velocity. Figure 7.12 plots these three approaches against the vertical y-axis, where the liquid inlet is at $y = 0.03m$ and the outlet is at $y = 0m$.

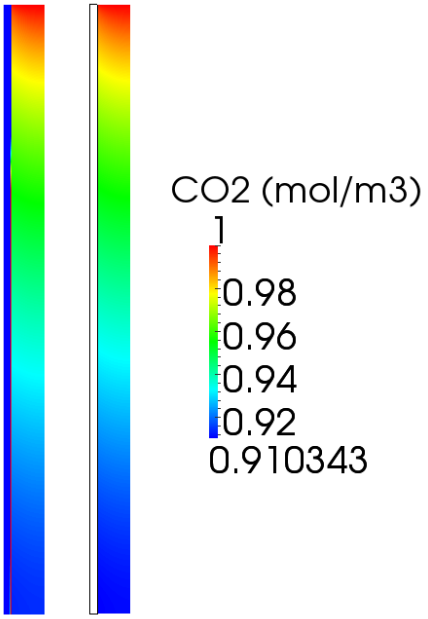

FIGURE 7.10: Concentration contours. (Left: VOF, right:ESF)

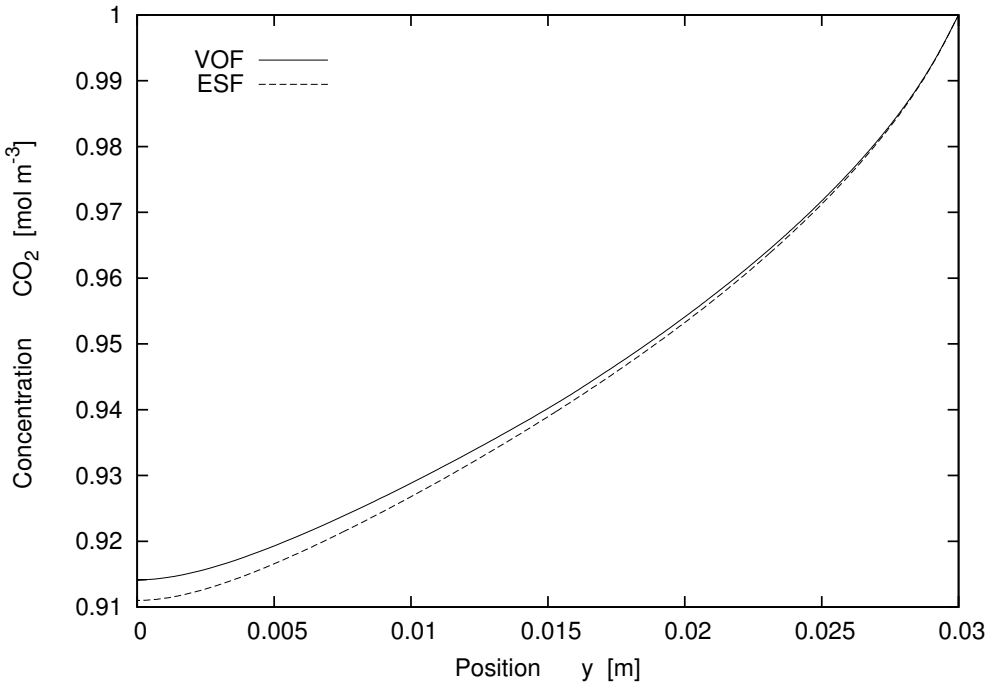

FIGURE 7.11: Plot of concentration profile along the central vertical slice.

It can be seen that the surface age predictions are all in agreement. This is positive validation, however, comparison still needs to be made on more complex flows. Comparison of the surface age predictions on a 3D partially wetted plate will be performed in the following section.

The simulations performed so far highlight a significant problem with the use of standard approaches to modelling acid-gas absorption into thin liquid films. VOF integrated with

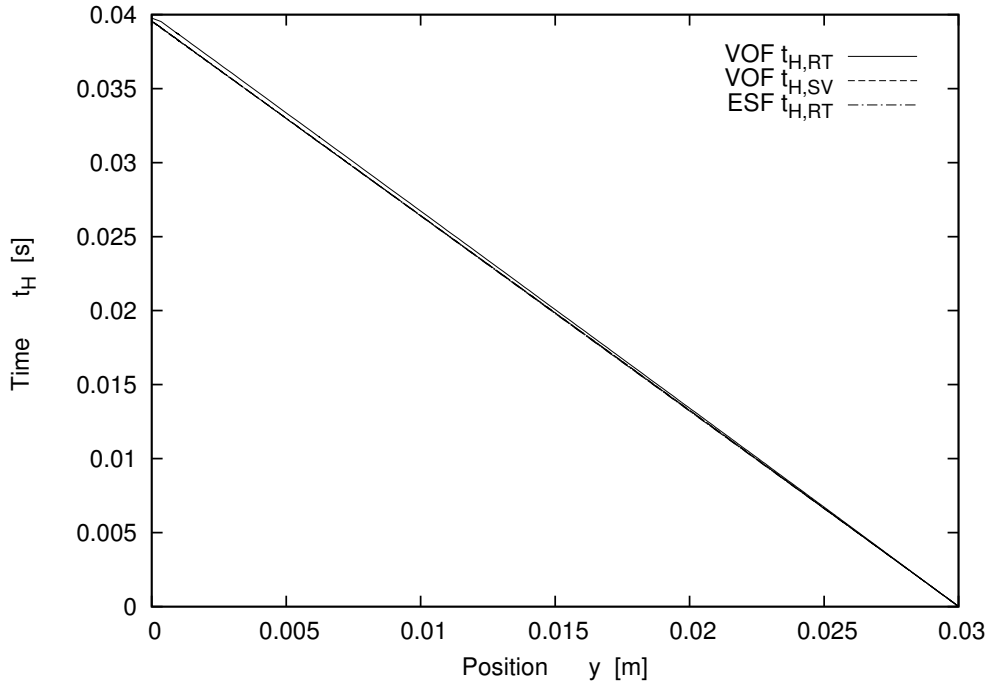

FIGURE 7.12: Comparison of exposure time plotted against distance from liquid inlet

mass transfer will work well for certain situations, but may not be applicable to areas of interest in carbon capture.

The small size of the 2D domain tested, using VOF, allowed many grid points to be used to ensure that the concentration gradient close to the interface was accurately resolved. Figure 7.14 plots the concentration at various horizontal slices along the column (0.0001m, 0.0004m, 0.0016m, 0.0064m and 0.0256m from the liquid inlet - see Fig. 7.13). It can be seen that the concentration gradient on the liquid-side of the interface is very thin, due to the small diffusion coefficient in the liquid. It is noted that the film is located in the region from $x = 0m$ to approximately $x = 0.0004m$, whilst the x-axis in Fig. 7.14 starts at $x = 0.0003m$. In order to accurately resolve this gradient the grid was composed of 88070 cells. This implies that for fully 3D simulations the number of cells required to resolve the concentration field would be prohibitively large. This is all with a diffusion coefficient in the liquid of $2.0 \times 10^{-7}\,\mathrm{m^2 s^{-1}}$, 100 times larger than the actual diffusion coefficient of CO_2 in aqueous MEA. For cases with the correct diffusion coefficient a larger number of cells would be required to accurately capture the smaller concentration boundary layer that exists on the liquid-side of the interface.

The ESF model does not have this restriction because it does not explicitly model the concentration within the liquid film. It only requires enough cells to accurately resolve the concentration gradients within the gaseous domain where the diffusion coefficients are much larger, hence requiring less cells. Therefore, the ESF model not only speeds-up purely hydrodynamic simulations, but this improvement will be further enhanced when mass transfer is included.

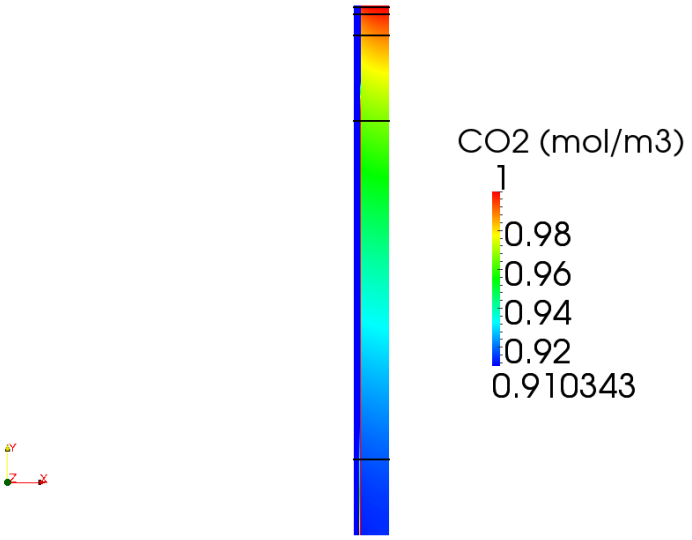

FIGURE 7.13: Slice locations in VOF domain

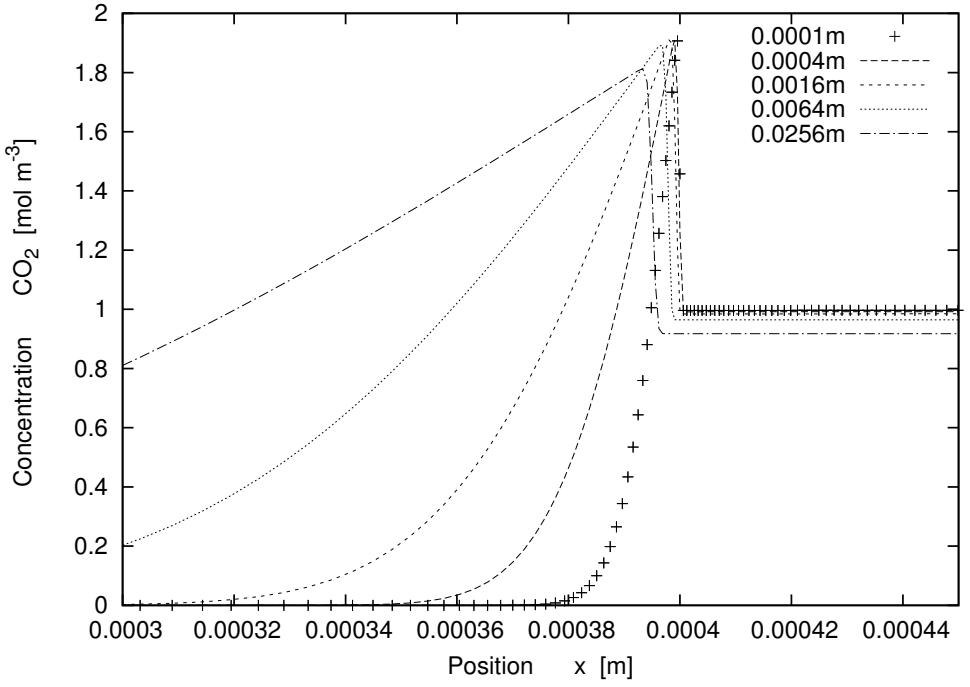

FIGURE 7.14: Plot of concentration gradient at various locations

7.3.3 3-Dimensional Mass Transfer

The ESF mass transfer model has been validated in two-dimensions by comparison against direct numerical simulation VOF techniques. However, it is concluded that it is not viable to complete 3D simulations of mass transfer with the VOF approach because too many cells would be required to capture the thin concentration layer close to the interface (see Appendix C). A mesh fine enough to simulate the partially wetted plate,

whilst capturing this thin boundary layer would be too computationally expensive, even with a liquid diffusion coefficient 100 times larger than that of CO_2.

The mass transfer model used in the ESF solver is based on Higbie Penetration Theory, a well-established theory in mass transfer. A large proportion of the literature researching absorption of gases into liquid films will validate against Higbie Penetration Theory. Therefore, it is reasonable to assume that validation of the exposure time, $t_{H,RT}$ predicted by the residence-time equation, is sufficient, considering that this variable is the main factor influencing mass transfer coefficients and rates of mass transfer between phases.

The residence-time equation for the ESF model has been validated in 2-dimensions and will now be validated in 3-dimensions. It is possible to compare the exposure time between the ESF approach and the VOF approach because less refinement is required to accurately predict its value in comparison to concentration.

7.3.3.1 Computational Domain & Simulation Set-up

Simulations were performed on the domain from Chapter 6, selecting a liquid flow rate to ensure a partially wetted plate. The initial conditions and boundary conditions were the same. The residence time was initially set to zero everywhere and fixed to zero at the inlets with a zero gradient condition at all other boundaries. An AMR-VOF simulation was performed to calculate the surface-age to provide a comparison with the ESF model. AMR-VOF was selected because it is more accurate than the standard VOF approach. The AMR-VOF mesh consisted of an initial coarse grid of 192,000 cells, with 2 levels of adaptive refinement around the gas-liquid interface, in the region $0.2 < \alpha < 0.8$ The surface film mesh consisted of 270000 cells is the gaseous domain and is shown in Fig. 6.3.

The simulations were performed at $Re_l = 156.85$ at an inclination angle of $\theta = 60^o$. The simulations were laminar, time-dependent runs, stepping to a steady state solution. All computations were run using a variable time-step to keep the Courant number below 1.0. Steady state convergence was assured by monitoring the specific wetted area of the plates as a function of time. The two timescales present in these simulations were the viscous time-scale, $\tau_v = \frac{L^2}{\nu}$ and the advection time-scale, $\tau_a = \frac{L}{U}$, where L is the characteristic length scale or the cell size, ν is the kinematic viscosity and U is the characteristic velocity of the simulation. In these simulations the smallest viscous timescale was approximately 9.7 times larger than the advection time scale for the AMR-VOF case, based on the smallest cell size after maximum refinement of the grid and approximately 21.6 times larger for the ESF case. This confirms the choice of time-step based on the courant number, $C_r = \frac{U\tau_a}{L}$.

TABLE 7.2: Phase Properties

Phase	μ [Pa · s]	ρ [Kg · m^{-3}]
Liquid	8.899×10^{-4}	997
Gas	1.831×10^{-5}	1.185

The dynamic viscosity and density of the constituent phases are given in Table 7.2. The surface tension was set to $\sigma = 0.0728$ N · m^{-1} and a static contact angle of $\theta_w = 70^o$ was selected [50].

7.3.3.2 Results & Conclusions

Comparisons are made between the exposure time, $t_{H,RT}$ predictions of both modelling approaches, derived from the residence time equation. These results are compared with the exposure time, $t_{H,SV}$ calculated using the film surface velocity and distance from the inlet. Contour plots are used to give an overall view of the exposure time and slices through these contours are taken at the stagnation position, oblique position and central position. These allow more detailed comparisons to be made.

Figure 7.15 shows a comparison of the exposure time, $t_{H,RT}$ plotted on the liquid interface contour, for the VOF model and ESF model, calculated by solving the residence time transport equations. The two approaches result in a very similar distribution of exposure time across the film, especially in regions near the stagnation position.

The exposure time calculated during the AMR-VOF is shifted in time, due to the fact that at the liquid inlet the velocity was set to constant value, rather than a velocity profile. This initial constant velocity transitions to the Nusselt profile shortly after entering the domain. This modelling approximation is required because it is difficult to apply a Nusselt velocity profile at the inlet, especially during AMR simulations where cell numbers and locations are adapted in response to the liquid interface. This means that the interfacial velocity is initially lower than it should be prior to the Nusselt velocity profile being established. This approximation has little effect on the overall shape of the film and the wetted area. However, it does affect the evolution of the exposure time, in the observed way.

This effect can also be observed in Figures 7.16-7.18, which plot the exposure time along slices at the central position, oblique position and the stagnation position. The exposure time, $t_{H,RT}$ is calculated using the VOF and ESF residence time equations, along with the exposure time, $t_{H,SV}$ calculated using the film surface velocity and distance from the inlet.

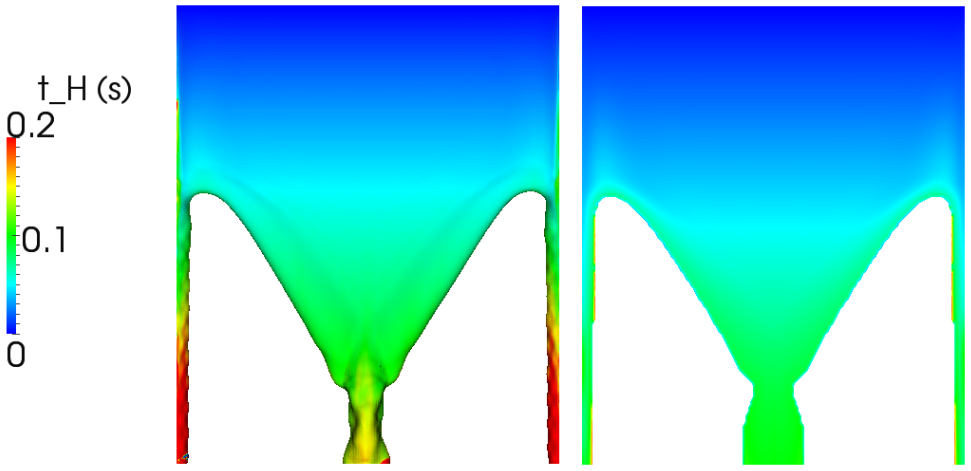

FIGURE 7.15: Plot of exposure time at interface contour - Partially Wetted Plate. Left: VOF $t_{H,RT}$, right: ESF $t_{H,RT}$

It is observed that for the ESF simulations $t_{H,RT}$ is more accurate than $t_{H,SV}$. This is especially significant in Figure 7.18, where the ESF $t_{H,SV}$ significantly over-predicts the exposure time close to the gas-liquid-solid contact line.

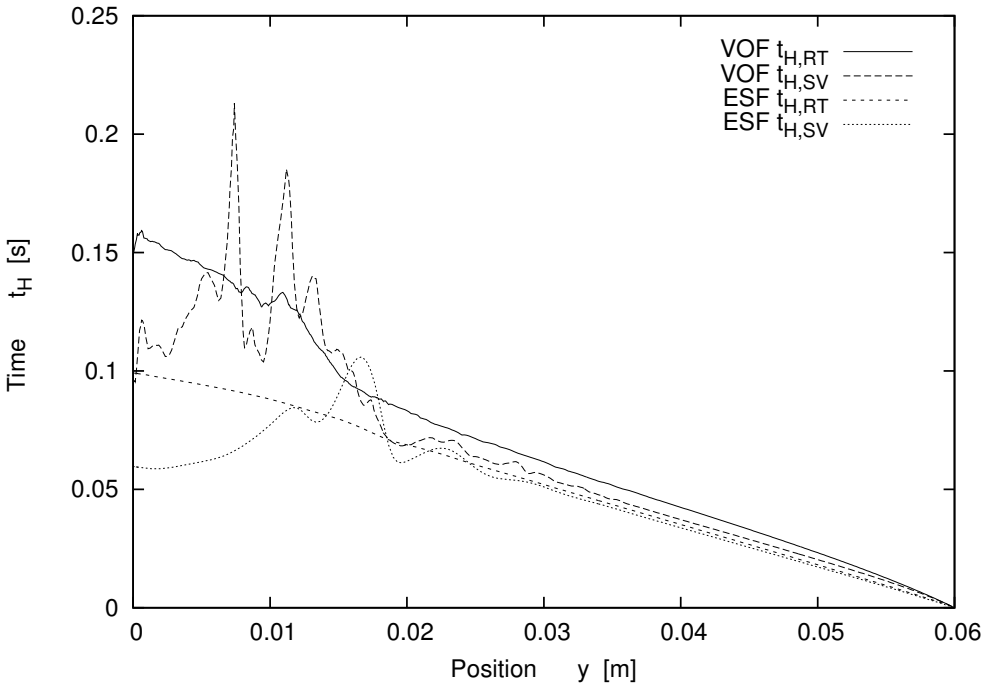

FIGURE 7.16: Plot of exposure time at central slice - Partially Wetted Plate

It is observed from all of the results that when using the ESF model it is more accurate to solve a residence time transport equation to determine the exposure time, rather than relying on a direct calculation of the exposure time from the interfacial velocity and distance from the inlet. This is particularly the case in regions where the film deviates from the Nusselt solution. One of the assumptions made to calculate the exposure time,

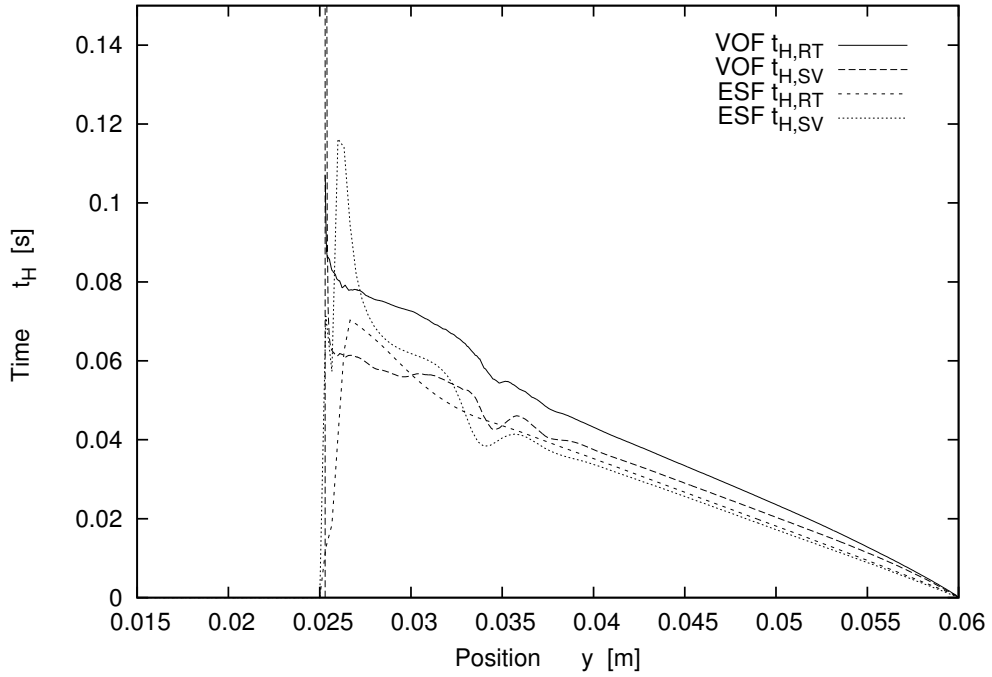

FIGURE 7.17: Plot of exposure time at oblique slice - Partially Wetted Plate

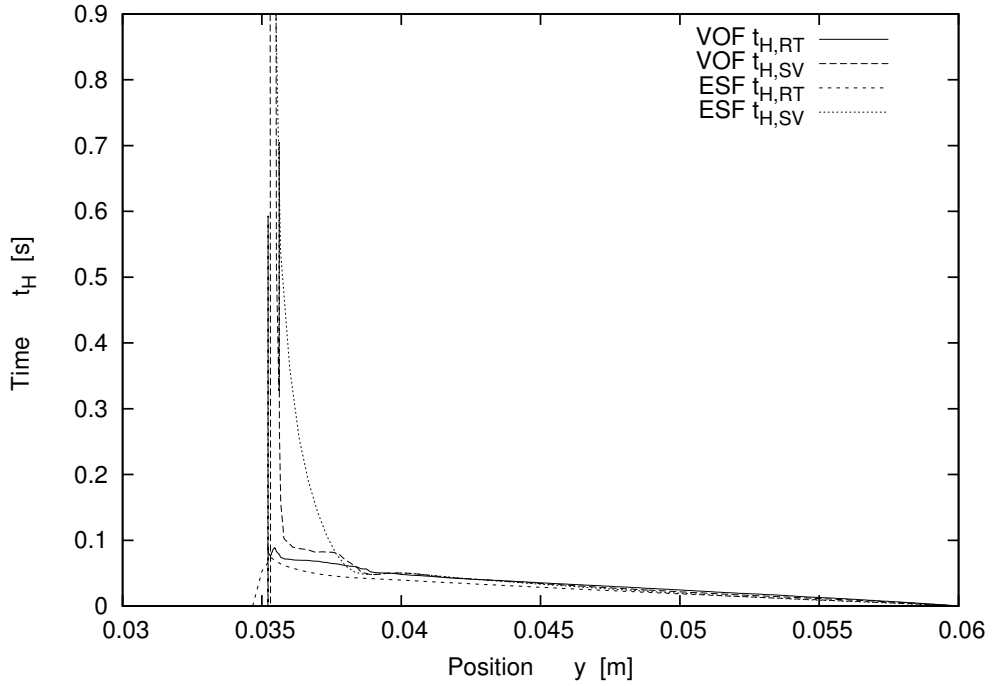

FIGURE 7.18: Plot of exposure time at stagnation slice - Partially Wetted Plate

$t_{H,RT}$ from the depth-average residence time equation is that the velocity profile within the liquid film is a Nusselt profile. However, this is not always the case and the interfacial velocity can be under- or over-predicted in certain regions of the flow. This has little effect on the total wetted/interfacial area because the surface velocity is not integral to

the solution. However, if this is used to calculate mass transfer then this will introduce errors into the solution for species transport.

7.4 Chemically Enhanced Mass Transfer in a Wetted-Wall Column

Puxty *et al.* [4] performed a comparison of CO_2 absorption into aqueous ammonia solutions and aqueous MEA solutions. The analysis was performed on a wetted wall column, which provides good validation of both, the mass transfer model and the reaction kinetics used in the enhanced surface film model.

7.4.1 Computational Domain

The computational domain consisted of wetted-wall column with a counter-current flow set-up, meaning that the solvent and gas flow in opposite directions. The apparatus consisted of an internal stainless steel column with an effective height of 8.21cm and diameter of 1.27cm in a vertical orientation [4]. The solvent solution was pumped through the centre of this column, over-flowing at the top to form a thin film along the sides of the column. The internal column was surrounded by a jacketed glass column, with an internal diameter of 2.54cm. This allowed the apparatus to remain at a constant fixed temperature. A diagram of the apparatus is shown in Fig 7.19.

The depth of liquid film flowing down the sides of the column was much smaller than the diameter of the internal column. This means that the assumption of 2D flow can be made, rather than solving on an axisymmetric mesh. Therefore, the problem was simplified to a rectangular 2D domain of width 0.635cm and height 8.21cm. This defined the gaseous region, which was subsequently extruded by one cell in the negative x-direction to form the separate depth-averaged fluid domain (see Fig. 7.20).

This grid consisted of 52544 structured, non-uniform hexahedral cells in the gaseous region, and 821 cells in the fluid region. Due to the small size of the domain, a fairly large number of cells could be chosen to ensure that the concentration gradients in the gaseous domain were captured accurately.

7.4.2 Simulation Set-up

To accurately replicate the results of Puxty *et al.'s* [4] experimental data, it was ensured that all parameters of the problem closely resembled their set-up. In particular, it was important to simulate counter-current flow. This can easily be performed with the surface film model, due to the fact that two separate domains are used. Whereas, with a

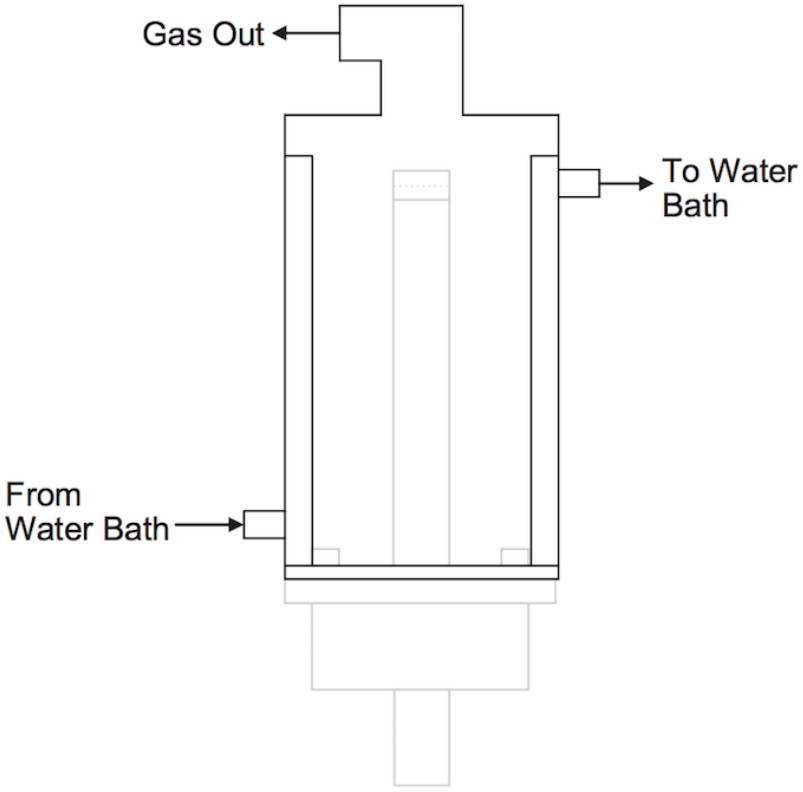

FIGURE 7.19: Wetted-Wall Column Apparatus (Puxty *et al.* [4])

VOF type simulation it would be much more complicated. This is due to the fact that at the bottom boundary of the domain, the gas and liquid would flow in opposite directions. It is effectively an inlet for the gas phase, but an outlet for the liquid phase. This presents problems for the specification of the boundary condition where a combination of inlet and outlet conditions must be applied.

The aqueous MEA solution was at a concentration of $5\,\mathrm{mol\,L^{-1}}$ (30% wt/wt), and flowed through the system at a flow rate of $220\,\mathrm{mL\,min^{-1}}$. As stated by Puxty *et al.* [4], this flow rate ensured the formation of a continuous, smooth flowing liquid film within the apparatus. A loading of 0 moles of CO_2 per mole of amine was selected.

The gaseous phase consisted of a binary mixture of N2 and CO_2 with inlet CO_2 concentrations of 1.25, 2.5, 4, 5 and 6 $\mathrm{mol\,m^{-3}}$. The gas flow rate through the apparatus was set at 5 $\mathrm{L\,min^{-1}}$.

The initial conditions were zero velocity everywhere and the depth-averaged domain was initially devoid of liquid with $h = 0$. All walls were set to no-slip boundaries with fixed pressure conditions at the outlets. The residence time was initially zero everywhere, fixed to zero at the inlets and zero gradient at all other boundaries. In the gaseous domain the concentration was set to fixed value boundaries at the inlet. The velocity boundary

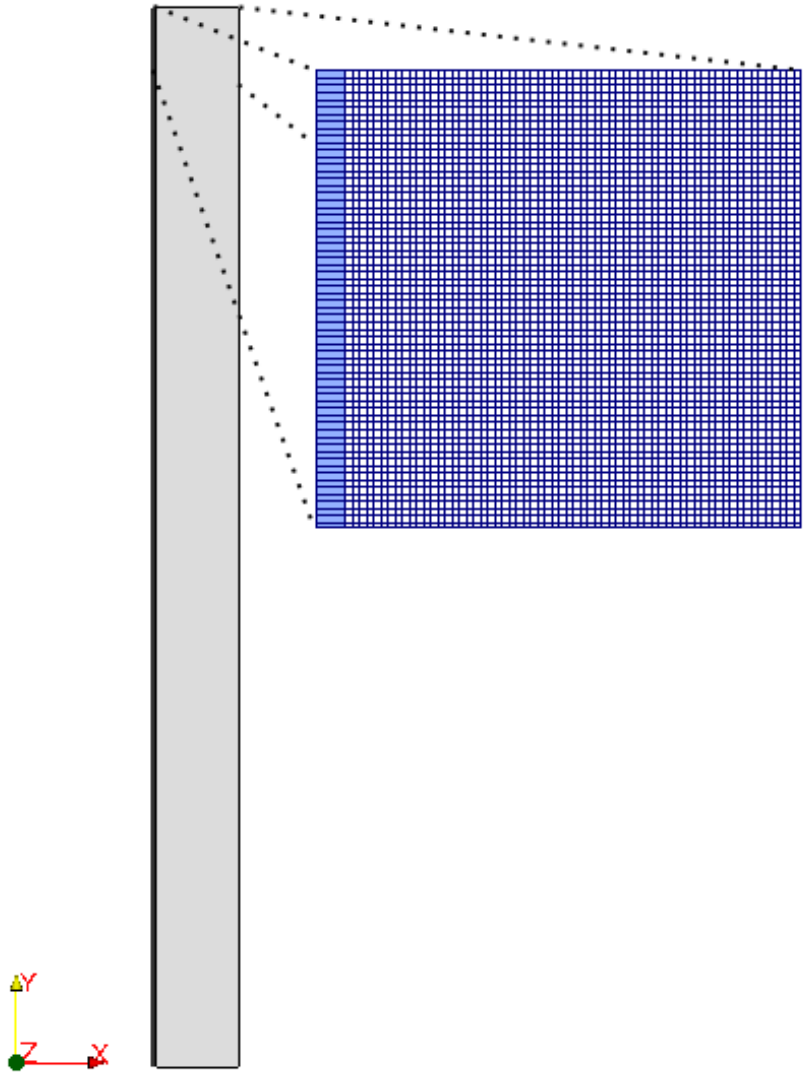

FIGURE 7.20: Wetted wall column domain adapted from Puxty *et al.* [4]

TABLE 7.3: Phase Properties

Phase	μ [Pa · s]	ρ [Kg · m^{-3}]
Liquid	1.600263×10^{-3}	1003.3
Gas	1.830825×10^{-5}	1.185

condition in the gas-phase domain at the boundary with the depth-averaged domain was mapped from the film interfacial velocity calculated within the depth-averaged domain.

The dynamic viscosity and density of the constituent phases are given in Table 7.3. The surface tension was set to $\sigma = 0.0728$ N · m^{-1} and a static contact angle of $\theta_w = 70^o$ was selected [50]. The simulations were run until a steady state was reached.

The computations were run at two different temperatures, 313K and 333K, due to the fact that temperatures within CCS absorber columns usually range between 313K an

333K [124]. Henry's constant was set to,

$$He = \left(\frac{1}{RT}\right) 2.82 \times 10^6 e^{-2044/T}, \tag{7.24}$$

to take account of the temperature dependence of He, where R is the universal gas constant. The diffusivity of CO_2 in the liquid phase was calculated using the expression of Versteeg & Dijck [74], given by:

$$D_{CO_2,L} = 2.35 \times 10^{-6} e^{-2199/T} \ \ \mathrm{m^2 s^{-1}}. \tag{7.25}$$

The diffusion coefficient of CO_2 in the gas phase was set to $D_{CO_2,g} = 1.785 \times 10^{-5}$ $\mathrm{m^2 s^{-1}}$ at 313K and $D_{CO_2,g} = 1.997 \times 10^{-5}$ $\mathrm{m^2 s^{-1}}$ at 333K [125]. The reaction rates were calculated using the equation of Versteeg & Dijck [74], to ensure that the temperature dependence of the reaction rate was taken account of, given by,

$$k = 4.4 \times 10^{11} \, e^{-5400/T} \, \mathrm{L \, mol^{-1} s^{-1}}. \tag{7.26}$$

The computations were run until steady state with an initial time step of 2×10^{-4}s with an adaptive time-step to keep the Courant number below 1.0. The four timescales present in these simulations were the viscous time-scale, $\tau_v = \frac{L^2}{\nu}$, the diffusion time-scale, $\tau_d = \frac{L^2}{D}$, the advection time-scale, $\tau_a = \frac{L}{U}$ and the reaction timescale, $\tau_r = \frac{1}{Ck}$ where L is the characteristic length scale or the cell size, D is the diffusion coefficient, ν is the kinematic viscosity, U is the characteristic velocity of the simulation, C is the concentration of CO_2 and k is the reaction rate constant. The smallest diffusion time was approximately 5×10^{-4}s, whilst the smallest viscous time scale was 6×10^{-4}s. The smallest reaction time scale for the simulations performed was 0.00418s, whilst the smallest advection time scale was approximately 2.5×10^{-4}s. This confirms the choice of time-step based on the courant number, $C_r = \frac{U\tau_a}{L}$.

If the characteristic length is taken as the hydraulic diameter of the wetted wall column, rather than the cell size, then the advection time was approximately 0.038s, the smallest diffusion time was approximately 8.08s and the smallest viscous time was approximately 10.44s.

7.4.3 Results & Discussion

According to Puxty *et al.* [4], the overall mass transfer coefficient, K_G during absorption processes is a combination of the liquid-side and gas-side mass transfer coefficients, as well as the enhancement due to chemical reaction. The absorption flux is given by,

$$N_{CO_2} = K_G(P_{CO_2} - P^*_{CO_2}), \tag{7.27}$$

where P_{CO_2} is the partial pressure of CO_2 in the bulk of the gas and $P^*_{CO_2}$ is the equilibrium CO_2 partial pressure.

Puxty *et al.* [4] state that at constant CO_2 loading, the equilibrium partial pressure is a constant. Therefore, by measuring the CO_2 absorption flux, N_{CO_2} and the corresponding applied partial pressure, P_{CO_2}, for various partial pressures, the overall mass transfer coefficient can be determined by a linear regression. The applied partial pressure is calculated as the log mean of the inlet and outlet CO_2 partial pressures, given by

$$P_{CO_2} = \frac{(P^{in}_{CO_2,bulk} - P^{*,in}_{CO_2}) - (P^{out}_{CO_2,bulk} - P^{*,out}_{CO_2})}{Ln((P^{in}_{CO_2,bulk} - P^{*,in}_{CO_2})/(P^{out}_{CO_2,bulk} - P^{*,out}_{CO_2}))}. \tag{7.28}$$

Following this methodology, Puxty *et al.* [4] performed linear regressions of the data according to the formula,

$$N_{CO_2} = K_G \,.\, P_{CO_2} \;\; + d. \tag{7.29}$$

resulting in the determination of the values of K_G and d for a range of conditions. This data was used in order to compare the results of the ESF model which included mass transfer and reaction kinetics.

Figures 7.21 and 7.22 plot the CO_2 absorption flux against applied CO_2 partial pressure at 313K and 333K, respectively. The CFD results of the ESF model are compared against the expression in equation 7.29 and the coefficients derived from regression of experimental data. First and second order reaction kinetics were performed to test the assumption that first order reaction kinetics is appropriate.

It is observed that the CFD results are in good agreement with the experimentally derived correlation and that the value of K_G is independent of the applied partial pressure, as expected. From the results it can be concluded that 1st order reaction kinetics are valid for this simulation, due to the low concentration of CO_2 in the gas stream and the fast reaction rates involved.

Table 7.4 compares the average K_G data derived from this work and the average K_G derived from the work of Puxty *et al.* [4] and Aboudheir *et al.* [89]. This further confirms the validity of the models used in the ESF approach. The values obtained from the experimental data of Aboudheir *et al.* [89] were performed at much higher applied partial pressures, which could explain why the results for K_G are slightly higher. This was probably due to the heat of reaction at the liquid film caused by the use of higher applied partial pressures [4].

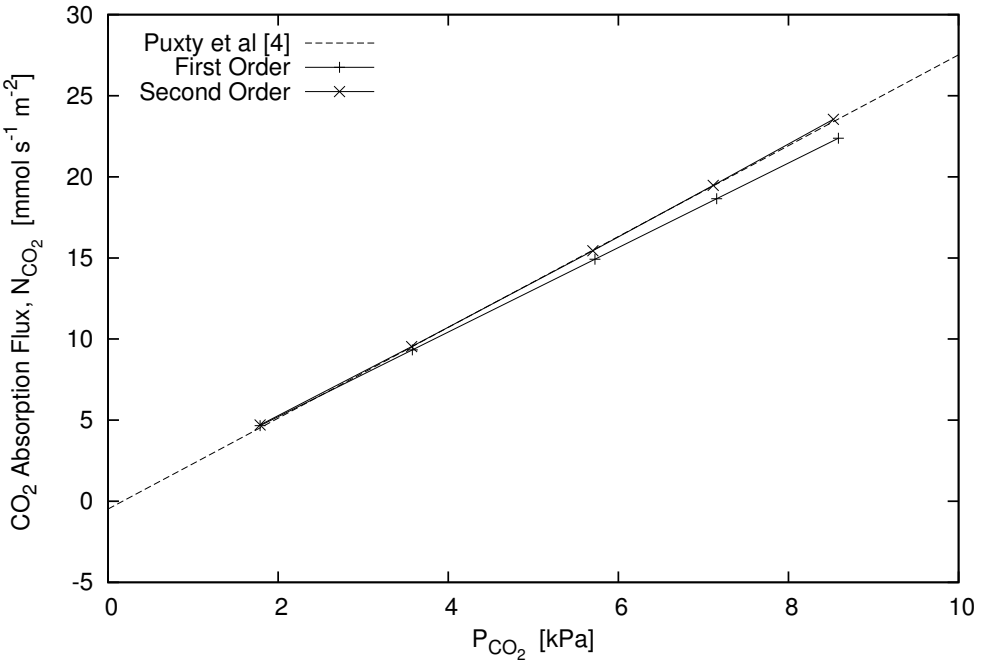

FIGURE 7.21: CO_2 absorption flux as a function of applied partial pressure (313K)

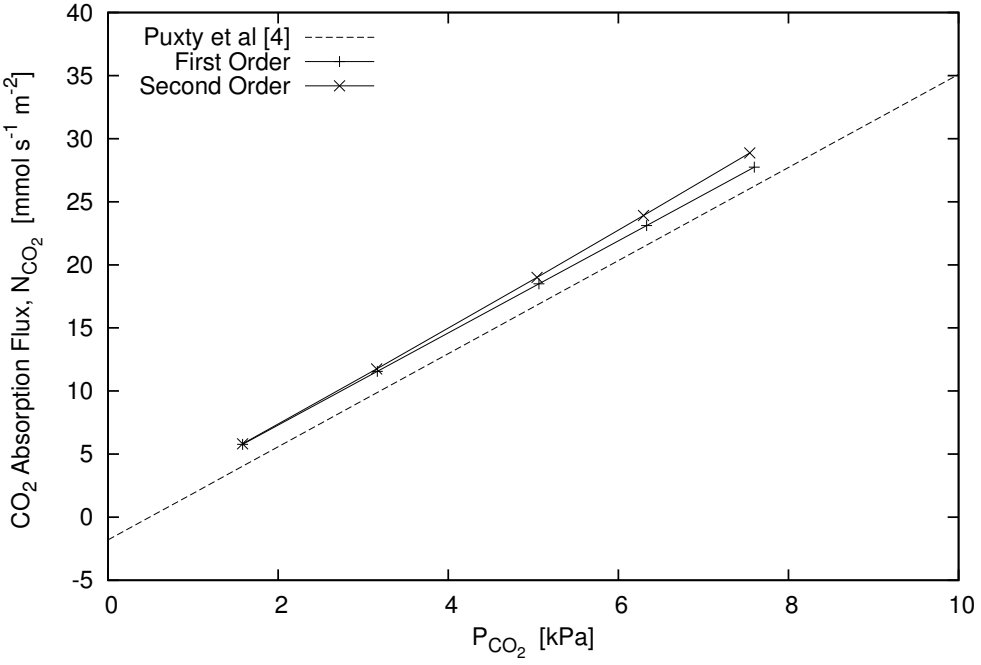

FIGURE 7.22: CO_2 absorption flux as a function of applied partial pressure (333K)

TABLE 7.4: Average K_G Data Comparison

Source	K_G [ms^{-1}] (313K)	K_G [ms^{-1}] (333K)
This Work (1st Order)	0.01072	0.02222
This Work (2nd Order)	0.01150	0.02353
Puxty et al [4]	0.01152	0.02247
Aboudheir et al [89]	0.01341	0.02464

7.5 Chemically Enhanced Absorption of CO_2 on a Partially Wetted Plate

In the previous chapters, the implementation of the enhanced surface film model has been validated against experimental data. The inclusion of mass transfer has been validated by comparison with theoretical solutions and refined ARM-VOF simulations. The inclusion of reaction kinetics into the model has been validated against the experimental data of a wetted wall column, and the residence-time equation approach has been validated against the AMR-VOF residence-time equation.

To conclude this thesis, all the elements will be combined to perform a 3D simulation of CO_2 absorption into a partially wetted film of aqueous MEA. This is a major advancement in the field and is an approach which promises much greater scalability, due to the speed of simulations, especially in comparison to alternative methods such as VOF, where large scale simulations are simply not possible with current computing capacities.

7.5.1 Computational Domain

The physical situation being modelled was gravity driven flow down an inclined plane. Therefore, the domain was the same that was used in Chapter 6. In summary, this consisted of a stainless steel plate of dimensions 0.05m in width and 0.06m in length. The plate was inclined at 60 degrees to the horizontal plane. The gaseous side of the domain consisted of 270000 cells and the liquid domain consisted of 27000 cells.

7.5.2 Simulation Set-up

The simulation performed was of CO_2 absorption into a falling liquid film of $5\,\mathrm{mol\,L}^{-1}$ aqueous MEA solution at 313K. The resulting properties of the gas and liquid phases are shown in Table 7.3. The diffusion coefficient of CO_2 in the liquid phase was given by equation 7.25, with the diffusion coefficient in the gas phase given by, $D_{CO_2,g} = 1.785 \times 10^{-5}\,\mathrm{m^2 s^{-1}}$ [125]. Henry's constant was specified by equation 7.24. The simulations were repeated with a gas-side diffusion coefficient 100 times greater than the actual value for

CO_2. This was to enable qualitative evaluation of the flow and mass transfer, since the concentration contours are easier to visualise.

The liquid flow rate was selected to ensure a partially wetted plate, $Re_l = 88.53$. The flow of gas was chosen to be co-current to the liquid film, with a flow rate of $4.2\,\mathrm{L\,min^{-1}}$. The inlet concentration of CO_2 was selected to be $C^{in}_{CO_2} = 5\,\mathrm{mol\,m^{-3}}$.

The initial conditions were zero velocity everywhere and the depth-averaged domain was initially devoid of liquid with $h = 0$. All walls were set to no-slip boundaries with fixed pressure conditions at the outlets. The top boundary in the gas domain was set to a wall condition with no-slip. At the plate side-walls within the depth-averaged domain a fixed gradient condition was set on the film depth, h to ensure the correct contact angle was formed. The residence time was initially zero everywhere fixed to zero at the inlets and zero gradient at all other boundaries. In the gaseous domain the concentration was set to fixed value boundaries at the inlet. The velocity boundary condition in the gas-phase domain at the boundary with the depth-averaged domain was mapped from the film interfacial velocity calculated in the depth-averaged domain.

The reaction was modelled using 1st order kinetics, as this was shown to be accurate for the physical situation, with the reaction rate given by equation 7.26. The film exposure time, $t_{H,RT}$ was calculated using the residence-time equation. The solution of the liquid film, the gas phase, species concentration and reaction kinetics were performed simultaneously. The simulation was also run without chemical reaction, to provide a comparison between physical absorption and reactive absorption of CO_2.

The computations were run until steady state with an initial time step of 1×10^{-4}s with an adaptive time-step to keep the Courant number below 0.2. The four timescales present in these simulations were the viscous time-scale, $\tau_v = \frac{L^2}{\nu}$, the diffusion time-scale, $\tau_d = \frac{L^2}{D}$, the advection time-scale, $\tau_a = \frac{L}{U}$ and the reaction timescale, $\tau_r = \frac{1}{Ck}$ where L is the characteristic length scale or the cell size, D is the diffusion coefficient, ν is the kinematic viscosity, U is the characteristic velocity of the simulation, C is the concentration of CO_2 and k is the reaction rate constant. The smallest diffusion time-scale was approximately 0.0062s, whilst the smallest viscous time scale was approximately 0.0072s. The smallest reaction time scale for the simulations performed was 0.0141s, whilst the smallest advection time scale is approximately 3.6×10^{-4}s. This confirms the choice of time-step based on the courant number, $C_r = \frac{U\tau_a}{L}$.

If the characteristic length is taken as the Nusselt film depth for the inlet flow rate, rather than the cell size, then the advection time was approximately 0.00038s, the smallest diffusion time was approximately 0.01s and the smallest viscous time was approximately 0.012s.

7.5.3 Results & Discussion

Figure 7.23 shows the film depth in the liquid domain. It can be seen that the film is in the partially wetted regime, as expected. The slices plot the concentration of CO_2 within the gaseous domain. They are taken through a central position and the stagnation position. The effect of mass transfer can be seen in the reduction of CO_2 concentration near the liquid interface. Figure 7.24 shows a contour plot of CO_2 concentration at the interface between the gas and liquid domains. In effect, this represents the CO_2 concentration at the liquid interface.

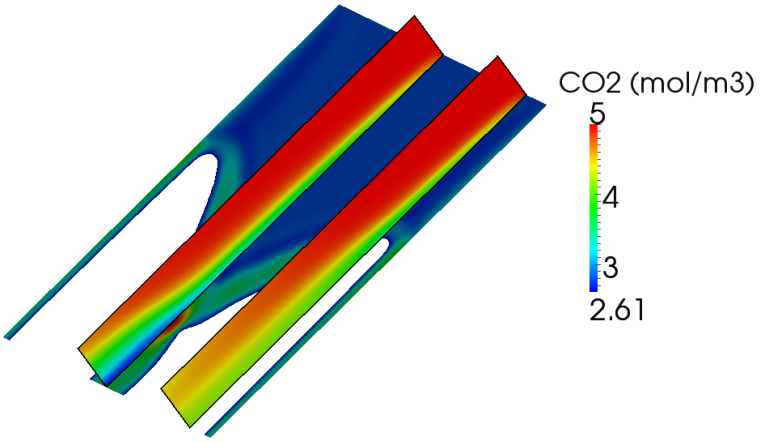

FIGURE 7.23: CO_2 concentration slices on partially wetted plate.

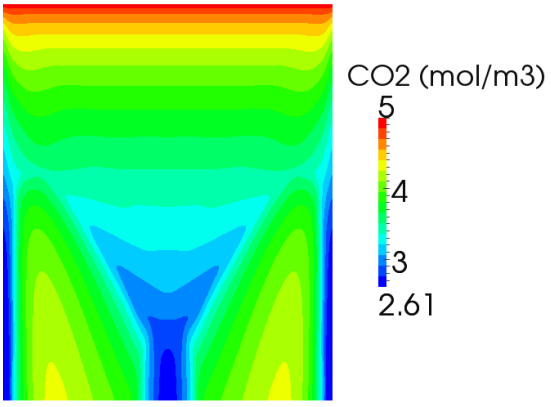

FIGURE 7.24: CO_2 concentration contours on the film surface for partially wetted plate

Figures 7.25-7.26 show the Hatta number and enhancement factor for this case at the steady state solution. It is observed that the reaction between CO_2 and MEA significantly enhances the rate of absorption from the gas phase into the liquid film. Since the Hatta number is large, the enhancement factor is approximately equal to the Hatta number in the majority of the domain.

The same slices, through a central position and the stagnation position, are used in Fig. 7.27 to plot the velocity magnitude within the gaseous domain. The velocity field that

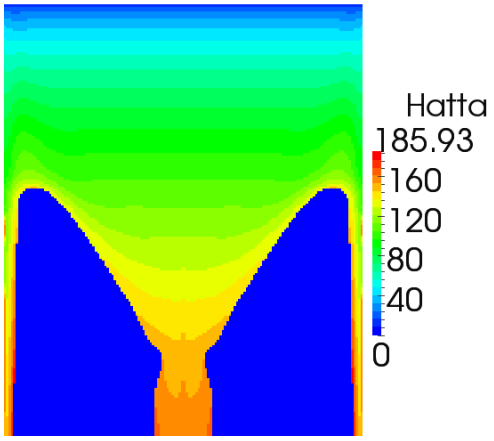

FIGURE 7.25: Hatta number for the partially wetted plate

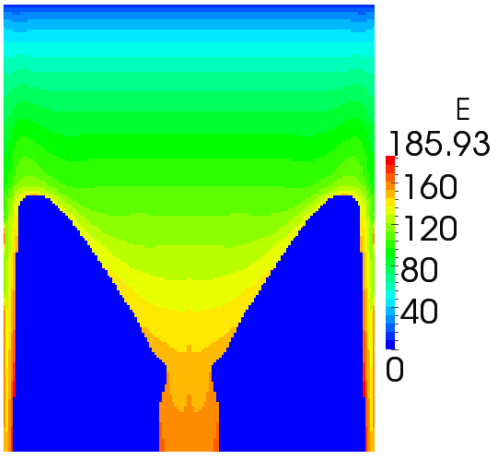

FIGURE 7.26: Enhancement factor for the first order irreversible reaction between CO_2 and MEA for the partially wetted plate

is plotted in the depth-averaged domain represents the surface velocity of the film. It is noted that because the film surface velocity is greater than the gas inlet velocity, the film causes an increase in the gas velocity near to the interface. It can also be seen that where there is no film present, the gas velocity is zero at the plate surface. This demonstrates the coupling between the gas-phase velocity and the liquid-phase velocity in the ESF model.

Comparisons are also made between physical absorption and chemically enhanced absorption for this case. The total absorption rate in the case of physical absorption was $4.996 \times 10^{-6}\,\mathrm{mol\,s^{-1}}$, whilst in the case of chemically enhanced absorption it was $3.228 \times 10^{-4}\,\mathrm{mol\,s^{-1}}$. This means that the CO_2 absorption rate with chemical reaction was 63.6 times greater than that of physical absorption. Despite the fact that absorption of CO_2 into aqueous MEA is always accompanied by a chemical reaction, this result clearly demonstrates the advantage of using a chemically reacting system over an alternative non-reacting system.

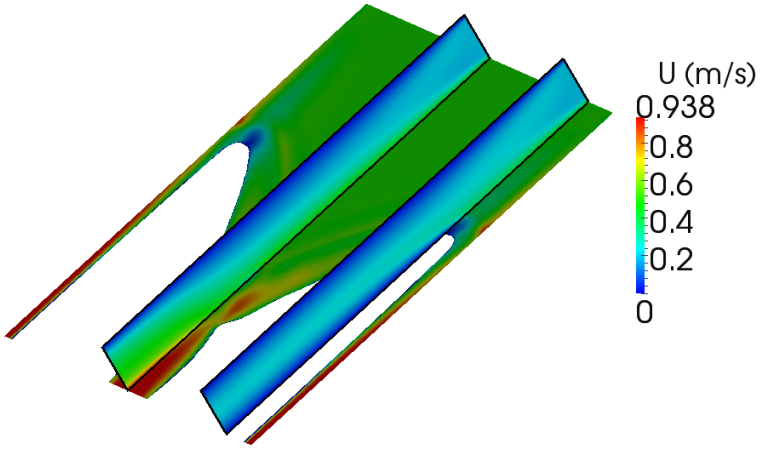

FIGURE 7.27: Velocity on partially wetted plate

It is noted that the simulations performed of chemical absorption in this thesis rely on simplified 1-step mechanisms for the reaction between MEA and CO_2. In reality, the reaction mechanism between MEA and CO_2 is very complex, consisting of many intermediate reaction steps. The full reaction mechanism can be represented as having 12 intermediate steps [89]. For a full description of the reaction all of these would need to be included in the model, with appropriate rate constants for the individual steps. However, as noted by Aboudheir *et al.* [89], the overall reaction can be represented by a single-step reaction between CO_2 and MEA using a general reaction rate constant. This approach has been used in this thesis and it should accurately represent the overall reaction between CO_2 and monoethanolamine. The addition of more reaction steps should increase the accuracy of the simulations, especially if the distribution of intermediate product has an influence on the overall reaction rate. Future research will focus on the addition of more reaction steps to better represent the reaction scheme.

In order to qualitatively view the effect of chemical absorption, the simulation was repeated with a gas-side diffusion coefficient 100 times greater than the actual value for CO_2. This enabled the concentration contours to be viewed more easily (Figs. 7.28-7.29), due to the process being diffusion dominated. The concentration is observed to drop near the liquid surface, as expected. Near to the inlet region, where full-film flow occurs across the width of the plate, the concentration contours are similar to a 2D model. This is expected since in this region the film is essentially 2D in nature. However, as the film moves down the plate and the rivulet begins to form, the CO_2 concentration profile also deviates. The concentration is seen to depend significantly on the location of the interface.

The total simulation time, for the reactive absorption of CO_2 into MEA, was 18489 seconds, which equates to 7 cpu hours per second of simulation. This completion time is significantly quicker than the the VOF simulations, which only modelled the hydrodynamics of the flow.

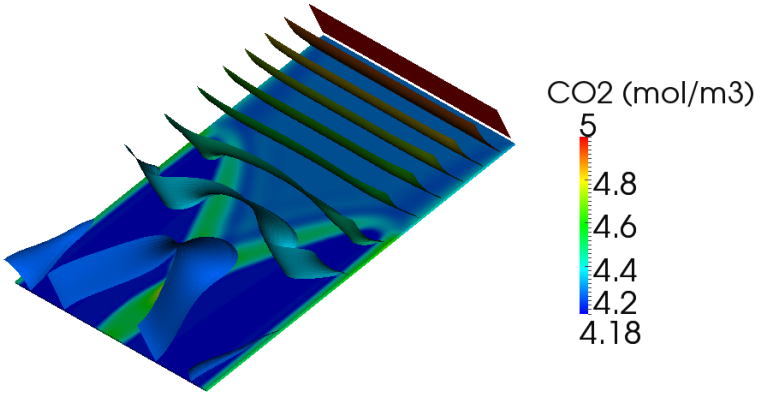

FIGURE 7.28: CO_2 concentration contours on partially wetted plate ($D_g = 100 \times D_g^{CO_2}$).

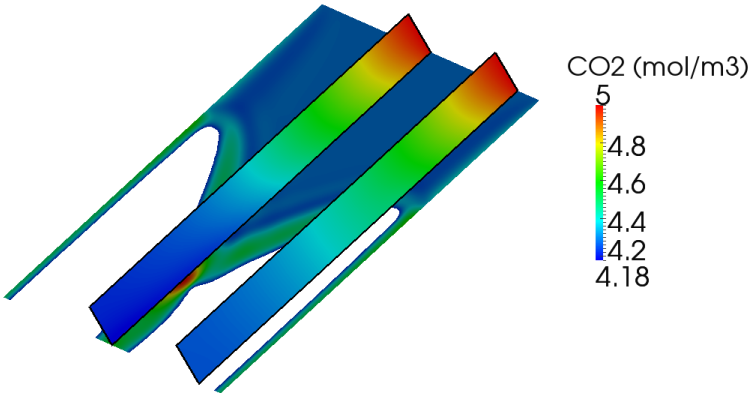

FIGURE 7.29: CO_2 concentration slices on partially wetted plate ($D_g = 100 \times D_g^{CO_2}$).

7.6 Conclusion

This chapter initially detailed the inclusion and validation of physical mass transfer into the enhanced surface film model. The results were validated against the method of Haroun *et al.* [97], due to the lack of experimental data for physical mass transfer. The implementation of Haroun *et al.'s* method into OpenFOAM was validated against analytical and theoretical solutions.

The enhanced surface film model was shown to be as accurate as the VOF approach in the situations tested, with the use of much reduced computational grid. This is mainly due to the fact that, in these situations, the diffusion coefficient of the transferred species is much larger in the gas-phase than it is in the liquid-phase. The ESF model does not explicitly solve for concentration in the liquid, meaning that it requires less computational grid to resolve the flow, resulting in a reduction in computational requirements.

The residence-time equation developed for use in the enhanced surface film model was validated against a VOF model of residence time. It was found that the usual approach of calculating the exposure time, $t_{H,SV}$ using the interfacial velocity and distance from the inlet was less accurate than deriving the exposure time, $t_{H,RT}$ from a residence-time equation. This is more so in regions where the ESF model was unable to accurately derive surface velocities from depth-averaged velocities, such as near the contact-line. It was concluded that the enhanced surface film model, using the residence-time equation, was sufficiently accurate to calculate physical mass transfer into liquid films, whilst significantly improving simulation run-times.

The main disadvantage of this approach is that it assumes that the concentration in the liquid bulk is negligible. Despite this, in many systems the concentration boundary layer is confined to a small region close to the liquid film interface, so it may not be a large disadvantage. However, if a lot of mixing occurs within the liquid film, due to turbulence, for example, then this would have to be taken account of in the model.

This chapter also described the novel implementation of chemically enhanced absorption within the enhanced surface film model. Validation was performed against experimental data of a wetted-wall column. The values of the overall mass transfer coefficient, K_G were within an acceptable range of the experimental data.

The next step combined all of the elements developed in this thesis to model a situation of real relevance to the carbon capture industry. This involved simulating CO_2 absorption into a thin film of aqueous monoethanolamine. The domain selected was a small-scale representation of flow within an absorber column filled with structured packing.

The final model was able to simulate, simultaneously, the liquid film hydrodynamics, the gas flow, the species transport and the chemically enhanced absorption of CO_2 into the film. The results clearly show the applicability of this novel approach to the CCS industry. The main advantage of this method is the economy of computational resources, due to the much reduced grid in comparison to the VOF approach. Further research into this area is clearly of benefit, to scale-up simulations to model much larger, more realistic sections of packing within absorber columns.

Improvements to the model will need to be made in order for successful scale-up to be made. These include the addition of a suitable model for momentum dispersion terms which may become more important at larger scales. The use of a moving mesh technique, as performed by Lavelle *et al.* [68], in the gas phase could also improve the accuracy of the approach. In particular, this would improve the accuracy of the gas phase flow and also the mass transfer through the interface because the interface would be more accurately modelled.

Chapter 8

Conclusion

This chapter provides a summary of the work developed within this thesis. This includes a review of the major contributions and the final conclusions that can be drawn. Finally, suggestions for future development of this work are listed, along with the wide ranging applicability of this work.

8.1 Hydrodynamic Modelling of Thin Films

Thin liquid films are a major aspect of carbon capture within packed column absorbers and they can have a significant impact on the efficiency of the processes. This characteristic is not limited to carbon capture, in fact, many industrial sectors rely on the thin-film for their efficient operation.

One of the main factors affecting the efficiency of gas absorption into a liquid film is the interfacial area available for absorption. This thesis initially focussed on a method to increase the wetted and interfacial areas of films on packing materials. The introduction of vertical grooves on a steel plate was found to significantly increase the wetted area and interfacial area, especially at lower liquid flow rates. These simulations were performed with the VOF method and it was found that despite a significantly reduced domain, in comparison to the size of absorber columns, the simulations were very computationally expensive.

Adaptive mesh refinement is a modelling approach which can be used to either increase accuracy in certain regions of interest, or reduce the computational requirements by reducing the number of cells in regions that are of little interest. AMR was used with the VOF model to simulate thin film flow down an inclined plane. An initial coarse mesh was used, which was then refined around the gas-liquid interface. It was found that AMR-VOF produced results in better agreement with experimental data in the literature. However, these simulations took longer to complete due to the overall increase

in the number of cells, despite the cells being more effectively distributed. The act of adapting the mesh, as the interface moves through the domain, also introduces additional overhead.

Careful consideration of the AMR-VOF parameters eventually enabled the AMR-VOF simulation to be completed in less computational time. This highlights that the use of AMR-VOF does not necessarily reduce the computational requirements and that the AMR parameters (such as initial mesh density and number of refinement levels) need to be chosen carefully to ensure fast, accurate simulations. Despite these tools, these type of simulations were still computationally expensive and scaling up the size of the domain would prove difficult. This would be further complicated by the addition of mass transfer and reaction kinetics.

From the outset of this work it was understood that the complexity of modelling carbon capture within packed columns would require the development of a novel approach, especially in modelling larger scales. Furthermore, it was confirmed in this work that even at scales much smaller than absorber columns, the VOF or AMR-VOF approaches would struggle to model the underlying mass transfer processes accurately. This is due to the large number of computational cells required to accurately resolve the large concentration gradients that exist close to the interface within the liquid-phase. Simulations using these types of fully three-dimensional approaches are too computationally intensive and this significantly hinders their applicability in the real-world application of CCS.

The Enhanced Surface Film (ESF) model developed within this thesis is an extension of the thin-film depth-averaged model. Surface tension is one of the significant forces affecting the flow of thin films, and can cause rivulet formation which reduce the efficiencies of devices which rely on thin-films for gas separation. The implementation of the CSF surface tension model along with the surface film approach allowed accurate simulations of thin film flow to be performed. This required the development of a model for the threshold thickness, a parameter required in the depth-averaged version of the CSF model.

The threshold thickness model was able to accurately simulate thin-film flow for various fluids with a wide variety of physical properties, from acetone to glycerol. Validation of the model was made by comparison with experimental data and highly refined AMR-VOF simulations. The results of the ESF model were within an acceptable range of the AMR-VOF results and matched well with experimental data. The significant flow features, such as rivulets and droplets were also captured by the model.

The limitation of the ESF model is the fact that the momentum dispersion terms are not included, due to the difficulties in modelling these non-linear depth-averaged terms. However, it was found that neglecting these terms did not effect the results largely, in terms of wetted area, due to them being balanced by other terms in the equations. It is proposed that at the larger Re_l, the inclusion of a momentum dispersion model may have

improved the results further. This is because at the larger Re_l the film contact line moved very slowly down the plate after the initial rivulet is formed. The slow moving contact line was not observed with the current ESF model, resulting in an under-predication of the wetted area at higher Re_l. A model for momentum dispersion is an important focus of future research in this area because it was shown in budget plots that these terms are not insignificant. Furthermore, the momentum dispersion terms would probably be more significant in larger domains at higher Re_l. A suitable model for the momentum dispersion terms will need to be determined for future scale-up of the ESF approach.

8.2 Mass Transfer and Reaction Kinetics

Mass transfer is a vital component in gas absorption equipment, such as in packed columns. The basic principle of these apparatus is the separation of a gaseous species by absorption into a thin film of solvent. The modelling of this process has been performed along with the VOF approach in the literature [41,97]. Haroun *et al.*'s [41,97] approach was implemented into OpenFOAM in order to provide additional validation of methods developed in this thesis.

However, simulations using this implementation highlighted further problems with the use of the VOF approach for the modelling of these processes. Particularly in carbon capture, the diffusion coefficient of CO_2 in the liquid phase very small and is two orders of magnitude smaller than that in the gaseous phase. The resulting concentration boundary layer on the liquid side of the interface is very small and requires many cells in this region to accurately capture this gradient. It was concluded that, even for the relatively small domains used in thesis, the VOF model with mass transfer would be too computationally expensive to simulate, when using the correct diffusion coefficients for CO_2.

The inclusion of mass transfer in the ESF model was a major development in this field of research. In order to account for mass transfer, sink terms were introduced in the gas phase where the mass transfer coefficient was calculated using Higbie Penetration Theory. This theory requires the definition of a film exposure time. In order to track the evolution of the exposure time throughout the domain, a depth-averaged version of the residence-time transport equation was developed and included in the ESF model. This allows the exposure time to be determined at any location on the surface of the film at any moment in time.

It was found that the mass transfer implementation of the ESF model was able to accurately solve for the hydrodynamics of thin films and the physical mass transfer through the gas-liquid interface, simultaneously. The limitation of this approach is that it assumes that the concentration in the bulk of the liquid film is negligible. Improvements to this could be made in future research. However, at present this is not seen as a major disadvantage because in many applications the concentration of absorbed species is very

low in the liquid bulk. This is due to the fact that the concentration is the gas bulk is usually low and the diffusion coefficient in the liquid phase is small. Chemical reactions in the liquid film also reduce the amount of absorbed species that can diffuse into the liquid bulk, since they are transformed into reaction products.

A natural extension of the mass transfer ESF solver, was to include chemically enhanced absorption. This is another advancement in this field of research. This was included using the Enhancement factor model, which is the ratio of the rate absorption with chemical reaction to the rate of absorption without chemical reaction. The Enhancement factor is usually defined in terms of the Hatta number, Ha, a non-dimensional number.

First and Second order reactions were tested in a two-dimensional representation of a wetted-wall column. This involved CO_2 absorbing into a liquid film composed of aqueous monoethanolamine. The model was validated against experimental data from the literature and it was found that the ESF model was able to accurately model chemically enhanced absorption. The prediction of the overall mass transfer coefficients were very similar to literature data for temperature values of 313k and 333k.

First order reactions kinetics gave similar results to second order reaction kinetics. This was expected since the concentration of CO_2 in the gas phase was low, as is the case in natural gas power station flue gas. The rate of reaction between CO_2 and monoethanolamine is also very fast, meaning that the assumption of first order reaction kinetics is valid. The work detailed in this thesis has proven that this is the case, for the set-up tested.

The final part of this thesis was to combine all of the elements developed for the ESF model. A simulation was performed of CO_2 absorption into a film of aqueous monoethanolamine. The flow rate of the liquid phase was chosen so that it was in the partially wetted regime. The model was able to simulate this domain with relative ease, the simulation only using 2.17 cpu hours per second of simulation. All of the aspects, such as the solution of hydrodynamics, mass transfer and reaction kinetics were solved simultaneously. Despite the limitations and assumptions of the ESF model, this clearly shows that this is a promising approach to simulating carbon capture on larger domains. Therefore, future research could focus on using the model to solve for larger sections of packing materials, even at the mesoscale.

8.3 Future Work

The ESF model in its present state can be used to model a variety of apparatus in numerous industries. The performance and efficiency of many apparatus is dependent on the structure of thin liquid films. Therefore, potential applications include thin

film microreactors, surface coating, biofluids and medical applications. It would be interesting to test the ESF model in other applications, such as these.

In terms of CCS, the size of the simulations could be scaled-up to model more realistic representations of the absorber columns. This could be made possible by the ESF model. Simulations of the mesoscale with the inclusion of surface film modelling and mass transfer would present an interesting challenge. A prerequisite to this research would be the development of a model for the momentum dispersion terms to properly account for momentum dispersion at higher Re_l.

The ESF model could also be extended from it current form to increase its accuracy. As mentioned previously, this could be achieved in terms of the hydrodynamics by developing a model for the momentum dispersion terms. In terms of mass transfer, the model could be extended to allow for a non-zero species concentration in the liquid bulk, or gas loadings greater than zero. This would allow a greater variety of carbon capture situations to be modelled including cases with larger values of CO_2 loading. Finally, a moving mesh technique could be introduced to improve the coupling between the gas and liquid phases.

Appendix A

Microscale Hydrodynamics

A.1 Mesh Independence Checks

Mesh independence checks were carried out to ensure the results were not effected by the choice of meshes during the investigation of flow down an inclined plane using VOF. It was observed that the wetted area of the plate was highly dependent upon the flow parameters and therefore, this variable was used as a good indication to mesh dependency. These checks were performed for the smooth plate and textured plate and are detailed below.

A.1.1 Smooth Plate

Due to the range of plate inclination angles it was important to ensure grid independent results for all angles. Simulations were run initially with a mesh of 0.6 million cells, increasing the number of cells in subsequent calculations until no significant difference in the solution was observed. Fig. A.1 and Fig. A.2 plot the specific wetted area against time for $\theta = 60^o$ and $\theta = 30^o$, respectively. It can be seen that there was very little difference in the solutions when using meshes of 0.8, 1.0 and 1.2 million cells. It was established that a cell count of 1.0 million cells allowed mesh dependency errors to be minimised for the range of inclination angles, whilst keeping run times to a reasonable level.

A.1.2 Textured Plate

Simulations were run initially with approximately 1.4 million cells, increasing the number of cells in subsequent calculations until no significant difference in the solution was observed. Fig. A.3 plots the specific wetted area against time for the various computational meshes. It can be seen that the solutions obtained with meshes of 2.0 and 2.5

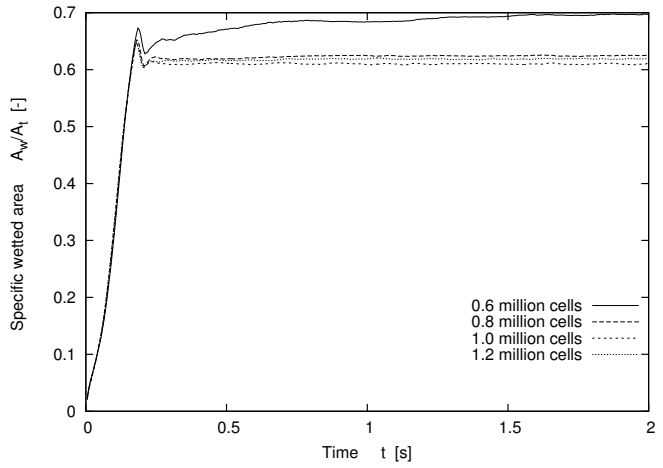

FIGURE A.1: Specific wetted area against time for smooth plate $\theta = 60^o$

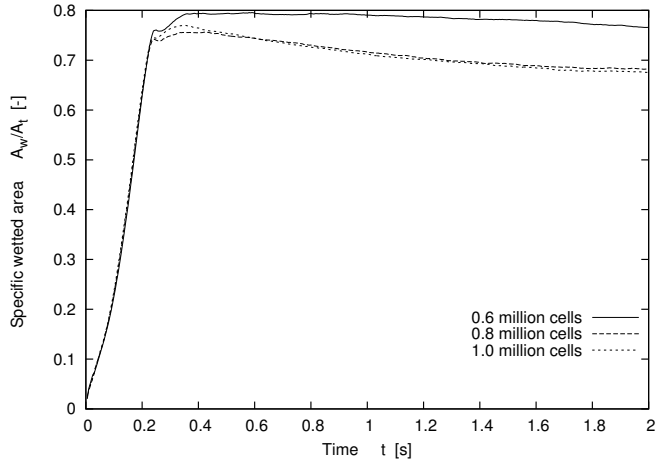

FIGURE A.2: Specific wetted area against time for smooth plate $\theta = 30^o$

million cells were consistent with each other. It was decided that a mesh of 2.5 million cells should be used in the investigation, considering the importance of good mesh refinement close to the ridges.

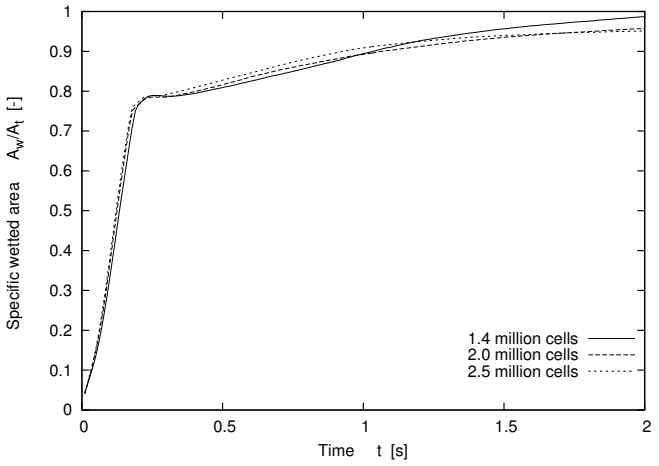

FIGURE A.3: Specific wetted area against time for textured plate $\theta = 60^o$

Appendix B

Derivation of Depth-Averaged Navier-Stokes Equations

This appendix shows the full derivation of the depth-averaged Navier-Stokes equations, followed by the derivation of the surface tension terms used in the ESF model. Initially, a recap is given of the tools used for the depth integration of the equations.

B.0.1 Tools for Depth Integration

Important tools for the depth integration of the Navier-Stokes equations are the Leibniz theorem, the fundamental theorem of integration, the kinematic boundary condition at the free surface and the kinematic boundary condition at the surface of the plate along which the liquid flows. It is assumed that the depth integration is performed in the z-direction from $z(t,x,y) = z_0$ to $z(t,x,y) = z_o + h$, where h is the film height and z_0 is the z-coordinate location of the underlying substrate. Since the simulations in this thesis were performed on a flat plate, $z_0 = 0$. The velocity field is denoted as $\boldsymbol{u} = [u, v, w]$.

B.0.1.1 The kinematic boundary condition at the free surface

If the surface is denoted by $z_s = z_0 + h$, then the kinematic boundary condition is derived by taking the derivative of $z_s = z_s(t,x,y)$,

$$w|_{z_0+h} = \frac{Dz_s}{Dt} = \frac{\partial(z_0+h)}{\partial t} + \frac{\partial x}{\partial t}\frac{\partial(z_0+h)}{\partial x} + \frac{\partial y}{\partial t}\frac{\partial(z_0+h)}{\partial y}, \tag{B.1}$$

which gives,

$$w|_{z_0+h} = \cancelto{0}{\frac{\partial z_0}{\partial t}} + \frac{\partial h}{\partial t} + u|_{z_0+h}\frac{\partial(z_0+h)}{\partial x} + v|_{z_0+h}\frac{\partial(z_0+h)}{\partial y}, \tag{B.2}$$

since the underlying plate surface is fixed and does not change with time. Therefore, for $z_0 = 0$ the kinematic boundary condition at the free surface is given by:

$$w|_h = \frac{\partial h}{\partial t} + u|_h \frac{\partial h}{\partial x} + v|_h \frac{\partial h}{\partial y}. \tag{B.3}$$

B.0.1.2 The kinematic boundary condition at the plate surface

The kinematic boundary condition at the plate surface is derived by assuming that there is no mass flux perpendicular to the plate. This means that $\boldsymbol{u}.\boldsymbol{n} = 0$, where $\boldsymbol{n}$ is the normal vector at the plate surface given by,

$$\boldsymbol{n} = (\frac{\partial z_0}{\partial x}, \frac{\partial z_0}{\partial y}, -1). \tag{B.4}$$

Therefore, the kinematic boundary condition at the plate surface is given by,

$$w|_{z_0} = u|_{z_0} \frac{\partial z_0}{\partial x} + v|_{z_0} \frac{\partial z_0}{\partial y}. \tag{B.5}$$

which for $z_0 = 0$ simplifies to,

$$w|_0 = 0. \tag{B.6}$$

B.0.1.3 The Leibniz theorem and fundamental theorem of integration

The Leibniz theorem for a general variable $\psi = \psi(t, x, y, z)$ is stated as,

$$\frac{\partial}{\partial x} \int_{z_0}^{z_0+h} \psi \mathrm{d}z = \int_{z_0}^{z_0+h} \frac{\partial \psi}{\partial x} \mathrm{d}z + \psi|_{z_0+h} \frac{\partial (z_0 + h)}{\partial x} - \psi|_{z_0} \frac{\partial z_0}{\partial x}, \tag{B.7}$$

and the fundamental theorem of integration is stated as,

$$\int_{z_0}^{z_0+h} \frac{\partial \psi}{\partial z} \mathrm{d}z = \psi|_{z_0+h} - \psi|_{z_0}. \tag{B.8}$$

B.0.2 The continuity equation

The continuity equation for a 3-dimensional incompressible flow is given by,

$$\nabla \cdot \boldsymbol{u} = 0. \tag{B.9}$$

Therefore, depth integrating this equation from the plate surface, $z = 0$ to the free surface, $z = h$ gives,

$$\int_0^h \frac{\partial u}{\partial x} \mathrm{d}z + \int_0^h \frac{\partial v}{\partial y} \mathrm{d}z + \int_0^h \frac{\partial w}{\partial z} \mathrm{d}z = 0. \tag{B.10}$$

Using the Leibniz theorem gives,

$$\frac{\partial}{\partial x}\int_0^h u\mathrm{d}z - u|_h\frac{\partial h}{\partial x} + \frac{\partial}{\partial y}\int_0^h v\mathrm{d}z - v|_h\frac{\partial h}{\partial y} + w|_h - w|_0 = 0. \tag{B.11}$$

Substituting the kinematic boundary condition at the free surface and at the plate surface gives,

$$\frac{\partial}{\partial x}\int_0^h u\mathrm{d}z + \frac{\partial}{\partial y}\int_0^h v\mathrm{d}z + \frac{\partial h}{\partial t} = 0. \tag{B.12}$$

The depth averaged velocity, $\overline{u}$ and $\overline{v}$ are defined by,

$$\int_0^h u\mathrm{d}z = \overline{u}h, \qquad \int_0^h v\mathrm{d}z = \overline{v}h, \tag{B.13}$$

and so the depth-averaged continuity equation is given by,

$$\frac{\partial h}{\partial t} + \frac{\partial(\overline{u}h)}{\partial x} + \frac{\partial(\overline{v}h)}{\partial y} = 0. \tag{B.14}$$

In vector calculus form the continuity equation is given by,

$$\frac{\partial h}{\partial t} + \nabla_s \cdot (h\overline{\boldsymbol{u}}) = 0, \tag{B.15}$$

where h is the film depth, $\overline{\boldsymbol{u}} = (\overline{u}, \overline{v})$ is the depth-averaged velocity and ∇_s is the 2D nabla given by,

$$\nabla_s = \left(\frac{\partial}{\partial x}, \frac{\partial}{\partial y}\right). \tag{B.16}$$

B.0.3 The momentum equations

The Navier-Stokes equation for a 3-dimensional incompressible flow are determined by the conservation of momentum. If the velocity of the fluid is denoted by $\boldsymbol{u} = [u, v, w]$ and the fluid is incompressible, the conservation of momentum leads to,

$$\rho\left(\frac{\partial \boldsymbol{u}}{\partial t} + \boldsymbol{u}\cdot\nabla\boldsymbol{u}\right) = -\nabla p + \mu\nabla^2\boldsymbol{u} + \rho\boldsymbol{g} + \boldsymbol{F}_{st}, \tag{B.17}$$

where ρ is the density, p is the pressure, μ is the kinematic viscosity, $\boldsymbol{g}$ is the gravitational force and $\boldsymbol{F}_{st}$ is the surface tension force. The depth integration will be performed on the x-momentum equation and an analogous approach can be used for the y-momentum equation. The x-momentum equation can be written as,

$$\rho\left(\frac{\partial u}{\partial t} + u\frac{\partial u}{\partial x} + v\frac{\partial u}{\partial y} + w\frac{\partial u}{\partial z}\right) = -\frac{\partial p}{\partial x} + \frac{\partial \tau_{xx}}{\partial x} + \frac{\partial \tau_{xy}}{\partial y} + \frac{\partial \tau_{xz}}{\partial z} + \rho g_x + F_x^{st}, \tag{B.18}$$

where τ is the deviatoric stress tensor, g_x represents the x-component of gravity and F_x^{st} represents the x-component of the body force $\boldsymbol{F}_{st}$.

Depth integration of equation B.18 from $z = 0$ to $z = h$ will be done in parts to ensure that the derivation is easy to follow. Firstly, the temporal derivative and convection terms will be integrated using the Leibniz theorem and the fundamental theorem on integration,

$$\begin{aligned}\int_0^h \left(\frac{\partial u}{\partial t} + u\frac{\partial u}{\partial x} + v\frac{\partial u}{\partial y} + w\frac{\partial u}{\partial z}\right) \mathrm{d}z = &\frac{\partial}{\partial t}\int_0^h u\mathrm{d}z - u|_h\frac{\partial h}{\partial t} \\ &+ \frac{\partial}{\partial x}\int_0^h u^2\mathrm{d}z - u^2|_h\frac{\partial h}{\partial x} \\ &+ \frac{\partial}{\partial y}\int_0^h uv\mathrm{d}z - (uv)|_h\frac{\partial h}{\partial y} \\ &+ (uw)|_h - (uw)|_0\end{aligned} \tag{B.19}$$

Rearranging this equation into the form,

$$\begin{aligned}\int_0^h \left(\frac{\partial u}{\partial t} + u\frac{\partial u}{\partial x} + v\frac{\partial u}{\partial y} + w\frac{\partial u}{\partial z}\right) \mathrm{d}z = &\frac{\partial}{\partial t}\int_0^h u\mathrm{d}z + \frac{\partial}{\partial x}\int_0^h u^2\mathrm{d}z + \frac{\partial}{\partial y}\int_0^h uv\mathrm{d}z \\ &- u|_h\left(\frac{\partial h}{\partial t} + u|_h\frac{\partial h}{\partial x} + v|_h\frac{\partial h}{\partial y} - w|_h\right) \\ &- u|_0(w|_0),\end{aligned} \tag{B.20}$$

and using the kinematic boundary conditions allows the final two terms to be removed as they are equal to zero, resulting in the following,

$$\int_0^h \rho\left(\frac{\partial u}{\partial t} + u\frac{\partial u}{\partial x} + v\frac{\partial u}{\partial y} + w\frac{\partial u}{\partial z}\right) \mathrm{d}z = \frac{\partial \rho h\overline{u}}{\partial t} + \frac{\partial \rho h\overline{uu}}{\partial x} + \frac{\partial \rho h\overline{uv}}{\partial y}. \tag{B.21}$$

The pressure derivative term will be depth integrated as follows using the Leibniz theorem,

$$\int_0^h -\frac{\partial p}{\partial x}\mathrm{d}z = -\frac{\partial}{\partial x}\int_0^h p\mathrm{d}z + p|_h\frac{\partial h}{\partial x}, \tag{B.22}$$

and therefore,

$$\int_0^h -\frac{\partial p}{\partial x}\mathrm{d}z = -\frac{\partial h\overline{p}}{\partial x} + p|_h\frac{\partial h}{\partial x} \tag{B.23}$$

where $\overline{p}$ is the depth-averaged pressure and $p|h$ will be defined in the following section.

The viscous terms will be integrated using the Leibniz theorem and the fundamental theorem of integration as follows,

$$\begin{aligned}\int_0^h \left(\frac{\partial \tau_{xx}}{\partial x} + \frac{\partial \tau_{xy}}{\partial y} + \frac{\partial \tau_{xz}}{\partial z}\right) \mathrm{d}z = &\frac{\partial}{\partial x}\int_0^h \tau_{xx}\mathrm{d}z - \tau_{xx}|_h\frac{\partial h}{\partial x} \\ &+ \frac{\partial}{\partial y}\int_0^h \tau_{xy}\mathrm{d}z - \tau_{xy}|_h\frac{\partial h}{\partial y} \\ &+ \tau_{xz}|_h - \tau_{xz}|_0.\end{aligned} \tag{B.24}$$

Rearranging this equation into the form,

$$\begin{aligned}\int_0^h \left(\frac{\partial \tau_{xx}}{\partial x}+\frac{\partial \tau_{xy}}{\partial y}+\frac{\partial \tau_{xz}}{\partial z}\right)\mathrm{d}z = \frac{\partial}{\partial x}\int_0^h \tau_{xx}\mathrm{d}z + \frac{\partial}{\partial y}\int_0^h \tau_{xy}\mathrm{d}z \\ -\tau_{xx}|_h\frac{\partial h}{\partial x}-\tau_{xy}|_h\frac{\partial h}{\partial y}+\tau_{xz}|_h \\ -\tau_{xz}|_0.\end{aligned} \tag{B.25}$$

and defining the wall shear stress, τ_x^{wall},

$$\tau_x^{wall} = -\tau_{xz}|_0, \tag{B.26}$$

and the gas shear stress, τ_x^{gas},

$$\tau_x^{gas} = -\tau_{xx}|_h\frac{\partial h}{\partial x}-\tau_{xy}|_h\frac{\partial h}{\partial y}+\tau_{xz}|_h, \tag{B.27}$$

allows the depth-integrated viscous terms to be written as,

$$\int_0^h \left(\frac{\partial \tau_{xx}}{\partial x}+\frac{\partial \tau_{xy}}{\partial y}+\frac{\partial \tau_{xz}}{\partial z}\right)\mathrm{d}z = \frac{\partial h\overline{\tau}_{xx}}{\partial x}+\frac{\partial h\overline{\tau}_{xy}}{\partial y}+\tau_x^{gas}+\tau_x^{wall}. \tag{B.28}$$

The gravity term is depth-integrated as follows,

$$\int_0^h \rho g_x \mathrm{d}z = \rho g_x h. \tag{B.29}$$

Combining these derivations gives the final depth-averaged Navier-Stokes momentum equation for the x-component as,

$$\frac{\partial \rho h\overline{u}}{\partial t}+\frac{\partial \rho h\overline{u}\overline{u}}{\partial x}+\frac{\partial \rho h\overline{u}\overline{v}}{\partial y} = -\frac{\partial h\overline{p}}{\partial x}+p|_h\frac{\partial h}{\partial x}+\frac{\partial h\overline{\tau}_{xx}}{\partial x}+\frac{\partial h\overline{\tau}_{xy}}{\partial y}+\tau_x^{gas}+\tau_x^{wall}+\rho g_x h+\int_0^h F_x^{st}\mathrm{d}z. \tag{B.30}$$

In vector calculus form this gives,

$$\frac{\partial \rho\overline{\boldsymbol{u}}h}{\partial t}+\nabla_s\cdot(\rho h\overline{\boldsymbol{u}}\overline{\boldsymbol{u}}) = -\nabla_s(h\overline{p})+p|_h\nabla_s h+\nabla_s\cdot(\mu h\nabla\overline{\boldsymbol{u}})+\boldsymbol{\tau}_g+\boldsymbol{\tau}_w+\rho\boldsymbol{g}h+\int_0^h \boldsymbol{F}_{st}\mathrm{d}z, \tag{B.31}$$

where ∇_s is the 2D nabla given by,

$$\nabla_s = \left(\frac{\partial}{\partial x},\frac{\partial}{\partial y}\right). \tag{B.32}$$

Closure models for the gas-shear stress, $\boldsymbol{\tau}_g$ and wall shear stress, $\boldsymbol{\tau}_w$ are needed and are detailed in Chapter 6.

B.0.4 Depth-averaged pressure and surface tension

The z-component of the incompressible 3-dimensional Navier-Stokes equations is given by,

$$\rho\left(\frac{\partial w}{\partial t}+u\frac{\partial w}{\partial x}+v\frac{\partial w}{\partial y}+w\frac{\partial w}{\partial z}\right)=-\frac{\partial p}{\partial z}+\mu\left(\frac{\partial^2 w}{\partial x^2}+\frac{\partial^2 w}{\partial y^2}+\frac{\partial^2 w}{\partial z^2}\right)+\rho g_z+\sigma\kappa(\boldsymbol{x})n_z\delta, \tag{B.33}$$

where δ is the Dirac delta function localising the surface tension force to the interface. The curvature, κ and normal, n_z can be calculated using the height, h and so have no dependence on the z-coordinate. This equation is applicable to the whole domain including both the liquid and gaseous phases. The z-component of the surface tension force can be included in the pressure derivative by integrating it with respect to the z-coordinate,

$$\int \sigma\kappa(\boldsymbol{x})n_z\delta \mathrm{d}z=\sigma\kappa(\boldsymbol{x})n_z H, \tag{B.34}$$

where H is the Heaviside step function. This function is defined as being zero for $z<h$ and 1 for $z>h$. Therefore, the pressure derivative term can be defined by,

$$-\frac{\partial(p-\sigma\kappa(\boldsymbol{x})n_z H)}{\partial z}. \tag{B.35}$$

This shows that the z-component of the surface tension force introduces a pressure jump at the interface between the liquid and gas phase. Within the gas phase, if we take the limit $z\rightarrow h^+$, this gives the pressure on the gas-side of the interface and is given by,

$$p_{gas}=p_{gas,h}-\sigma\kappa(\boldsymbol{x})n_z, \tag{B.36}$$

since the Heaviside function is defined to be equal to 1 in the limit $z\rightarrow h^+$. Here, $p_{gas,h}$ is the hydrodynamic pressure in the gas-phase at the interface.

Now, under the assumption that the characteristic horizontal length scale is much larger than the vertical length scale and that the characteristic vertical velocity is much smaller than the horizontal velocity component, the z-momentum equation (Equation B.33) within the liquid film only can be reduced to,

$$0=-\frac{\partial p}{\partial z}-\rho g cos(\theta)+\sigma\kappa(t,x,y)n_z\delta. \tag{B.37}$$

Integrating this equation in z gives an expression for the pressure,

$$\begin{aligned} p(z)&=\int(-\rho g cos(\theta)+\sigma\kappa(t,x,y)n_z\delta)\mathrm{d}z \\ &=-\rho g z cos(\theta)+\sigma\kappa(t,x,y)n_z H+c(x,y), \end{aligned} \tag{B.38}$$

This defines the pressure in the liquid phase. Taking the limit $z \rightarrow h^-$ and defining $p(z = h) = p_{gas}$, the constant of integration can be determined,

$$p(z = h) = -\rho g h cos(\theta) + c(x, y) = p_{gas} = p_{gas,h} - \sigma\kappa(\boldsymbol{x})n_z, \tag{B.39}$$

since the Heaviside function is defined to be equal to 0 in the limit $z \rightarrow h^-$ at the interface. The constant of integration is then given by,

$$c(x, y) = p_{gas,h} - \sigma\kappa(\boldsymbol{x})n_z + \rho g h cos(\theta) \tag{B.40}$$

Therefore, the pressure in the liquid phase is given by,

$$p(z) = p_{gas,h} + \rho g(h - z)cos(\theta) - \sigma\kappa(t, x, y)n_z. \tag{B.41}$$

Integrating $p(x)$ with respect to z from $z = 0$ to $z = h$ defines the depth-averaged pressure by,

$$\begin{aligned} \overline{p} &= \frac{1}{h}\int_0^h (p_{gas,h} + \rho g(h - z)cos(\theta) - \sigma\kappa(t, x, y)n_z)\mathrm{d}z \\ \overline{p} &= p_{gas,h} + \frac{1}{2}\rho g h cos(\theta) - \sigma\kappa(t, x, y)n_z. \end{aligned} \tag{B.42}$$

The horizontal components of surface tension are included directly as momentum source terms in equation B.31. Therefore, for the x-component:

$$\begin{aligned} \int_0^h F_x^{st}\mathrm{d}z &= \int_0^h \sigma\kappa n_x \mathrm{d}z, \\ &= \frac{1}{2}\sigma\kappa n_x, \end{aligned} \tag{B.43}$$

since the integration of the Dirac delta function, located at the interface, from $z = 0$ to $z = h$ is equal to $\frac{1}{2}$. A similar procedure can be used for the y-component.

Appendix C

Mass Transfer with AMR-VOF

This appendix outlines the attempts made to simulate acid-gas absorption using the VOF method with adaptive mesh refinement. It was shown in Chapter 7 that during acid-gas absorption, a thin concentration boundary layer is formed on the liquid-side of the gas-liquid interface. In order to resolve this thin concentration boundary layer a large number of cells is required in this region.

It was concluded that the AMR-VOF approach would not be possible on domains of practical interest, due to the very large number of computational cells required. This conclusion was confirmed and is detailed in the following.

C.1 Computational Domain and Grid

The domain was selected as a microscale representation of gravity-driven flow over structured packing (see Chapter 5). In order to take full advantage of adaptive mesh refinement, an initial very coarse grid was constructed, which would then be heavily refined about the gas-liquid interface. The domain was also divided along the centre-line ($x = 0.025m$), with the introduction of a symmetry plane, to further reduce the computational requirements.

The initial grid consisted of 12096 cells and is shown in Figure C.1. The adaptive refinement was performed for volume fractions in the range, $0.2 > \alpha > 0.8$ and 5 levels of refinement were selected. The grid refinement was chosen to occur every 75 time steps. This was selected to reduce the overhead involved with physically adapting the grid, whilst maintaining the stability of the simulation. Too large a value resulted in instabilities, due to the fact that changes to the mesh lagged behind the evolution of the interface. The time-step was limited to give a courant number below 0.7, resulting in time-steps of approximately 3×10^{-6} seconds. The simulation was run in parallel on 100 processors on the Southampton Iridis3 cluster.

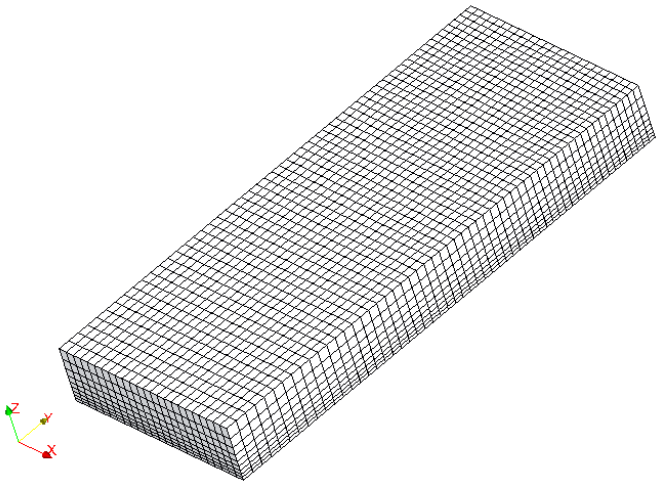

FIGURE C.1: Initial AMR-VOF Grid 12096 cells.

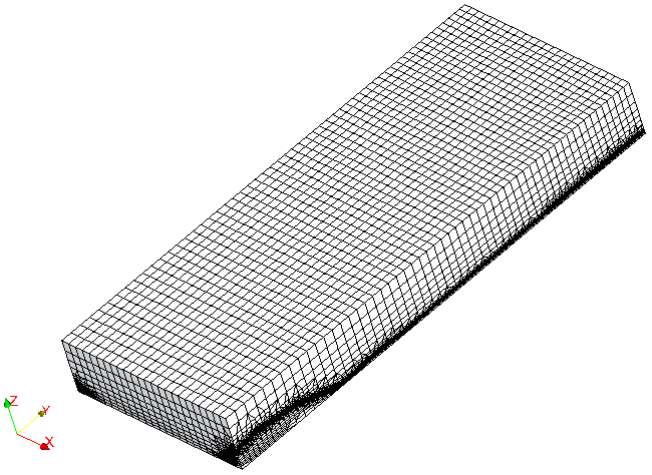

FIGURE C.2: Final AMR-VOF Grid 6.7 million cells.

C.1.1 Results

The final converged solution resulted in a grid of 6.7 million cells and is shown in Figs. C.2-C.4. It can be seen that even with 5 levels of adaptive mesh refinement the number of cells close to the interface is not adequate to accurately resolve the thin concentration layer, especially for CO_2. Even for a fluid with a liquid diffusion coefficient 100 times greater than CO_2, the grid did not provide enough points to resolve the concentration boundary layer (see Figure 7.14).

The simulation was completed in 136 hours on 100 processors. This clearly shows that the use of ARM-VOF is not a viable approach to simulating acid-gas absorption, where thin concentration layers are present at the gas-liquid interface. Further levels of refinement would be required to accurately resolve the concentration gradients at the interface, which would increase the simulation run-times to much more unmanageable levels.

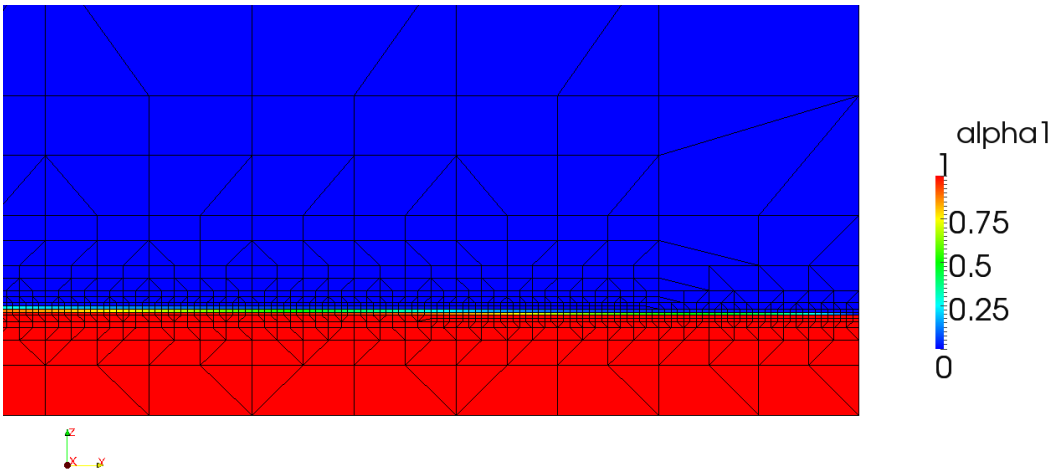

FIGURE C.3: Close view of AMR-VOF Grid 6.7 million cells. (α_1)

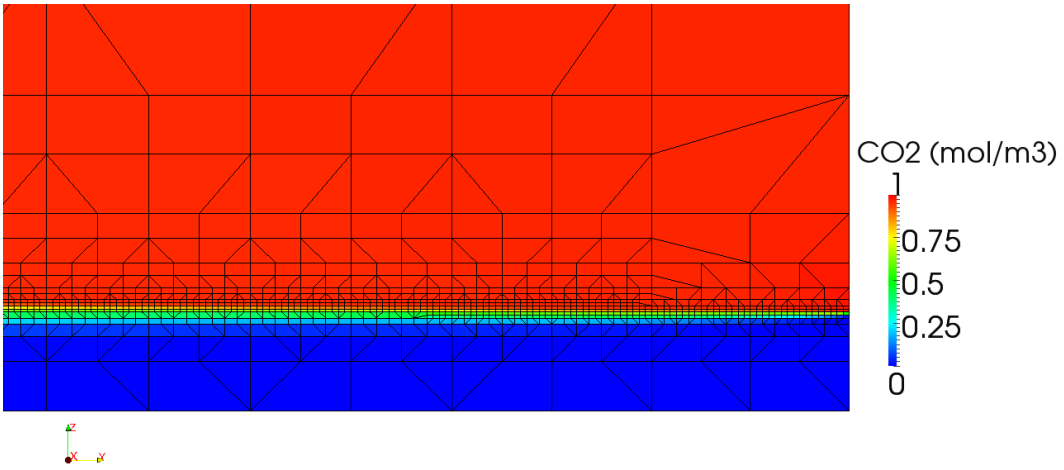

FIGURE C.4: Close view of AMR-VOF Grid 6.7 million cells. (CO_2)

An unresolved grid increases the amount of diffusion through the interface, increasing the absorption flux of acid-gas into the liquid film. It was observed that, for the ESF case the mass transfer through the interface was 26.77% lower in comparison to the AMR-VOF model, as expected, due to the lack of resolution in the AMR-VOF grid.

Bibliography

[1] L. Raynal, P. A. Bouillon, A. Gomez, and P. Broutin, "From MEA to demixing solvents and future steps; a roadmap for lowering the cost of post-combustion carbon capture," *Chemical Engineering Journal*, vol. 171, pp. 742–752, 2011.

[2] P. Alix and L. Raynal, "Liquid distribution and liquid hold-up in modern high capacity packings," *Chemical Engineering Research and Design*, vol. 86, no. 6, pp. 585–591, 2008.

[3] K. Meredith, A. Heather, J. de Vries, and Y. Xin, "A numerical model for partially-wetted flow of thin liquid films," *Computational Methods in Multiphase Flow, VI*, pp. 239–250, 2011.

[4] G. Puxty, R. Rowland, and M. Attalla, "Comparison of the rate of CO¡ sub¿ 2¡/sub¿ absorption into aqueous ammonia and monoethanolamine," *Chemical Engineering Science*, vol. 65, no. 2, pp. 915–922, 2010.

[5] S. Freguia and G. T. Rochelle, "Modeling of CO2 capture by aqueous monoethanolamine," *AIChE Journal*, vol. 49, no. 7, pp. 1676–1686, 2003.

[6] L. Raynal, J. P. Ballaguet, and C. Barrere-Tricca, "Determination of mass transfer characteristics of co-current two-phase flow within structured packing," *Chemical Engineering Science*, vol. 59, no. 22-23, pp. 5395–5402, 2004.

[7] V. Bessou, D. Rouzineau, M. Prévost, F. Abbé, C. Dumont, J. P. Maumus, and M. Meyer, "Performance characteristics of a new structured packing," *Chemical Engineering Science*, vol. 65, no. 16, pp. 4855–4865, 2010.

[8] "Intergovernment panel on climate change (IPCC)," http://www.ipcc.ch/, 2014.

[9] G. Marland, T. Boden, R. Andres, A. Brenkert, and C. Johnston, "Global, regional, and national fossil fuel CO2 emissions," *Trends: A Compendium of Data on Global Change*, pp. 37 831–6335, 2007.

[10] E. Chen, "Carbon Dioxide Absorption into Piperazine Promoted Potassium Carbonate using Structured Packing," Ph.D. dissertation, The University of Texas at Austin, December 2007.

[11] J. Brackbill, D. Kothe, and C. Zemach, "A continuum method for modeling surface tension," *Journal of Computational Physics*, vol. 100, no. 2, pp. 335–354, 1992.

[12] R. Higbie, "The rate of absorption of pure gas into a still liquid during short periods of exposure," *Transactions of the American Institute of Chemical Engineers*, vol. 31, pp. 36–60, 1935.

[13] E. R. Dugas, "Pilot plant study of carbon dioxide capture by aqueous monoethanolamine," Ph.D. dissertation, The University of Texas at Austin, May 2006.

[14] H. Mangalapally and H. Hasse, "Pilot plant study of post-combustion carbon dioxide capture by reactive absorption: Methodology, comparison of different structured packings, and comprehensive results for monoethanolamine," *Chemical Engineering Research and Design*, vol. 89, pp. 1216–1228, 2011.

[15] M. Kohrt, I. Ausner, G. Wozny, and J. U. Repke, "Texture influence on liquid-side mass transfer," *Chemical Engineering Research and Design*, vol. 89, pp. 1405–1413, 2011.

[16] A. Zakeri, A. Einbu, and H. F. Svendsen, "Experimental investigation of pressure drop in structured packings," *Chemical Engineering Science*, vol. 73, no. 0, pp. 285 – 298, 2012.

[17] A. Muzen and M. C. Cassanello, "Liquid holdup in columns packed with structured packings: Countercurrent vs. cocurrent operation," *Chemical Engineering Science*, vol. 60, no. 22, pp. 6226–6234, 2005.

[18] J. M. Plaza, D. V. Wagener, and G. T. Rochelle, "Modeling CO2 capture with aqueous monoethanolamine," *Energy Procedia*, vol. 1, no. 1, pp. 1171–1178, 2009.

[19] L. Øi, "CO2 removal by absorption: challenges in modelling," *Mathematical and Computer Modelling of Dynamical Systems*, vol. 16, no. 6, pp. 511–533, 2010.

[20] L. Raynal and A. Royon-Lebeaud, "A multi-scale approach for CFD calculations of gas-liquid flow within large size column equipped with structured packing," *Chemical Engineering Science*, vol. 62, no. 24, pp. 7196–7204, 2007.

[21] F. Larachi, C. F. Petre, I. Iliuta, and B. Grandjean, "Tailoring the pressure drop of structured packings through CFD simulations," *Chemical Engineering and Processing: Process Intensification*, vol. 42, no. 7, pp. 535 – 541, 2003.

[22] C. F. Petre, F. Larachi, I. Iliuta, and B. P. A. Grandjean, "Pressure drop through structured packings: Breakdown into the contributing mechanisms by CFD modeling," *Chemical Engineering Science*, vol. 58, no. 1, pp. 163–177, 2003.

[23] A. Rafati Saleh, S. H. Hosseini, S. Shojaee, and G. Ahmadi, "CFD Studies of Pressure Drop and Increasing Capacity in MellapakPlus 752.Y Structured Packing," *Chemical Engineering & Technology*, vol. 34, no. 9, pp. 1402–1412, 2011.

[24] Z. Olujic, H. Jansen, B. Kaibel, T. Rietfort, and E. Zich, "Stretching the capacity of structured packings," *Industrial & Engineering Chemistry Research*, vol. 40, no. 26, pp. 6172–6180, 2001.

[25] X. Wen, A. Afacan, K. Nandakumar, and K. Chuang, "Development of a Novel Vertical-Sheet Structured Packing," *Chemical Engineering Research and Design*, vol. 83, no. 5, pp. 515 – 526, 2005.

[26] L. Raynal, C. Boyer, and J. Ballaguet, "Liquid holdup and pressure drop determination in structured packing with CFD simulations," *The Canadian Journal of Chemical Engineering*, vol. 82, no. 5, pp. 871–879, 2004.

[27] L. Raynal, F. Ben Rayana, and A. Royon-Lebeaud, "Use of CFD for CO2 absorbers optimum design: from local scale to large industrial scale," *Energy Procedia*, vol. 1, no. 1, pp. 917–924, 2009.

[28] J. Fernandes, P. Simões, J. Mota, and E. Saatdjian, "Application of CFD in the study of supercritical fluid extraction with structured packing: Dry pressure drop calculations," *The Journal of Supercritical Fluids*, vol. 47, no. 1, pp. 17–24, 2008.

[29] J. Fernandes, P. F. Lisboa, P. C. Simões, J. P. B. Mota, and E. Saatdjian, "Application of CFD in the study of supercritical fluid extraction with structured packing: Wet pressure drop calculations," *The Journal of Supercritical Fluids*, vol. 50, no. 1, pp. 61–68, 2009.

[30] W. Said, M. Nemer, and D. Clodic, "Modeling of dry pressure drop for fully-developed gas flow in structured packing using CFD simulations," *Chemical Engineering Science*, vol. 66, pp. 2107–2117, 2011.

[31] M. Wehrli, S. Hirschberg, and R. Schweizer, "Influence of Vapour Feed Design on the Flow Distribution Below Packings," *Chemical Engineering Research and Design*, vol. 81, no. 1, pp. 116 – 121, 2003.

[32] D. Beugre, S. Calvo, M. Crine, D. Toye, and P. Marchot, "Gas flow simulations in a structured packing by lattice Boltzmann method," *Chemical Engineering Science*, vol. 66, no. 17, pp. 3742 – 3752, 2011.

[33] X. Wen, S. Akhter, A. Afacan, K. Nandakumar, and K. T. Chuang, "CFD modeling of columns equipped with structured packings: I. Approach based on detailed packing geometry," *Asia-Pacific Journal of Chemical Engineering*, vol. 2, no. 4, pp. 336–344, 2007.

[34] M. R. Khosravi Nikou, M. R. Ehsani, and M. Davazdah Emami, "CFD Simulation of Hydrodynamics, Heat and Mass Transfer Simultaneously in Structured Packing," *International Journal of Chemical Reactor Engineering*, vol. 6, p. A91, 2008.

[35] B. Mahr and D. Mewes, "CFD Modelling and Calculation of Dynamic Two-Phase Flow in Columns Equipped with Structured Packing," *Chemical Engineering Research and Design*, vol. 85, no. 8, pp. 1112 – 1122, 2007.

[36] B. Mahr and D. Mewes., "Two-phase flow in structured packings: Modeling and calculation on a macroscopic scale," *AIChE Journal*, vol. 54, no. 3, pp. 614–626, 2008.

[37] C. D. Ho, H. Chang, H. J. Chen, C. L. Chang, H. H. Li, and Y. Y. Chang, "CFD simulation of the two-phase flow for a falling film microreactor," *International Journal of Heat and Mass Transfer*, vol. 54, pp. 3740–3748, 2011.

[38] P. Chasanis, A. Lautenschleger, and E. Y. Kenig, "Numerical investigation of carbon dioxide absorption in a falling-film micro-contactor," *Chemical Engineering Science*, vol. 65, no. 3, pp. 1125–1133, 2010.

[39] J. Chen, C. Liu, X. Yuan, and G. Yu, "CFD simulation of flow and mass transfer in structured packing distillation columns," *Chinese Journal of Chemical Engineering*, vol. 17, no. 3, pp. 381–388, 2009.

[40] Y. Y. Xu, S. Paschke, J. U. Repke, J. Q. Yuan, and G. Wozny, "Computational Approach to Characterize the Mass Transfer between the Counter-Current Gas-Liquid Flow," *Chemical Engineering & Technology*, vol. 32, no. 8, pp. 1227–1235, 2009.

[41] Y. Haroun, D. Legendre, and L. Raynal, "Direct numerical simulation of reactive absorption in gas-liquid flow on structured packing using interface capturing method," *Chemical Engineering Science*, vol. 65, no. 1, pp. 351–356, 2010.

[42] B. Szulczewska, I. Zbicinski, and A. Górak, "Liquid flow on structured packing: CFD simulation and experimental study," *Chemical Engineering & Technology*, vol. 26, no. 5, pp. 580–584, 2003.

[43] H. Lan, J. Wegener, B. Armaly, and J. Drallmeier, "Developing laminar gravity-driven thin liquid film flow down an inclined plane," *Journal of Fluids Engineering*, vol. 132, p. 081301, 2010.

[44] M. Johnson, R. Schluter, M. Miksis, and S. Bankoff, "Experimental study of rivulet formation on an inclined plate by fluorescent imaging," *Journal of Fluid Mechanics*, vol. 394, pp. 339–354, 1999.

[45] Y. Y. Xu, S. Paschke, J. U. Repke, J. Q. Yuan, and G. Wozny, "Portraying the Countercurrent Flow on Packings by Three-Dimensional Computational Fluid Dynamics Simulations," *Chemical Engineering & Technology*, vol. 31, no. 10, pp. 1445–1452, 2008.

[46] F. Gu, C. J. Liu, X. G. Yuan, and G. C. Yu, "CFD simulation of liquid film flow on inclined plates," *Chemical Engineering & Technology*, vol. 27, no. 10, pp. 1099–1104, 2004.

[47] P. Valluri, O. K. Matar, G. F. Hewitt, and M. A. Mendes, "Thin film flow over structured packings at moderate Reynolds numbers," *Chemical Engineering Science*, vol. 60, no. 7, pp. 1965–1975, 2005.

[48] A. Hoffmann, I. Ausner, J. U. Repke, and G. Wozny, "Fluid dynamics in multiphase distillation processes in packed towers," *Computers & Chemical Engineering*, vol. 29, no. 6, pp. 1433–1437, 2005.

[49] A. Hoffmann., I. Ausner, J. U. Repke, and G. Wozny, "Detailed investigation of multiphase (gas-liquid and gas-liquid-liquid) flow behaviour on inclined plates," *Chemical Engineering Research and Design*, vol. 84, no. 2, pp. 147–154, 2006.

[50] Y. Iso and X. Chen, "Flow Transition Behavior of the Wetting Flow Between the Film Flow and Rivulet Flow on an Inclined Wall," *Journal of Fluids Engineering*, vol. 133, p. 091101, 2011.

[51] Y. Iso, J. Huang, M. Kato, S. Matsuno, and K. Takano, "Numerical and Experimental Study on Liquid Film Flows on Packing Elements in Absorbers for Post-combustion CO2 Capture," *Energy Procedia*, vol. 37, pp. 860 – 868, 2013.

[52] L. Schwartz and D. Weidner, "Modeling of coating flows on curved surfaces," *Journal of Engineering Mathematics*, vol. 29, no. 1, pp. 91–103, 1995.

[53] R. V. Roy, A. J. Roberts, and M. E. Simpson, "A lubrication model of coating flows over a curved substrate in space," *Journal of Fluid Mechanics*, vol. 454, pp. 235–261, 3 2002.

[54] R. J. Braun and A. Fitt, "Modelling drainage of the precorneal tear film after a blink," *Mathematical Medicine and Biology*, vol. 20, no. 1, pp. 1–28, 2003.

[55] J. Grotberg, "Pulmonary flow and transport phenomena," *Annual Review of Fluid Mechanics*, vol. 26, no. 1, pp. 529–571, 1994.

[56] A. Oron, S. H. Davis, and S. G. Bankoff, "Long-scale evolution of thin liquid films," *Rev. Mod. Phys.*, vol. 69, pp. 931–980, Jul 1997.

[57] R. V. Craster and O. K. Matar, "Dynamics and stability of thin liquid films," *Rev. Mod. Phys.*, vol. 81, pp. 1131–1198, Aug 2009.

[58] S. Kalliadasis, C. Ruyer-Quil, B. Scheid, and M. G. Velarde, *Falling liquid films*. Springer Science & Business Media, 2011, vol. 176.

[59] S. V. Alekseenko, V. Y. Nakoryakov, and B. G. Pokusaev, "Wave formation on a vertical falling liquid film," *AIChE Journal*, vol. 31, no. 9, pp. 1446–1460, 1985.

[60] S. V. Alekseenko, V. A. Antipin, V. V. Guzanov, S. M. Kharlamov, and D. M. Markovich, "Three-dimensional solitary waves on falling liquid film at low reynolds numbers," *Physics of Fluids*, vol. 17, no. 12, 2005.

[61] C. Park and T. Nosoko, "Three-dimensional wave dynamics on a falling film and associated mass transfer," *AIChE Journal*, vol. 49, no. 11, pp. 2715–2727, 2003.

[62] W. Nusselt, "Die Oberflchenkondensation des Wasserdampfes," *Zeitschrift des Vereines Deutscher Ingenieure*, vol. 60, pp. 541–546 and 569–575, 1916.

[63] C. Ruyer-Quil and P. Manneville, "Modeling film flows down inclined planes," *European Physical Journal B*, vol. 6, no. 2, pp. 277–292, NOV 1998.

[64] V. Y. Shkadov, "Wave flow regimes of a thin layer of viscous fluid subject to gravity," *Fluid Dynamics*, vol. 2, no. 1, pp. 29–34, 1967.

[65] C. Ruyer-Quil and P. Manneville, "Improved modeling of flows down inclined planes," *European Physical Journal B*, vol. 15, no. 2, pp. 357–369, MAY 2000.

[66] D. Tseluiko and S. Kalliadasis, "Nonlinear waves in counter-current gas-liquid film flow," *Journal of Fluid Mechanics*, vol. 673, pp. 19–59, APR 2011.

[67] R. Vellingiri, D. Tseluiko, and S. Kalliadasis, "Absolute and convective instabilities in counter-current gas-liquid film flows," *Journal of Fluid Mechanics*, vol. 763, pp. 166–201, 1 2015.

[68] G. Lavalle, J.-P. Vila, G. Blanchard, C. Laurent, and F. Charru, "A numerical reduced model for thin liquid films sheared by a gas flow," *Journal of Computational Physics*, vol. 301, pp. 119 – 140, 2015.

[69] S. Troian, E. Herbolzheimer, S. Safran, and J. Joanny, "Fingering instabilities of driven spreading films," *EPL (Europhysics Letters)*, vol. 10, no. 1, p. 25, 1989.

[70] W. Whitman, "Preliminary experimental confirmation of the two-film theory of gas absorption," *Chem. Metall. Eng.*, vol. 29, pp. 146–148, 1923.

[71] P. Danckwerts, "Significance of liquid-film coefficients in gas absorption," *Industrial & Engineering Chemistry*, vol. 43, no. 6, pp. 1460–1467, 1951.

[72] A. Kohl and R. Nielsen, *Gas purification 5th ed.* Houston: Gulf Publishing Company, 1997.

[73] M. Baniadam, J. Fathikalajahi, and M. R. Rahimpour, "Incorporation of Eulerian-Eulerian CFD framework in mathematical modeling of chemical absorption of acid gases into methyl diethanol amine on sieve trays," *Chemical Engineering Journal*, vol. 151, no. 1-3, pp. 286–294, 2009.

[74] G. Versteeg, L. Dijck, and W. Swaaij, "On the kinetics between co2 and alkanolamines both in aqueous and non-aqueous solutions. an overview." *Chemical Engineering Communications*, vol. 144, pp. 113–158, 1996.

[75] K. Asano, *Mass Transfer: From Fundamentals to Modern Industrial Applications*. John Wiley & Sons, 2007.

[76] E. P. van Elk, "Gas-liquid reactions: influence of liquid bulk and mass transfer on process performance," Ph.D. dissertation, Universiteit Twente, Oct 2001.

[77] R. Bottoms, "Process for separating acid gases," Dec. 2 1930, US Patent 1,783,901.

[78] O. Bavbek and E. Alper, "Reaction mechanism and kinetics of aqueous solutions of primary and secondary alkanolamines and carbon dioxide," *Turkish Journal of Chemistry*, vol. 23, pp. 293–300, 1999.

[79] M. Caplow, "Kinetics of carbamate formation and breakdown," *Journal of the American Chemical Society*, vol. 90, no. 24, pp. 6795–6803, 1968.

[80] P. Danckwerts, "The reaction of CO2 with ethanolamines," *Chemical Engineering Science*, vol. 34, no. 4, pp. 443–446, 1979.

[81] G. Versteeg and W. Swaaij, "On the kinetics between CO2 and alkanolamines both in aqueous and non-aqueous solutions–I. Primary and secondary amines," *Chemical Engineering Science*, vol. 43, no. 3, pp. 573–585, 1988.

[82] A. Kidnay, W. Parrish, and D. McCartney, *Fundamentals of Natural Gas Processing, Second Edition*, ser. Mechanical engineering. CRC Press, 2011.

[83] T. Letcher, *Future Energy: Improved, Sustainable and Clean Options for our Planet*. Elsevier Science, 2013.

[84] A. Bahadori, *Natural Gas Processing: Technology and Engineering Design*. Elsevier Science, 2014.

[85] M. Goel, *Carbon Capture, Storage and, Utilization: A possible climate change solution for energy industry*. Energy and Resources Institute, 2014.

[86] G. Couchaux, D. Barth, M. Jacquin, A. Faraj, and J. Grandjean, "Kinetics of carbon dioxide with amines. i. stopped-flow studies in aqueous solutions. a review," *Oil & Gas Science and Technology–Revue d?IFP Energies nouvelles*, vol. 69, no. 5, pp. 865–884, 2014.

[87] H. Kierzkowska-Pawlak and A. Chacuk, "Kinetics of carbon dioxide absorption into aqueous mdea solutions," *Ecol. Chem. Eng. S*, vol. 17, no. 4, pp. 463–475, 2010.

[88] B. Mandal, M. Guha, A. Biswas, and S. Bandyopadhyay, "Removal of carbon dioxide by absorption in mixed amines: modelling of absorption in aqueous MDEA/MEA and AMP/MEA solutions," *Chemical Engineering Science*, vol. 56, no. 21-22, pp. 6217 – 6224, 2001, proceedings of the 5th International Conference on Gas-Liquid and Gas-Liquid-Solid Reactor Engineering.

[89] A. Aboudheir, P. Tontiwachwuthikul, A. Chakma, and R. Idem, "Kinetics of the reactive absorption of carbon dioxide in high CO2-loaded, concentrated aqueous monoethanolamine solutions," *Chemical Engineering Science*, vol. 58, no. 2324, pp. 5195 – 5210, 2003.

[90] G. Wang, X. Yuan, and K. Yu, "Review of Mass-Transfer Correlations for Packed Columns*," *Industrial & Engineering Chemistry Research*, vol. 44, no. 23, pp. 8715–8729, 2005.

[91] M. Klöker, E. Kenig, and A. Górak, "On the development of new column internals for reactive separations via integration of CFD and process simulation," *Catalysis Today*, vol. 79, pp. 479–485, 2003.

[92] Y. Haroun, L. Raynal, and D. Legendre, "Mass transfer and liquid hold-up determination in structured packing by CFD," *Chemical Engineering Science*, vol. 75, pp. 342 – 348, 2012.

[93] M. Ohta and M. Suzuki, "Numerical analysis of mass transfer from a free motion drop in a solvent extraction process," *Solvent Extraction Research and Development*, vol. 3, pp. 138–149, 1996.

[94] M. R. Davidson and M. Rudman, "Volume-of-fluid calculation of heat or mass transfer across deforming interfaces in two-fluid flow," *Numerical Heat Transfer Part B: Fundamentals*, vol. 41, no. 3-4, pp. 291–308, 2002.

[95] D. Bothe, M. Koebe, K. Wielage, and H. Warnecke, "VOF simulations of mass transfer from single bubbles and bubble chains rising in the aqueous solutions," in *Proceedings of FEDSM*, vol. 3, 2003, pp. 6–11.

[96] C. Yang and Z. Mao, "Numerical simulation of interphase mass transfer with the level set approach," *Chemical Engineering Science*, vol. 60, no. 10, pp. 2643–2660, 2005.

[97] Y. Haroun, D. Legendre, and L. Raynal, "Volume of fluid method for interfacial reactive mass transfer: Application to stable liquid film," *Chemical Engineering Science*, vol. 65, no. 10, pp. 2896–2909, 2010.

[98] A. A. Ganguli and E. Y. Kenig, "A CFD-based approach to the interfacial mass transfer at free gas-liquid interfaces," *Chemical Engineering Science*, vol. 66, pp. 3301–3308, 2011.

[99] A. Hassanvand and S. H. Hashemabadi, "Direct numerical simulation of interphase mass transfer in gas-liquid multiphase systems," *International Communications in Heat and Mass Transfer*, vol. 38, pp. 943–950, 2011.

[100] J. Liu, S. Wang, B. Zhao, H. Tong, and C. Chen, "Absorption of carbon dioxide in aqueous ammonia," *Energy Procedia*, vol. 1, no. 1, pp. 933–940, 2009.

[101] OpenCFD, *OpenFOAM: The Open Source CFD Toolbox. User Guide Version 2.0.1.* OpenCFD Ltd., Reading UK, 2011.

[102] OpenCFD., *OpenFOAM: The Open Source CFD Toolbox. Programmer's Guide Version 2.0.1.* OpenCFD Ltd., Reading UK, 2011.

[103] C.W. Hirt and B.D. Nichols, "Volume of fluid (VOF) method for the dynamics of free boundaries," *Journal of Computational Physics*, vol. 39, no. 1, pp. 201 – 225, 1981.

[104] H. Rusche, "Computational Fluid Dynamics of Dispersed Two-Phase Flows at High Phase Fractions," Ph.D. dissertation, Imperial College, University of London, Dec 2002.

[105] E. Berberović, N. P. van Hinsberg, S. Jakirlić, I. V. Roisman, and C. Tropea, "Drop impact onto a liquid layer of finite thickness: Dynamics of the cavity evolution," *Physical Review E*, vol. 79, no. 3, p. 036306, 2009.

[106] Y. Haroun, "Etude du transfert de masse réactif gaz-liquide le long de plans corrugués par simulation numérique avec suivi d'interface," Ph.D. dissertation, Institut National Polytechnique de Toulouse, 2008.

[107] H. Jasak, "Error analysis and estimation for the finite volume method with applications to fluid flows." Ph.D. dissertation, Imperial College London (University of London), 1996.

[108] J. H. Ferziger and M. Perić, *Computational methods for fluid dynamics*, 3rd ed. Springer Berlin, 2002.

[109] R. I. Issa, "Solution of the implicitly discretised fluid flow equations by operator-splitting," *Journal of Computational physics*, vol. 62, no. 1, pp. 40–65, 1986.

[110] G. F. Dietze, W. Rohlfs, K. Nhrich, R. Kneer, and B. Scheid, "Three-dimensional flow structures in laminar falling liquid films," *Journal of Fluid Mechanics*, vol. 743, pp. 75–123, 3 2014.

[111] C. Huh and L. Scriven, "Hydrodynamic model of steady movement of a solid/liquid/fluid contact line," *Journal of Colloid and Interface Science*, vol. 35, no. 1, pp. 85–101, 1971.

[112] M. Renardy, Y. Renardy, and J. Li, "Numerical simulation of moving contact line problems using a volume-of-fluid method," *Journal of Computational Physics*, vol. 171, no. 1, pp. 243–263, 2001.

[113] J. Walther, R. Jaffe, T. Werder, T. Halicioglu, and P. Koumoutsakos, "On the boundary condition for water at a hydrophobic, dense surface," *Center for Turbulence Research, Proceedings of the Summer Program*, 2002.

[114] A. Theodorakakos and G. Bergeles, "Simulation of sharp gas–liquid interface using VOF method and adaptive grid local refinement around the interface," *International Journal for Numerical Methods in Fluids*, vol. 45, no. 4, pp. 421–439, 2004.

[115] H. Jasak and A. Gosman, "Automatic resolution control for the finite-volume method, Part 2: Adaptive mesh refinement and coarsening," *Numerical Heat Transfer: Part B: Fundamentals*, vol. 38, no. 3, pp. 257–271, 2000.

[116] P. Brambilla and A. Guardone, "Automatic tracking of corona propagation in three-dimensional simulations of non-normal drop impact on a liquid film," *Computing*, pp. 1–10, 2013.

[117] N. Nikolopoulos, A. Theodorakakos, and G. Bergeles, "Three-dimensional numerical investigation of a droplet impinging normally onto a wall film," *Journal of Computational Physics*, vol. 225, no. 1, pp. 322–341, 2007.

[118] J. Cooke, S. Gu, L. Armstrong, and K. Luo, "Gas-Liquid Flow on Smooth and Textured Inclined Planes," *World Academy of Science, Engineering and Technology*, vol. 68, pp. 1712–1719, 2012.

[119] J. A. Diez and L. Kondic, "Computing three-dimensional thin film flows including contact lines," *Journal of Computational Physics*, vol. 183, no. 1, pp. 274–306, 2002.

[120] A. A. King, L. J. Cummings, S. Naire, and O. E. Jensen, "Liquid film dynamics in horizontal and tilted tubes: Dry spots and sliding drops," *Physics of Fluids (1994-present)*, vol. 19, no. 4, p. 042102, 2007.

[121] J. Cooke, L. Armstrong, K. Luo, and S. Gu, "Adaptive Mesh Refinement of Gas-Liquid Flow on an Inclined Plane," *Computers and Chemical Engineering*, vol. 60, pp. 297–306, 2014.

[122] P. Danckwerts, *Gas-Liquid-Liquid Reaction.* McGraw-Hill, New York., 1970.

[123] W. DeCoursey, "Absorption with chemical reaction: development of a new relation for the danckwerts model," *Chemical Engineering Science*, vol. 29, no. 9, pp. 1867–1872, 1974.

[124] M. Wanga, A. Lawala, P. Stephenson, J. Sidders, C. Ramshawa, and H. Yeunga, "Post-combustion co2 capture with chemical absorption: A state-of-the-art review," *Chemical Engineering Research and Design*, vol. 89, no. 9, pp. 1609–1624, 2011.

[125] H. D. Baehr and K. Stephan, *Heat and Mass Transfer, 2nd ed.* Springer , Berlin, 2006.